UNIVERSITY OF STRATHCLYDE
Department of Physics

Hybrid GaN-based optoelectronics for Visible Light Communications

by

João Miguel Melo Santos

A thesis presented in fulfilment of the
requirements for the degree of
Doctor of Philosophy

January 2017

Declaration of Authorship

This thesis is the result of the author's original research. It has been composed by the author and has not been previously submitted for examination which has led to the award of a degree.

The copyright of this thesis belongs to the author under the terms of the United Kingdom Copyright Acts as qualified by University of Strathclyde Regulation 3.50. Due acknowledgement must always be made of the use of any material contained in, or derived from, this thesis.

Signed:

Date:

Frontispiece

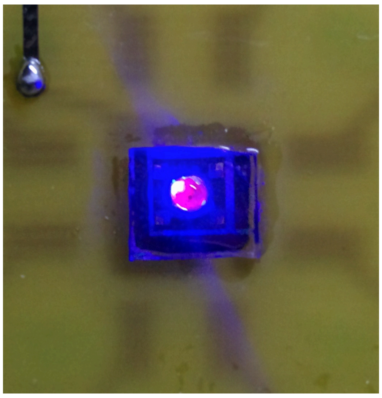

(i) Hybrid GaN µLED and III-V colour-converter with integrated sapphire lens under operation.

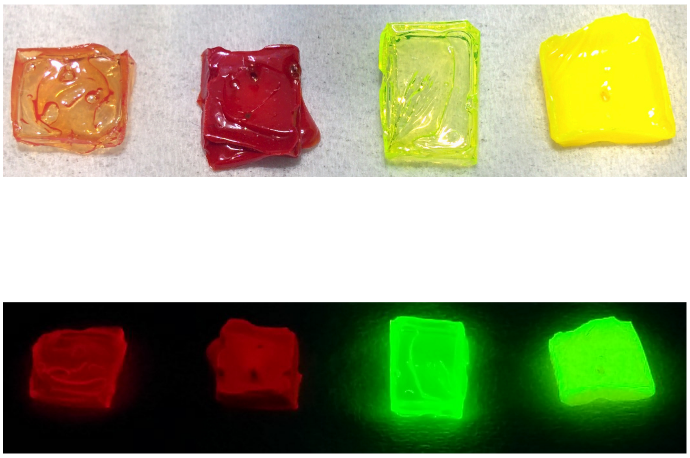

(ii) White-light reference images and UV-excited fluorescence of red and green colloidal quantum dot composites at different concentrations.

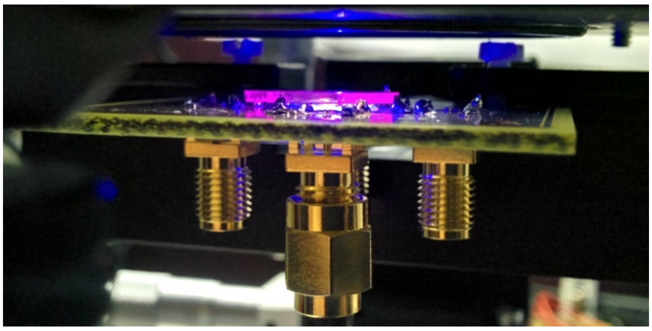

(iii) III-V semiconductor capillary bonded onto a glass cover and pumped with a blue GaN µLED.

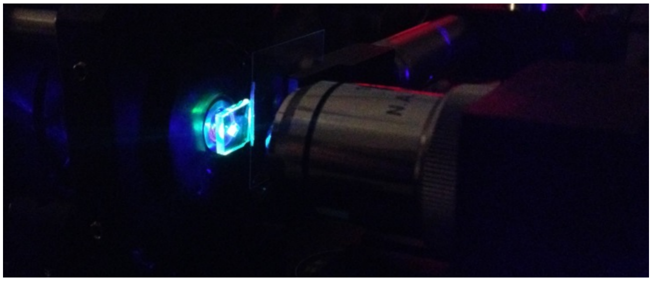

(iv) II-VI semiconductor on a glass cover pumped with a GaN laser diode.

Abstract

Development of light-emitting diode technology is driven mainly by the need for efficient solid-state lighting, but it is also creating opportunities for new applications such as visible light communications (VLC). Here, the solid-state visible light sources are used to transmit data with the added requirement of a short excited-state lifetime so that sources can be modulated at high speed. This research focuses on hybrid optical sources for visible light communications with an emphasis on novel formats of colour-converters for multi-wavelength photoluminescence as well as white-light generation. Such converters include red and green colloidal quantum dots, the organic semiconductor BBEHPV and II-VI / III-V epitaxial structures.

Solution-processable and environmentally stable polymeric films based on red and green colloidal quantum dots are demonstrated. Modulation bandwidth up to 24 MHz, photoluminescence quantum yields up to 61% and peak emission tunability across the visible spectrum makes these materials interesting as colour-converters for VLC. Free-space data transmission was demonstrated in this case with data rates up to 400 Mbit/s and 500 Mbit/s using 2-PAM modulation scheme for green and red quantum dots, respectively.

Hybrid sources consisting of 450nm InGaN LEDs with capillary-bonded micron-thick ZnCdSe/ZnCdMgSe multi-quantum-well colour-converting membranes with peak emission at 540 nm are reported. After processing, the membrane was capillary bonded onto the sapphire side of the μLED resulting in a maximum converted average power of 37 μW. The -3dB optical modulation bandwidth of the bare LED, hybrid device and II-VI were 79 MHz, 51 MHz and 145 MHz, respectively.

Visible light communication using both InGaN LEDs and a InGaN laser diode, down-converted by a red-emitting AlInGaP multi-quantum-well nanomembrane are also reported. Similarly to the previous devices, the AlInGaP nanomembrane was bonded onto the μLED array. For the down-converted laser diode approach, the nanomembrane can be sandwiched between a sapphire lens and optionally onto a distributed feedback reflector. The down-converter structure is remotely excited by the laser diode. Data transmission up to 870 Mb/s using *M*-PAM and OFDM modulation schemes is demonstrated for the μLED integrated nanomembrane. ODFM transmission at 1.2Gb/s is achieved for the laser diode pumped sample.

Acknowledgements

First of all, I would like to thank my supervisor, Prof. Martin Dawson for the opportunity to do my PhD in such thrilling project at the Institute of Photonics, for his help, knowledge and guidance throughout these years.

I would like to thank in particular my second supervisor, Dr. Nicolas Laurand for his guidance, knowledge, patience and highly valuable discussions during my PhD.

To Dr. Benoit Guilhabert for all his help, training, advices and significant discussions during my studies.

To Dr. Enyuan Xie for taking time in the fabrication of the µLEDs used along this work.

A big thanks goes to Dr. Jonathan McKendry, Dr. Scott Watson and Dr. Anthony Kelly for the help, discussions and letting me use the equipment at Glasgow University to perform the bandwidth measurements.

To Dr. Sujan Rajbhandari for is patience and help during the telecom measurements at Oxford University.

My colleagues at IoP for these three years. I'm fortunate enough to have made some good friends here.

At last, the most important thanks goes to my family. I was fortunate enough to have you. *Obrigado por tudo*!

Contents

List of Figures

List of Tables

Abbreviations

ADC	Analogue-to-Digital Converter
Al	Aluminium
Al_20_3	Sapphire
APD	Avalanche Photodiode
Au	Gold
AWG	Arbitrary Waveform Generator
BBEHP-PPV	Poly[2,5-bis(2',5'-bis(2"-ethylhexyloxy)phenyl)-p-phenylenevinylene]
BER	Bit Error Rate
c	Speed of Light
CCD	Charge-Coupled Device
Cd	Cadmium
CFD	Constant Function Discriminator
CQDs	Colloidal Quantum Dots
CW	Continuous Wave
DC	Direct Current
DI	Deionized water
e	Electron charge
EAM	Electro-Absorption Modulator
E_c	Conduction Band Energy
E_g	Bandgap Energy
EQE	External Quantum Efficiency
E_v	Valence Band Energy
FEC	Forward Error Correction
FES0500/FEL0550/FEL0500	Bandpass optical filters
FRET	Förster/Fluorescence Resonance Energy Transfer
FWHM	Full Width Half Maximum
Ga	Gallium
GaN	Gallium Nitride

Ge	Germanium
GoF	Goodness of the Fit
GPS	Global Positioning System
h	Planck constant
H_20_2	Hydrogen Peroxide
H_2O	Water
H_3PO_4	Phosphoric Acid
HCl	Hydrogen Chloride
HOMO	Highest Occupied Molecular Orbital
I	Current
I-V	Current-voltage
IFFT	Inverse Fast Fourier Transform
IM/DD	Impulse Modulation / Direct Detection
In	Indium
IQE	Internal Quantum Efficiency
IRR	Imprisonment of Resonant Radiation
ISI	Intersymbol interference
k	Boltzmann constant
L-I	Optical power-current
λ	Wavelength
LD	Laser Diode
LED	Light-Emitting Diode
LUMO	Lowest Unoccupied Molecular Orbital
m^*	Carrier Effective Mass
MBE	Molecular Beam Epitaxy
m_e	Effective Mass of Electrons
Mg	Magnesium
m_h	Effective Mass of Holes
μLED	micro-LED
MOCVD	Metal-Organic Chemical Vapour Deposition
MOVPE	Metalorganic vapour phase epitaxy
MQW	Multi-Quantum Well
N	Nitride

NA	Numerical Aperture
Ni	Nickel
NRZ	Non-Return-to-Zero
OFDM	Orthogonal Frequency-Division Modulation
OOK	On-Off Keying
P	Phosphorous
PAM	Pulse-Amplitude Modulation
PDMS	Poly(dimethylsiloxane)
PECVD	Plasma-Enhanced Chemical Vapour Deposition
PGA	Programmable Gain Amplifier
PL	Photoluminescence
PLQY	Photoluminescence Quantum Yield
PMMA	Poly(methyl methacrylate)
PPM	Pulse-Position Modulation
RF	Radio Frequency
RGB	Red, Green and Blue
RGBY	Red, Green, Blue and Yellow
RPM	Revolutions-per-Minute
RZ	Return-to-Zero
S	Sulphur
Se	Selenium
SHR	Shockley, Read and Hall
Si	Silicon
SiC	Silicon Carbide
SSL	Solid-State Lighting
SU8	High-aspect ratio negative photoresist
T	Temperature
TAC	Time-to-Amplitude converter
TCSPC	Time-Correlated Single-Photon Counting
Ti	Titanium
$\tau_{\nu\rho}$	Non-Radiative lifetime
τ_{ρ}	Radiative lifetime
UV	Ultraviolet

f/v	Frequency
V	Voltage
VECSEL	Vertical External Cavity Surface Emitting Laser
VLC	Visible Light Communications
V_{th}	Threshold voltage
WD	Window Discriminator
WDM	Wavelength-Division Multiplexing
WLED	White Light-Emitting Diode
Zn	Zinc
ZnO	Zinc Oxide

Chapter 1

Introduction

1.1 Motivation

Solid-state lighting, a technology based on electroluminescence, has been under development for over a century. Electroluminescence was first noticed by Henry Joseph Round in 1907 during an experiment in which, on electrically driving different crystals, a yellow, blue and green luminescence signal could be seen [1]. The first experiments in this area used II-VI alloys such as silicon carbide (SiC), named 'carborundum' by Round at the time [1]. The following years were spent in the development of new growth processes and deposition mechanisms to improve the light-emitting diodes (LEDs) based on these semiconductor alloys, however the electrical to optical efficiencies were very low due to the alloys' indirect bandgap [2]. During the 1950s Heinrich Welker started to develop III-V compounds as an alternative, creating new paths for novel optoelectronic devices. By the 1990's, efficient red and near-infrared III-V LEDs were being developed but visible emitters based on nitrides were of low efficiency mainly due to the lack of a *p*-type conductivity. However, work by Isamu Akasaki, Hiroshi Amano and Shuji Nakamura allowed increased efficiencies of nitride LEDs and laser diodes through both improved crystal growth techniques and the activation of *Mg* dopants using either electron beam irradiation or a high-temperature post-growth annealing process [2]. These developments permitted the creation of efficient blue light-emitting diodes and facilitated the emergence of solid-state white lighting, contribution for which these investigators received the 2014 Nobel Prize in Physics.

The rapid development of light-emitting diodes allied to research on novel photonic materials, has allowed this device technology to mature to the point where advanced visible LEDs are now starting to pervade our daily life. The widespread application of these devices, driven mainly by the development of efficient solid-state illumination systems, are due to their high electrical-to-optical efficiency, low power consumption and long lifetime as well as their compatibility for integration, making them greatly superior to the standard incandescent and fluorescent light bulbs that have been used for lighting so far [3]. Nowadays, efficient visible LED technology can be found for example in displays [4], in lighting systems [5] and in cars as head/tail lights [6].

Solid-state lighting and other related applications rely on white-emitting LEDs. The ideal approach to achieve this would use three-colour LED chips, *i.e.* it is possible to generate white light by the combination of red, blue and green chips. However, this is currently expensive and complicated since each chip has a different efficiency and spectral variation with temperature and can age differently. Furthermore, although efficient blue and red LEDs can be fabricated using InGaN and AlGaInP alloys, respectively, nitrides offer relatively poor performance in the yellow/green spectral region. This is known as the 'green gap' and is represented in Figure 1.1, [7].

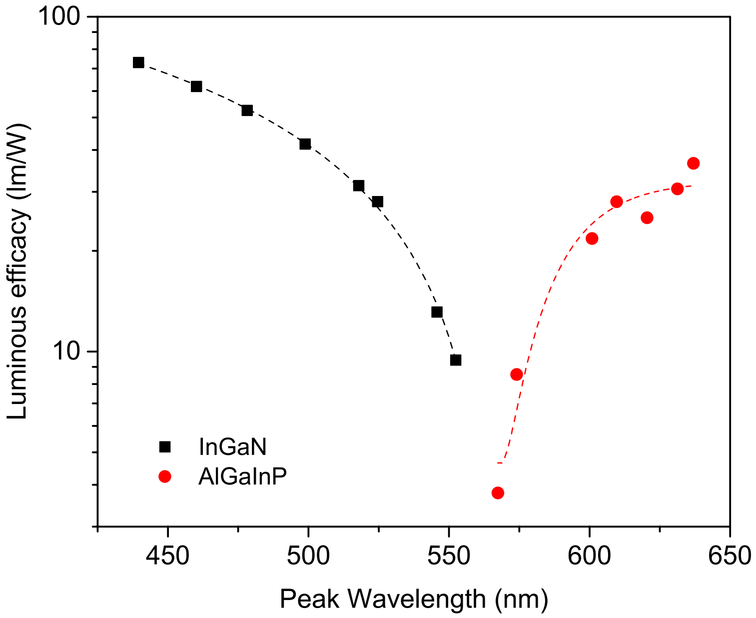

Figure 1.1 – Luminous efficacy for InGaN and AlGaInP LEDs (after [7], [8]*).*

To address the lack of efficient yellow/green LEDs, photoluminescent materials started to be used. The generation of white-light in this case occurs mainly through the combination of the blue light from an InGaN LED and yellow light from a phosphor, although several phosphors can be combined for improved light quality. Commercial white LEDs are generally based on a blue InGaN chip over-coated with a phosphor material such as Ce:YAG for colour-conversion. These types of white LEDs (WLEDs) are now rapidly replacing traditional light-bulbs and their fast deployment combined with their optoelectronic characteristics is creating novel applications.

Very recently, there has been a growing interest in utilising such white LEDS for Visible Light Communications (VLC), to complement established RF communications [3]. This is primarily because the increasing requirement for more and faster RF communication systems faces severe challenges because of the limited RF spectrum. VLC aims to create a 'smart' lighting solution by adding the function of communication to illumination. Some advantages associated with this kind of configuration are related to the potential for high speed modulation of the LED source, offering a high data bandwidth wherever lighting is present. Such modulation is imperceptible to the human eye, allowing useful data rates while not affecting the LED's primary illumination function [9], [10]. VLC as a wireless (optical wireless) communication solution also has the advantage of not producing or being susceptible to electromagnetic interference, allowing its use in places where radio-frequencies are prohibited such as in aeroplanes or in medical diagnostics areas. Furthermore, VLC uses unlicensed bandwidth and provides a more secure information exchange since the emitted light is confined in a room or a particular area [3], [9], [10], [12]. Figure 1.2 shows a schematic illustrating a few possible ways envisioned for future use of VLC. We note that the impact of VLC is not only limited to white-light communications, as discrete coloured visible sources can be used as well.

One bottleneck of using commercial white LEDs for VLC is the modulation speed of the current devices. In a hybrid system, as depicted in the schematic presented in Figure 1.3, the modulation speed is set by the response time of the slowest component. In the case of an LED and a traditional phosphor, the maximum bandwidth is set by the latter since the fluorescence mechanism is much slower than the electron-hole recombination time in the LED. Rare-earth phosphors used in current white LEDs have an upper-state lifetime between μs to *ms,* which limits the overall white-light modulation speed to a few *MHz* [3], [13].

Figure 1.2 – a) Scheme of a VLC configuration [3].

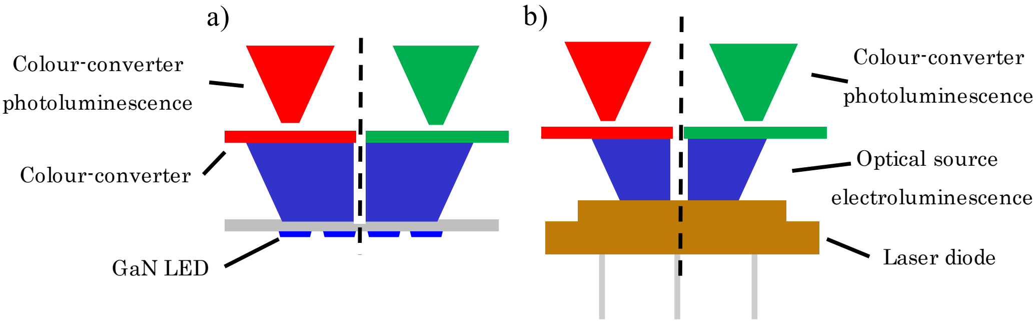

Figure 1.3 – Schematic of a hybrid configuration using a) a GaN LED and b) InGaN laser diode. Organic semiconductors, colloidal quantum dots and epitaxial structures can be used as colour-converter materials for the red and green spectral regions.

One way to improve the bandwidth of VLC systems is to use a filter at the receptor end in order to remove the phosphor component but this introduces a reception signal penalty because of a lower detected signal [3]. Due to these constraints, there is a critical need to find alternatives to phosphor colour-converters, both for white-light generation and also for single-colour emission, with faster modulation response and no compromise on other characteristics.

There are other application areas where modulated visible and/or white light can be applied such as underwater and vehicle-to-vehicle communications [6], [14], indoors GPS [15] and the Internet of Things [16]. The implementation and deployment of this technology will increase safety and address current limitations. Underwater communications at the moment mainly use ultrasonic communications, however they are limited by noise caused by reflections at the surface and the ocean floor [17].

With the recent deployment of solid-state lighting by car/motorbike manufacturers as tail or headlights, visible light communications can be employed to add the capability for inter-vehicle communication or even vehicle-infrastructure communications. The implementation of such system can potentially speed-up the introduction of self-driving cars. The main constraint is that sunlight and ambient light can impair the system functionality by the creation of noise at the receiver side limiting the performance of VLC [14].

1.2 Thesis outline

The main focus of this thesis is on novel organic/inorganic semiconductors as colour-converters for VLC. Candidate materials that were studied and are presented here include Colloidal Quantum Dots (CQDs), III-V and II-IV semiconductor epitaxial structures and organic semiconductors such as BBEHP-PPV. All of them have the particularity of emitting in the visible with shorter lifetimes than the typical colour-converter phosphors. This makes it possible to increase the data transmission speed and possibly the number of telecommunication channels when used in a wavelength-division multiplexing configuration.

The rest of this chapter presents the physical background and working principles of the down-converter materials and optical sources used. A very brief explanation of telecommunications will be presented in order to support some of the work performed with the optical sources and colour-converters. In Chapter 2, the experimental set-ups used during this work and the results of the optical tests performed on the optical sources will be presented. Chapter 3 and Chapter 4 describe the down-converters' CW and dynamic characteristics and their respective analysis. Work towards the creation and manipulation of white light is presented in Chapter 5. Finally, concluding remarks and tentative future work are presented in Chapter 6.

1.3 Solid-state lighting

Solids can be grouped in three different categories according to their capability to conduct electricity. There are the conductors, semiconductors and insulators. Solid-state lighting is based on semiconductor materials.

These materials can be described by reference to a diagram of energy bands. In this diagram, there are two main energy level manifolds, the conduction and valence bands, with the conduction band at a higher energy level than the valence band. Between them there can be an energy bandgap which is characterised by an absence of energy levels. This plays a major role in the determination of electrical and optical properties of a material, as will be explained below.

In insulating materials, the band separation can be higher than 4 eV making the excitation of an electron to the conduction band very difficult. Thermally excited electrons do not have the required energy 'to jump' the bandgap (kT at room temperature is ~25meV) leading to zero conductivity or extremely high resistance to the flow of charges through insulators. For conductive materials, there is band overlap so it is much easier for electrons to flow through the material's crystal lattice. Besides, conduction electrons are not tightly bound to the atoms making them easier to be externally excited.

Semiconductor materials present electrical characteristics in between those of insulators and conductors. At T=0K, the valence band of a semiconductor is completely filled with electrons whilst the conduction band is totally empty. The electrical properties of semiconductors can be tuned accordingly via temperature change, through the introduction of impurities (or dopants) or via external excitation (*e.g.* optical or electrical). These materials can be further split in two categories, the intrinsic or elemental and extrinsic semiconductors.

Elemental semiconductors are materials in which the crystal lattice is made from only one type of atom. The most studied elemental semiconductors so far are silicon (*Si*) and germanium (*Ge*). In an intrinsic silicon semiconductor, for example, each atom from the crystal lattice is connected to its neighbours by a covalent bond since each has four valence electrons (electrons in the outer shell). With temperature rise, the electrons may gain energy and dissociate the bond, leaving a vacancy or 'hole' to be filled by another electron. In this condition, for every free electron there is only one free vacancy and so intrinsic semiconductors are considered neutrally charged.

The density of carriers can be increased through the incorporation of impurities. Considering a replacement of a silicon atom by an atom from group V (with five electrons in the valence band) in the periodic table, four out of the five electrons will form covalent bonds with the neighbouring atoms leaving one electron free. The free charge can then be excited to become a conduction electron and the material becomes negatively charged or *n*-type. Similarly, replacing silicon atoms from the initial structure by elements from group III (with three valence electrons) will make the material positively charged, or *p*-type, since a hole is created from the missing electron to complete the four covalent bonds. The movement of free electrons and holes across the crystal lattice is the mechanism responsible for the conduction of electricity.

1.3.1 Radiative and non-radiative recombination

The recombination of an electron in the conduction band with a hole in the valence band results in the emission of energy either by heat (associated with vibration of the atoms in the crystal lattice, known as phonons) or by the emission of a photon (luminescence). The dissipated energy during the process in both cases can be determined through the difference in energy between the minimum of the conduction band and the maximum of the valence band:

$$E_g = E_c - E_v \tag{1.1}$$

where E_g, E_c and E_v are the bandgap, the conduction and the valence band energies, respectively. If a photon is emitted, its wavelength or frequency can be determined through the bandgap energy. This relation can be described by:

$$E_g = hv = h\frac{c}{\lambda} \tag{1.2}$$

where h is the Planck constant, c is the speed of light and v and λ are the frequency and the wavelength associated with the emitted photon. This is interesting since through the manipulation of the bandgap energy, semiconductors can be designed in order to adjust the optical properties of the emitted light. In compound semiconductors, such as AlGaInP or InGaN, the emission tuning is performed by adjusting the relative amount of the various elements (alloys) in the structure.

Semiconductors can be separated in two categories, namely direct and indirect bandgap semiconductors [2], [18].

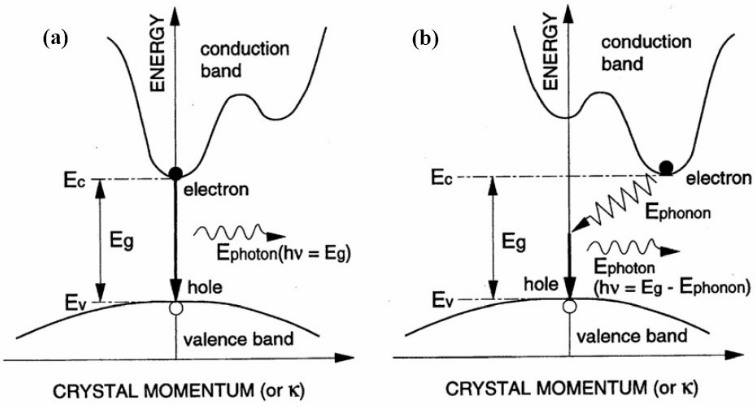

Figure 1.4 – Electron-hole recombination schematic for the band structure of a) a direct and b) an indirect bandgap semiconductor (after [18]*).*

Figure 1.4 depicts the electron-hole recombination of semiconductors with direct and indirect bandgaps. Each band in the crystal lattice is characterised by a certain crystal momentum, that is proportional to the electron wavenumber k, in the Brillouin zone. Direct bandgap structures are characterised by having the maximum of the valence band and the minimum of conduction band at the same point in k-space such that electron transitions may occur without change in the crystal momentum. For indirect bandgap semiconductors, the valence band minimum and conduction band maximum are not in the same point in k-space. In order to obey the momentum conservation principle, the recombination process here has to involve a phonon with momentum equal to the difference between the electron and hole. This is why radiative transitions are more likely to occur in direct as opposed to indirect semiconductors and radiative recombination is slower in indirect bandgap materials.

For solid-state lighting it is preferable to have as much radiative recombination as possible since non-radiative recombination reduces device efficiency and impairs performance.

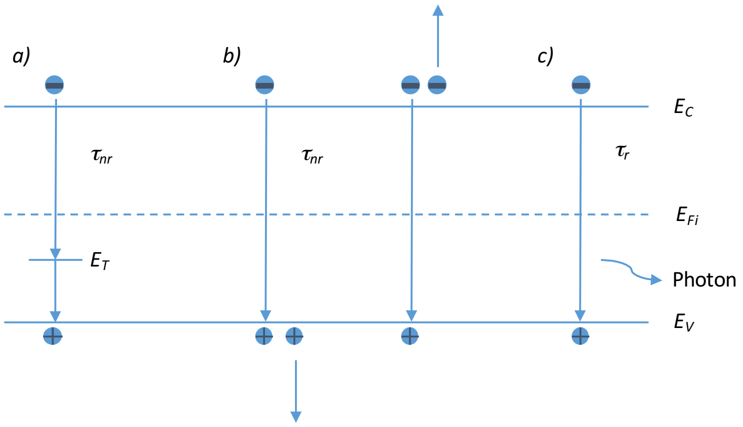

Figure 1.5 – Band diagram showing a) deep-level non-radiative recombination, b) Auger non-radiative recombination and c) radiative recombination (after [2]*).*

Radiative and non-radiative recombination are shown in the schematic depicted in Figure 1.5. At equilibrium, *i.e.* no external stimulation such as light or current, the concentration of holes and electrons is constant:

$$n_0 p_0 = n_i^2 \tag{1.3}$$

where n_0 and p_0 are the concentration of electrons and holes, respectively, and n_i is the intrinsic carrier concentration [2]. Under external stimulation, the previous equality is not met and the total carrier concentration is then given by:

$$n = n_0 + \Delta n \tag{1.4}$$

$$p = p_0 + \Delta p \tag{1.5}$$

where Δn and Δp are the respective concentration of the excess electrons and holes [2]. The radiative recombination rate of the carriers can be determined using the bimolecular recombination rate equation, where B is the bimolecular recombination coefficient [2]:

$$R = Bnp \tag{1.6}$$

From the equation, increased carrier concentration will induce an increased rate of recombination. This is desirable in solid-state lighting since it will generate more light making the devices more efficient [2]. Nowadays to achieve such recombination rates, heterojunctions are used as will be explained later.

Non-radiative recombination occurs due to the defects in the semiconductor structure. There are two main mechanisms responsible for this, deep level recombination, also known as Shockley, Read and Hall (SRH) recombination, mainly caused by interstitials, vacancies and dislocations in the crystal lattice and Auger recombination which involves energy transfer to a third charge carrier [2]. These respective processes are illustrated in Figure 1.5a and b.

Deep-level or luminescence killers are caused by the appearance of recombination centres within the semiconductor bandgap mainly due to the different energy levels from defects and substitutional semiconductor atoms. These trap levels are efficient non-radiative recombination centres especially when the energy level is close to the middle of the bandgap [2]. The recombination rate for this process can be determined using expression (1.7) [2]. If the trap level is positioned at the Fermi level, then the concentration of electrons, n_1, and holes, p_1, can be determined respectively through expressions (1.8) and (1.9):

$$R_{SR} = \frac{p_0\Delta n + n_0\Delta p + \Delta n\Delta p}{\left(N_T v_p \sigma_p\right)^{-1}(n_0 + n_1 + \Delta n) + (N_T v_n \sigma_n)^{-1}(p_0 + p_1 + \Delta p)} \tag{1.7}$$

$$n_1 = n_i \exp\left(\frac{E_T - E_{Fi}}{kT}\right) \tag{1.8}$$

$$p_1 = n_i \exp\left(\frac{E_T - E_{Fi}}{kT}\right) \tag{1.9}$$

Here, E_T and N_T represent the deep-level trap energy and concentration, respectively. The parameters v_n and v_p are the electron and hole thermal velocity, σ_n and σ_p are the respective cross sections of the traps, E_{Fi} and n_i the Fermi level and carrier concentration in the intrinsic semiconductor, respectively [2].

Apart from the reduction of efficiency, carrier lifetimes (τ) can be influenced by non-radiative processes. The contribution of SRH recombination can be analysed [2] through:

$$\frac{1}{\tau} = \frac{p_0 + n_0 + \Delta n}{\tau_{p0}(n_0 + n_1 + \Delta n) + \tau_{n0}(p_0 + p_1 + \Delta p)} \tag{1.10}$$

where,

$$\frac{1}{\tau_{no}} = N_T v_n \sigma_n \tag{1.11}$$

$$\frac{1}{\tau_{po}} = N_T v_p \sigma_p \tag{1.12}$$

Auger recombination is, as introduced above, another process responsible for non-radiative recombination. In this particular case, the carrier recombination process involves a third particle, either an electron that is excited high into the conduction band or a hole excited deep into the valence band. The energy is then dissipated through phonon emission until the excited particles are close to the band edge [2]. Since two carriers of the same type (either two electrons or two holes) are required for the recombination to occur, the rate equations for *n*-type and *p*-type semiconductors are, respectively:

$$R_{Auger} = C_n n^2 p \tag{1.13}$$

$$R_{Auger} = C_p n p^2 \tag{1.14}$$

where C_n and C_p are the Auger coefficients. In a non-equilibrium condition, induced by an external excitation, the coefficient (C) and Auger rate equation can be expressed:

$$R_{Auger} = (C_n + C_p)n^3 = Cn^3 \tag{1.15}$$

The relationship above shows a cubic carrier concentration dependence for Auger recombination. At low carrier concentrations, therefore Auger recombination can be neglected. However, high external excitation will increase Auger recombination leading to a reduction of luminescence efficiency.

Both phenomena described above play a major role in the internal and external quantum efficiencies of solid-state lighting. These efficiencies represent a figure of merit and provide an evaluation parameter for comparing different light sources (*c.f.* Figure 1.1).

Internal quantum efficiency (IQE) is defined as ratio between the number of electrons injected into the semiconductor and the number of photons generated. Ideally, for every injected electron in the active region a photon would be emitted. However, as explained previously it is not possible to completely eliminate non-radiative recombination. The internal quantum efficiency can be determined using:

$$\eta_{int} = \eta_{inj}\eta_r = \frac{P_{int}/hv}{I/e} \tag{1.16}$$

where P_{int} is the emitted optical power from the active region, I the injected current and e the electron charge [2], [19]. Here, η_{inj} and η_r are the electron injection efficiency and the radiative efficiency, respectively. The latter defines the rate at which radiative carrier recombination occurs in the active region [19]. The radiative rate can be expressed using the rate equation (1.17):

$$\eta_r = \frac{Bn^2}{An + Bn^2 + Cn^3} \tag{1.17}$$

Here, the coefficients A, B and C are for SRH recombination, spontaneous radiative recombination and Auger recombination, respectively. The carrier density is denoted by n. This is true at low input current densities, however at high current densities the coefficients do not describe completely the radiative and Auger recombination rates. Mathematically, this can be addressed using expressions (1.18) and (1.19) where n^* is a fitting parameter common between them [19].

$$B = \frac{B_0}{\left(1 + \frac{n}{n^*}\right)} \tag{1.18}$$

$$C = \frac{C_0}{\left(1 + \frac{n}{n^*}\right)} \tag{1.19}$$

The internal quantum efficiency can also be deduced from the radiative (τ_r) and non-radiative (τ_{nr}) lifetimes:

$$\eta_{int} = \frac{\tau_r^{-1}}{\tau_r^{-1} + \tau_{nr}^{-1}} \qquad (1.20)$$

In real device operation, not all the generated photons escape the active region into free-space due to possible reabsorptions in the substrate, total internal reflections or absorption in the metal driving contacts. The ratio of photons emitted into free space to the number emitted from the active region, defined as external extraction efficiency (EQE or η_{eqe}), can be determined using the expressions:

$$\eta_{eqe} = \eta_{ext}\eta_{inj}\eta_r = \frac{P/hv}{P_{int}/hv} \qquad (1.21)$$

$$\eta_{ext} \cong \sum_{b=1}^{\infty} \frac{1}{2}(1-T)^{b-1}T[R_m^{b-1} + R_m^b\,] \qquad (1.22)$$

Here, the extraction efficiency (η_{ext}) equation is based on a simplified model for random light emission [19]. It considers that light rays have the same probability of being absorbed or bouncing several times until they escape. Besides, they can be generated and emitted in different directions [19]. The b term represents the b^{th} bounce at the exit surface, and T and R are the angle-average transmission and reflectivity coefficients [19]. To date, several techniques have been studied to increase the escape cone angle of light and reduce the waveguide modes within the structure (both strongly affected by the relatively high refractive index of the semiconductor active region) through the increase of scattering and light-rays randomisation. Most of them include mechanical action on the semiconductor surface, such as roughening and substrate patterning [20]–[23]. Photonic structures have also been designed and implemented in LEDs with promising results for light extraction [24], [25].

1.3.2 ***P-N* junction**

As the name implies, *p-n* junctions are the combination of semiconductors layers that are of *p* and *n* type. Such structures are referred to as homojunction when both layers are made of only one semiconductor material or heterojunctions when different materials are used. Usually, these layers are epitaxially grown, *i.e.* atomic layer by atomic layer on the same substrate rather than being grown on separate substrates and then joined together. In a *p-n* junction, a depletion region will be formed due to the diffusion of electrons from the heavily doped *n*-type semiconductor into the heavily doped, with holes, *p*-type semiconductor. With carrier exchange between the doped regions, the *p* and *n* type materials will respectively acquire a net negative and positive charge. This will generate a potential difference across the depletion region, known as the diffusion voltage V_D, opposing the diffusion of electrons and holes. In order to inject carriers for recombination the diffusion voltage must be overcome. The diffusion voltage can be determined through the expression:

$$V_D = \frac{kT}{e} ln \frac{N_A N_D}{n_i^2} \tag{1.23}$$

Where k is the Boltzmann constant, T is the temperature, e is the electron charge, N_A the acceptor concentration, N_D the donor concentration and n_i the intrinsic carrier density of the semiconductor.

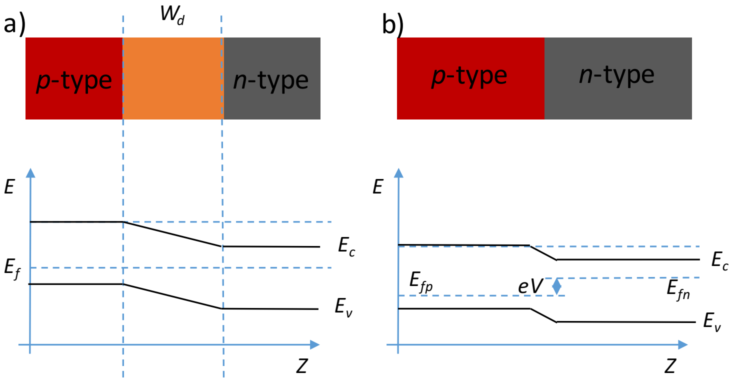

Figure 1.6 – Schematic representation of a p-n junction showing the energy diagram a) under zero bias and b) under forward bias. The z-axis is the spatial dimension perpendicular to the junction.

Figure 1.6 presents a typical *p-n* junction under *a)* zero and *b)* forward bias. The behaviour of such a junction can be modelled through the Shockley equation which describes the current-voltage (usually denoted as I-V) characteristics of an ideal diode:

$$I = I_s\left(e^{\frac{eV}{kT}} - 1\right) \tag{1.24}$$

where,

$$I_s = eA\left(\sqrt{\frac{D_p}{\tau_p}}\frac{n_i^2}{N_D} + \sqrt{\frac{D_n}{\tau_n}}\frac{n_i^2}{N_A}\right) \tag{1.25}$$

Here D_n and D_p are the electron and hole diffusion coefficients and τ_n and τ_p are the electron and hole lifetimes. V is the external bias voltage applied to the junction. A particular characteristic of a *p-n* junction is the capability of conducting current only in one direction, blocking current flow in the opposite direction, *i.e.* acting as a rectifier. Applying a forward voltage to the junction (or a positive voltage drop in which the positive and negative terminal are connected to the *p-* and *n-* type semiconductor) will cause the carriers to diffuse to the junction, screening the depletion region diffusion voltage. When this happens $V >> kT/e$, and thus $([\exp(eV/kT)-1] \approx \exp(eV/kT))$ the Shockley equation for the I-V characteristic can be re-written as:

$$I = eA\left(\sqrt{\frac{D_p}{\tau_p}}N_A + \sqrt{\frac{D_n}{\tau_n}}N_D\right)\left(e^{\frac{eV - V_D}{kT}}\right) \tag{1.26}$$

where V is the forward bias voltage. From this expression, the current will increase as the applied bias voltage gets closes to the diffusion voltage. The voltage at this exponential turning point is referred as the threshold voltage (V_{th}). For an ideal diode, it can be expressed by:

$$V_{th} = \frac{E_g}{e} \tag{1.27}$$

As described before, these structures are in practice not ideal so in real applications electrical resistance has to be considered. For a forward biased junction with a parasitic series resistance (R_s), the previous Shockley equation can be re-written in the form:

$$I = I_s\left(e^{\frac{e(V-IR_s)}{kT}} - 1\right) \tag{1.28}$$

1.3.3 Quantum wells structures

The main drawback of a typical *p-n* junction is that minority carriers are distributed over a large volume. Such carriers have an associated diffusion length (mean distance a minority carrier diffuses before recombination) which are typically several micrometres, resulting in low concentration of minority carriers, see Figure 1.7a. The radiative recombination rate can be determined using the bimolecular recombination equation – expression (1.6) presented in subchapter 1.3.1. Analysing it closely, a low concentration of carriers will result in a low recombination rate impairing the junction efficiency. An approach to circumvent the lack of low carrier concentration is the use of a double heterostructure (DH). Here, a semiconductor with small bandgap – active region – is sandwiched between heavily doped *n*-type and *p*-type layers usually referred to as confinement layers, see Figure 1.7b. A particular case of double heterostructures are the p-*i*-*n* junctions, which are usually used to design high-efficiency LEDs, where a thin layer of an intrinsic semiconductor is used as active region.

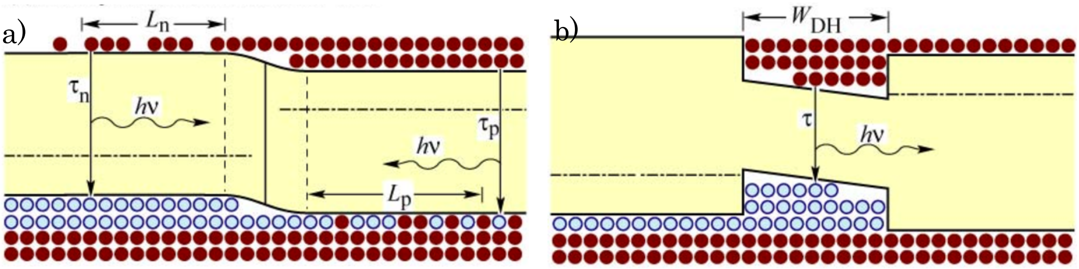

Figure 1.7 – Carrier distribution in a) p-n homojunction b) heterojunction both under forward bias [2].

The semiconductor in the active region presents a lower bangap energy than that of the confinement layers. This is important to create a potential barrier to confine the carrier within the narrow intrinsic layer. The thickness of the intrinsic semiconductor (W_{DH}) in this structures is then designed in order to be much thinner than the diffusion length (L_n or L_p) in a p-n junction in order to increase the carrier concentration in that area, improving the radiative recombination efficiency. Apart from this, it needs to be designed considering possible photon reabsorptions in the confinement layers in the case they present lower bandgap energy than the photon energy or through multiple internal reflections caused by the different refractive index of each layer.

Quantum wells are thin layers of semiconducting materials with thickness close to the de Broglie wavelength, where the charge carriers are confined perpendicular to the planar region, *i.e.* in one direction. This is achieved employing epitaxial crystal growth techniques to produce a semiconductor material (well) in between a n- and p- type semiconductor (barriers) [26]. The de Broglie wavelength is given by:

$$\lambda = \frac{h}{p} = \frac{h}{\sqrt{2m^* kT}} \tag{1.29}$$

where p is the carrier momentum, h and k the Plank and Boltzmann constant, respectively, m^* is the carrier effective mass and T is the temperature [2].

In quantum wells, the permitted energy levels form a quantised states with discrete energies values. They can be determined by solving the Schrödinger equation:

$$\frac{-\hbar^2}{2m^*}\frac{d^2\emptyset_n}{dz^2} + V(z)\emptyset_n = E_n\emptyset_n \tag{1.30}$$

where $V(z)$ is the quantum well potential seen by the particle, m^* is the particle's effective mass and E_n and $\emptyset_n$ are the eigenenergy and eigenfunction associated with the n^{th} solution of the equation [26].

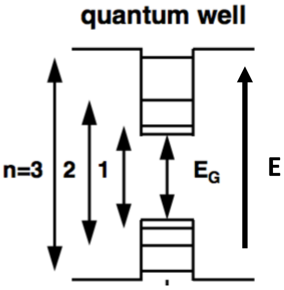

Figure 1.8 – Band diagram of a quantum well structure presenting the energies of the optical transitions. Adapted from [26].

Considering a one-dimensional infinite-potential well ($V = \infty$), the discrete quantised energy levels of a carrier can be determined through:

$$E_n = \frac{\hbar^2}{2m}\left[\frac{n\pi}{L_z}\right]^2 ; n = 0, 1, 2, \dots \tag{1.31}$$

$$\emptyset_n = A\sin\left(\frac{n\pi z}{L_z}\right) \tag{1.32}$$

where L_z is the quantum well width [26]. For narrow wells the energy level becomes larger inducing an increase of energy level separation, affecting the optical transitions occurring between levels. By adjusting the well thickness, it is possible to tune the photon emission wavelength. Besides, to further improve the confinement energy and improve the quantum efficiency several well layers can be epitaxially grown. Such structures are referred to as multi-quantum-wells (MQWs) and as discussed in the next subchapters, this structures can be used to fabricate high-performance LEDs and/or to fabricate epitaxial colour-converters. Figure 1.9 displays a schematic of a multi-quantum-well under bias. The red and blue arrows depict the electron and hole injection and recombination in the active region. In addition to the *n* and *p*-regions, an electron blocking layer (EBL) is grown between the *p* and the multi-quantum well regions in order to prevent electrons escaping and overflowing the active region. This is possible since the blocking layer has the highest bangap energy which works as a potential barrier.

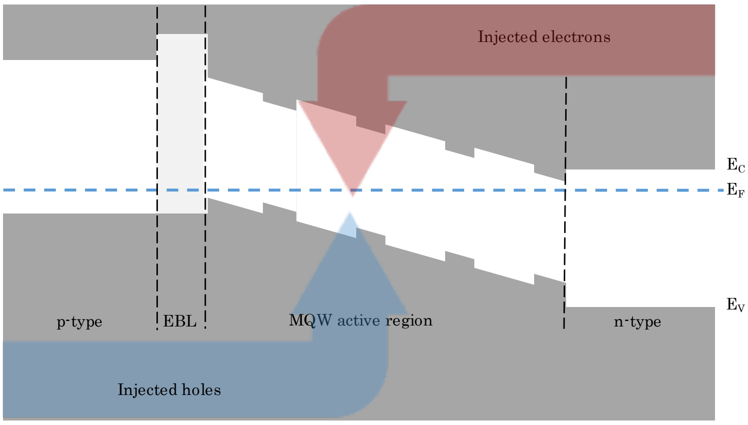

Figure 1.9 – Schematic of a multi-quantum-well heterostructure. The blue and red arrows display the hole and electron injection and recombination within the active region (adapted from [2]*).*

1.4 AlInGaN structures

The LED sources used throughout the present work are all AlInGaN-based alloyed structures. The in-house fabricated µLED arrays (to be discussed later) were manufactured using commercial AlInGaN wafers. The present section will cover the basics of epitaxial growth, the processing and the layout of such structures.

The AlInGaN alloy system consists of three different binary III-nitride materials, namely Aluminium Nitride (AlN), Gallium Nitride (GaN) and Indium Nitride (InN). By altering the relative ratio of the individual materials the bandgap can in theory be tuned to cover the range of wavelengths between the deep-UV to the near-infrared as shown in Figure 1.10. Here, the relative ratio of the alloys is denoted by the subscript x. A higher percentage of aluminium in the ternary system results in an increase of the bangap energy, shifting the emission to bluer wavelengths. For visible light communications we are looking to epitaxial structures with bandgap energies between 1.9 – 2.7 eV, which correspond to emissions in the visible range of the electromagnetic spectrum.

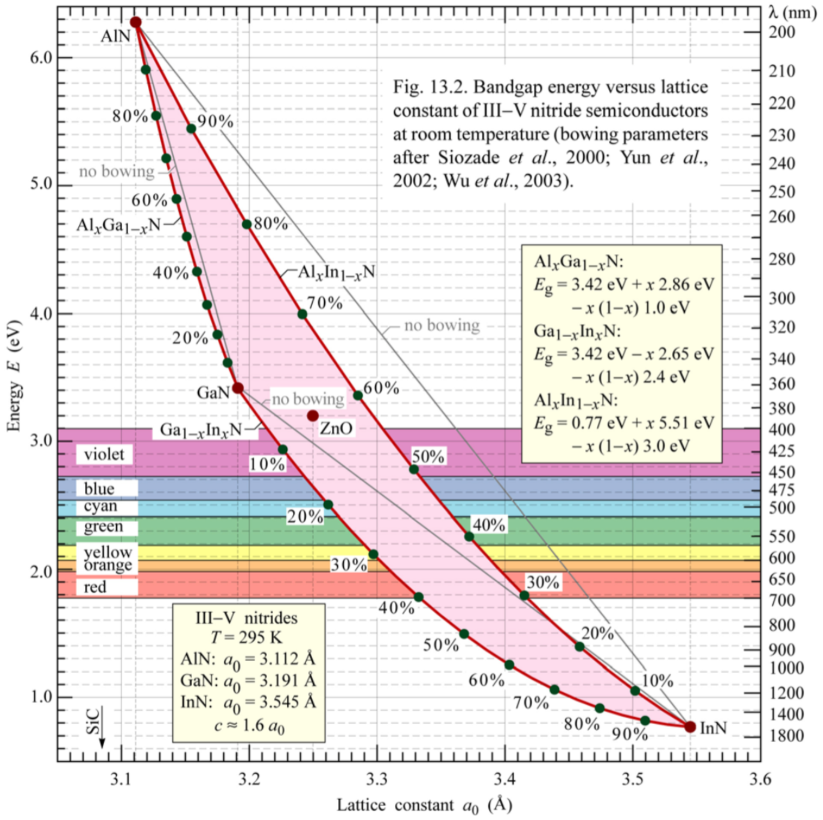

Figure 1.10 – Energy bandgap at room-temperature and wavelength of emission versus lattice constant for AlInGaN-nitride alloyed system [2].

1.4.1 AlInGaN – alloyed structures

Alloyed wafers for lighting solutions can be grown by Metal-Organic Chemical Vapour Deposition (MOCVD), also known as Metal-Organic Vapour Phase Epitaxy (MOVPE) or Organic-Metallic Vapour Phase Epitaxy (OMVPE). Here, the thin-film crystalline structure formed through a chemical reaction of the different vapour phase (or a mixture of vapours) materials is deposited onto a heated substrate.

There are several materials that can be used as substrates for this alloy system, such as Zinc-Oxide (ZnO), SiC and Si. However, the LEDs used in this work were all grown on sapphire (Al_2O_3). Amongst its advantageous properties are optical transparency, good thermal and mechanical stability and low production cost. However, when growing AlInGaN on sapphire one must consider that sapphire is not electrically conductive. To circumvent the lack of electrical conductivity the *p* and *n*-contacts that electrically drive the pixels in the LEDs are defined by etching on the semiconductor side. Alternatively, the sapphire substrate can be removed by laser lift-off [27].

During the growth process the substrate is exposed to metal-organic precursors containing the atoms that will form the epitaxial structure (*e.g.* aluminium, gallium, indium and nitrogen), such as trimethylaluminium (TMA), trimethylgallium (TMG), trimethylindium (TMI) and dimethylhydrazine (DMHy). The high growth temperatures (~1000 °C) break up the organic molecules leaving only the respective atoms to form a single crystalline thin film. The deposition temperature is related with the chemical bond strength of the precursors. The higher the content of carbon the weaker the covalent bonds, permitting a much lower growth temperature. This poses a challenge for the selection of a deposition substrate since it has to withstand the high temperatures while being chemically stable. As stated previously, most III-nitrides devices use sapphire as the substrate, however there is a significant lattice mismatch that results in a high density of threading dislocations. In order to reduce the dislocations, which through non-radiative centres reduce the LED efficiency, low-temperature nucleation or buffer layers of AlN or GaN are grown.

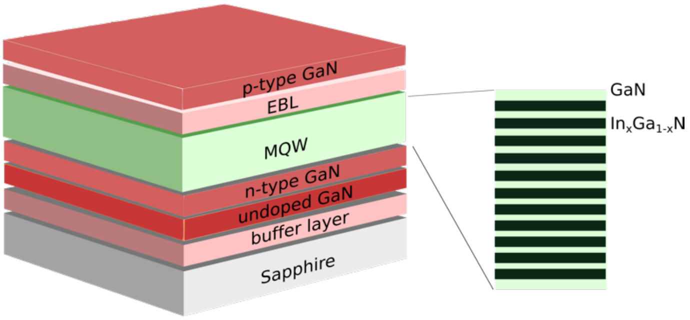

Figure 1.11 – Schematic of an epitaxial structure grown on a sapphire substrate. The right side of the picture presents the MQW region expanded showing the GaN and InGaN layers that compose it.

Figure 1.11 presents a schematic of a typical AlInGaN structure used to fabricate the μLEDs tested in this work as excitation sources for colour-converters. As stated previously and shown in Figure 1.10, the electroluminescence of these structures can be tuned by the relative composition (and thickness) of $In_xGa_{1-x}N$ that composes the MQW region. This region is preceded by a *n*-type and an undoped GaN layers. On top of the MQWs the electron blocking layer, which is usually made of Mg-doped AlGaN since it presents higher bangap energy than GaN in the MQW, and the *p*-layer are deposited.

1.4.2 **LED structures**

After the design and growth the AlInGaN wafers are ready to be processed to create LEDs. The schematic of the most common structural configurations of such LEDs are presented in Figure 1.12.

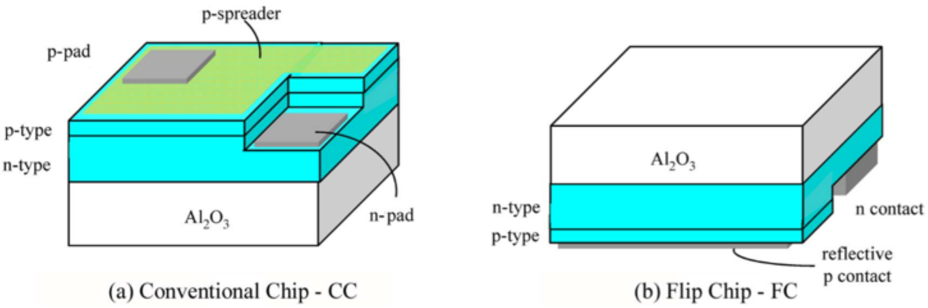

(a) Conventional Chip - CC

(b) Flip Chip - FC

Figure 1.12 – Schematic of two LEDs structures. a) conventional chip and b) flip-chip. After [28].

In the conventional chip design or as often called ‘top-emission’ configuration, the electroluminescence emission occurs through the top layer of the device, *i.e.* through the *p*-layer. LEDs fabricated with this design present some drawbacks. In order to achieve a low contact resistance and provide a uniform current injection in the device a thin current spreading layer, based on Ni/Au, is deposited on top of the *p*-GaN layer resulting in the reduction of external efficiency since some light output is absorbed. Apart from this, ohmic metal pads to electrically drive the device are deposited on the *n* and *p*-layers reducing the fill factor – *i.e.* the ratio of the LED’s emitting area to its total area. The flip-chip configuration can circumvent some of these issues since the optical emission occurs through the sapphire. This means thicker ohmic contacts can be deposited reducing their resistance. To further improve the extraction efficiency, the spreading layer can also work here as a mirror, redirecting the emission through the sapphire substrate that otherwise would be lost. Besides, and as will be presented in Chapter 4, the smooth and chemically inert sapphire surface can be used as a medium to integrate a colour-converter.

1.4.3 Fabrication steps for LEDs and µLEDs

To reach an LED die form, the AlInGaN wafer must undergo several processing steps. The main ones are photolithography, pattern transfer through an etching process and deposition of metal contacts. Figure 1.13 presents some of these steps.

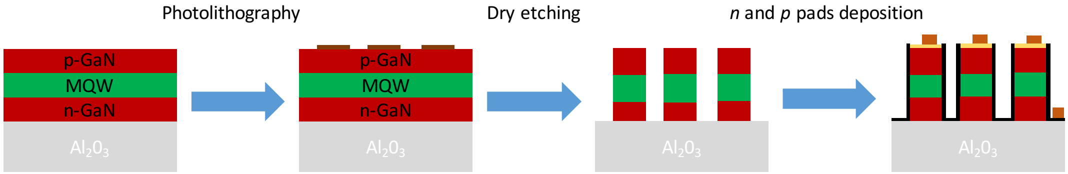

Figure 1.13 – Process flow for LED fabrication.

In the first step, the layout, the pixel size and shape are defined using a photomask through photolithography which is a standard technique for patterns definition in the electronic and semiconductor industries. In order to pattern the surface of the semiconductor structure a photosensitive material, usually called photoresist, is spin-coated on its surface – to achieve a thin and even layer. After careful alignment of the photomask which contains transparent and opaque regions, ultraviolet light is used to photo-chemically change the photoresist properties. There are two types of photoresists, namely positive and negative. Using a positive resist, the area under the mask exposed to light is removed. Here, the chemical structure of the photoresist exposed to light will make it more soluble, thus easier to remove. On the other hand, negative resist that is exposed to light will harden up becoming more difficult to wash away.

The second step in the fabrication process consists in the removal of the excess material in the epitaxial structure by one of two etching processes. In the case of wet etch the material in excess is removed by a chemical process. The material selectivity and etching speed depends on factors such temperature, concentration of etching solution and crystallographic orientations. The dry etching process uses gaseous etchants – plasma of reactive gases – that by ion bombardment or pure chemical etching remove material from the exposed surface. The ion bombardment etching uses high-energy ions to remove exposed material being the etching rate dependent on energy and flux of ions whilst the pure chemical etching forms volatile byprodutcs through the chemical reactions of the gaseous etchants with the material surface. In here, the etch rate relies on the chemical reaction between both parts, the etched material and the etchants.

The final step provides the metal contacts needed to drive the LED. To deposit the tracks on the *p*-layer, a technique called electron-beam evaporation is employed whilst in the case of *n*-layer tracks, magnetron sputtering is used. Usually the *p* and *n*-contacts are made of Ni/Au and Ti/Au respectively. Since *p*-type GaN materials present high resistivity, the metal contacts can work as spreading layer in order to guarantee uniformity of injection current through the *p*-layer.

1.5 Laser diodes

In addition to the LEDs, a semiconductor laser – commonly called a laser diode (LD) – was used to optically excite the colour-converters. LEDs are in general cheaper and suffer less safety restrictions than LDs. However, and as presented in Chapter 2, LEDs present lower modulation bandwidth and optical power than laser diodes. Therefore, laser diodes can be considered as an interesting alternative to LEDs for VLC. Thus, the fundamentals of semiconductor lasers will be introduced in this subchapter.

The photon-electron interaction can result in three physical effects, namely optical absorption, spontaneous emission and stimulated emission. In laser diodes the optical gain is produced in a semiconductor material through stimulated emission. Such a physical phenomenon occurs through the interaction of an incoming photon with an electron in the conduction band that can result in a radiative electron-hole recombination. Energy is then released in the form of a photon with the same phase, frequency, polarisation and direction of the initial photon. A schematic showing the stimulated emission principle is presented in Figure 1.14.

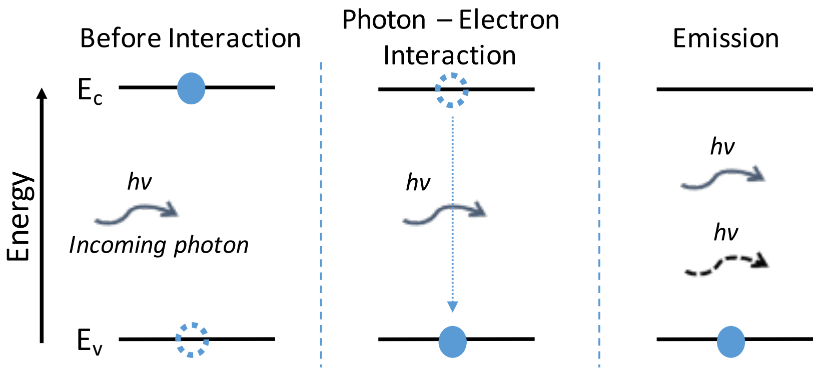

Figure 1.14 – Schematic of stimulated emission principle. Here, the conduction band is populated with an excited electron that will interact with an incoming photon. A radiative recombination occurs resulting in an emission of a photon with equivalent properties to the incoming photon.

As described previously, in thermal equilibrium the electron concentration in conduction band (E_c) is lower than in the valence band (E_v). Thus, optical absorption is more likely to occur than stimulated emission. In order to achieve stimulated emission, the electron concentration in E_c should be larger than in E_v, a phenomenon described as population inversion. In addition, and in order to achieve lasing, the rate of stimulated emission has to be higher than spontaneous emission. This is achieved using an optical resonant cavity, in which the photon density can be build up to a large value through multiple internal reflections. In the case of semiconductor lasers, the multi-reflections occur via the semiconductor cleaved facets. The amplified laser light eventually emerges from the least reflective facet, Figure 1.15.

As for the LEDs, the emission wavelengths of the laser diodes are determined by the bandgap energy of the semiconductor material and the thickness of the quantum wells in the case of heterostructure based lasers. Usually, laser diodes operating in the blue range of the visible spectrum are made of $In_xGa_{1-x}N$ alloyed structures grown on SiC whereas in the red region they are made of $(Al_xGa_{1-x})_yIn_{y-1}P$, alloyed structures on GaAs.

Here, a commercial InGaN blue laser diode was used – OSRAM PL450B – with maximum forward optical power of 100 mW. The spectral response and L-I-V curve for the laser diode are presented in Chapter 2 Figure 2.11.

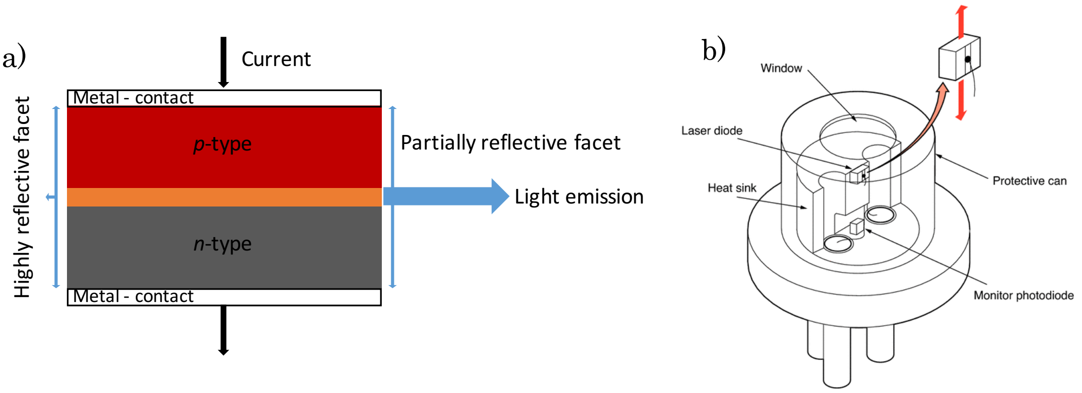

Figure 1.15 – a) Laser diode schematic under operation and b) schematic of a laser diode in a TO-Can package. Adapted from [29].

1.6 Colour-converters

Several materials were studied in this work as a potential replacement for the standard phosphor-based colour-converters used in nitride LEDs. These include polymers, colloidal quantum dots (CQDs) and inorganic semiconductor membranes based on III-V and II-VI multi-quantum wells, all selected as being of promise for visible light communications (Chapter 3 – 4). The basic physical properties of these materials are presented below.

1.6.1 Organic semiconductors

Organic semiconductors are organic materials – molecules based mainly on carbon atoms – with semiconducting properties. Such properties arise from the charge transport characteristics determined by an electronic band structure containing a bandgap, which is conceptually similar to inorganic semiconductors.

Organic semiconductors are made of small repeating molecular units, called monomers, that have the capacity of connecting through covalent bonds with other molecules to create polymers or oligomers (few repeats). Atoms are surrounded by electrons distributed in different orbitals accordingly to their electronic configuration. The carbon atom has six electrons in total. Its electronic configuration is $1s^2 2s^2 2p^2$ where $2p^2$ comprises three orbitals, $2p_x^1 2p_z^1 2p_z^0$. According to this, the carbon should form two covalent bonds since it has two unpaired electrons. However, carbon atoms in this configuration are highly reactive becoming stable only when four covalent bonds are made. An explanation for this is the overlap of the 2*s* and 2*p* orbitals, which may also be referred as hybridisation. Three different hybridisations can occur, namely sp^3, sp^2 and *sp* as shown in Figure 1.16 [30].

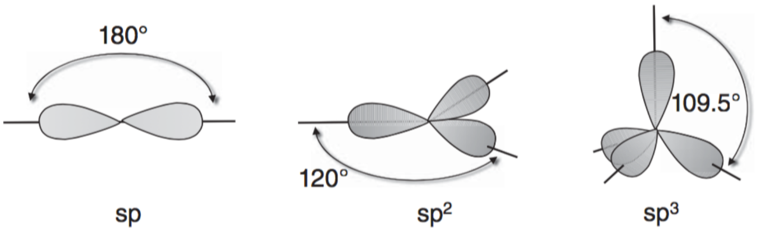

Figure 1.16 – Representation of sp, sp^2 and sp^3 hybrid orbitals [30].

In the first case, four orbitals will contribute to the bond, one of the 2*s* and the other three from the 2*p* orbitals, resulting in the sp^3 configuration. The resulting molecules form a tetrahedral structure with angles between bonds of 109.5^0 as thereby the electron repulsion is minimised. Similarly, the sp^2 hybridization comprises the mixture of one 2*s* and two 2*p* orbitals. The molecule thus formed will have a trigonal shape with bond angles of 120^0. The *sp* orbital is formed by conjugation of one 2*s* and one 2*p* orbital. The angle between bonds is 180^0 resulting in a molecule with linear a shape.

The *s* and *p* orbitals have a spherical charge distribution centred around the atom (Figure 1.17a) and their overlap will form covalent bonds of two kinds, the sigma (σ) and pi (π) bonds [30]. σ bonds correspond to a linear overlap of the shared orbitals centred around the axis joining the two atoms (Figure 1.17b), whilst in π bonds the electrons forming the connection are above or below the sigma bond (Figure 1.17b). Due to the spatial confinement of both bonds and the fact they have higher distance to the atom nuclei, the π-bond is much weaker. This allows the electrons to become delocalised, *i.e.* to move along the molecular structure more easily [30], [31].

The newly formed molecular orbitals, at equal or similar energy, will interact forming two new orbitals each, one with higher energy than the other. The highest formed energy orbital is denominated highest occupied molecular orbital (HOMO) whilst the orbital with lower energy is denominated lowest unoccupied molecular orbital (LUMO). This is analogous to inorganic semiconductors with valence and conduction bands [30], [31]. By adjusting the molecule' size and the confinement energy it is possible to tune the electronic transition energy and consequently its optical emission [32].

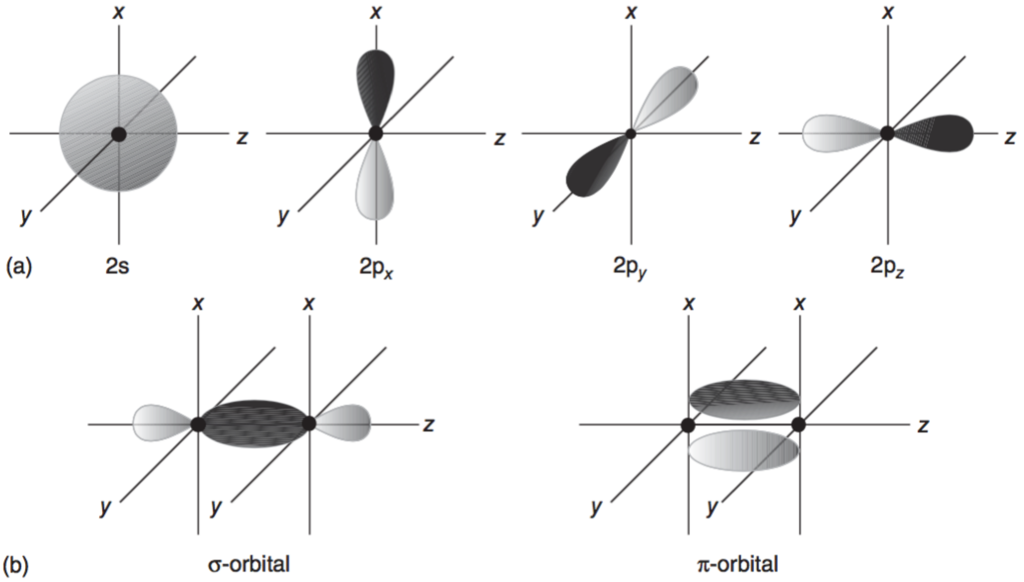

Figure 1.17 – a) Atomic s and p orbitals and b) σ and π orbitals formed from overlap of two p_z and two p_x orbitals [30].

The electrons spin configuration in each molecular level can be defined as a singlet or triplet state, with a spin contribution per electron of 1/2. When the spin sum is 1, *i.e.* the electrons have the same spin value (+1/2, +1/2 or -1/2, -1/2), the state is referred to as a triplet. If the electron's spin is paired with sum of 0, *i.e.* the electrons present different spin values (-1/2, +1/2 or +1/2, -1/2), the state is called a singlet [30], [31], [33].

Figure 1.18, known as a Jablonski diagram illustrates the possible electronic transitions of a molecule where S represents singlet and T triplet states, respectively. After external excitation (labelled absorption here for the case of photoexcitation) two types of electronic transitions can occur, namely a fluorescent or a phosphorescent transition. Fluorescence occurs due to the radiative relaxation of an electron from the lowest level energy vibrational state of S_1. However, if there was excitation to a higher level of S_1 or S_2 internal conversion/relaxation can occur initially. This process usually occurs within 10^{-12}s whilst fluorescence lifetimes are around 10^{-9}s meaning the internal conversion is generally complete prior to fluorescence emission. The transitions which result in the emission of a photon occur at lower energies than transitions during absorption. This is known as the Stokes shift. Molecules within the S_1 state can also undergo a spin-conversion to the first triplet state T_1 (intersystem crossing). Relaxation of electrons from this level is called phosphorescence as it is forbidden, resulting in relaxation times between 10^{-3}s to 10^{2}s, much longer than for fluorescence emission [31].

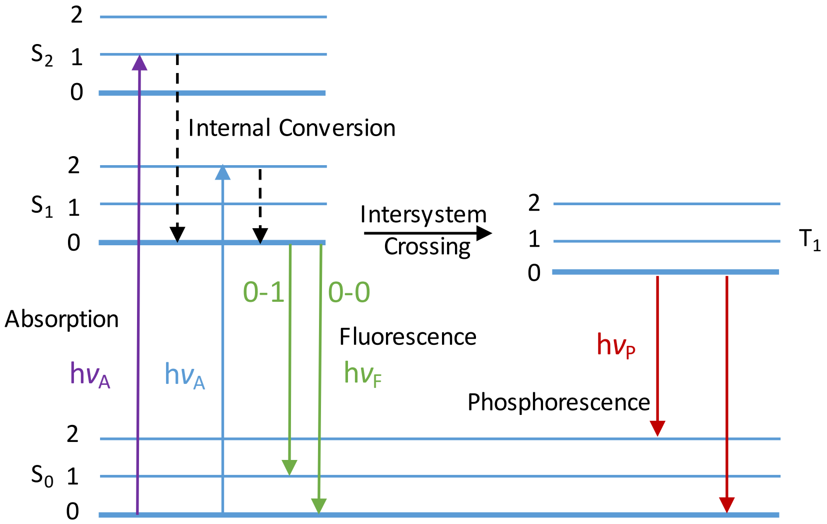

Figure 1.18 – Schematic of a Jablonski diagram representing fluorescence and phosphorescence mechanisms in an organic molecule. Illustration based on [31].

The important characteristics of quantum yield and carrier lifetimes can be determined for the organic semiconductors. In this case, quantum yield is defined [31] as the ratio of emitted photons relative to those absorbed:

$$Q = \frac{\Gamma}{\Gamma + k_{nr}} \tag{1.33}$$

Where Γ and k_{nr} are the radiative and the non-radiative relaxation rates of the molecule to the ground state.

The lifetime is defined as the average time a molecule is in the excited state prior to relaxation. Thus, the fluorescence lifetime is the average time a molecule spends in excited state before decay to the ground level, equation (1.34.

$$\tau = \frac{1}{\Gamma + k_{nr}} \tag{1.34}$$

An effect to consider when working with these materials is fluorescence quenching, *i.e.* the reduction of emission intensity. There are two main quenching mechanisms, the collisional quenching which results from the interaction of an excited-state molecule with another one in the ground-state, mostly due to electron transfer between molecules or spin-orbit coupling and intersystem crossing to the triplet state. The decrease of energy through this process is described by the Stern-Volmer equation:

$$\frac{\tau_0}{\tau} = 1 + K[Q] = 1 + k_q\tau_0[Q] \tag{1.35}$$

Here, K is the Stern-Volmer quenching constant which indicates the sensitivity of a fluorophore to a quencher, k_q is the bimolecular quenching constant, τ_0 and τ are the unquenched and quenched lifetimes, respectively, and $[Q]$ the quencher concentration. The most common quenchers are oxygen and electron-deficient molecules. Based on the organic molecule and quencher the reduction of intensity may result from the transfer of electrons in the excited state or spin-orbit coupling and intersystem crossing to the triplet state [31].

The other mechanism responsible for fluorescence quenching is called static quenching. In here, there is a formation of non-fluorescent molecules due to the combination of fluorophore molecules with quenchers. This process takes place in the ground state and does not depend on molecules collisions [31].

In this work BBEHP-PPV, which is an organic polymer, was studied as a possible colour-converter in order to be used in VLC and down-convert the blue excitation light coming from the optical source to green photoluminescence emission. BBEHP-PPV is poly[2,5-bis(2′,5′-bis(2″-ethylhexyloxy)phenyl)-p-phenylene vinylene] and has been previously used in applications such as lasers and sensors mostly due to its low stimulated emission threshold, high quantum yield and photo-stability when compared with other organic semiconductors [34], [35]. Figure 1.19 presents the molecular structure of BBEHP-PPV and its absorption and photoluminescence spectrum. The spectra present two emission peaks, one centred at 496 nm, which corresponds to a transition from $|S1, 0_{S1}>$ to $|S0, 0_{S0}>$ or ‘0-0’, whilst the other at 528 nm corresponds to a transition from $|S1, 0_{S1}>$ to $|S0, 1_{S0}>$ or ‘0-1’. The organic semiconductor has a maximum absorption peak at 431 nm. As measured and reported in [35] the BBEHP-PPV exhibits PLQY (photoluminescence quantum yield) above 75%.

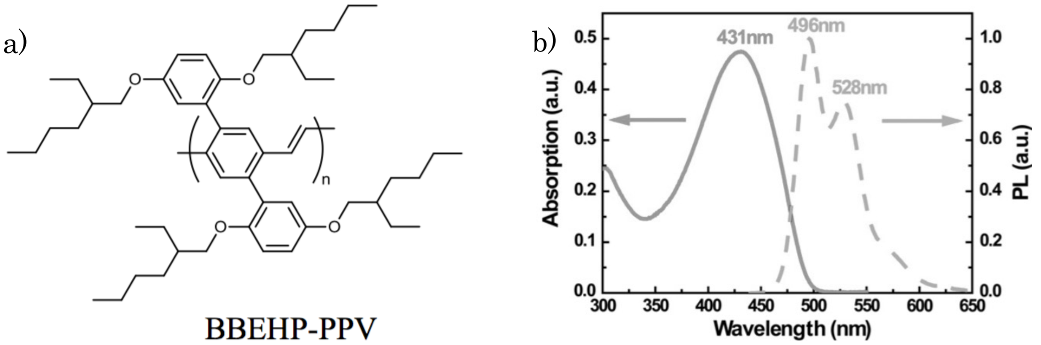

Figure 1.19 – a) BBEHP-PPV molecular structure and b) absorption (solid line) and photoluminescence spectrum (dashed line) of a neat BBEHP-PPV film. After [34], [35].

1.6.2 **Colloidal Quantum Dots**

Quantum Dots are semiconductor particles that have nano-size, ranging from a few to tens of nanometres. These materials are interesting for use as colour-converters since they combine some of the physical characteristics of the bulk semiconductor from which they are made with single atom properties. Furthermore, they possess broad absorption spectra, tunable emission and long term photostability [36]–[38]. Here we focus on colloidal quantum dots (CQDs) which are individual nanoparticles with organic surface functionalization to make them soluble and solution processable.

Since their diameter is comparable to the electron de Broglie wavelength, they show the effect of quantum confinement. As described before for the heterostructures, the de Broglie wavelength can be determined by:

$$\lambda = \frac{h}{p} = \frac{h}{\sqrt{2m^{*}kT}} \tag{1.36}$$

where h and k are the Planck and Boltzmann constants, respectively, m^* is the carrier effective mass and T is the temperature.

The movement of electrons is confined as if they were in a ‘cage’, leading to the quantisation of the energy levels [6], [41]. As previously explained, the last filled ‘band’ of allowed states is called the valence band and the next empty band is called the conduction band. A number of transitions between these energy levels are possible, see Figure 1.20 [42]. The figure also shows the effect of quantum dot size in colour emission, for II-VI CQDs studied in our work.

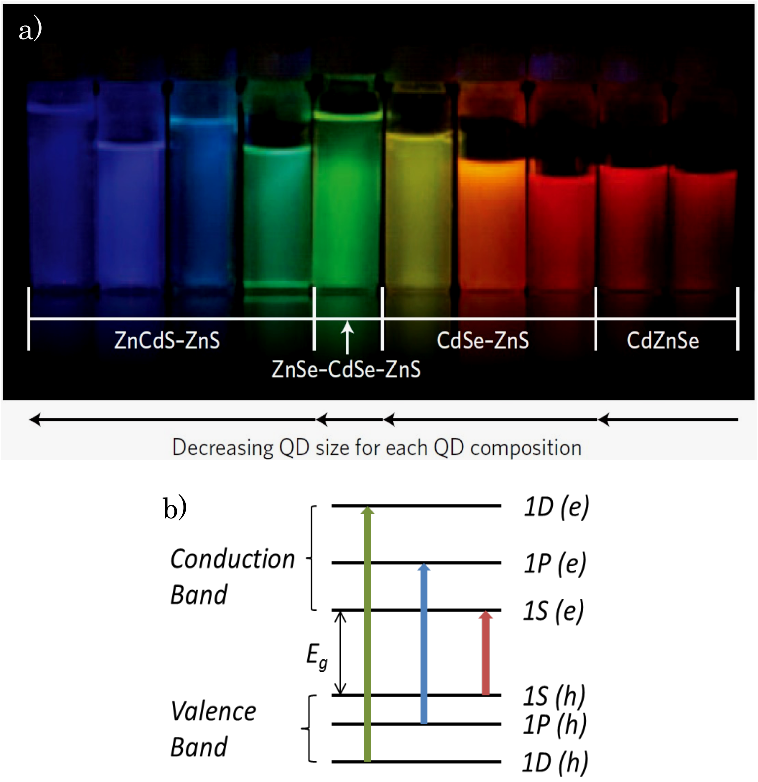

Figure 1.20 – a) Photoluminescence emission for different II-VI CQDs sizes [43], *b) representation of the discrete energy levels of a quantum dot modelled as a simple ‘nano-box’.*

The energy gap, E_g, between highest occupied energy level and the lowest unoccupied energy level for CQDs of diameter R is given by:

$$E_g(QDs) = \frac{\hbar^2\pi^2}{2m_{eh}R^2} + E_{g\,bulk} \qquad (1.37)$$

where,

$$m_{eh} = \frac{m_e^* m_h^*}{m_e^* + m_h^*} \tag{1.38}$$

Here m_e and m_h are respectively the effective mass of the electrons and holes [42], [44]. By controlling E_g one can tune the wavelength of the emission. This is possible by controlling R, the mean size of the CQDs. The lower the particle size the stronger will be the effect of quantum confinement resulting in bigger bandgap energies and a shift to shorter wavelength emission, see expression (1.37) [45]. This size-tunability of the bandgap means that a wide spectral range can be addressed with CQDs made from a single material system [46]. For example, CQDs based on (*Cd*, *Se*, *Zn*, *S)* alloys cover wavelengths from the blue to the red (Figure 1.20a). The most studied CQDs are those based on cadmium selenide (*CdSe*) alloys passivated and confined by a zinc sulphide (*ZnS*) shell around the core. Passivating the nanocrytals allows increased photoluminescence quantum yield due to the reduction of surface carrier trapping [45], [47]. Organic ligands attached to the outer surface of the shell enable a better dispersion in solvents and polymeric matrices as used in this work [37].

Depending in the synthesis process different kinds of CQDs can be designed. One important type is the so-called core-shell CQD, which has an abrupt interface between a core and shell, for instance, *CdSe*/*ZnS* (Figure 1.21a) [45]. A second important design exhibits a gradual compositional transition between a mostly *CdSSe*-core and a mostly *ZnS*-shell, Figure 1.21b. This approach allows to tune the CQD photoluminescence through the manipulation of the alloy ratio in the core without the need to change the particle size [48], [49].

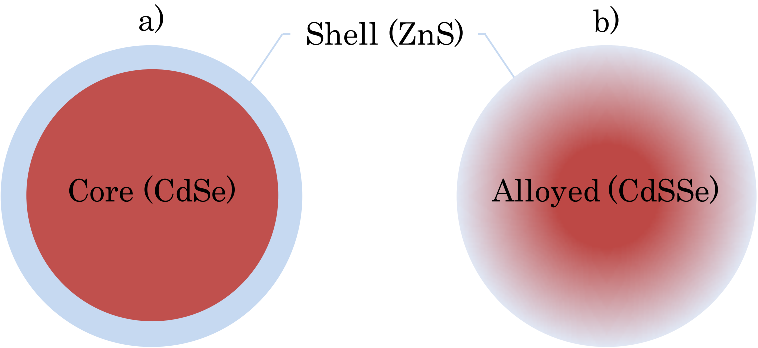

Figure 1.21 – Schematic cross-section of a) core-shell CQD and b) alloy CQD.

Typical absorption and emission spectra for such CQDs are shown in Figure 1.22. Whatever the emission wavelength, such CQDs absorb strongly in the UV-blue range spectrum, making them ideal for use in applications where InGaN LEDs are used as optical excitation sources.

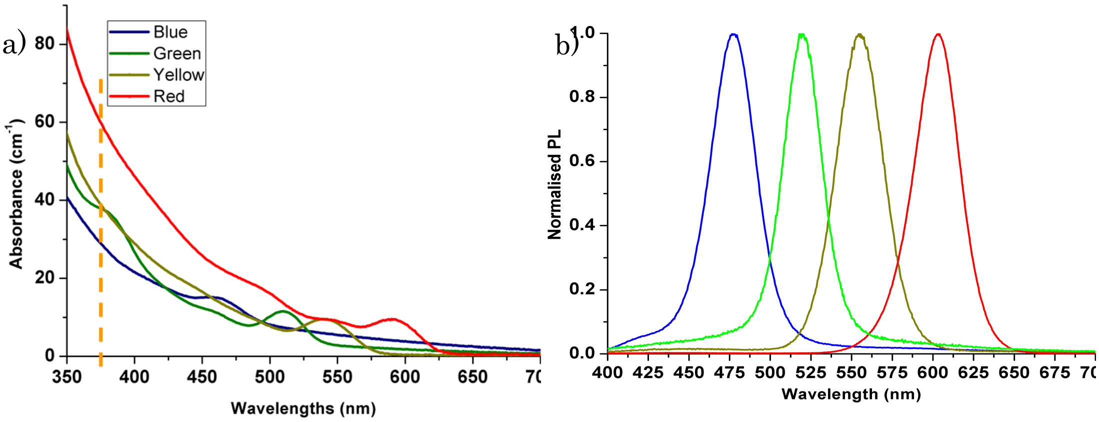

Figure 1.22 – Absorption and emission spectra for CQDs encapsulated by an epoxy composite. The absorption and fluorescence spectra were acquired using a UV-VIS Cary and a Perkin Elmer LS 50B spectrophotometer system, respectively [50].

This kind of nanocrystal can be synthesised in solution by wet-chemistry through the decomposition of metal-organics and chalcogenides in a high temperature organic solvent [37], [51], [52]. Therefore, they share the processing flexibility of organics such as the compatibility with solution-processing and soft-lithography techniques important for the development and improvement of new technologies like VLC.

The CQD particles are usually provided in a solvent solution that can be removed by evaporation or precipitated. As discussed in Chapter 3, they can be incorporated in a polymer in order to create thin films with different sizes and shapes. However, they can be used in a 'neat' form, *i.e.* they can be drop-coated or spin-coated on any given surface. After solvent evaporation, the quantum dots particles can be found to be freestanding.

1.6.3 II- VI and III-V epitaxial structures

The epitaxial structures used in this work for colour-conversion were made of II-VI or III-V semiconductors in order to obtain green and red photoluminescence, respectively. As discussed in Chapter 4, such structures present several advantages over organic semiconductors and colloidal quantum dots. The longer photostability, the fact they are encapsulated by design, their higher bandwidth and the capacity to design them to cover the visible spectrum promising white-light generation makes them attractive candidates to replace conventional phosphors for VLC.

Two different growth techniques were employed to achieve the II-VI and III-V structures. The II-VI green structure was grown at City College of New York by molecular beam epitaxy (MBE) on an InP substrate. The III-V red structure was grown at the University of Sheffield by metalorganic vapour phase epitaxy (MOCVD) on a GaAs substrate. In the MOCVD the crystal is grown by chemical reactions while in the MBE through physical deposition in an ultra-high vacuum chamber. The substrate is heated in both cases and in both cases, it is possible to control the thickness of the layers to be grown at atomic scale.

The II-VI structure was originally designed for use as a vertical-external-cavity surface-emitting-laser (VECSEL) gain region. It consists of nine ZnCdSe quantum wells in ZnCdMgSe barriers designed to emit at 540 nm in a resonant periodic gain configuration. As a laser structure, it was designed to include a five period DBR of ZnCdMgSe, which turned out to be out of resonance with 540 nm and therefore has no noticeable incidence on the colour-conversion, as presented in Chapter 4. The epitaxial structure was grown by MBE on a InP substrate and is encapsulated through a ZnCdSe layer which works as an anti-oxidation cap and a wet-etch stop barrier for post-processing in order to remove the substrate. Its layer structure is depicted in Table 1.1.

The III–V MQW membrane structure consists of six GaInP quantum wells with AlGaInP barriers. Here, AlAs was used to shield the structure from the wet-etch acid used to remove the GaAs substrate and the GaInP anti-oxidation cap. The resulting structure is the colour-converting platelet. Table 1.2 presents all the layers that comprise the III-V epitaxial structure.

Table 1.1 – II-VI epitaxial structure layer, thicknesses and mole fraction of each alloy.

Layer	Alloy	Mole fraction x	Mole fraction y	Thickness (nm)	Purpose
17	$(Zn_xCd_{1-x})_{1-y}Mg_ySe$	0.48	0	10	Cap
16	$(Zn_xCd_{1-x})_{1-y}Mg_ySe$	0.56	0.6	103	Carrier confinement
15	$(Zn_xCd_{1-x})_{1-y}Mg_ySe$	0.5	0.32	104	Barrier
14 x 8	$(Zn_xCd_{1-x})_{1-y}Mg_ySe$	0.48	0	2.1	QW
13 x 8	$(Zn_xCd_{1-x})_{1-y}Mg_ySe$	0.5	0.32	103	Barrier
12	$(Zn_xCd_{1-x})_{1-y}Mg_ySe$	0.48	0	2.1	QW
11	$(Zn_xCd_{1-x})_{1-y}Mg_ySe$	0.5	0.32	251	Barrier
10	$(Zn_xCd_{1-x})_{1-y}Mg_ySe$	0.56	0.6	20	Carrier confinement
9	$(Zn_xCd_{1-x})_{1-y}Mg_ySe$	0.5	0.32	464	Pump absorption
8	$(Zn_xCd_{1-x})_{1-y}Mg_ySe$	0.56	0.6	113	Transparent window
7 x 5	$(Zn_xCd_{1-x})_{1-y}Mg_ySe$	0.56	0.6	56.5	Low-n DBR
6 x 5	$(Zn_xCd_{1-x})_{1-y}Mg_ySe$	0.493	0.25	51.7	High-n DBR
5	$(Zn_xCd_{1-x})_{1-y}Mg_ySe$	0.56	0.6	96	Low-n DBR
4	$(Zn_xCd_{1-x})_{1-y}Mg_ySe$	0.48	0	20	Etch-stop/cap
3	ZnCdSe	-	-	-	Low-T buffer
2	$In_xGa_{1-x}As$	0.53	-	200	Buffer layer
1	InP	-	-	-	Substrate

Table 1.2 – III-V epitaxial structure layer, thicknesses and mole fraction of each alloy.

Layer	Alloy	Mole fraction x	Mole fraction y	Thickness (nm)	Purpose
16	$Ga_yIn_{1-y}P$	0	0.6	10	Cap
15	$(Al_xGa_{1-x})_yIn_{1-y}P$	0.6	0.51	76.5	Barrier
14	$Ga_yIn_{1-y}P$	0	0.5	4	QW
13	$(Al_xGa_{1-x})_yIn_{1-y}P$	0.6	0.51	7	Barrier
12	$Ga_yIn_{1-y}P$	0	0.5	4	QW
11	$(Al_xGa_{1-x})_yIn_{1-y}P$	0.6	0.51	79	Barrier
10	$Ga_yIn_{1-y}P$	0	0.5	4	QW
9	$(Al_xGa_{1-x})_yIn_{1-y}P$	0.6	0.51	7	Barrier
8	$Ga_yIn_{1-y}P$	0	0.5	4	QW
7	$(Al_xGa_{1-x})_yIn_{1-y}P$	0.6	0.51	79	Barrier
6	$Ga_yIn_{1-y}P$	0	0.5	4	QW
5	$(Al_xGa_{1-x})_yIn_{1-y}P$	0.6	0.51	7	Barrier
4	$Ga_yIn_{1-y}P$	0	0.5	4	QW
3	$(Al_xGa_{1-x})_yIn_{1-y}P$	-	-	76.5	Barrier
2	AlAs	0.53	-	10	Etch stop
1	GaAs	-	-	500	Substrate

1.7 Telecommunications

As discussed in the previous sections, VLC relies on the visible spectrum to transmit data rather than the radio frequency (RF) spectrum used nowadays for wireless communications. The low cost, high efficiency and huge deployment of solid-state lighting is making VLC a serious emerging complement to the capacity-limited RF band [53]. However, solid-sate light only permits data modulation in the intensity regime contrary to conventional coherent channels where information is sent through the modulation of amplitude and phase of the carrier electromagnetic waves. Thus, the receivers will only detect the modulated signal’s intensity requiring the transmitted signal to be positive and real. This type of communications is called intensity modulation with direct detection (IM/DD) [54]. A basic scheme illustrating a potential IM/DD configuration is depicted in Figure 1.23.

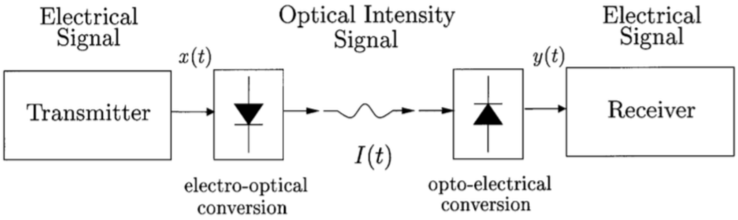

Figure 1.23 – Schematic of an intensity modulation with direct detection communications system [55].

Due to this, only modulation schemes that work in the intensity modulation regime can be applied to VLC, such as on-off keying (OOK) and pulse-position modulation (PPM). However, where the system bandwidth and optical channel is limited, multi-level schemes like unipolar pulse-amplitude modulation (PAM) can circumvent these limitations. Recently a modified orthogonal frequency-division multiplexing (OFDM) scheme suitable for IM/DD was proposed to overcome the intersymbol interference (ISI) resulting from the distortion at high communication speeds when OOK and PAM are used [56].

The modulation signal is encoded onto the light source through its combination with a DC bias signal. As explained in Chapter 2, this combination is performed using a bias-tee.

In the following, a very brief explanation of the modulation schemes used throughout this work will be presented.

1.7.1 Amplitude modulation domain schemes

There are several modulation schemes suitable to transmit data over optical fibre or free-space. The most common and easiest to implement, at the expense of lower spectral efficiency, are the formats in which the data is encoded in the amplitude domain. Schemes that fall into this category are on-off keying (OOK), that can be split into return-to-zero (RZ) or non-return-to-zero (NZR), and pulse-amplitude modulation (PAM). In OOK-NRZ, the data is modulated in two distinct levels, the pulse per bit occupying the entire bit interval. So, considering the data is in the binary form, to send the bit 1 the optical source is driven at a determined current, to transmit the bit 0, the source is turned off, *i.e.* no pulse is used – see Figure 1.24b. The OOK-RZ signal, the bits 1 and 0 are transmitted the same way as NRZ, however the pulse per bit only occupies part of the bit interval Figure 1.24a [57], [58].

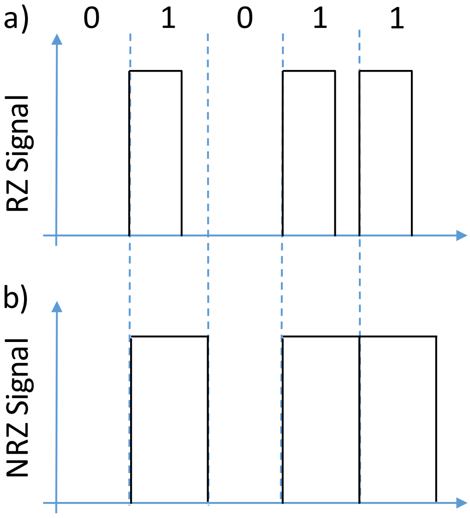

Figure 1.24 – a) OOK-RZ b) OOK-NRZ modulation formats. Illustration based on [58].

There are several ways to generate the modulation signal. Usually, an electrical wave signal with the shape of a return-to-zero will modulate the optical carrier. Alternative approaches use optical modulators, such as electro-absorption modulators (EAMs) or Mach-Zehnder modulators.

In pulse-amplitude modulation the transmitted signal can have single or double polarity. In the former case, an offset is added to the signal so that all the pulses are positive. In the double polarity configuration, the pulses present positive and negative amplitudes. OOK – which can be seen as the basic PAM scheme – has two discrete pulse amplitudes, however it is possible to achieve more discrete levels. The relation between the number of bits and the number of quantised signal levels is given by:

$$M = 2^m \quad \text{or} \quad m = \log_2 M \tag{1.39}$$

Where, m is the number of bits to be encoded and M the number of codification levels [58], *e.g.* the 8-PAM refers to a pulse-amplitude modulation scheme with 8 levels of codification.

Another modulation scheme that is partially based on amplitude modulation is the Quadrature Amplitude Modulation (QAM). Here, the carriers are encoded through the amplitude and phase of the modulation signal which is usually sinusoidal. Since the carrier waves are 90° out of phase, it uses the available frequency spectrum more efficiently than an only amplitude modulated signal which requires twice the bandwidth. Phase modulation schemes, such as phase-shift keying (PSK), in which the carrier's amplitude remains unchanged can be considered as variants of QAM.

Usually QAM is represented by a constellation diagram with the number of the points – usually of powers of two – that constitute the constellation being the allowed levels to encode data. The most common constellations have 16, 64 or 256 points. The higher the number of points in the constellation more bits per symbol it is possible to encode. Figure 1.25 depicts a 16-QAM constellation diagram followed by a table showing two possible combinations of amplitude and phase required to encode a certain bit stream.

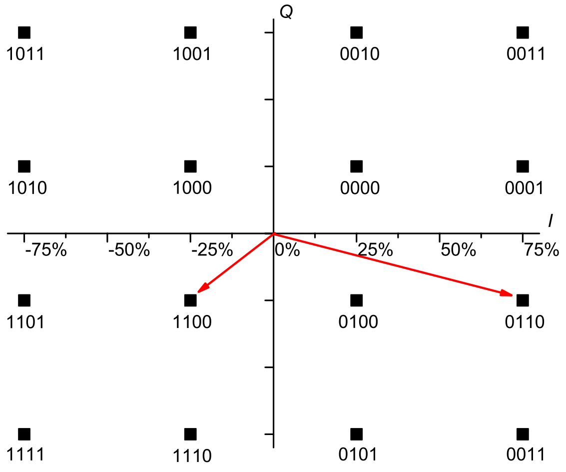

Amplitude	Phase	Data
25%	225%	1100
75%	337%	0110

Figure 1.25 – Illustration of an 16-QAM constellation and a table with the amplitude, phase and corresponding bits.

1.7.2 **OFDM**

Another approach to transmitting a bit stream in which each bit is represented by a significant condition, *e.g.* different voltage levels, is to modulate the data in the frequency domain, usually referred to as frequency-division multiplexing (FDM) modulation. A special case of this type is orthogonal frequency-division multiplexing. The particularity of OFDM lies in the capacity of modulating the carriers orthogonally, a condition that permits an increase the bit stream in limited bandwidths systems. Here, the 'raw' bit stream is initially split in smaller groups, usually called sub-carriers, and then modulated using quadrature amplitude or phase-shift keying modulations.

Following this principle and considering the bit stream presented in Figure 1.26a, it can be initially split in four subcarriers, each one of them being made of six bits, see Figure 1.26b.

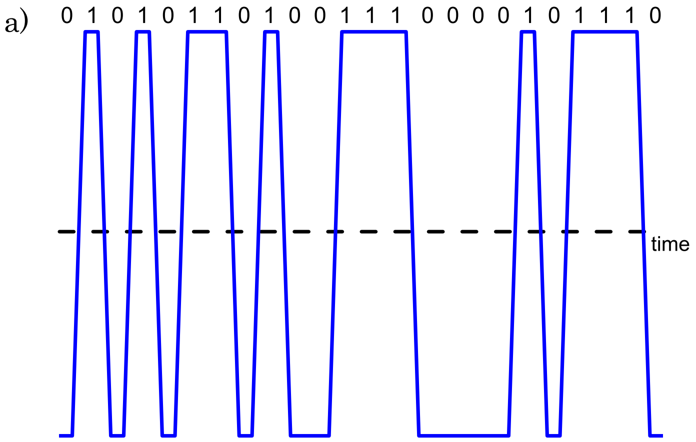

b)

c_1	c_2	c_3	c_4
0	1	0	1
0	1	1	0
1	0	0	1
1	1	0	0
0	0	1	0
1	1	1	0

Figure 1.26 – a) Representation of a bit stream and b) its division in four subcarriers.

After the division each subcarrier is then modulated. For simplicity, binary phase-shift keying (BPSK) is here employed. In BPSK the bits 1 and 0 are mathematically represented, respectively, by,

$$s_0(t) = \sqrt{\frac{2E_b}{T_b}} \cos\left(2\pi f_c t + \pi\right) \tag{1.40}$$

$$s_1(t) = \sqrt{\frac{2E_b}{T_b}} \cos(2\pi f_c t) \tag{1.41}$$

where E_b is the energy per bit, T_b the bit duration and f_c the frequency of the subcarrier. Figure 1.27 presents the four-modulated subcarriers determined by referring to the previous expressions.

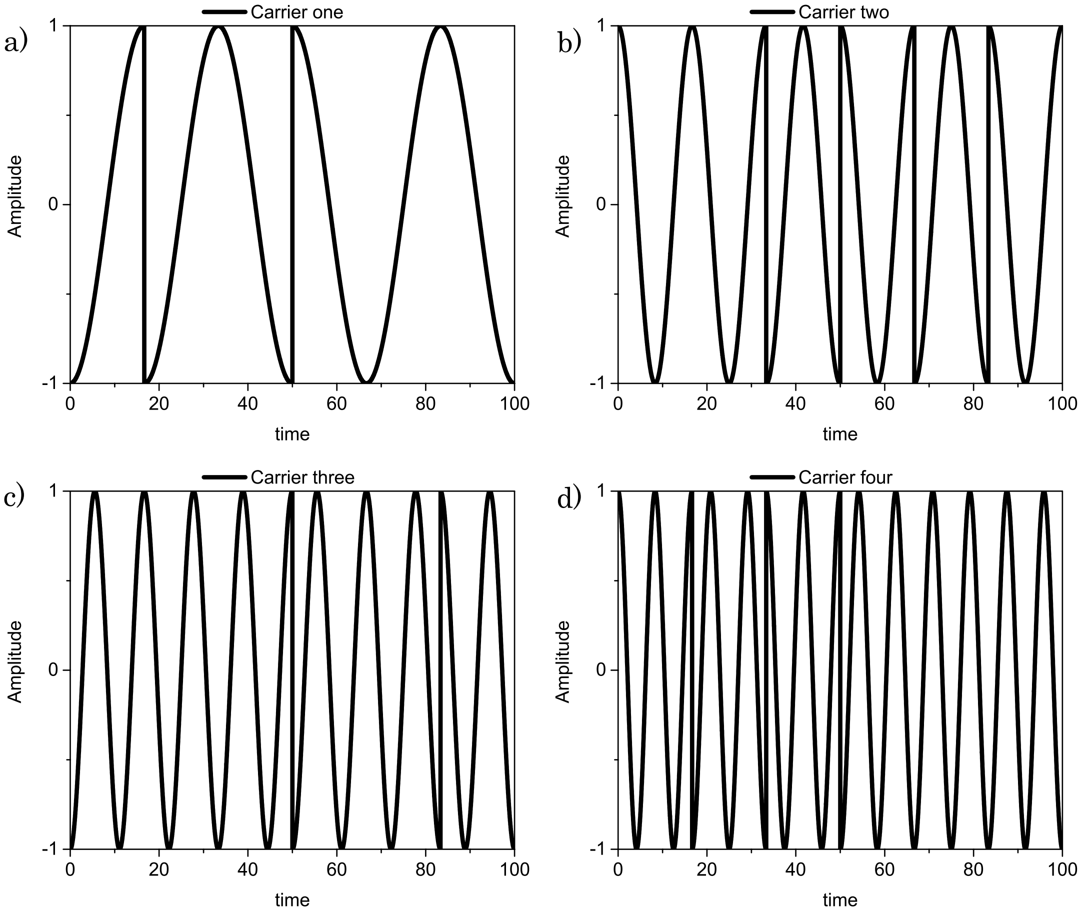

Figure 1.27 – Representation of the sub-carriers modulated using BPSK. The bits that constitute each sub-carrier are presented in Figure 1.26b.

At the end of the process, the OFDM signal results from the combination of the different subcarriers through the use of an inverse fast Fourier Transform (IFFT) [59]. A typical resulting OFDM signal is depicted in Figure 1.28.

The advantages of using OFDM in VLC are its robustness against intersymbol interference, cross-talk and, most important, the capacity of transmitting data with low-frequency distortion from background lighting reducing the complexity of the system at the receiver end [53], [60].

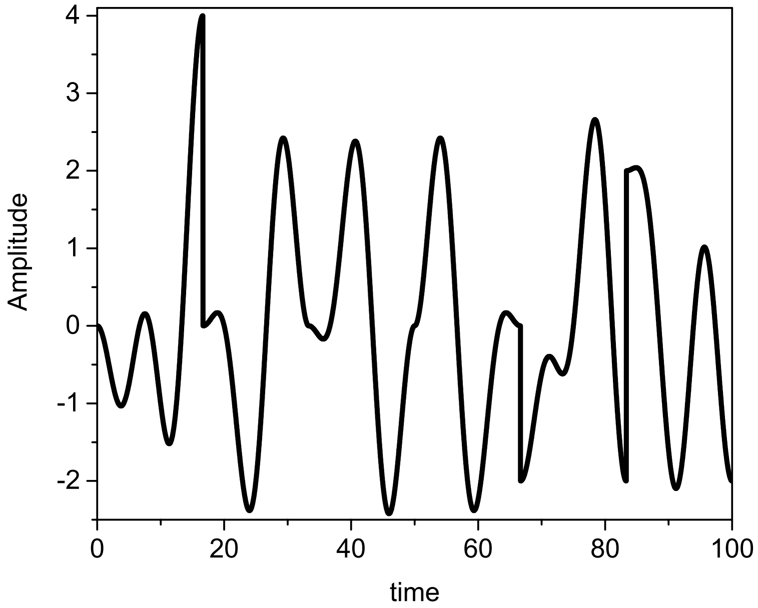

Figure 1.28 – Illustration of a typical OFDM signal.

Figure 1.29 presents the set-up for free-space data transmission used in this work for studying the performance of colour-converters when using an OFDM scheme. After converting the desired bit stream from the frequency-domain to the time-domain using the IFFT block, the processed signal is fed to the waveform generator which converts it in to an analogue-signal. Afterwards, it is amplified and merged with a dc-signal through a bias-tee. Here, a blue optical source, such as a μLED or a laser diode, is used to optically excite the colour-converter. The photoluminescence is then imaged onto a photoreceiver and captured by an oscilloscope. Using a Matlab® script, the signal is then converted to the frequency domain using a fast Fourier transform (FFT) and demodulated [61].

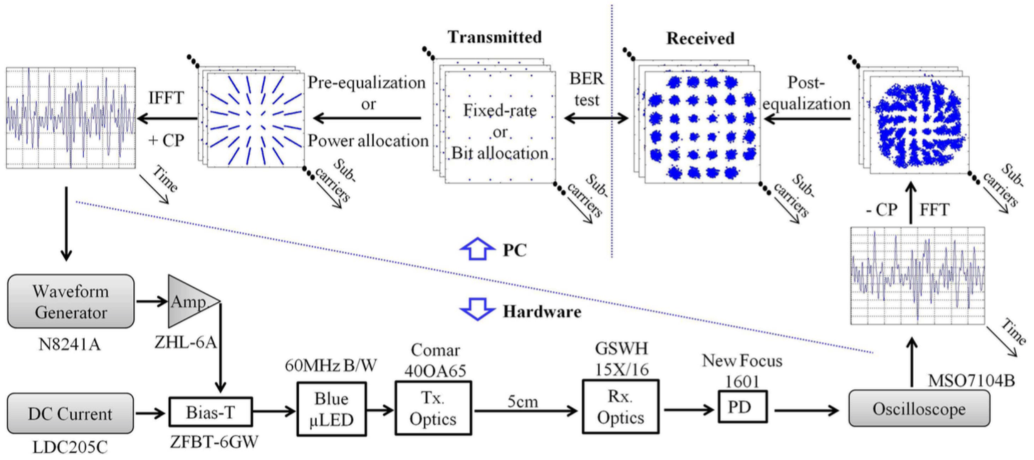

Figure 1.29 – Illustration of an optoelectronic set-up for data transmission using OFDM [61].

Due to imperfections in the data link such as interference or distortion the bit-stream can be totally or partially lost. In order to quantify the number of bits errors a metric called Bit Error Rate (BER) is used. BER is determined through the division of bit with errors by the total number of bits in the bit-stream. Considering the bit-stream presented in Figure 1.24a, if two out of five bits were lost, the BER would be 0.4 or 40%. There are several techniques to control the errors in telecommunications, automatic repeat request (ARQ), forward error correction (FEC) and hybrid automatic repeat request, which is a combination of ARQ and FEC. Here, FEC was employed. It defines the maximum number of errors that can occur within a bit-stream, and the ability to correct them, without the need to retransmit the same bit-stream.

1.8 Optical Receivers

The optical power resulting from electroluminescence in the case of the optical sources and the photoluminescence in the case of the colour-converters can be quantified using an optical receiver. This converts the optical signal into an electronic signal. Depending on the application, different kinds of optical receivers can be used. To carry out this work, a *Si* photodetector and an avalanche photodiode (APD) were used.

Semiconductors photodiodes can be designed based on reverse bias *p-n* or *p-i-n* junctions. Figure 1.30 presents a reversed-biased *p-n* junction from a *p-n* photoreceiver. Photons can be absorbed at any depth within the semiconductor structure resulting in electron-hole pair generation. However, only the electrons and holes under an electric field – which is present in the depletion region – will drift to the *n* and *p* layers, respectively, thus generating an electric current. The resulting current is then proportional to the amount of photons. Photons absorbed outside of the depletion region can still generate electron-hole pairs but due to the absence of an electric field they are annihilated by recombination and do not contribute to the generation of the electric current. Electron-hole pairs that are generated close enough to the depletion region, thus under the presence of a very low electric field can still diffuse to the depletion region contributing to the generation of an electric current [62], [63].

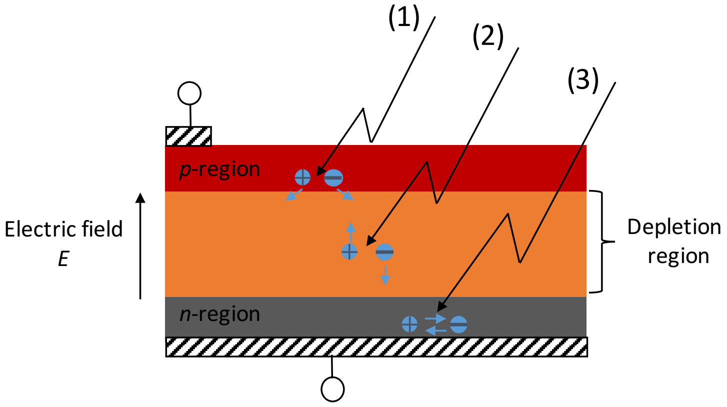

Figure 1.30 – Schematic of a reverse-biased p-n junction in a photoreceiver under external illumination. (1) diffusion of an electron and hole to the depletion region, (2) absorption of a photon within the depletion region and respective formation of an electron-hole pair and (3) annihilation of an electron-hole pair. After [62], [63].

By introducing an intermediate layer – *i*-layer – of undoped semiconductor in between the *p* and *n* layers a *p*-*i*-*n* junction is created. The introduction of the *i*-layer allows sensitivity of a detector to be improved or tailored by its thickness since the depletion region of the device is increased. However, bigger depletion regions reduce the junction capacitance and increase the carrier transit time, resulting in lower bandwidths and reducing their ability to be applied in fast modulation systems such as VLC [62]. Apart from this, *p*-*i*-*n* photodetectors which are not amplified, *i.e.* one photon only produces one electron-hole pair, are limited in low light applications by noise. In order to circumvent these issues, avalanche photodiodes can be used. They can be thought of as a *p*-*i*-*n* photodetector with an amplification stage where electron multiplication occurs. When a photon is absorbed it generates an electron-hole pair where the electron drifts to the *n*-layer and the hole to the *p*-layer. Due to biasing the junction near its breakdown voltage, the carriers collide with the atoms in the crystal lattice and the resultant ionisation creates more electron-hole pairs, which in turn can generate further electron-holes pairs starting a chain reaction [63].

Due to the intrinsic properties of the semiconductor photodetectors and the nature of photon detection, the noise produced during light detection can influence their performance. At very low optical signals the noise floor of the detector is set by the shot noise, the dark current noise and thermal noise. The shot noise derives from the discrete nature of electric charge, *i.e.* photons can be seen as particles that are not detected or reach the detector at exactly the same time inducing a time-dependent current fluctuation following a Poisson distribution. The dark current noise results from the flow of current in the device even when there is no light, behaviour that comes from the crystal defects in the depletion region. Apart from this, thermal noise – also called Johnson noise or Nyquist noise – results from the thermal agitation of electrons at equilibrium [62], [63]. The combination of these factors limits the photoreceiver's sensitivity and in the case of detectors used for telecommunications, it increase the bit-error rate of the system, *i.e.* data bits of a bit stream are lost.

The optical characterisation carried out here was based on a commercial silicon photodetector, Thorlabs S121C. It presents a wavelength range between 400-1100 nm with maximum detectable optical power up to 500 mW and active area of 9.7 x 9.7 mm [64]. The photoreceiver spectral response is shown in Figure 1.31.

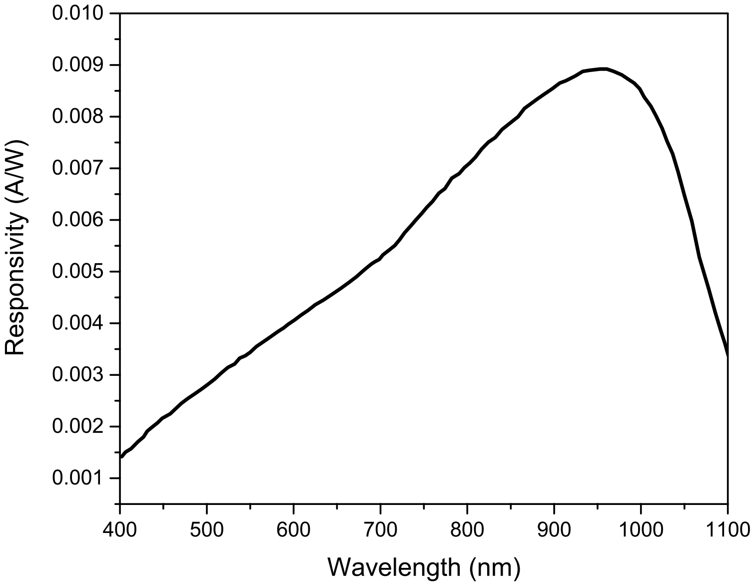

Figure 1.31 – Thorlabs photodetector spectral response. After [64].

1.9 Summary

This chapter started by describing the motivation for the execution of this work and how it can be important for visible light communications and lighting solutions.

This was followed by the introduction of semiconductor physics important for the understanding of how the optical sources, such as LEDs and laser diodes, work, their main limitations and the required physical process to fabricate them.

Subsequently, the physics of the colour-converters used throughout this work was presented. We started by introducing organic semiconductors, namely BBEHP-PPV, followed by colloidal quantum dots and finally the epitaxial structures based on II-VI and III-V alloyed semiconductors. There, a brief explanation of the techniques employed to create each of them was presented, followed by description of their structures.

The rest of this chapter provided a very brief explanation of modulation schemes employed in visible light communications, such as PAM and OFDM, and the physics behind the optical receivers to support some of the work done with the optical sources and colour-converters presented.

References

[1] H. J. Round, “A note on carborundum,” *Electr. World*, vol. 39, no. 309, 1907.

[2] E. F. Schubert, *Light-Emitting Diodes*, 2nd ed. Cambridge University Press, 2006.

[3] C. W. Chow, C. H. Yeh, Y. Liu, and Y. F. Liu, “Digital Signal Processing for Light Emitting Diode Based Visible Light Communication,” *IEEE Photonics Soc. Newletter*, pp. 9–13, 2012.

[4] H. Masui, J. S. Speck, and S. P. Denbaars, “Non-polar-oriented InGaN light-emitting diodes for liquid-crystal-display backlighting,” *J. Soc. Inf. Disp.*, vol. 16, no. 4, pp. 571–578, 2012.

[5] S. Nakamura and M. R. Krames, “History of gallium-nitride-based light-emitting diodes for illumination,” *Proc. IEEE*, vol. 101, pp. 2211–2220, 2013.

[6] T. Yamazato, I. Takai, H. Okada, T. Fujii, T. Yendo, and S. Arai, “Image-Sensor-Based Visible Light Communication for Automotive Applications,” *IEEE Commun. Mag.*, no. July, pp. 88–97, 2014.

[7] A. Khan, “Semiconductor photonics: Laser diodes go green,” *Nat. Photonics*, vol. 3, no. 8, pp. 432–434, 2009.

[8] J. Lin, “Osram Prototype InGaN LEDs Bridges Green Gap,” 2014. [Online]. Available: http://www.ledinside.com/news/2014/11/osram_prototype_ingan_leds_bridges_green_gap.

[9] A. Jovicic, J. Li, and T. Richardson, “Visible Light Communication : Opportunities , Challenges and the Path to Market,” *IEEE Commun. Mag.*, vol. 51, no. 12, pp. 26–32, 2013.

[10] A. Tsiatmas, P. M. J. Baggen, F. M. J. Willems, J.-P. M. G. Linnartz, and J. W. M. Bergmans, “An Illumination Perspective on Visible Light Communications,” *IEEE Commun. Mag.*, vol. 52, no. 7, pp. 64–71, 2014.

[11] D. Graham-Rowe, “From dots to devices,” *Out Lab*, vol. 3, no. June, pp. 307–309, 2009.

[12] S. Haruyama, “Visible Light Communication using sustainable LED lights,” *ITU Kaleidosc. Acad. Conf.*, 2013.

[13] D. C. O’Brien, L. Zeng, H. Le-Minh, G. Faulkner, J. W. Walewski, and S. Randel, “Visible light communications: Challenges and possibilities,” *2008 IEEE 19th Int. Symp. Pers. Indoor Mob. Radio Commun.*, pp. 1–5, Sep. 2008.

[14] S. Yu, O. Shih, and H. Tsai, “Smart Automotive Lighting for Vehicle Safety,” *IEEE Commun. Mag.*, no. December, pp. 50–59, 2013.

[15] L. C. Png, L. Chen, S. Liu, and W. K. Peh, “An Arduino-based indoor positioning system (IPS) using visible light communication and ultrasound,” *2014 IEEE Int. Conf. Consum. Electron. - Taiwan*, pp. 217–218, 2014.

[16] G. Corbellini, K. Aksit, S. Schmid, S. Mangold, and T. R. Gross, “Connecting Networks of Toys and Smartphones with Visible Light Communication,” *IEEE Commun. Mag.*, no. July, pp. 72–78, 2014.

[17] H. Uema, T. Matsumura, S. Saito, and Y. Murata, “Research and Development on Underwater Visible Light Communication Systems,” *Electron. Commun. Japan*, vol. 98, no. 3, pp. 9–13, 2015.

[18] M. Fukuda, *Optical Semiconductor Devices*. New York: John Wiley & Sons, 1999.

[19] J. J. Wierer, J. Y. Tsao, and D. S. Sizov, "Comparison between blue lasers and light-emitting diodes for future solid-state lighting," *Laser Photonics Rev.*, vol. 993, no. 6, pp. 963–993, 2013.

[20] E. Matioli and C. Weisbuch, "Impact of photonic crystals on LED light extraction efficiency: approaches and limits to vertical structure designs," *J. Phys. D. Appl. Phys.*, vol. 43, no. 35, p. 354005, 2010.

[21] K. H. Li, C. Feng, and H. W. Choi, "Analysis of micro-lens integrated flip-chip InGaN light-emitting diodes by confocal microscopy," *Appl. Phys. Lett.*, vol. 104, no. 5, p. 51107, 2014.

[22] C. Chiu, C. Lee, C. Liu, B. Lin, C. Lin, W. Hsu, and J. Sheu, "Enhancing light extraction from LEDs," *SPIE*, vol. 1, pp. 2–4.

[23] Y.-C. Lee, C.-H. Ni, and C.-Y. Chen, "Enhancing light extraction mechanisms of GaN-based light-emitting diodes through the integration of imprinting microstructures, patterned sapphire substrates, and surface roughness.," *Opt. Express*, vol. 18 Suppl 4, no. November, pp. A489–A498, 2010.

[24] C. J. Lewins, D. W. E. Allsopp, P. A. Shields, X. Gao, B. Humphreys, and W. N. Wang, "Light Extracting Properties of Buried Photonic Quasi-Crystal Slabs in InGaN/GaN LEDs," *J. Disp. Technol.*, vol. 9, no. 5, pp. 333–338, May 2013.

[25] C. J. Lewins, E. D. Le Boulbar, S. M. Lis, P. R. Edwards, R. W. Martin, P. A. Shields, and D. W. E. Allsopp, "Strong photonic crystal behavior in regular arrays of core-shell and quantum disc InGaN/GaN nanorod light-emitting diodes," *J. Appl. Phys.*, vol. 116, no. 4, p. 44305, Jul. 2014.

[26] D. A. B. Miller, “Optical Physics of Quantum Wells,” *AT&T Bell Lab.*, vol. 1, no. 1, pp. 1–28.

[27] M. K. Kelly, O. Ambacher, R. Dimitrov, R. Handschuh, and M. Stutzmann, “Optical process for liftoff of Group III-nitride films,” *Phys. Status Solidi*, pp. 1–2, 1996.

[28] M. R. Krames, O. B. Shchekin, R. Mueller-Mach, G. O. Mueller, L. Zhou, G. Harbers, and M. G. Craford, “Status and future of high-power light-emitting diodes for solid-state lighting,” *IEEE/OSA J. Disp. Technol.*, vol. 3, no. 2, pp. 160–175, 2007.

[29] Newport, “Laser Diode Technology,” 2016. [Online]. Available: https://www.newport.com/t/laser-diode-technology.

[30] A. Kohler and H. Bassler, *Electronic Processes in Organic Semiconductors: An Introduction*. Wiley-VCH, 2015.

[31] J. R. Lakowicz, “Principles of Fluorescence Spectroscopy,” in *Principles of Fluorescence Spectroscopy*, 3 rd., Sptinger.

[32] M. Fox, *Optical Properties of Solids*. Oxford University Press, 2001.

[33] H. D. Young, R. A. Freedman, and A. L. Ford, *University Physics with Modern Physics*, 13th ed. Addison-Wesley.

[34] Y. Chen, J. Herrnsdorf, B. Guilhabert, A. L. Kanibolotsky, A. R. Mackintosh, Y. Wang, R. A. Pethrick, E. Gu, G. A. Turnbull, and P. J. Skabara, “Laser action in a surface-structured free-standing membrane based on a π-conjugated polymer-composite,” *Org. Electron.*, vol. 12, no. 1, pp. 62–69, 2011.

[35] M. T. Sajjad, P. P. Manousiadis, H. Chun, D. A. Vithanage, S. Rajbhandari, A. L. Kanibolotsky, G. Faulkner, D. O'Brien, P. J. Skabara, I. D. W. Samuel, and G. A. Turnbull, "Novel Fast Color-Converter for Visible Light Communication Using a Blend of Conjugated Polymers," *ACS Photonics*, vol. 2, no. 2, pp. 194–199, 2015.

[36] A. P. Alivisatos, "Semiconductor Clusters, Nanocrystals, and Quantum Dots," *Science (80-.).*, vol. 271, pp. 5–7, 1996.

[37] C. B. Murray, D. J. Norris, and M. G. Bawendi, "Synthesis and characterization of nearly monodisperse CdE (E = sulfur, selenium, tellurium) semiconductor nanocrystallites," *J. Am. Chem. Soc.*, vol. 115, no. 19, pp. 8706–8715, Sep. 1993.

[38] D. Ratchforda, K. Dziatkowskia, T. Hartsfield, X. Li, Y. Gao, and Z. Tang, "Photoluminescence dynamics of ensemble and individual CdSe/ZnS quantum dots with an alloyed core/shell interface," *J. Appl. Phys.*, 2011.

[39] J. J. D. Mckendry, D. Massoubre, S. Zhang, B. R. Rae, R. P. Green, E. Gu, R. K. Henderson, A. E. Kelly, and M. D. Dawson, "Visible-Light Communications Using a CMOS-Controlled Micro-Light-Emitting-Diode Array," *J. Light. Technol.*, vol. 30, no. 1, pp. 61–67, 2012.

[40] V. I. Klimov, "Nanocrystal Quatum Dots From fundamental photophysics to multicolor lasing," *Los Alamos Sci.*, no. 28, pp. 214–220, 2003.

[41] K. Kyhm, J. H. Kim, S. M. Kim, and H. Yang, "Gain dynamics and excitonic transition in CdSe colloidal quantum dots," *Opt. Mater. (Amst).*, vol. 30, no. 1, pp. 158–160, Sep. 2007.

[42] D. Bimberg, "Quantum dots: Paradigm changes in semiconductor physics," *Semiconductors*, vol. 33, no. 9, pp. 951–955, Sep. 1999.

[43] Y. Shirasaki, G. J. Supran, M. G. Bawendi, and V. Bulović, “Emergence of colloidal quantum-dot light-emitting technologies,” *Nat. Photonics*, vol. 7, no. December 2012, 2013.

[44] Alexander Y. Šik, *Quantum Wells: Physics and Electronics of Two-Dimensional Systems*. 1997.

[45] B. O. Dabbousi, F. V Mikulec, J. R. Heine, H. Mattoussi, R. Ober, K. F. Jensen, and M. G. Bawendi, “(CdSe) ZnS Core-Shell Quantum Dots : Synthesis and Characterization of a Size Series of Highly Luminescent Nanocrystallites,” *J. Phys. Chem. C*, vol. 9463, no. 97, pp. 9463–9475, 1997.

[46] P. Kathirgamanathan, L. Bushby, and M. Kumaraverl, “Red and Green Quantum Dot Based LEDs Demonstrating Excellent Color Coordinates,” *SID Tec. Dig.*, pp. 266–269, 2015.

[47] M. A. Hines and P. Guyot-Sionnest, “Synthesis and characterization of strongly luminescing ZnS- Capped CdSe nanocrystals,” *J. Phys. Chem.*, vol. 100, no. 2, pp. 468–471, 1996.

[48] W. K. Bae, K. Char, H. Hur, and S. Lee, “Single-Step Synthesis of Quantum Dots with Chemical Composition Gradients,” *Am. Chem. Soc.*, no. 22, pp. 531–539, 2008.

[49] K. Boldt, N. Kirkwood, G. A. Beane, and P. Mulvaney, “Synthesis of Highly Luminescent and Photo-Stable, Graded Shell CdSe/Cd,” pp. 1–8, 2013.

[50] B. Guilhabert, D. Elfström, A. J. C. Kuehne, D. Massoubre, H. X. Zhang, S. R. Jin, A. R. Mackintosh, E. Gu, R. A. Pethrick, and M. D. Dawson, “Integration by self-aligned writing of nanocrystal/epoxy composites on InGaN micro-pixelated light-emitting diodes.,” *Opt. Express*, vol. 16, no. 23, pp. 18933–41, Nov. 2008.

[51] G. Ozin, A. Arsenault, and L. Cadermartiri, *Nanochemistry A Chemical Approach to Nanomaterials*, 2nd Editio. RSC Publishing, 2009.

[52] C. B. Murray and C. R. Kagan, “Synthesis and Characterization of Monodisperse Nacocrystals and Close-Packed Nanocrystal Assemblies,” pp. 545–610, 2000.

[53] S. Dimitrov and H. Haas, *Principles of LED Light Communications Towards Networked Li-Fi.* Cambridge University Press 2015, 2015.

[54] M. Tavan, E. Agrell, J. Karout, and S. Member, “Bandlimited Intensity Modulation,” *IEEE Glob. Commun. Conf.*, pp. 1–28, 2011.

[55] S. Hranilovic and F. R. Kschischang, “Optical intensity-modulated direct detection channels: Signal space and lattice codes,” *IEEE Trans. Inf. Theory*, vol. 49, no. 6, pp. 1385–1399, 2003.

[56] J. Armstrong and A. J. Lowery, “Power efficient optical OFDM,” *Electron Lett*, vol. 42, no. 6, 2006.

[57] R. Ramaswani, K. N. Sivarajan, and G. Sasaki, *Opitcal Networks A Pratical Perspective*, 3th ed. Elsevier, 2012.

[58] G. P. Agrawal, *Fiber Optic Communication Systems*, 4th ed. Wiley, 2010.

[59] J. Armstrong, “OFDM for optical communications,” *J. Light. Technol.*, vol. 27, no. 3, pp. 189–204, 2009.

[60] H. Burchardt, N. Serafimovski, D. Tsonev, S. Videv, and H. Haas, “VLC : Beyond Point-to-Point Communication,” *IEEE Commun. Mag.*, no. July, pp. 98–105, 2014.

[61] D. Tsonev, H. Chun, S. Rajbhandari, J. J. D. Mckendry, S. Videv, E. Gu, M. Haji, S. Watson, A. E. Kelly, G. Faulkner, M. D. Dawson, H. Haas, and D. O. Brien, "A 3-Gb / s Single-LED OFDM-Based Wireless VLC Link Using a Gallium Nitride μLED," *IEEE Photonics Technol. Lett.*, vol. 26, no. 7, pp. 637–640, 2014.

[62] B. E. A. Saleh and M. C. Teich, *Fundamentals of Photonics*, 1st Editio. A Wiley-Interscience Publication, 1991.

[63] J. G. Graeme, *Photodiode Amplifiers Op Amp Solutions*. McGraw-Hill, 1996.

[64] Thorlabs, "S121C - Standard Photodiode Power Sensor, Si, 400 - 1100 nm, 500 mW," 2009. [Online]. Available: https://www.thorlabs.com/thorproduct.cfm?partnumber=S121C.

Chapter 2

Characterisation of optical sources

The preceding chapter focused on introducing the physics of the optical sources and the colour-converters. In addition, a brief explanation of modulation formats used in telecommunications was presented since the main purpose of this study is to analyse a possible integration of these down-converters as part of communication systems. In order to fully characterise the presented materials for a possible system implementation a set of tests needed to be developed. Before this though, the main optical sources for visible light communications used here, namely commercial GaN LEDs, GaN μLEDs and GaN laser diodes had to be characterised. The current chapter will start by providing an overview of the set-ups used for optical source and sample characterisation along with a brief explanation of the tests performed. The set-ups and tests will be applied throughout the following chapters that will focus on presenting the most important results for each one of the down-converters, *i.e.* colloidal quantum dots, BBEHP-PPV, II-VI and III-V materials. At the end of the chapter, the data obtained from the optical sources used throughout this thesis will be presented. For simplicity, the CW and dynamic characteristics for each one of the devices and colour-converters will be split into two sections.

2.1 Experimental setups

In our work, three separate excitation sources were used for VLC colour-conversion, namely commercial GaN LEDs, custom-fabricated GaN μLEDs and commercial GaN laser diodes. Initial tests were performed with colour-converters not integrated with these sources, therefore an optical lens system to collimate and focus the excitation light and then to collect and relay the colour-converted light was required. At first, a set of small diameter lenses was used, however due to the LED's divergent (Lambertian) emission profile and the low lens numerical apertures (NA) most of the light was not focused onto the down-converter. So, they were replaced by a set of aspheric condenser lenses, ACL4532-A which offer a large NA (NA = 0.61). By increasing the numerical aperture one can increase the amount of light that goes through the optics resulting in more light reaching the colour-converter. For small angles, a two-fold increase in the numerical aperture will approximately double the acceptance cone angle. This follow from the definition of numerical aperture:

$$NA = n \sin\theta \qquad (2.1)$$

where n and θ are the refractive index of the medium and the acceptance cone angle, respectively.

The same principle was applied after the colour-converter, *i.e.* the emitted down-converted light from it was collimated and then focused onto a power meter, fibre spectrometer or photoreceiver. During some tests, a microscope objective was incorporated in the set-up, after the last condenser lens, to reduce the beam diameter for light detection improvement, especially in the bandwidth measurements since there the photoreceiver's active area was quite small. In general, a FEMTO HSA-X-S-1G4-SI photoreceiver with an effective active area diameter of ∅8 mm was used.

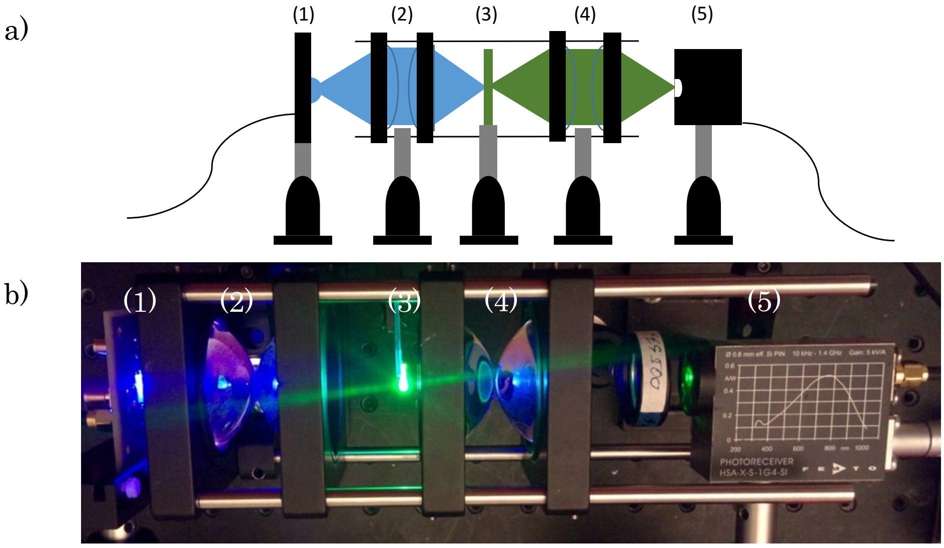

Figure 2.1 – Schematic illustration (a) and photograph (b) of the system used to characterise the optical sources and colour-converters. (2) and (4) refer to the set of aspheric lenses, (1) to the optical source, (3) to the colour-converter and (5) to the photoreceiver.

Figure 2.1 presents an illustration of the main set-up. To improve the system alignment two translation stages are used, one to hold and control the optical source and the other one photoreceiver. Depending on the test being made, edge-pass optical filters were also used to block the remaining light from the optical pump or the light from the colour-converter. In this case, the filter can be placed right before the detector. Since the colour-converters have emissions in the longer wavelength visible range (540nm and 630nm) and the optical sources emit around 450 nm, three filters were used, namely FES0500, FEL0500 and FEL0550 from Thorlabs. Their cut-off wavelengths and respective transmissions are presented in Figure 2.2.

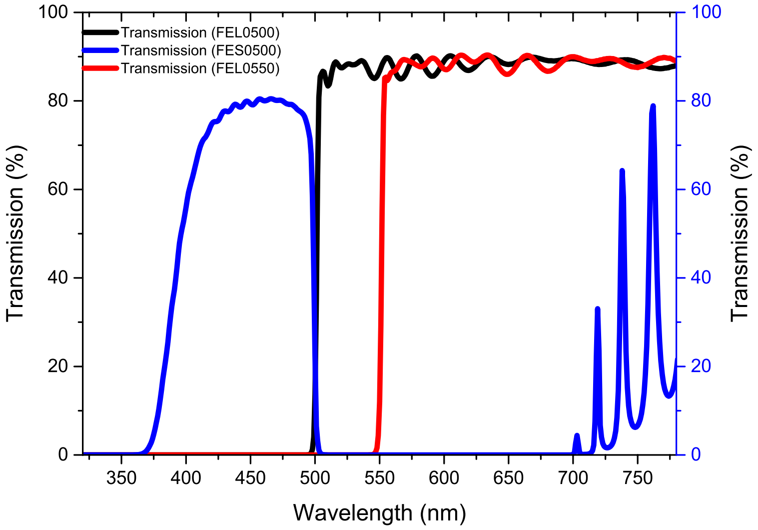

Figure 2.2 – Transmission spectra of the optical filters used during characterisation of the optical sources and colour-converter samples.
Figure based on [1].

As indicated in Figure 2.2, the optical filters still absorb around 10% of the transmitted light, in the case of the long-pass filters, and around 20% in the case of the short-pass filter. This was taken into consideration in the data analysis. A ‘figure of merit’ for the colour-converter samples is the absorption and relative emission efficiency. These are calculated, respectively, using the following equations:

$$absorption\ (\%) = \frac{P_{source} - (P_{transmitted} + \alpha(\lambda) \times P_{transmitted})}{P_{source}} \times 100\% \qquad (2.2)$$

$$relative\ efficiency\ (\%) = \frac{P_{colour-converter}}{P_{source} - (P_{transmitted} + \alpha(\lambda) \times P_{transmitted})} \times 100\% \qquad (2.3)$$

where P_{source} is the power from the optical source without any colour-converter, $P_{transmitted}$ the power from the optical source that was not absorbed by the colour-converter, $P_{colour\text{-}converter}$ the power from the colour-converter and $\alpha(\lambda)$ the optical filter absorption. As said before, the light that is not absorbed by the colour-converter is measured by using a short pass filter to block the down-converted light. The same principle but using a long pass filter is used to measure only the down-converted light.

In the case of organic semiconductors like BBEHP-PPV, it is important to assess how stable the material is and for how long it can be used in visible light communications since under continuous illumination it will photobleach – *i.e.* show a decrease of photoluminescence intensity over time. Assessment of this was performed using a similar setup to that depicted in Figure 2.1, but with a beam splitter placed immediately before the sample under test. The power was then measured for both excitation and colour-converted light during a defined period of time using a controlling LabVIEW® programme created for this purpose. It is important to measure the power from the optical source and the sample from the beginning since the test can run for several days and temperature fluctuations affect both optical powers.

Apart from the steady-state measurements, time-resolved and frequency-domain measurements were also carried out. They allow the study of characteristics that are not possible to analyse in the steady-state regime. The main differences between these measurements are related to the test's sensitivity. The time-resolved measurements are able to temporally resolve the acquired signals in a way that it is possible, through the intensity and decay curve, distinguish a mixture of two or more components in the same sample and retrieve information about the shape and molecular flexibility, something that would be difficult using steady-state techniques since the acquired signal is averaged over time [2], [3]. Knowing the carrier lifetimes which, as will be shown later, are directly related to the colour-converter's bandwidths, it is possible to infer how fast a certain material can be modulated for data transmission.

In the time-domain regime the measurements are performed using time-correlated single-photon counting (TCSPC). Here, the samples are excited using pulsed light sources with excitation pulses in the range of picoseconds (*ps*) or femtoseconds (*fs*), shorter than the sample's fluorescence decay times, τ. The sample is periodically excited by a repetitive train of these pulses and the intensity decay profile over time is recorded and displayed in a histogram form [3]. A schematic of such a time-domain system is presented in Figure 2.3.

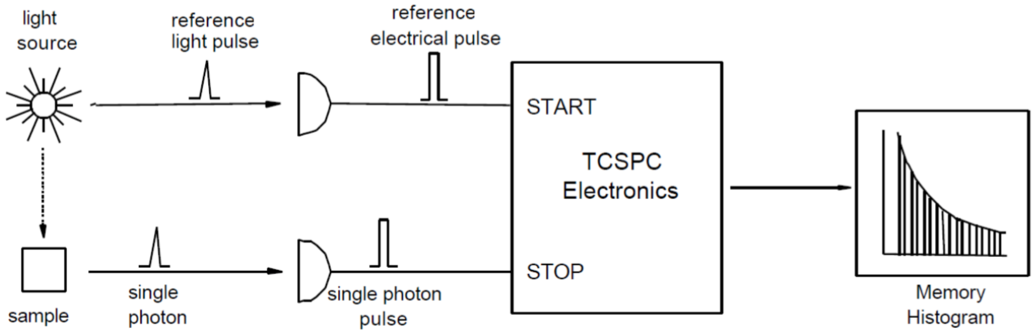

Figure 2.3 – Working principle illustration of TCSPC equipment [4].

The system relies on the capability of photon detection and ability to determine the exact arrival time of a photon at the photoreceiver. The measurement starts by recording the exact time the excitation source sends a pulse using a constant fraction discriminator (CFD). The signal is then fed to a time-to-amplitude converter (TAC), which will create a voltage signal that increases linearly with time on the nanosecond scale. The arrival time of the fluorescence signal is accurately determined through another CFD using a second channel. This will work as a switch stopping the voltage signal being created by the TAC. This signal is then proportional to the start-stop signal. After amplification, using a programmable gain amplifier (PGA), the generated analogue signal is converted to a digital signal by an ADC (analogue-to-digital converter). The converted signal is then sampled as a histogram, where the x-axis is the time interval between the excitation source pulse and the photon detection from the fluorescent material and the y-axis the number of photons detected in those intervals. The system response is further improved by removing low intensity signals such as noise or false readings which will impair the calculated response. This is done by setting a minimum threshold intensity level for the detected signal to be considered. This detection range is limited by using a window discriminator (WD) [2].

The TCSPC can have two operating modes, the forward mode in which the starting signal is set by the excitation source and the reverse mode where the acquisition is started by the fluorescent photons. The photon lifetime is directly related with the TAC signal, the ability to sense a photon will depend on how fast the TAC can be reset, set to zero and detect another incoming photon, this process is usually referred to as dead time and no photon is detected during this period. TCSPC conditions are set to detect one photon or less per pulse, otherwise only the first photon is detected and the following ones lost. This leads to an oversampling of early photons biasing the histogram to shorter times and increase of order in the exponential decay curve, such effect is called pulse pile-up [2]. To avoid this, the photon detection rate should be smaller than the repetition rate of the excitation source [4]. By using a reverse mode, the signal does not need to be reset at every iteration. The only constraint comes from the required pump's shift delay that needs to be set so it will arrive at the input of the TAC later than the fluorescent pulses from the detector [2], [4]. By repeating this process until the desired number of counts is obtained, it is possible to create a histogram displaying the average decay lifetime. The decay time is then calculated by fitting the data with a multi-exponential decay model:

$$I(t) = \sum_i a_i \exp\left(-t/\tau_i\right) \tag{2.4}$$

where, a_i is the intensity at time *0* and τ_i is the decay time. The intensity decay can be single-exponential or multi-exponential. Depending on the decay complexity, one can always define a mean decay time. In the case of a single decay time, the lifetime is given when the initial intensity drops by *1/e*.

In this work, the fluorescence lifetime of a sample was determined through the reconvolution of the system response and the theoretical equation of the intensity decay presented above, *I(t)*. This was done using the commercial software T900® from Edinburgh Instruments®. Here, the instrument response, *E(t')*, and the convoluted response, *F(t)*, are measured separately. Then, the software fits the convoluted sample response $F(t)$ to the data in order to find the parameters a_i and τ_i from the decay model equation, expression (2.5) [5].

$$F(t) = \int_0^t E(t')I(t - t')dt' \tag{2.5}$$

Another approach to measure the decay time is by a frequency-domain method. Here, instead of being pumped with very short optical pulses the samples are excited with an intensity modulated signal. From this, it is possible to infer the samples' maximum bandwidths and modulation speeds. The lifetime can be determined by the phase-shift between the excitation modulation and the modulated emission or by the decrease in signal amplitude relative to the excitation modulation. This is possible due to the delay set by the absorption-emission of photons. In addition, the finite carrier excited lifetime results in the demodulation of the emission usually expressed by the factor m_ω, expression (2.11). The demodulation will cause a reduction of peak-to-peak amplitude of the modulated signal. Figure 2.4 illustrates schematically the phase-shift and modulated emission from a down-converter.

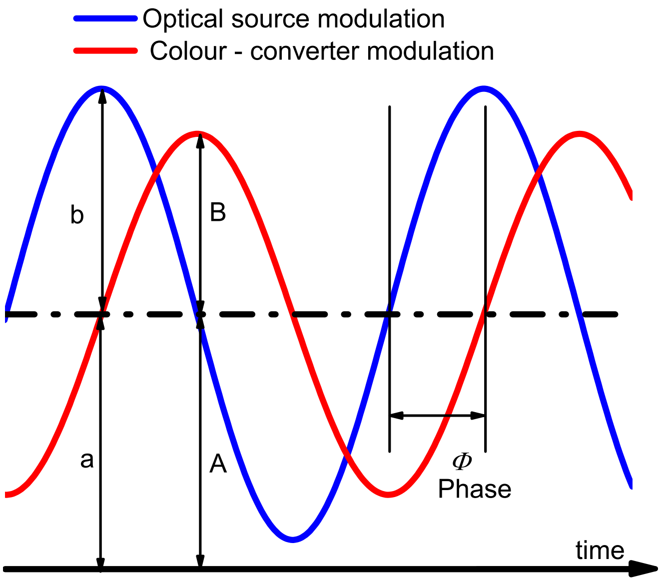

Figure 2.4 – Schematic of the phase shift and modulation from the optical modulator and colour-converter at the same frequency (figure based on [2]). The modulation factor between each wave can be determined by using expression (2.7).

The intensity drop from the emission with increase of modulation frequency comes from the inability of the excited carriers to follow the modulation due to their lifetime. Consider for example a sample with carrier lifetime of 10 ns modulated by a sine wave with a period of 200 ns, which corresponds to a frequency of 5 MHz. This means the carriers will follow closely the excitation intensity with a low phase-shift from the initial signal since the carriers will have time to relax and to be photo-pumped again. Increasing the modulation up to 200 MHz, which corresponds to a period of 5 ns, that is half of the carrier lifetime, means they will be excited twice in the same modulation cycle. This results in an averaging of the decay across the full modulation, resulting in a phase-shift and decrease of signal amplitude with increase of modulation frequency. Considering a single-exponential decay, the lifetimes can be determined using the phase-shift and the modulation factor by:

$$tan\emptyset_{\omega} = 2\pi f\tau \qquad (2.6)$$

$$m_{\omega} = \frac{B/A}{b/a} = \frac{1}{\sqrt{1+(2\pi f)^2\tau^2}} \qquad (2.7)$$

Here, $\emptyset_{\omega}$ is the phase-shift angle, f is the modulation frequency and τ the lifetime. By sampling the single-exponential over a pre-determined set of frequencies it is thus possible to determine the frequency response. A single-exponential decay will not fully describe a sample containing multiple components, where the lifetime must be considered as a weighted contribution. Such a multi-decay can be expressed by:

$$N(\omega) = \frac{\sum_i \frac{a_i\omega\tau_i^2}{(1+\omega^2\tau_i^2)}}{\sum_i a_i\tau_i} \qquad (2.8)$$

$$D(\omega) = \frac{\sum_i \frac{a_i\tau_i}{(1+\omega^2\tau_i^2)}}{\sum_i a_i\tau_i} \qquad (2.9)$$

where *N(ω)* and *D(ω)* are, respectively, the sine and cosine Fourier transforms of the intensity decay, expression (2.4) [6]. From this, the phase angle and the demodulation factors can be obtained by:

$$tan\emptyset_{\omega} = \frac{N_{\omega}}{D_{\omega}} \tag{2.10}$$

$$m(\omega) = (N(\omega)^2 + D(\omega)^2)^{1/2} \tag{2.11}$$

There are different processes to acquire a frequency response from any device/down-converter, however they follow the same principle. An optical source is modulated over a certain range of frequencies and the modulated emission is recorded and mathematically processed to obtain the lifetime.

In this work, in order to obtain the bandwidths and/or the lifetimes from the optical sources and the colour-converters the set-up used is as depicted in Figure 2.1. The modulation signal, hereafter referred to as the RF signal, was electrically coupled to a DC signal and fed to the optical source using a wideband Bias-Tee (working range from 0.1 up to 6000 MHz). The modulated signal, coming from the optical source or the colour-converter was then imaged onto the photoreceiver, Femto HSA-X-S-1G4-SI with bandwidth up to 1.4 GHz. An Agilent HP 8753ES Network Analyser was used to generate and record the measured frequency response, see Figure 2.5.

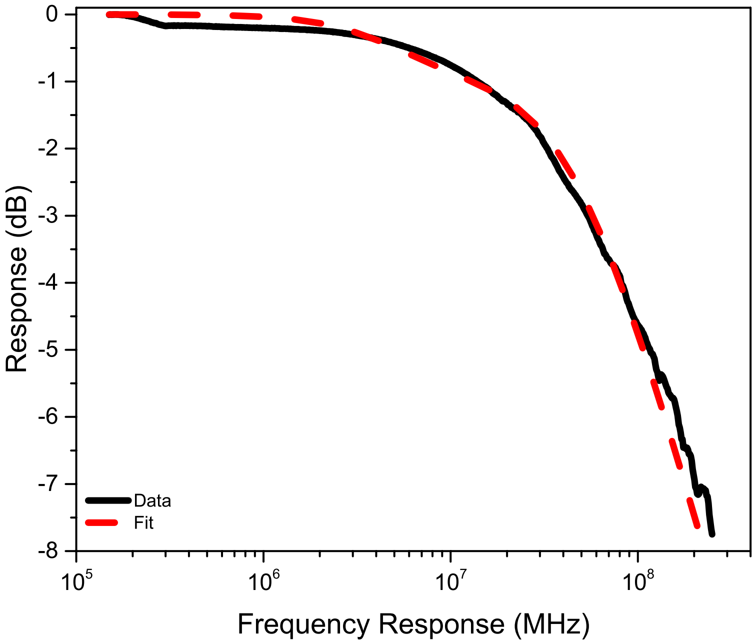

Figure 2.5 – Typical frequency response of a modulated µLED (black curve) and the respective fit (red curve) to obtain the bandwidth.

The bandwidths are obtained by fitting the frequency response with a single- or multi-exponential decay, following expression (2.11). This was done using a Matlab® script. In the case of the colour-converters however, a pre-fitting step is required in order to determine their intrinsic frequency response. Similarly with the TCSPC method, the resulting system response is the convoluted signal from the frequency response of the colour-converter and the optical excitation source, equation (2.12).

$$m_{system\ response}(\omega) = m_{optical\ source}(\omega) * m_{colour-converter}(\omega) \tag{2.12}$$

$$S = \sum_{i=1}^{N} \left(x(i) - x_{ref}(i)\right)^2 \tag{2.13}$$

After the data acquisition, it is loaded into the software, de-convoluted, normalised and linearized. Then, using a least-square method, as presented in expression (2.13), where N is the number of data points, the software minimises the sum of the squares of the raw data, $x(i)$, and the predicted model, $x_{ref}(i)$. After minimisation, the data is interpolated in order to obtain the value of bandwidth. Care should be taken in this step, as one should determine if the recorded data corresponds to electrical or optical power. The network analyser used for bandwidths measurements converts the current generated in the photoreceiver, produced by the incoming photons, into an electrical power, so the electrical bandwidth will correspond to the value in which this power drops to half of its initial value [7]. There is, though, some equipment in which the optical power is proportional to a current and where the optical bandwidth is the value at which the current drops by half. The relationship between bandwidths of the electrical and the optical powers can be seen in Figure 2.6, showing that the optical -3 dB is equivalent to the electrical -6 dB value. All the recorded data is in electrical dB, but throughout this thesis it will be presented as optical dB and thus the bandwidths described are the -3dB optical bandwidths [7].

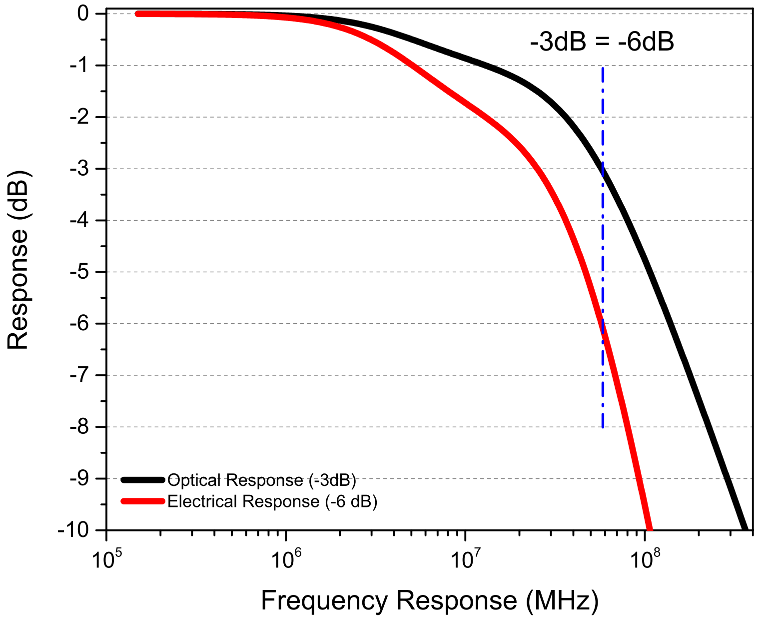

Figure 2.6 – Illustration of the difference between electrical and optical bandwidths from a typical frequency response of a μLED.

In addition to the bandwidth measurements, several data encoding schemes were considered to assess the device feasibility as a data transmitter (see Chapter 1). The optical set-up for this was the same as previously described. For the Pulse-Amplitude Modulation (PAM) an Agilent Technologies 81150A Pulse Function Arbitrary Generator was used to provide the required data stream. The modulation signal was then coupled to a bias signal using a wideband Bias-Tee. At the receiver end, the signal was focused onto an OMEGA avalanche photodiode (APD) that was connected to an Agilent Technologies MSO71043 oscilloscope [8]. For the OFDM test, an Agilent 81180A Arbitrary Waveform Generator was used to deliver the desired analogue signal. The signal before being transmitted through the device was amplified (Mini-Circuits ZHL-6A). The optical response was then acquired by the APD and mathematically processed using a Matlab® script. Here, the detected signal is converted to the time domain using a fast Fourier Transform (FFT) and demodulated [9].

The APD was designed and built at Oxford University and it is based on a commercial avalanche photodetector, Hamamatsu S8890, combined with a commercial transimpedance amplifier, Maxim MAX 3665. The generated analogue signal from the arriving photons is then passed to a limiting amplifier creating a logic level. In order to increase the light collection, and consequently the system gain, an optical concentrator can be placed on top of the avalanche detector window [8].

The data transmission can be further analysed by referring to an eye pattern, more commonly known as an eye diagram. This is used in first instance to evaluate the transmitted signal and identify possible issues that will impair the signal integrity [10]. The eye-diagram is so-called since the pattern displayed by an oscilloscope presents a shape similar to an eye. This is done by overlapping sets of bits from the main data stream with a desired periodicity, see Figure 2.7.

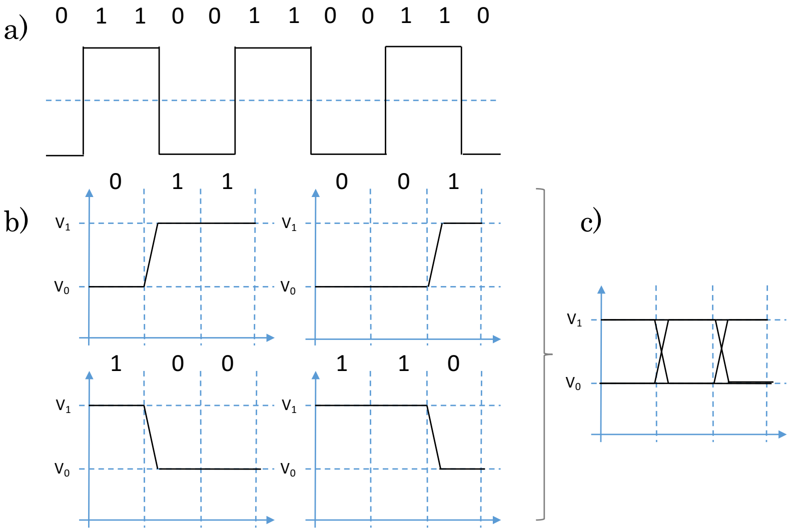

Figure 2.7 – Illustration of an eye-diagram pattern. a) Representative set of bits, b) bit modulation and c) periodic overlap of the set of bits forming an eye-diagram.

In a real telecommunication system, the eye diagram will present distortion due to system impairments such finite rise and fall times, impedance mismatches, jitter and interference from cables and connectors. This will cause a reduction of amplitude in the detected signal and results in eye diagram 'closure' leading to an increase of data errors, see Figure 2.8. The distinction between bits is made by setting a threshold level in which the signals above it are recognized as 1's and below as 0's. The noisier the signal the more difficult it is to resolve it, leading to an increase in the Bit Error Rate (BER), expressed as:

$$BER = \frac{number\ of\ errors}{total\ number\ of\ transmitted\ bits} \tag{2.14}$$

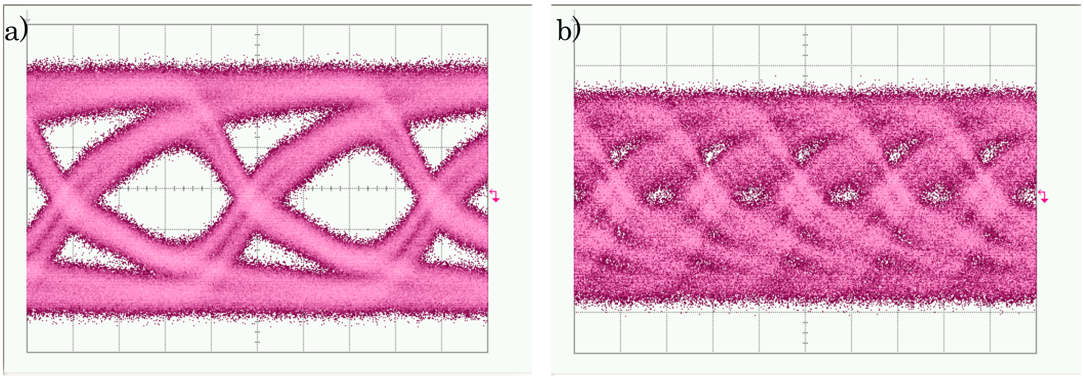

Figure 2.8 – Eye-diagram at a) 50Mbit/s and b) 100Mbit/s from the same quantum dot samples under the same pumping conditions (see Chapter 3). The eye diagram closes at the higher data rates due to factors including the upper state lifetime.

As explained in subchapter 1.5 and demonstrated in the following chapters, different advanced modulation formats can be employed in certain circumstances to overcome these limitations.

2.2 Optical source characterisation (µLED, commercial LED, Laser Diode)

The basic optical characterisation data from each of the optical sources used during this work will be presented below and was obtained using the set-ups described above. Three different optical sources were used. The tests started with a commercial OSRAM Dragon PowerStar GaN LED for slow colour-converter tests, followed by InGaN µLEDs fabricated in house by Dr. Enyuan Xie for faster modulation. Since the samples initially were tested in non-integrated format and then were integrated onto the optical sources, three different µLED chips were utilised. For the non-integrated test, a chip containing four pixels of the same size, 100 x 100 µm^2, was used. For inorganic semiconductor platelet integration, two further chips were designed. As will be presented in Chapter 4, the II-VI membrane was integrated onto a chip with 10 pixels of the same size, 100 x 100 µm^2. In the case of the III-V membrane, a chip with 8 pixels of sizes 50 x 50 µm^2, 75 x 75 µm^2, 100 x 100 µm^2 and 150 x 150 µm^2, respectively, was fabricated. In addition, to study the down-converters at high power densities an OSRAM PL450B GaN laser diode was used.

The following subchapter will start by presenting the data measured in continuous-wave regime followed by the dynamic characterisation.

2.2.1 **Continuous wave (CW) characteristics**

The first optical source we consider is the OSRAM Dragon PowerStar GaN LED, see Figure 2.9a. This is a commercial blue light source that can be used for down-converter excitation. The light-emitting die, which has an active area of 300x300 μm^2, is covered with an epoxy dome that increases the light extraction efficiency and can redirect the emitted light. The epoxy dome also mechanically protects the GaN chip and the fragile wire bonds, as depicted in Figure 2.9b. This device is coupled to a small star-shaped passive heat sink in order to minimise heating effects, see Figure 2.9a. As explained in Chapter 1, heat causes an increase in the non-radiative carrier recombination causing a reduction in LED performance or even resulting in permanent device failure. Furthermore, if one needs to integrate down-converter materials in such devices, heat management issues will be reduced since they already have a passive heat sink. To further improve the heat management, the LEDs were mounted onto a metallic plate.

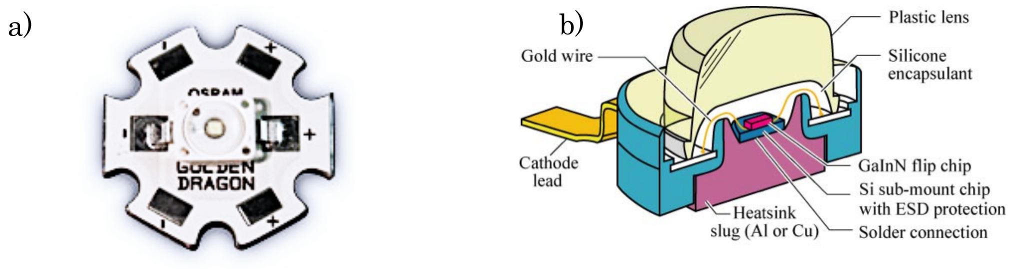

Figure 2.9 – a) Picture of an OSRAM Dragon PowerStar LED and b) schematic of an LED die. The schematic depicts the epoxy dome that is used to protect and redirect the LED´s output. Also, all the wiring and the heatsink are shown. (after [11], [12]*)*

According to the datasheet the LED can be driven up to 1000 mA and presents a Lambertian emission with viewing angle of 120°. However, the maximum driving current was set at 300 mA which corresponds to an optical power output around 110 mW. This is the maximum power that can be measured by our power meter before saturation in the set-up used, see Figure 2.10a.

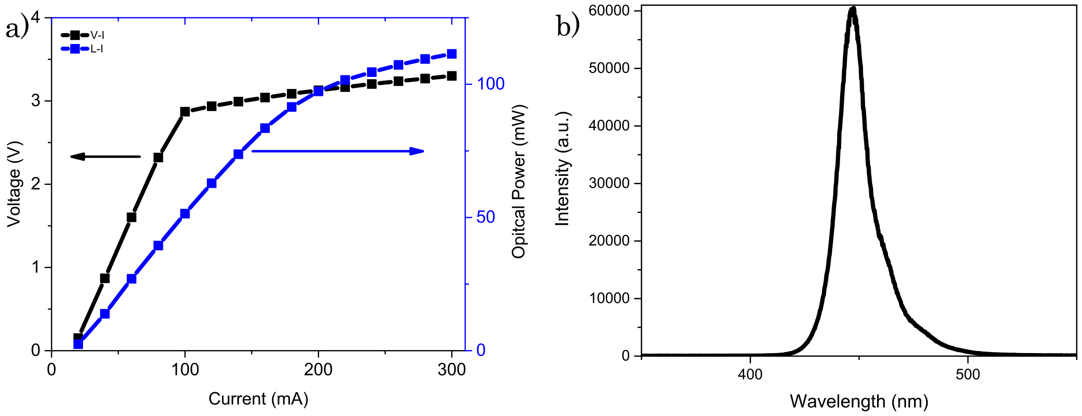

Figure 2.10 – a) L-I-V curves and b) optical spectrum at 100 mA for the OSRAM PowerStar LED.

Figure 2.10b presents the commercial LED spectrum measured at 100 mA. It shows a peak-emission centred at 450nm, with FWHM of 15 nm.

As previously stated three different flip-chip μLEDs were fabricated, one for testing the samples without integration and the other two for inorganic semiconductor platelets integration. The optical tests of these devices were also performed using the setup depicted in Figure 2.1. For emission at 450 nm the μLEDs are based on epi-structures containing eleven $In_{0.18}GaN_{0.82}$/GaN multi-quantum wells with a 0.16 μm Mg-doped cap epilayer, 4 μm of undoped GaN and 2.5 μm Si-doped GaN grown on *c*-plane sapphire substrate. After designing the desired pixel sizes and layout, a photo mask was fabricated in order to pattern a photoresist layer deposited onto the wafer before plasma etching. This allowed creation of the LED mesas with the desired pixel size. Afterwards, a passivation layer of silicon oxide (SiO_2) was deposited by plasma-enhanced chemical vapour deposition (PECVD). To electrically drive the pixels, *p*-contacts were created by evaporating Ni/Au (10/15 nm) metal multilayers onto small apertures created in the passivation layer by buffered oxide wet etch. The *n*-contact for each chip is shared between all pixels, using pads made of Ti/Au (50/200 nm) [13]. After fabrication the chip was then bonded onto a printed circuit board and each pixel electrically connected to a SMA connector by wire-bonding the *n*- and *p*- contacts to the desired metal tracks. The L-I-V curves and spectral response from each device, free-space μLED, II-VI and III-V μLEDs are presented in Figure 2.12, respectively. (*N.B.*: what we refer to as II-VI and III-V μLEDs are here the underlying GaN μLEDs later bonded to these materials).

A commercial InGaN OSRAM laser diode was also used to test the fabricated colour-converters. The use of a laser diode allows the study of these materials in high power regimes that are not achieved with LEDs. Their modulation bandwidths are also much higher than the light emitting diodes, making them interesting for visible light communications. The blue laser diode used is based on the same III-V alloys as the μLEDs, however the detailed epitaxial structures and fabrication process is different. Cleaved and polished/etched facets form an optical resonator in this case, and the device is driven until feedback combines with stimulated emission to reach laser threshold [14]. The spectral response and L-I-V curve for the laser diode used are presented in Figure 2.11.

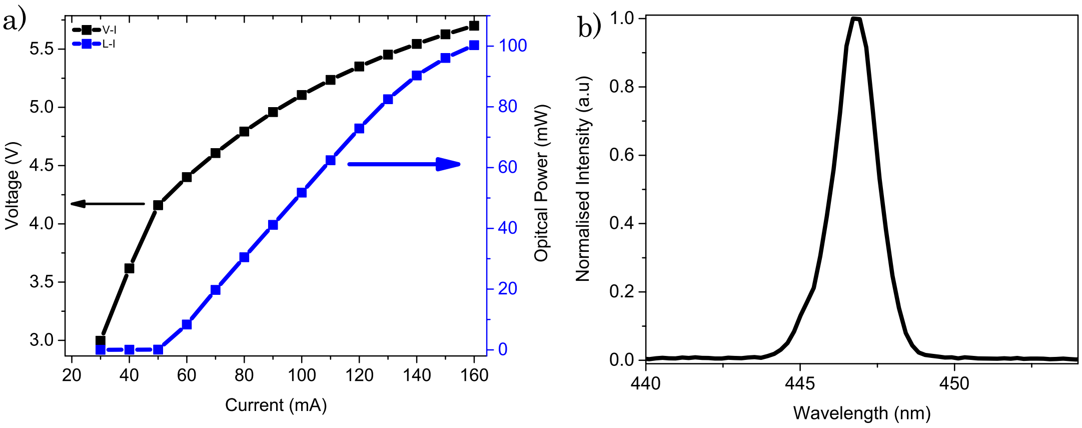

Figure 2.11 – L-I-V curve and spectral response for the commercial laser diode.

As will be presented in Chapter 5, the dependence of modulation frequency response on the excitation power density at the colour-converter was studied. The power density was determined using a Coherent Beam Master to measure the spot size of each optical source. In order to focus the beam onto the detector, a pair of aspheric lenses ACL4532-A were used. To avoid irreversible damage to the detector's head a neutral density filter was placed inside the detector slit alongside an external attenuator wheel. Using a translation stage, a range of distances along the focused beam were swept in order to determine the focal point position and spot size. The data was then stored in a file which registers the optical power and the detector's reference axis components *V* and *W* of the beam.

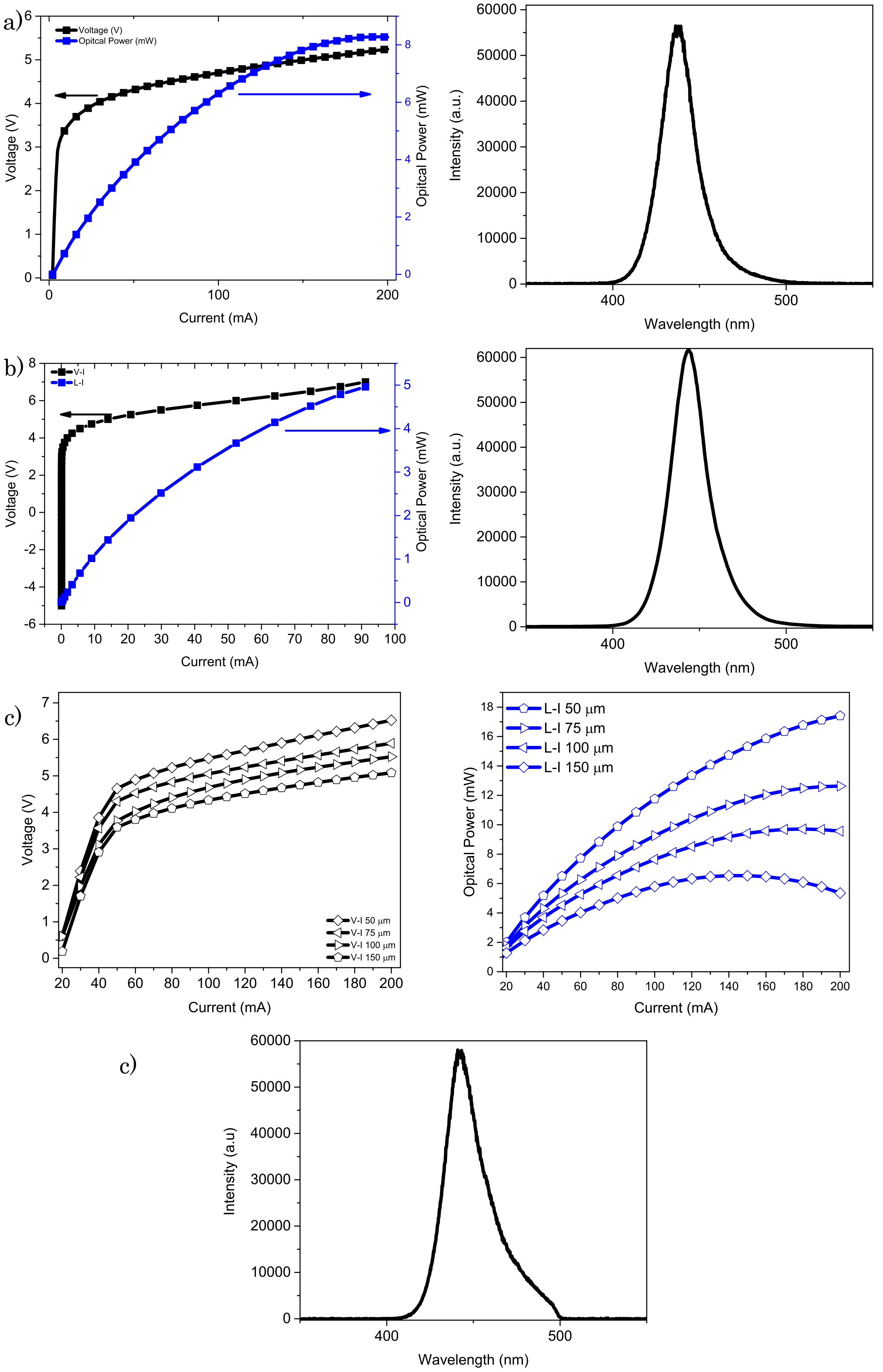

Figure 2.12 – L-I-V curves and spectral response for, a) free-space, b) II-VI and c) III-V µLEDs. As noted in the introduction to section 2.2, the III-V µLEDs contain pixels of several sizes.

From the Lambertian emission profile one needs to extract the Full Width Half Maximum (FWHM) from both profile components in order to calculate the spot size. This was done using a Matlab® script in which the values were obtained using a Gaussian fit, see expressions (2.15) and (2.16):

$$y = y_0 + Ae^{-\left[\frac{(x-x_0)^2}{2w^2}\right]} \tag{2.15}$$

$$FWHM = 2w\sqrt{\ln(4)} \tag{2.16}$$

where A corresponds to the Gaussian fit amplitude, x_0 the value where the maximum of the peak amplitude is localized and $2w$ the Gaussian RMS width. Since the beam profile was fitted with a Gaussian function there is an intrinsic fitting error in the power density determination. In order to determine this error, both FWHM components were obtained by a weighted average from the measured currents at focal point. From this, the area of the beam was calculated. It was considered to be a circular focal point for the LED's and elliptical for the laser diode.

The reduction of emission efficiency at higher driving currents – usually referred to as efficiency droop – depicted in all L-I curves is due to the increase of current density. Such behaviour may result from heat or, as described in Chapter 1, Auger non-radiative recombination.

2.2.2 **Dynamic characteristics**

As stated previously, in addition to the CW characteristics the optical sources and the colour-converters were also studied dynamically. For this, the optical set-up was basically the same as presented previously with the main difference being the use of a Bias-Tee to combine a DC and RF signal. The output signal then modulated the optical source and, when required, also drove the source to excite the down-converter samples. The bandwidths obtained from the optical sources will be presented below.

2.2.2.1 **Modulation Bandwidth**

To understand how the frequency response changes with different driving conditions, the devices were first powered at low currents which was increased afterwards until the maximum optical power before roll-over. For each of the currents, the frequency response was determined using the method presented in subchapter 2.1, equation (2.11). In the case of the commercial LED, the maximum achievable bandwidth was found to be around 11 MHz, see Figure 2.13. As previously explained, the bandwidths are intrinsically related to the material under study. The faster the carrier recombination the faster the device can be modulated. Furthermore, the bandwidths are related to the current density. By increasing the driving current within the same device, there is an improvement of frequency response. The mechanism behind this behaviour is still under scientific debate but recently some groups have suggested that Auger non-radiative recombination plays a major role in this process [15], [16]. By employing the ABC model (described in Chapter 1), where A, B and C represent, respectively, the Shockley-Read-Hall, radiative and Auger recombination, it is possible to match the differential carrier lifetime measured experimentally to the radiative and non-radiative contribution to the lifetime [16]. It is thereby shown that the carrier lifetime will be reduced by an increase of current density. Apart from this, other possible explanations were presented by other groups such as, recombination at defect sites at higher carrier density and leakage of electrons from the active region [17], [18].

From the above discussion, we can expect an increase of modulation speed when the active area of the LED is decreased, because in that case modest currents give high current densities and thus reduced differential carrier lifetimes. This effect has been studied previously for µLEDs by M^{c}Kendry *et al.* [19]. This behaviour is confirmed for µLED devices in Figure 2.13 and Figure 2.14. The smallest µLED, 50 x 50 µm^2, presents a maximum current density of 64 A/cm^2 whilst the 75 x 75 µm^2, 100 x 100 µm^2 and 150 x 150 µm^2 devices present maximum current densities of 35.5 A/cm^2, 20 A/cm^2 and 8.9 A/cm^2, respectively.

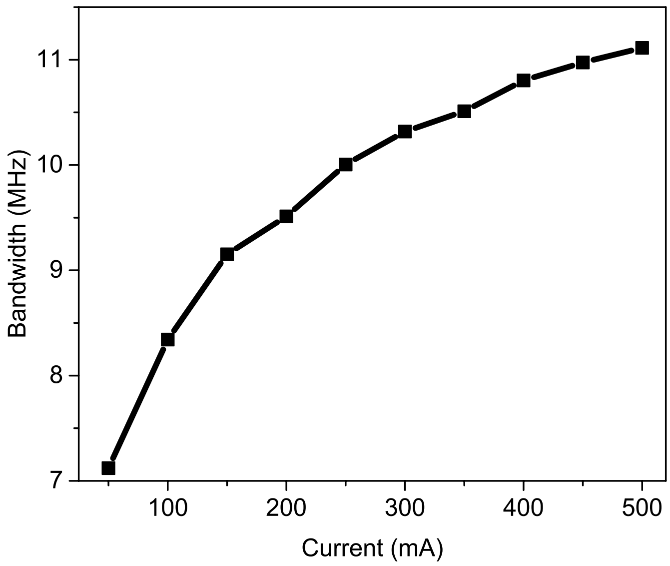

Figure 2.13 – The commercial LED's bandwidth as a function of driving currents.

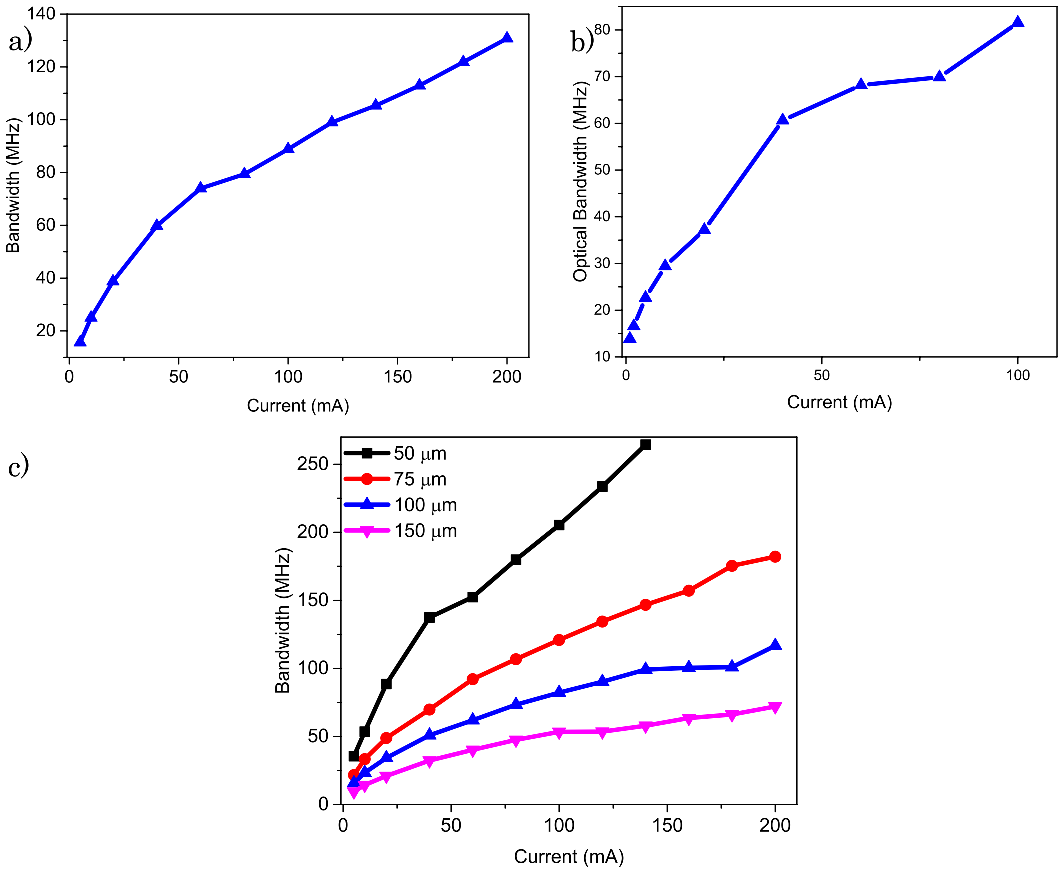

Figure 2.14 – Frequency response for, a) free-space, b) II-VI and c) III-V μLEDs.

The bandwidths of the different 100 μm^2 devices are similar reaching a maximum of 120 MHz at 200 mA or 20 A/cm^2, which corresponds to the current before thermal roll-over. Higher bandwidths can be achieved with smaller pixels, meaning higher current densities, reaching a maximum of 250 MHz in the studied 50 μm device.

The laser diode bandwidth was measured as well following the principles described above. However, it was found that its frequency response is higher than the bandwidth of the FEMTO photoreceiver of 1.4 GHz, see Figure 2.15, so no definite measurement was possible.

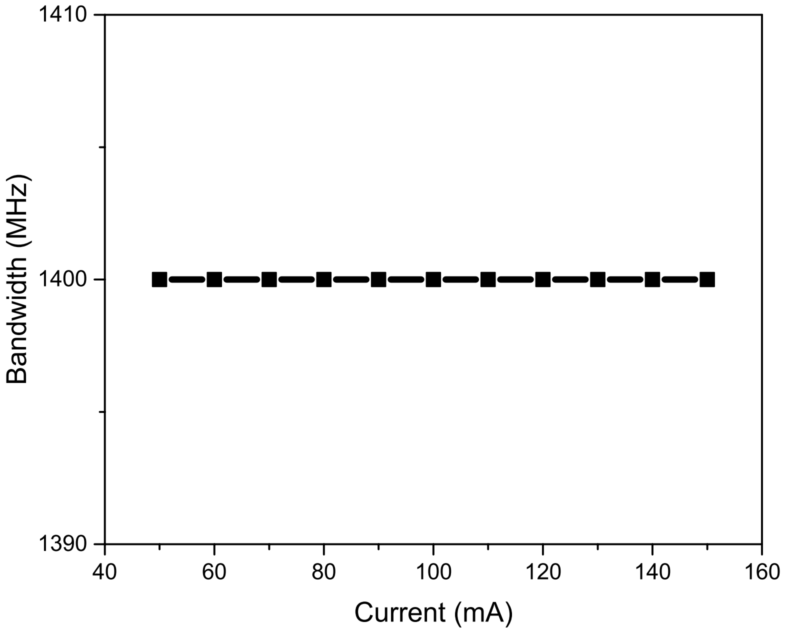

Figure 2.15 – Frequency response of the FEMTO photoreceiver measured when trying to determine the frequency response of the laser diode.

2.3 Summary

In this chapter, the tests and set-ups used to analyse the optical sources and colour-converters throughout the present work were described. Section 2.1 provided an in-depth description of the experimental setups and consideration taken in order to be able to compare the performance of the different down-converters. A basic time-correlated single-photon counting system used to determine the semiconductor carrier's lifetime has been discussed. In addition, a description was given of the calculations to extract the frequency response of the optical sources and down-converters. An important test for telecommunications performance analysis uses eye diagram patterns to assess the data transmission quality. Such tests were described here and through the manipulation of a bit stream, an eye diagram construction was presented.

In section 2.2, the optoelectronic characteristics of the different GaN optical sources were presented. This began by presenting the continuous wave characteristics for a commercial LED. It was found that a maximum driving current of 300 mA gave an optical output power of 110 mW with a peak wavelength emission centred around 450 nm. Smaller LED pixel sources, with emission at 450 nm, were fabricated in house and used to pump down-converters. In this case, it was found that the maximum achievable optical power output was 16 mW for a driving current of 200 mA with a pixel size of 150μmx150μm. The smallest tested pixel was 50μmx50μm and presented a maximum optical output of 6 mW at 150 mA. A commercial laser diode was used as well to characterise down-converters. This presented a peak emission centred at 450 nm with an optical power output of 100 mW at 160 mA. The dynamic characteristics section presented the bandwidths of all the optical sources described in the continuous wave section. The commercial LED showed a maximum bandwidth of 11 MHz at 500 mA and the μLED bandwidths were between 250 MHz and 50 MHz depending on their size. As was discussed, smaller pixels present a higher frequency response.

The bandwidth of the laser diode was studied as well. However, its bandwidth was higher than the 1.4 GHz bandwidth of the photodetector used.

References

[1] Thorlabs, "Edgepass Filters: Longpass and Shortpass." [Online]. Available: https://www.thorlabs.com/NewGroupPage9.cfm?ObjectGroup_ID=918.

[2] J. R. Lakowicz, "Principles of Fluorescence Spectroscopy," in *Principles of Fluorescence Spectroscopy*, 3 rd., Sptinger.

[3] M. Wahl, "Time-correlated single photon counting," no. PicoQuant Techincal Note, pp. 1–14, 2014.

[4] E. Instruments, "What is TCSPC? Time-Correlated Single-Photon Counting," *Tech. Note*, pp. 1–4, 2012.

[5] E. Instruments, *Edinburgh Instruments mini-tau User Guide*, Issue No. 2013.

[6] J. R. Lakowicz, G. Laczko, and H. Cherek, "Analysis of Fluorescence decay kinetics form variable-frequency phase shift and modulation data," *J. Biophys. Soc.*, vol. 46, no. October, pp. 463–477, 1984.

[7] Picometrix: An API Company, "Bandwidth Terminology," *Response*. [Online]. Available: http://advancedphotonix.com/hsor/application-notes/bandwidth-terminology/.

[8] D. O'Brien, R. Turnbull, H. Le Minh, G. Faulkner, O. Bouchet, P. Porcon, M. El Tabach, E. Gueutier, M. Wolf, and L. Grobe, "High-Speed Optical Wireless Demonstrators: Conclusions and Future Directions," *J. Light. Technol.*, vol. 30, no. 13, pp. 2181–2187, 2012.

[9] D. Tsonev, H. Chun, S. Rajbhandari, J. J. D. Mckendry, S. Videv, E. Gu, M. Haji, S. Watson, A. E. Kelly, G. Faulkner, M. D. Dawson, H. Haas, and D. O. Brien, "A 3-Gb / s Single-LED OFDM-Based Wireless VLC Link Using a Gallium Nitride μLED," *IEEE Photonics Technol. Lett.*, vol. 26, no. 7, pp.

637–640, 2014.

[10] D. Behera, S. Varshney, and S. T. Sunaina Srivastava, “Eye Diagram Basics: Reading and applying eye diagrams,” *EDN Network*, 2011. [Online]. Available: http://www.edn.com/design/test-and-measurement/4389368/Eye-Diagram-Basics-Reading-and-applying-eye-diagrams.

[11] “LED Dragon PowerStars.” [Online]. Available: http://i-led.co.uk/LED-Light-Engines/LED-PowerStars/Dragon.php.

[12] E. F. Schubert, *Light-Emitting Diodes*, 2nd ed. Cambridge University Press, 2006.

[13] Z. Gong, S. Jin, Y. Chen, J. McKendry, D. Massoubre, I. M. Watson, E. Gu, and M. D. Dawson, “Size-dependent light output, spectral shift, and self-heating of 400 nm InGaN light-emitting diodes,” *J. Appl. Phys.*, vol. 107, no. 1, p. 13103, 2010.

[14] J. Luft, M. Behringer, and L. Sources, “Diode Lasers Small devices with great performance,” *Laser J.*, vol. 2, no. 2, pp. 57–63, 2005.

[15] Y. C. Shen, G. O. Mueller, S. Watanabe, N. F. Gardner, a. Munkholm, and M. R. Krames, “Auger recombination in InGaN measured by photoluminescence,” *Appl. Phys. Lett.*, vol. 91, no. 14, pp. 37–40, 2007.

[16] A. David and M. J. Grundmann, “Droop in InGaN light-emitting diodes: A differential carrier lifetime analysis,” *Appl. Phys. Lett.*, vol. 96, no. 10, pp. 1–4, 2010.

[17] B. Monemar and B. E. Sernelius, “Defect related issues in the ‘current roll-off’ in InGaN based light emitting diodes,” *Appl. Phys. Lett.*, vol. 91, no. 18, pp. 181101–181103, 2007.

[18] S. Choi, H. J. Kim, S. S. Kim, J. Liu, J. Kim, J. H. Ryou, R. D. Dupuis, A. M. Fischer, and F. A. Ponce, "Improvement of peak quantum efficiency and efficiency droop in III-nitride visible light-emitting diodes with an InAlN electron-blocking layer," *Appl. Phys. Lett.*, vol. 96, no. 2010, pp. 6–9, 2010.

[19] J. J. D. Mckendry, D. Massoubre, S. Zhang, B. R. Rae, R. P. Green, E. Gu, R. K. Henderson, A. E. Kelly, and M. D. Dawson, "Visible-Light Communications Using a CMOS-Controlled Micro-Light-Emitting-Diode Array," *J. Light. Technol.*, vol. 30, no. 1, pp. 61–67, 2012.

Chapter 3

CQD and BBEHP-PPV colour-converters

Following the optical sources characterisation chapter where the optical set-ups were described and the optoelectronic characteristics of such sources discussed, the study of down-converters for visible light communications will now be introduced. The materials for colour-conversion which are considered here are red and green colloidal quantum dots and the green-emitting polymer poly[2,5-bis(2′,5′-bis(2″-ethylhexyloxy)phenyl)-p-phenylene vinylene] denoted BBEHP-PPV [1].

The chapter will start with a detailed description on preparing the colour-converters as composites, followed by the CQDs' continuous wave characteristics, L-I-V curves, spectral response and absorption and relative conversion efficiency dependence with increased PMMA concentration in the composite. The dynamical characteristics are also presented and comprise measurements of bandwidth, lifetimes and advanced modulation formats. The CQD bandwidth measurement was made in collaboration with Dr. Sujan Rajbhandari at the University of Oxford. The chapter will end with the results from the CW and stability tests performed with the BBEHP-PPV colour-converter.

3.1 Preparation of CQ composites

As was introduced in Chapter 1, we study two main types of colloidal quantum dots (CQDs), namely 'alloyed' and 'core-shell'. The main difference between them comes from their physical structure. In the case of core-shell dots the core and the shell are well defined by an interface (potential barrier) whilst the alloyed ones have graded composition radially from the centre. A schematic illustrating both types of CQDs was presented in Figure 1.10.

As explained in Chapter 1, the emission properties of colloidal quantum dots depend on the composition, size and alloy ratio constituting these semiconductor nanoparticles. With a decrease in size, there is a spectral shift to bluer wavelengths, behaviour easily seen when quantum dots with the same alloyed structure but with different sizes are optically pumped using the same source. With size reduction, there is a higher quantum confinement that increases the band gap energy resulting in the emission of photons with higher energies. Additionally, in the case of core-shell CQDs, the shell thickness is important since it will influence the photoluminescence intensity and electron-hole recombination lifetime. The combination of these characteristics makes the CQDs an interesting material to be studied for visible light communications [2], [3]. In our work, graded/alloyed quantum dots based on the ternary II-VI semiconductor CdSSe/ZnS were studied. As mentioned in Chapter 1, the graded quantum dots offer higher quantum efficiencies than core-shell, reaching in some cases up to 50%. This is due to the reduction of non-radiative processes, such as Shockley, Read and Hall recombination, caused by the surface/interface trap states in the core-shell interface [4], [5]. The emission properties of these alloyed nanoparticles can be tuned by adjusting the ratio of CdS_xSe_{1-x}. A higher percentage of sulphur, *S*, will have a predominant emission at high energies (bluer wavelengths), whilst higher percentage of selenium, *Se*, will shift the emission to lower energies (redder wavelengths) [6].

The CQDs used throughout this thesis were bought from Sigma-Aldrich and are provided in a monodisperse solution of toluene with a concentration of 1mg/mL. Both the red and green CQDs have a mean diameter of 6 nm and they have peak spectral emissions at 540 and 630 nm, respectively. The nanoparticles are of the same ternary alloy CdS_xSe_{1-x} passivated with a ZnS layer, however the alloy composition ratio is different. A higher percentage of *S* than *Se* will induce a spectral shift towards the blue region of the spectrum. In order to integrate this kind of down-converter onto GaN optical sources, a range of different approaches for sample fabrication were studied. Initial tests included spin-coating or drop-coating the CQDs at different concentrations on glass slides and then encapsulating them using similar glass covers. This approach proved ideal for some of the first optical tests, however due to the encapsulation system most of the light is trapped and waveguided within the glass slides. Furthermore, a higher density of semiconductor dots was found near the edges of the substrate, resulting from a high substrate surface smoothness allied with a low viscosity CQD solution. To increase the uniformity of the QD film and eliminate the need for an 'external' encapsulation, composites with PDMS (Poly(dimethylsiloxane)) or PMMA (Poly(methyl methacrylate)) polymeric matrices were studied. This approach provides a homogeneous mix at different concentrations. After solidification, the polymer also provides a transparent host matrix and has the advantage of protecting the down-converting medium from degradation by isolating it from the surrounding ambient. In addition, after fabrication the samples can be detached from the carrier substrate/stamp, giving free-standing membranes more suitable for optical tests.

The desired shape and sample thickness was achieved using a PDMS mould and pouring the CQD/PMMA compound into it. To do this, a few squares of glass were cut from a glass cover slide with a thickness around 1.25 mm and a few mm^2 of area. After cleaning the glass squares, they were placed onto an aluminium dish and the PDMS solution poured until the squares were covered in order to create a well. A schematic of the process is presented in Figure 3.1, where step 1 shows the placement of small glass squares into a Petri dish that will provide the desired colour-converter size and volume. Step 2 shows the pouring mechanism of a polymer such as PDMS. In step 3, and after allowing some time to dry the polymer, it was removed from the Petri dish. The moulds were removed and the mix CQD/PMMA poured into the vacant wells created by the impression of the glass slides. Finally, in step 4 the dried colour-converter/polymer mix was released from the PDMS and at this stage the samples are ready to be tested.

The PDMS solution is made by the combination of two silicon rubber compounds, SSR1V615A and SSRTV615B, at a ratio of 10:1. The compound is then left to dry overnight and after drying, cut and washed in a methanol bath using an ultrasonic cleaner to avoid contamination during the sample fabrication.

During this study several CQD-to-PMMA weight ratios were analysed. Below will be presented CQD/PMMA weight ratios of 1, 5 and 10%, respectively, for the green and red nanoparticles. To achieve the desired ratios, the mass of the CQDs needed to be determined.

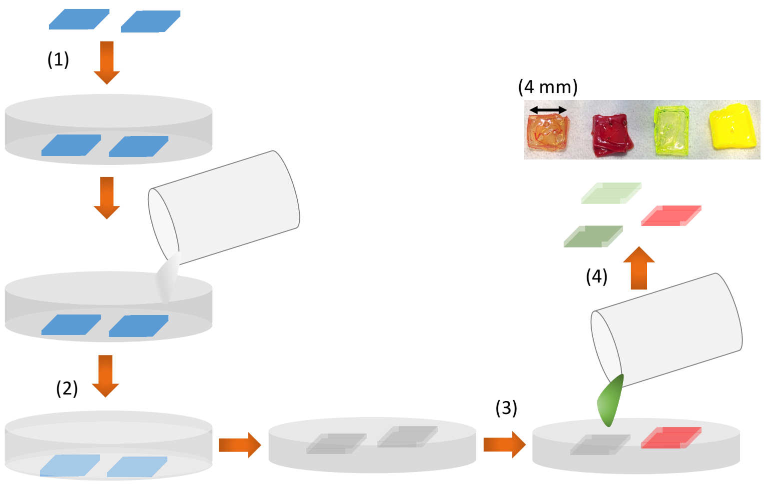

Figure 3.1 – Schematic showing the fabrication process of the PDMS stamps.

To do so, a 2000 μL vial was initially weighed and filled with the desired volume of monodisperse alloyed CQDs. Using an extraction pump, the toluene solvent was evaporated to leave a precipitate of CQDs. The vial with the precipitate was weighed again and the overall mass of the CQDs determined. The corresponding weight of PMMA was then added in order to get the desired ratios. At this stage, we have a precipitate of CQDs and PMMA so, in order to mix both and create a homogenous film, one needs to add a solvent such as toluene. It was found the best concentration of PMMA/solvent to achieve this goal was 250 mg/mL. So, knowing the overall mass, the necessary solvent volume was pipetted into the vial. The final solution was then left to stir overnight at room temperature to obtain a homogeneous film. Some of the fabricated samples are presented in Figure 3.2.

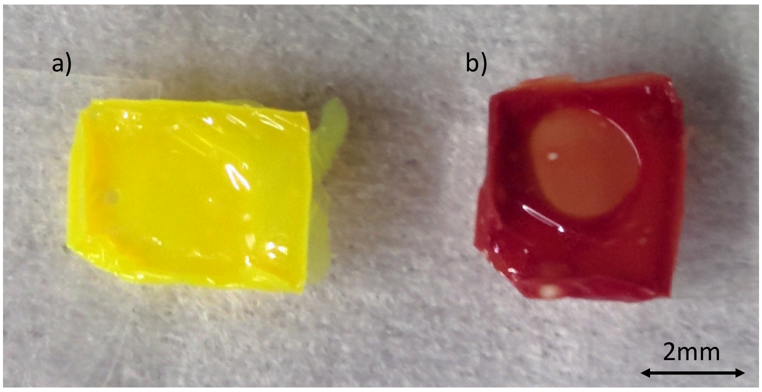

Figure 3.2 – a) Green and b) red alloyed quantum dots in PMMA, 400 μm thick, at 10% w.r.

3.2 Preparation of BBEHP-PPV composites

The BBEHP-PPV polymer was synthetized by Dr. Oleksandr Kanibolotsky in the Chemistry Department of the University of Strathclyde. The down-converter preparation for optical characterisation is similar to that discussed previously for the quantum dots. Initially, as for the quantum dots, several approaches were studied in terms of suitability for allowing integration with the optical excitation sources. The best approach resulted from the combination of this organic semiconductor with PDMS, rather than PMMA, used with at a weight ratio of 4% (BBEHP-PPV/PDMS). In order to dissolve the organic semiconductor, since after synthesis it becomes a powder, chloroform was added until the desired concentration was achieved. The solution was then left to stir until full uniformity was observed. Afterwards, PDMS was added at the desired weight ratio. The resulting mix was further left to stir at room temperature for a few days until the BBEHP-PPV was fully mixed with the polymeric matrix. The resulting composite could then be poured into a PDMS mould or spin-coated onto a glass slide and left to dry overnight, see Figure 3.3a. For BBEHP-PPV/PDMS film fabrication, the material can be poured onto a dish or drop-coated onto a glass slide, Figure 3.3b and c. Using one of these approaches, the final samples show properties such as high mechanical flexibility and high surface adhesion.

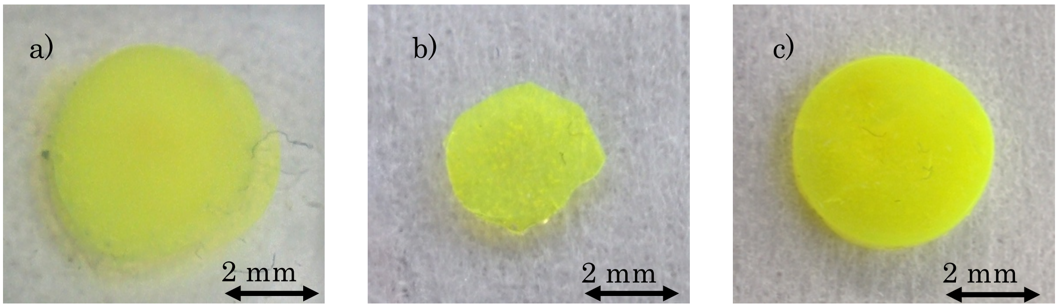

Figure 3.3 – BBEHP-PPV/PDMS samples fabricated using a) a PDMS stamp and b, c) drop coated to create a down-converter film with different thicknesses.

To test these samples two sets of condenser lenses and optical filters to block the remnant light from the pump or the colour-converter were used. A more detailed explanation of the optical tests and the set-ups is provided in Chapter 2. A schematic is depicted in Figure 2.1.

The following sections of this chapter are organised as follows. The data acquired from the CQDs in the CW regime will be presented first followed by the results in the dynamic regime. Afterwards, the data obtained from the BBEHP-PPV samples in the CW regime will be presented. At this stage, high data rate transmission was not studied for the organic samples.

3.3 CW characteristics of the CQD materials

Two GaN optical sources were used for continuous wave (CW) characterisation, namely a μLED and an off-the-shelf OSRAM laser diode (PL450B). They can be driven up to 200mA and 160 mA, providing a maximum forward optical power output of 8mW and 100mW, respectively. The samples were placed in the optical cage system set-up (Chapter 2, Figure 2.1) and for all of them the input and output optical power was recorded. This procedure was performed using both of the optical sources, initially for the stand-alone optical source, then optical source plus alloyed quantum dots and finally for the colloidal quantum dots (the unconverted light, if any, from the source was blocked using one of two long pass filters, FEL0500 or FEL0550 with cut-off wavelength of 500 nm or 550 nm, respectively). The optical power from the colour-converter (stand-alone) and the unconverted blue light from the source have a 10% and 20% correction which corresponds to the light absorbed by the optical filter within that range (Figure 2.2). Due to the green spectral tail from the GaN optical sources, and only when using the FEL500 optical filter, the data from the green quantum dots was corrected by subtracting this contribution from the standalone colour-converters' optical power.

The calculated absorption of the pump and relative optical-to-optical conversion efficiency from the green quantum dots in PMMA at different weight ratios when respectively pumped with a GaN laser diode (LD) and a μLED are presented in Figure 3.4.

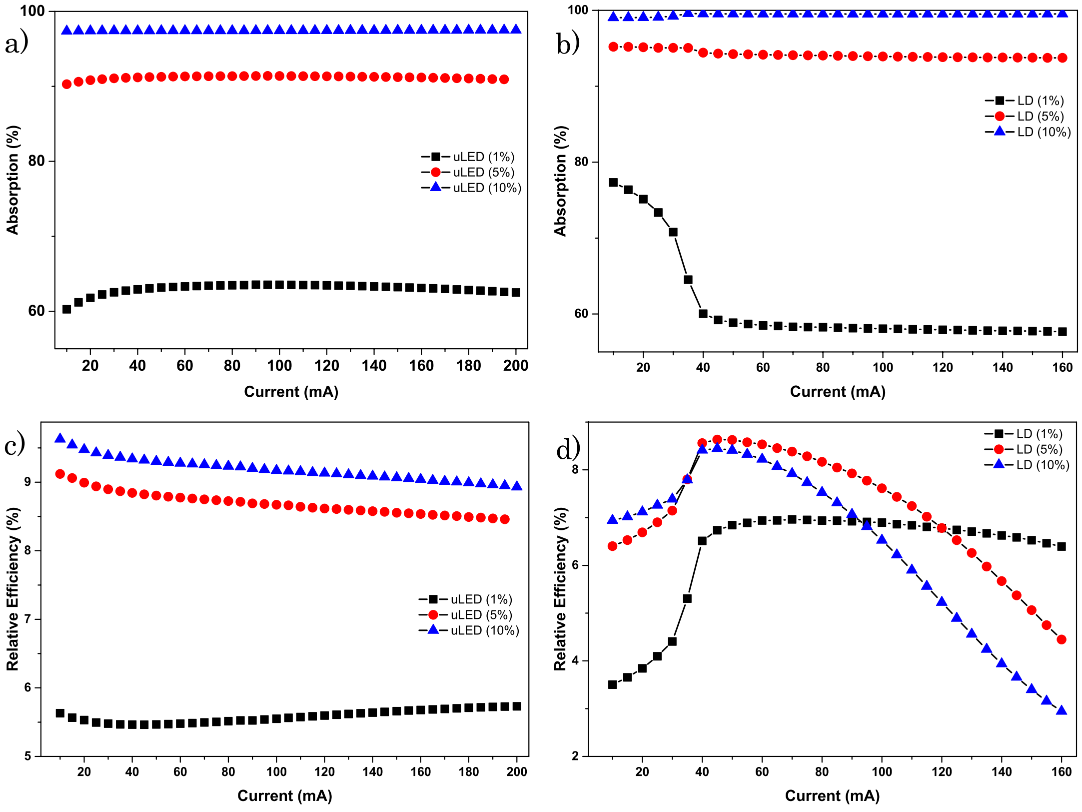

Figure 3.4 – Absorption and relative conversion efficiency for the alloyed CQDs with emission at 540 nm pumped a) and c) with a μLED and b) and d) with a LD. The samples have weight ratios of 1%, 5% and 10%, respectively.

A summary table with the mean absorption and relative conversion efficiency of the green samples is shown in Table 3.1. The absorption and relative efficiencies presented in the table have an associated error of around 2% that result from the samples' weight ratio and thickness uncertainty.

Table 3.1 – The average absorption and relative conversion efficiency for the green quantum dot samples at different weight ratios when pumped with a LED and a laser diode (LD).

CQDs 540 nm	Absorption (%)		Relative Efficiency (%)	
	μLED	LD	μLED	LD
1%	63.0	61.1	5.6	6.3
5%	91.2	94.2	8.7	7.1
10%	97.4	99.5	9.2	6.4

From the graphs and the values presented in the previous table, there is an increase of absorption with almost a doubling of relative efficiency between 1% and 10% when using the μLEDs. Between optical sources, μLEDs were the ones achieving higher relative efficiencies of around 9% against 7% for the LD. Such difference, could be explained by the different beam diameter from the excitation sources, 260 μm for the μLED *vs* 69 μm for the LD. A wider beam area is able to excite more CQDs resulting in a higher conversion efficiency. On the other hand, with smaller beam diameter and higher optical power than the μLEDs, the LD presents a much higher power density which may deform, due to heat, the polymer matrix in which the quantum dots are incorporated. Such behaviour may be seen in Figure 3.4d in which there is an increase of efficiency up to 40 mA and then a noticeable roll-over. Under that current, as shown in Figure 2.11a from Chapter 2, the laser diode is still below lasing threshold, presenting similar emission characteristics and similar optical power as a μLED.

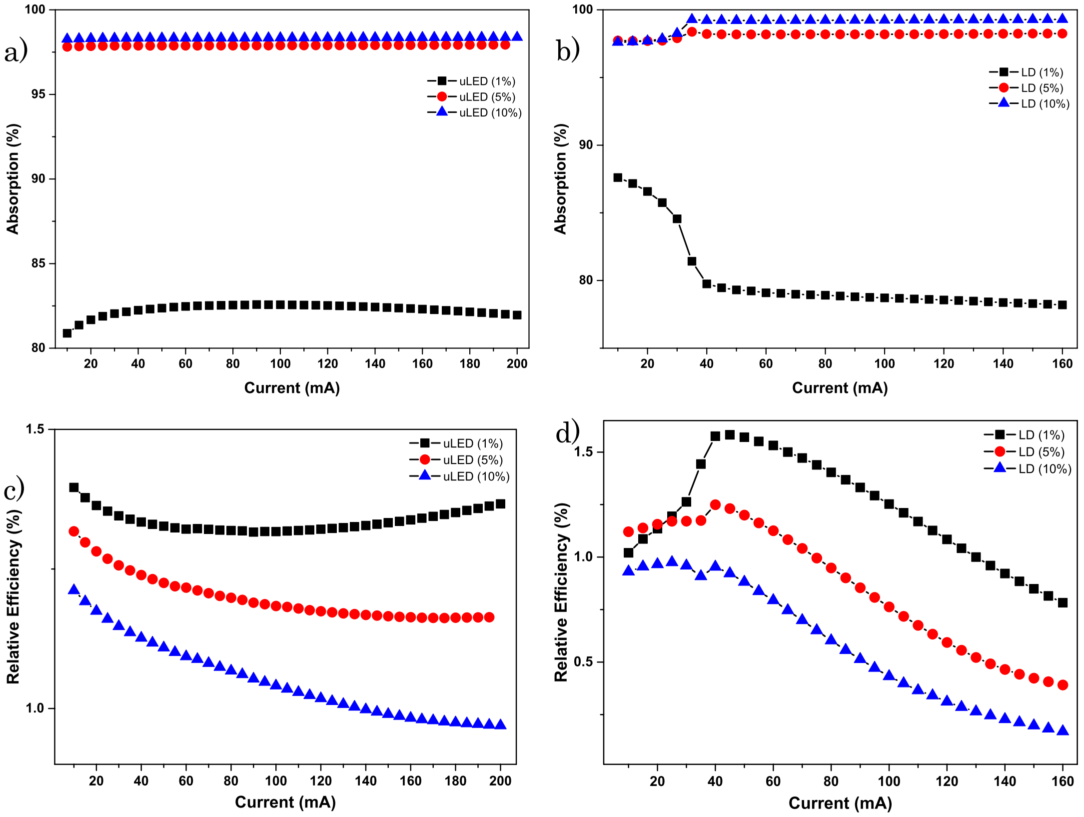

Figure 3.5 – Absorption and relative conversion efficiency for the alloyed CQDs with emission at 630 nm. The samples have weight ratios of 1%, 5% and 10%, respectively.

In addition to the green CQDs, the red alloyed dots were also tested. The mean absorption and relative optical-to-optical conversion efficiency are presented in Figure 3.5, at the same concentrations and using the same excitation sources and experimental conditions as before.

A summary table with the mean absorption and relative conversion efficiency of the red samples is shown in Table 3.2. As mentioned before, they present an associated error of around 2% that results from the samples' weight ratio and thickness uncertainty.

Table 3.2 – The average absorption and relative conversion efficiency for the red quantum dots samples with different weight ratios.

CQDs 630 nm	Absorption (%)		Relative Efficiency (%)	
	μLED	LD	μLED	LD
1%	82.3	80.1	1.3	1.2
5%	97.9	98.1	1.2	0.9
10%	98.3	99.0	1.1	0.6

For the green CQDs, considering the data from the μLED excitation, the samples with the biggest absorption were those with weight ratios around 10%. In the case of the red colloidal quantum dots, there is no noticeable difference in relative conversion efficiency for the different ratios, being in all cases around 1%. The green CQDs, however, show efficiencies of between 6% to 9%. The difference in the efficiencies between the green and red quantum dots is due to the different *Se:S* ratios in the alloyed structure. The cores of these dots are based on *CdSe* being gradually graded to *CdS*. With the reduction of *S*, and consequent spectral peak shift to the red wavelengths, the lattice mismatch between the *CdSe* core and the *ZnS* will create an increase of non-radiative Auger recombination leading to a reduction of efficiency [7]. To provide a better insight of the quantum dot properties, the photoluminescence quantum yield (PLQY) was measured for the 1% and 10% samples. For this we used a Hamamatsu integrating sphere C9920−02 luminescence system with a laser as excitation source with peak emission at 450 nm. The results obtained are presented in Table 3.3. The quantum yields differ from the earlier efficiency measurements primarily because an integrating sphere is used, resulting in the detection of all the emitted light from the sample, whilst in the relative efficiency measurement only the forward emitted light was collected and measured.

Table 3.3 – PLQY values from the quantum dots in PMMA at different weight ratios.

CQDs 540 nm	PLQY (%)
1%	60.7
10%	56.4
CQDs 630 nm	**PLQY (%)**
1%	14.2
10%	13.2

Despite this difference, a similar trend was observed confirming the initial tests. The green quantum dots show higher efficiency due to the lower band-gap offset, and consequently lower surface trap density, mainly from the interface of *ZnS* and *CdS,* when compared with the red quantum dots.

Another noticeable aspect when examining Table 3.2 is the efficiency drop with increasing weight ratios when a laser diode is used as the optical source. This could indicate a stronger effect from pump light re-absorption at this particular thickness or polymeric matrix degradation with increasing power densities due to heat. In order to analyse which effect impaired the efficiency, the forward optical powers from the green and red colloidal quantum dots, pumped with both optical sources, are presented as a function of drive current in Figure 3.6 and Figure 3.7 (*N.B.*: an optical filter was placed before the power meter in order to remove the unconverted blue light from the optical sources). Here we plot forward optical power emitted by the colour-converter against the drive current of the excitation source. From the gathered data, it is apparent the main factor impairing the efficiency drop is due to the higher optical power densities on the sample when using a laser diode, resulting on irreversible structural damage of the polymer matrix. Such behaviour is more apparent at high weight ratios where there is an optical power droop.

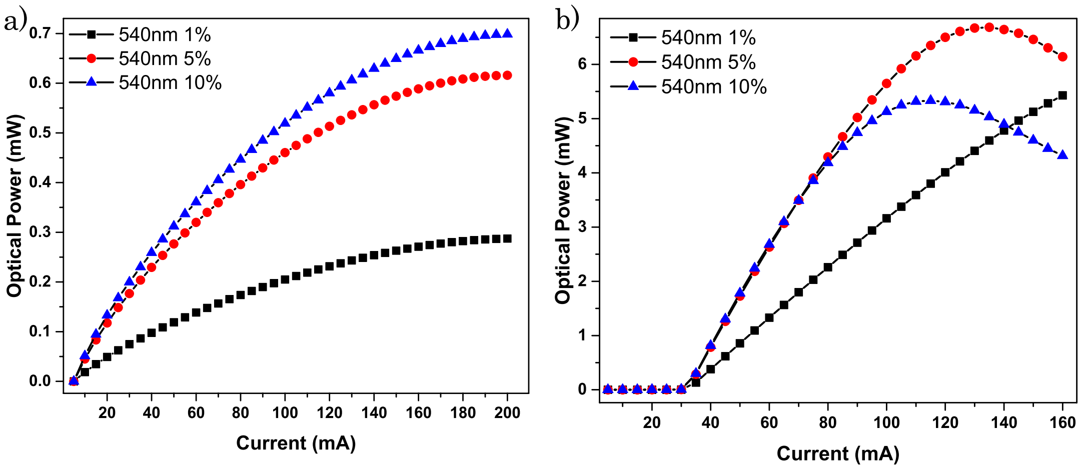

Figure 3.6 – L-I curves for the green colloidal quantum dots, at different weight ratios, pumped with a) a micro-LED and b) a commercial laser diode.

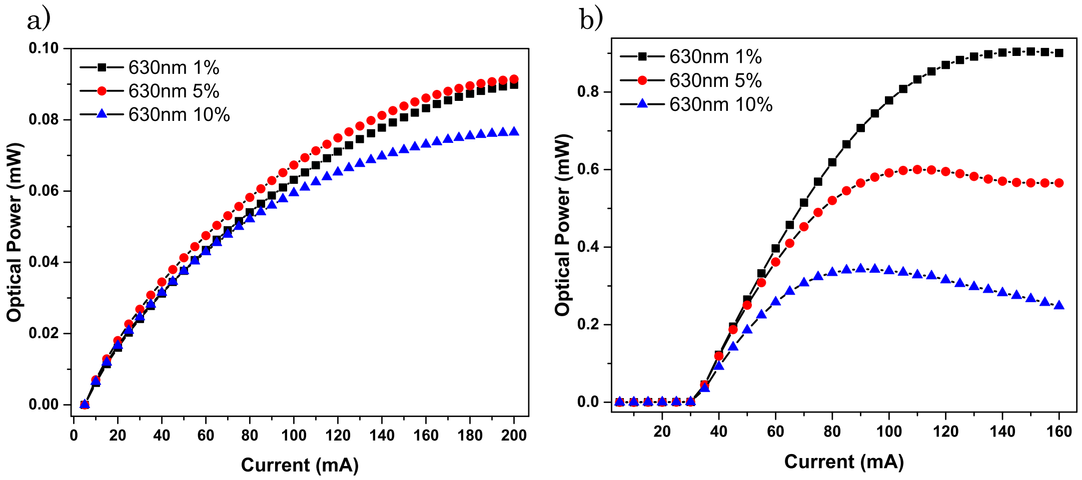

Figure 3.7 - L-I curves for the red colloidal quantum dots, at different weight ratios, pumped with a) a micro-LED and b) a commercial laser diode.

In summary, green CQD's show PLQY's ~60% and red CQD's ~15% for weight ratios in PMMA of a few %. When measured under the forward emission condition we see reduced efficiencies of ~5-9% and ~1% respectively, when excited by both a μLED and a GaN LD. This corresponds to maximum colour-converted output powers of ~0.7mW for green and ~0.1mW for red when pumped with the LD. However, damage is observed under these LD pumping conditions.

The optical spectra from the 1, 5 and 10% samples were also measured and are shown in Figure 3.8. As can be observed, there is a red shift in the emission with increasing weight ratio. The spectra were all recorded under the same conditions excited by a μLED with a driving current of 50 mA. The spectral shifts between 1% and 10% are 16 nm and 13 nm for the green and red QDs, respectively. With the weight ratio increase there is a higher density of quantum dots in the host matrix permitting energy transfer between slightly smaller (higher energy) to bigger (lower energy) CQDs. Depending in the mean separation between dots the process can be based on radiative or non-radiative energy transfer. For separations smaller than ~10 nm, non-radiative energy transfer, described as Förster/fluorescence resonance energy transfer (FRET), can dominate [8]. However, for higher separations, the energy transfer happens through a radiative decay in which an emitted photon from the CQD is absorbed by another CQD in the ground state. This process is known as the ‘imprisonment of resonant radiation’ (IRR) [9].

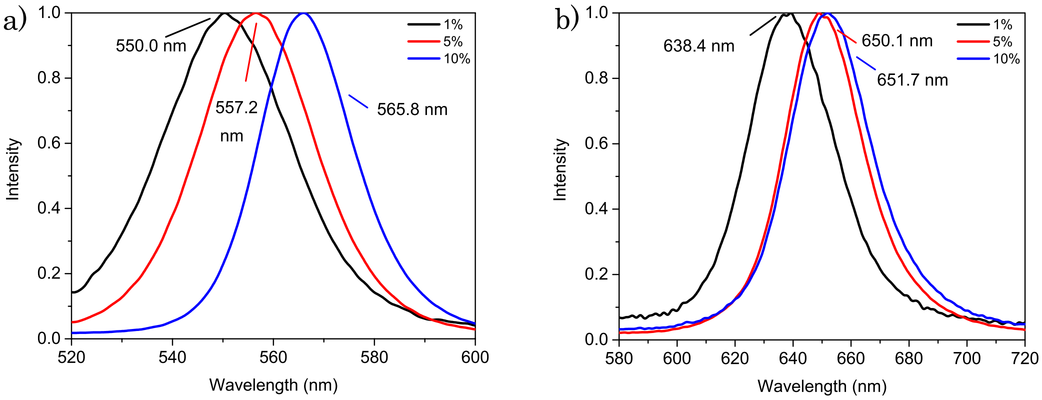

Figure 3.8 – Optical spectra from the a) green and b) red CQDs at different weight ratios, all recorded under the same excitation conditions.

Absorbance measurements versus wavelength of excitation were also performed on the QD samples to determine the range of wavelengths absorbed. An Ocean Optics HL-2000 white light source with emission across the visible spectrum was used. Two aspheric lenses focussed the white light onto the sample and another two aspheric lenses were used to couple the sample’s emission onto the collection optical fibre of the spectrometer. The reference spectrum from the white light source was measured using the setup depicted in Figure 2.1.

The samples’ transmissivities were calculated considering the light transmitted from the samples, Φ_t, when pumped with this white light. To acquire the reference spectrum, a PMMA matrix without quantum dots, but with the same thickness, was placed in between the white light source and the spectrometer, Φ_r. The transmissivity was then determined using expression (3.1):

$$Transmissivity = \frac{\Phi_t}{\Phi_r} \tag{3.1}$$

By definition the absorbance can be determined as the negative logarithm of the transmissivity, expression (3.2):

$$Absorbance = -\log_{10}(Transmissivity) \tag{3.2}$$

Figure 3.9 presents the respective absorbance spectra for the green and red quantum dots for the 1% weight ratio. The PL spectrum of each sample is presented alongside, for reference.

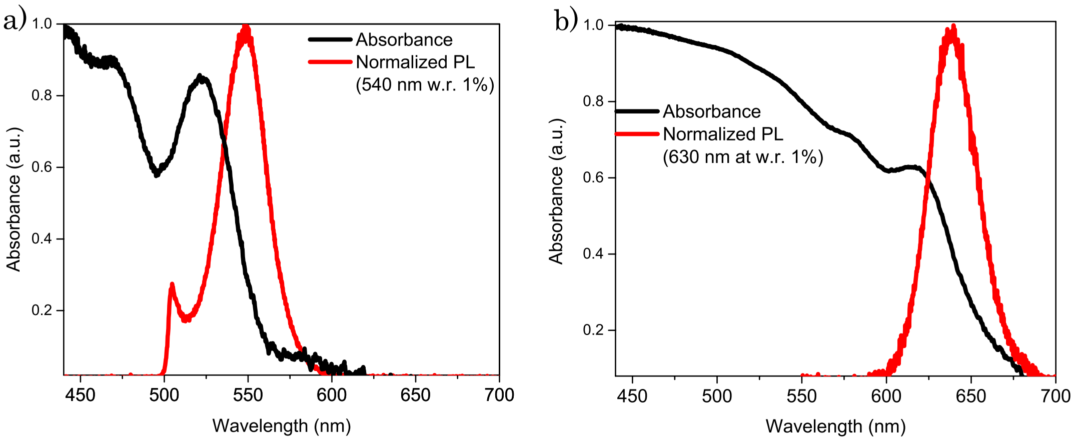

Figure 3.9 – Absorbance curve and PL spectrum of the w.r. = 1% sample of the 540 nm CQDs in PMMA. b) Absorbance curve and PL spectrum of the w.r. = 1% sample of the 630 nm CQDs in PMMA.

The first absorption peak occurs at 522 nm, corresponding to $|S_{(e)}|S_{(h)}>$ transition (Fig. 1.20), and the Stokes shift is 26 nm for the green CQDs. The red CQDs, present the first absorption peak at 615 nm and the Stokes shift is 23 nm. Generally, a high Stokes shift is desirable for photonics applications in order to minimize re-absorption effects in the colour-converters materials.

Both types of quantum dots present high absorption at lower wavelength with the first absorption peak occurring at 615 nm and 520 nm for the red and green CQDs, respectively. The small indent in the PL curve from Figure 3.9

results from the cut-off filter wavelength used in order to block the unconverted light from the optical pump.

3.4 Dynamic characteristic (Quantum Dots)

The modulation properties of the optical sources and the colloidal quantum dots are important for VLC applications and represent the main focus of this study. This section looks into the dynamic characteristics of down-converter samples and presents the bandwidths and maximum achieved modulation speeds and what this implies for visible light communications. The data presented will be from the red and the green CQDs at 1%, 5% and 10% weight ratio, respectively.

3.4.1 **Bandwidth and Lifetimes**

For the determination of bandwidths and lifetimes, the set-up used was as presented in Figure 2.1. In order to compare the results between samples, the same driving and pumping conditions were used for all the tests. The acquired data, after removing the μLED's intrinsic response, was fitted using the method presented in Chapter 2.

Figure 3.10 presents the intrinsic bandwidths for the green and red CQDs at different (μLED) driving currents and the combined response of the optical source and down-converters. It is important to determine the overall response of the system since in a real telecommunication configuration both components have to work in a tandem configuration, being limited by the slowest of the components. As depicted below, in this case, the response is limited by the quantum dots. The optical source has bandwidths up to 140 MHz whilst the CQDs maximum bandwidths are 24 MHz.

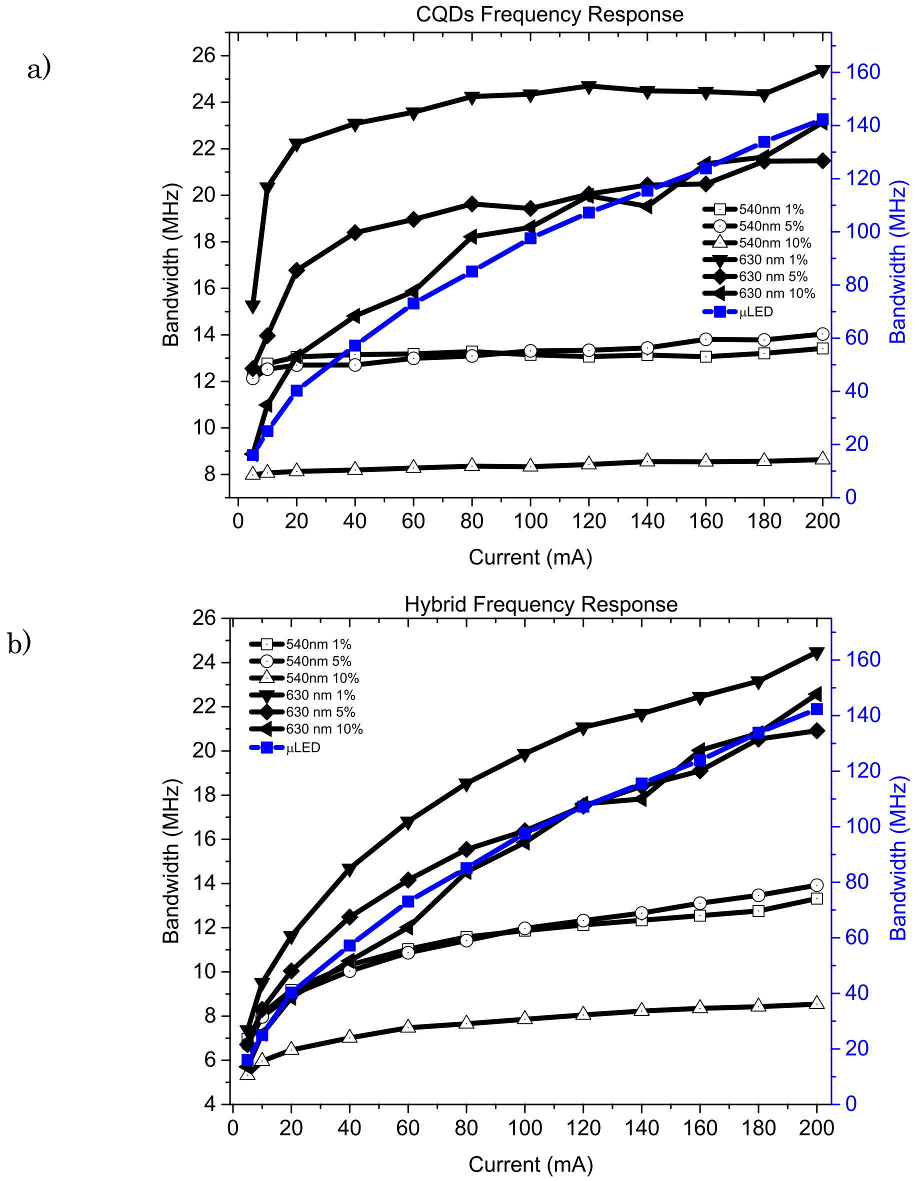

Figure 3.10 – a) Intrinsic and b) hybrid response at different currents for the green and red colloidal quantum dots at 1%, 5% and 10% (weight ratios), respectively. The right hand axis represents the bandwidth of the excitation source.

The samples that present higher bandwidths were the ones with a weight ratio of 1% and the red samples were faster than the green ones. In order to confirm the previous data, the luminescence lifetimes for each of them were measured. This was performed using TCSPC equipment (Chapter 2 – subchapter 2.1). The system response and sample measurements thus taken are presented in Figure 3.11. During the system response measurement, a sample consisting only of PMMA was used. From Figure 3.11, one can see that there is a fast and slower decay so, the overall response was fitted with a double exponential decay function.

$$y(t) = y_0 + a_1 e^{-t/\tau_1} + a_2 e^{-t/\tau_2} \tag{3.3}$$

where y_0 is the value when $y_0 = y(0)$ and a_1 and a_2 the weight of each exponential component in the double exponential function.

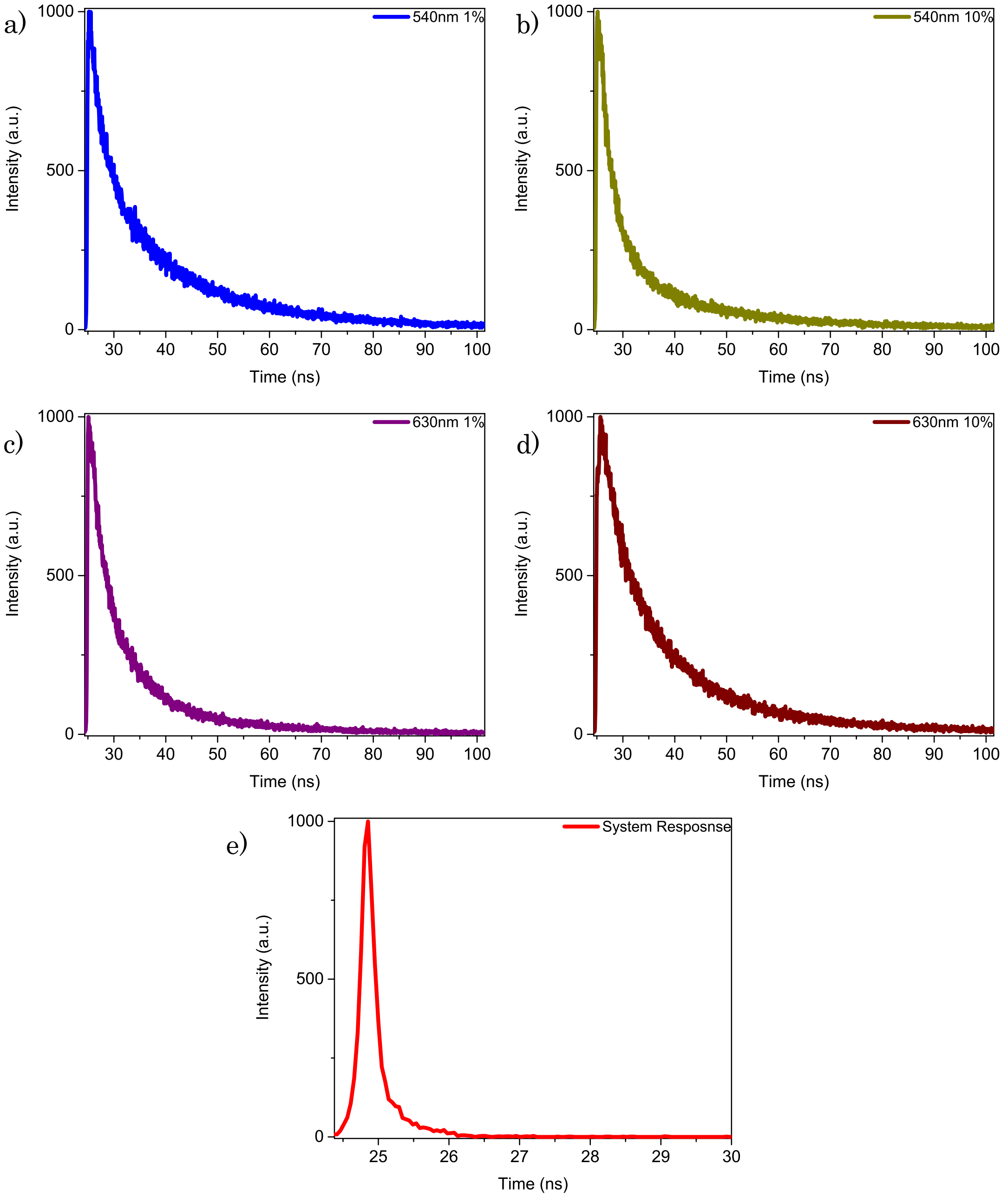

Figure 3.11 – Lifetime measurements taken using TCSPC for the different CQDs samples. Emission and w.r. of a) 540 nm at 1%, b) 540 nm at 10%, c) 630 nm at 1%, d) 630 nm at 10% and e) system response.

A table with all the fitting parameters is presented below (Table 3.4). The average lifetime was determined using the following expression,

$$\bar{\tau} = \frac{a_1 t_1^2 + a_2 t_2^2}{a_1 t_1 + a_2 t_2} \tag{3.4}$$

where a_1, a_2 are the weight of each exponential component in the double exponential function and t_1, t_2 are the fitted lifetimes.

Table 3.4 – Double exponential decay fitting parameters, with the mean lifetime and bandwidth theoretical calculations.

CQDs	a_1	τ_1 (s)	a_2	τ_2 (s)	$\bar{\tau}$ (s)	f (MHz)
540nm 1%	0.10	3.7e-9	6.4e-2	2.0e-8	1.6e-08	16.95
540nm 10%	0.24	3.4e-8	7.6e-1	1.1e-8	2.2e-08	12.30
630nm 1%	0.13	3.9e-9	3.5e-2	1.6e-8	1.0e-08	26.92
630nm 10%	0.12	7.2e-9	4.3e-2	2.7e-8	1.5e-08	17.84

From the obtained mean lifetimes, the maximum bandwidths from the tested samples can be predicted. Considering Figure 3.10a and the theoretical bandwidths, determined through the mean average lifetimes using expression 3.4 and presented in the previous table, one can verify the values are within the same range, confirming the maximum modulation bandwidths that can be used for data transmission. As shown, an increase of concentration leads to an increase of overall lifetime resulting in a reduction of bandwidth.

3.4.2 Advanced modulation formats

After emission characterisation and bandwidth determination, free-space high-level encoding data transmission was studied. In order to determine the best performing modulation scheme for kind of configuration, three different modulations were analysed, namely 2-PAM, 4-PAM and OFDM. As described in Chapter 1, in pulse-amplitude modulation (PAM) schemes the signal is encoded in amplitude, so in the first case there are only two encoding levels (most commonly known as OOK, ON-OFF Keying) whilst in 4-PAM there are four. The detected signal is then demodulated accordingly with the acquired amplitude. In the case of OFDM (orthogonal frequency-division multiplexing), the available frequency range is divided into orthogonal subcarriers as explained in Chapter 1.

All the modulation schemes used were pre-loaded onto the Agilent 81180A Arbitrary Waveform Generator (AWG) using a Matlab® script. For each one of the pixels the driving bias and clipping conditions were optimised in order to obtain the maximum transmission data rate. When using OFDM to transmit data, the bit stream created in Matlab® script was encoded and then converted to the frequency domain using an inverse fast Fourier transform (IFFT). This signal was then clipped to avoid nonlinear distortion caused by the transmitter and receiver components. Afterwards, it was converted into an analogue-signal by an AWG. The signal was then optically transmitted and acquired by the APD. Comparing the transmitted and received signal it is then possible to determine the Bit-Error-Rate (BER) for each of the devices. The Forward-Error-Correction (FEC) limit considered for this measurement is 3.8×10^{-3}. It defines the maximum number of error that can occur within a 'message', and the ability to correct them, without the need to retransmit the same 'message'. This technique is usually employed in systems were retransmission of signal are impossible or very expensive. The acquired data rates for these samples are presented in Figure 3.12.

The best data rates for each sample in the different modulation formats is summarised in Table 3.5. As depicted, the best performing data rate for all the samples is 2-PAM, known more conventionally as OOK.

Table 3.5 – Maximum data rate in Mbit/s for red and green CQDs at 1% and 10% w.r..

	Green CQD (1%)	Green CQD (10%)	Red CQD (1%)	Red CQD (10%)
2-PAM	400	255	500	415
4-PAM	330	220	475	325
OFDM	255	185	345	255

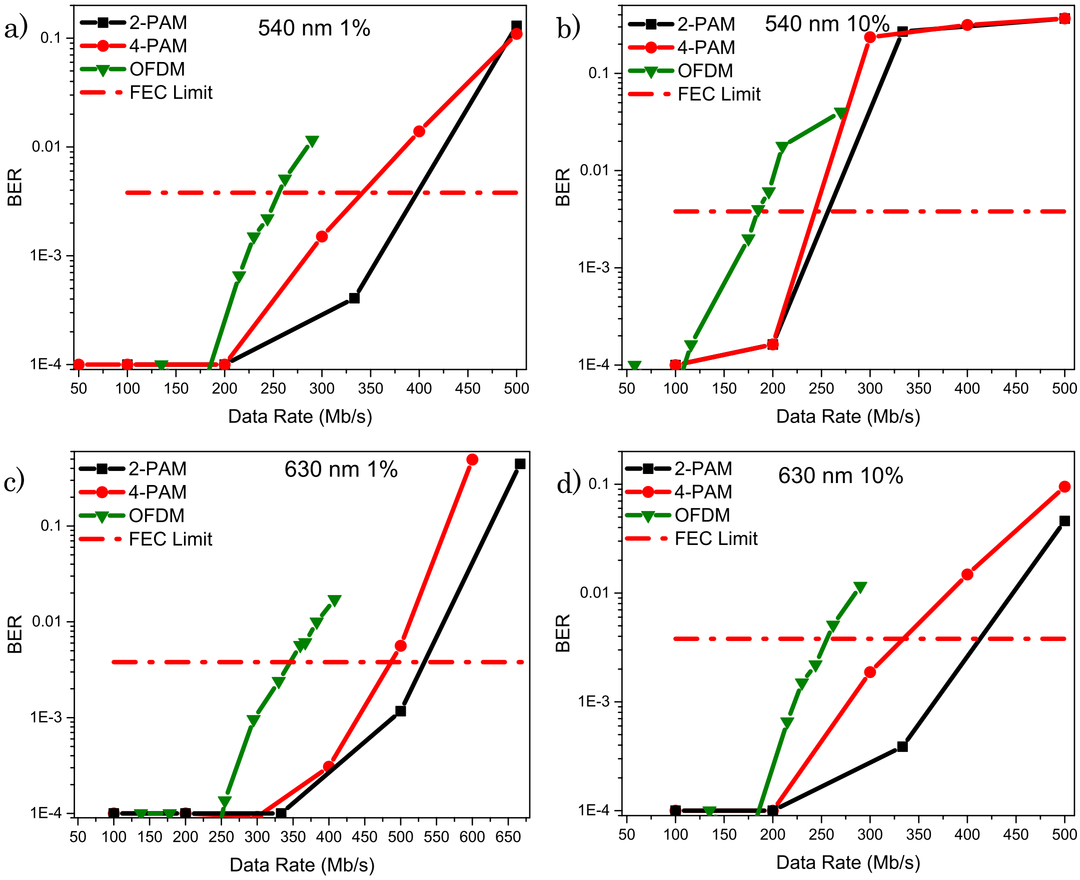

Figure 3.12 – BER vs data rate for the different samples. a, b) red quantum dots at 1% and 10%, c, d) green quantum dots at 1% and 10%, respectively.

From the above, we can see that the down-converter CQDs show higher bandwidths and faster data rates than the standard phosphor approach which is limited to responses of a few MHz. Furthermore, since the photoluminescence emission can be tuned by CQD size selection to the wavelengths desired they offer new approaches to Wavelength-Division Multiplexing (WDM) systems in which each wavelength can be used to transmit data. Besides, the combination of several wavelengths in the visible spectrum can offer a further degree of control over the characteristics of the resulting light.

3.5 CW characteristics (BBEHP-PPV)

Following the same principles described in subchapter 3.1 for the quantum dots, and with the same set-up and optical sources, the absorption and relative efficiencies were also measured for polymer BBEHP-PPV. As a reminder, the optical characteristics of this polymer are shown in Figure1.19.

As described earlier, the samples can be fabricated using a PDMS mould and by drop- or spin- coating the colour-converter onto a desired substrate. The first BBEHP-PPV samples were spin-coated onto a glass slide at different revolutions-per-minute (*rpm*) with the same concentration and spinning time. The first sample was spin-coated at 1000 rpm, the second at 2000 rpm and the third at 3000 rpm. At this stage the polymer was just mixed with chloroform in order to achieve a desired concentration of 20 mg/mL. The optical power, absorption and relative (optical-to-optical) forward efficiencies were determined using the same steps as described for the quantum dots. The calculated absorptions and relative efficiencies are summarised in Table 3.6.

Table 3.6 – Absorption and relative efficiency for BBEHP-PPV samples with the same concentration but spin-coated at different speeds.

Spin-coated BBEHP-PPV	Absorption (%) at 450 nm	Relative Efficiency (%)
1000 rpm	99.4	6.9
2000 rpm	73.0	8.5
3000 rpm	73.2	8.9

From the data, the sample with highest absorption is the one spin-coated at lowest *rpm*. This behaviour is expected since the colour-converter film is thicker. However, above 2000 rpm the samples presented similar absorptions and relative efficiencies.

The forward optical power from each sample was measured and is presented in Figure 3.13. At maximum driving current of 100 mA a colour-converted optical power of 0.22 mW was achieved for the sample made at lower *rpm*. However, the optical power difference between the best performing sample and the one with less photoluminescence signal is of 0.03mW which corresponds to a power drop of around 14% that could be related with photodegradation. The main contributor to this degradation is heat, which may affect the atomic and molecular bonds leading to the formation of new inert molecules and oxidation. Here, oxygen atoms react with the organic molecules, a process that can be accelerated by exposure to light.

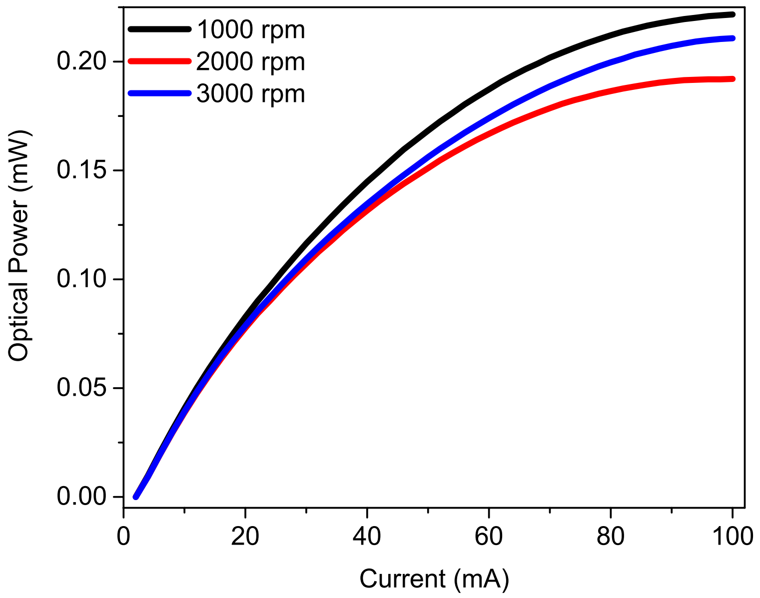

Figure 3.13 – Forward optical power for the BBEHP-PPV samples spin-coated on glass at different rpm.

Apart from the optical characterisation, photostability tests were also carried out in order to analyse the behaviour of BBEHP-PPV in this configuration when pumped continuously. This test is very important since for visible light communications and lighting solutions the down-converters need to retain the same efficiency during the operation time and the life-span of the product. To test this, a μLED was used as excitation source and its optical power measured during the experiment in order to track any power fluctuation from the down-converter data. The test lasted 35 min and the power was measured every second. The obtained response is depicted in Figure 3.14. There is a substantial power drop in the initial seconds after the sample starts to be pumped due to photodegradation, however this process is followed by a slight increase of power resulting from a possible annealing altering the material structure.

In order to facilitate the integration and reduce the quenching of BBEHP-PPV a PDMS matrix was used as explained at the beginning of the chapter and depicted in Figure 3.3. Using the procedure explained above and the same optical source and setup, an absorption of 100% was found with a respective relative efficiency of 5±2%. Similarly, the photodegradation was studied using the same optical source but during longer times, see Figure 3.15. At this stage, only a monotonic decay is visible. A possible explanation for this difference could come from the fact that a polymeric matrix is used and is acting as a thermal spreading layer protecting the organic molecules from the heat of the optical excitation. At this time of writing, these issues prevented a full examination of BBEHP-PPV for visible light communications applications.

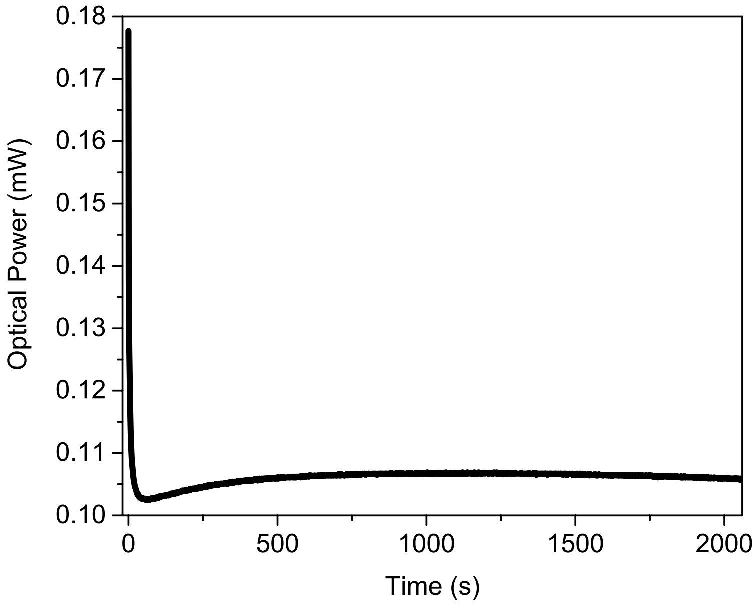

Figure 3.14 – Spin-coated BBEHP-PPV photodegradation during 35min.

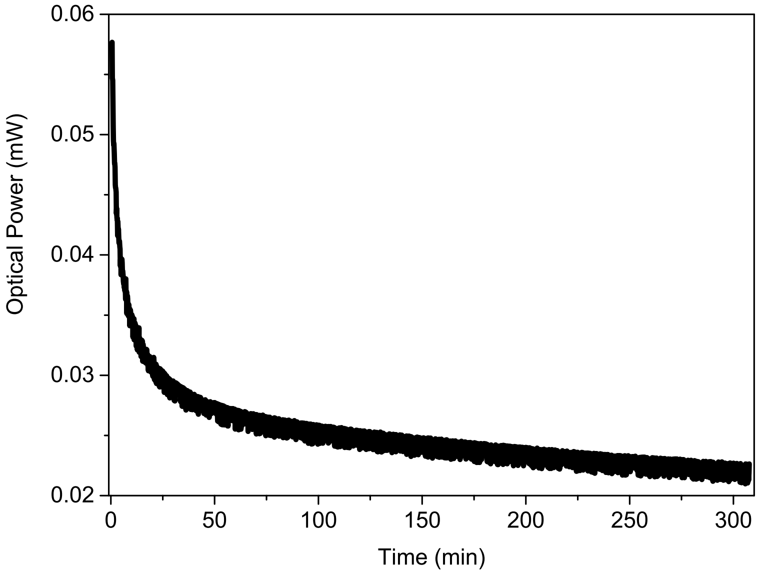

Figure 3.15 – Photodegradation of BBEHP-PPV in PDMS.

3.6 Summary

The present chapter started by describing the preparation of the red and green CQDs and BBEHP-PPV colour-converters. It was found that the best polymer matrix to fabricate samples was PMMA for CQDs and PDMS for BBHEP-PPV, respectively. In order to achieve the best colour-converter/polymer matrix ratio, several samples were fabricated.

Subchapter 3.2 started by presenting the CW characteristics of red and green CQDs at w.r. of 1%, 5% and 10%. It was found that the maximum absorption was around 99% with the maximum relative efficiency around 9% and 7% for the green samples when pumped with a μLED and a laser diode, respectively. In the case of red CQDs, and using the same optical sources, a maximum absorption of 98% was found when using a μLED and 99% when using a laser diode with the maximum relative efficiency around 1.3% and 1.2%, respectively. In addition to the absorption and relative efficiencies, the PLQY for the different colour CQDs and the L-I curves were measured. We conclude that the green CQDs present the highest PLQY, around 60%, with a maximum output power of 0.7 mW and 7 mW when pumped respectively with a μLED and a laser diode. The influence of the weight ratio on the spectral shift was studied as well. To do this, three samples with different weight ratios were optically excited under the same power density and a red shift was found with increasing weight ratio of 16 nm and 13 nm for the green and red CQDs, respectively. Finally, from the absorption and PL spectra the Stokes shift was determined, being 26 nm and 23 nm for the green and red samples, respectively.

In the following subchapter the dynamic characteristics of the CQDs including the bandwidths, the carrier lifetimes and the maximum achieved data transmission using advanced modulation formats were presented. It was found that the red CQDs present higher bandwidths, around 24 MHz, than the green ones, which have bandwidths reaching a maximum of 13 MHz. As explained, the carrier lifetime and the bandwidths are intrinsically related, so a TCSPC measurement was performed in order to correlate both intrinsic properties. It was found that the obtained data points are within the same range. After determining the bandwidths, the data rate for different modulation schemes was measured and a maximum data rate of 500 Mbit/s for OOK, was found.

A similar CW characteristic study was performed for the BBEHP-PPV colour-converter. In this case, the maximum absorption found was 99.4% with a relative efficiency of 7%. The bandwidth and data transmission rates were not possible to measure at the time of this thesis writing due to photodegradation issues. This degradation effect is mainly due to heat and photo-oxidation. A deficient heat dissipation will break the main chain of molecules in the organic material giving origin to small inert molecules inducing irreversible damage. In the case of photo-oxidation, molecular oxygen groups are formed through the association of oxygen atoms to the main molecules, process that is accelerated by the exposure to UV radiation. A possible mechanism to increase the photostability of such samples could include the encapsulation in a material that could promote the heat dissipation while isolating the molecules from the surrounding environment.

Due to the inability to extend the BBEHP-PPV photostability during this work, CQDs present an interesting alternative to the standard phosphors for Visible Light Communications. They present bandwidths an order of magnitude higher than the current solution allowing the increase of telecommunication data rates even further. Besides, as demonstrated here they can be incorporated in a polymer matrix which can act as barrier to the surrounding medium with the advantage of easier integration in solid state lighting. However, more works needs to be done in order to increase the CQDs efficiency.

References

[1] Y. Chen, J. Herrnsdorf, B. Guilhabert, A. L. Kanibolotsky, A. R. Mackintosh, Y. Wang, R. A. Pethrick, E. Gu, G. A. Turnbull, and P. J. Skabara, “Laser action in a surface-structured free-standing membrane based on a π-conjugated polymer-composite,” *Org. Electron.*, vol. 12, no. 1, pp. 62–69, 2011.

[2] N. Laurand, B. Guilhabert, J. McKendry, A. E. Kelly, B. Rae, D. Massoubre, Z. Gong, E. Gu, R. Henderson, and M. D. Dawson, “Colloidal quantum dot nanocomposites for visible wavelength conversion of modulated optical signals,” *Opt. Mater. Express*, vol. 2, no. 3, p. 250, Feb. 2012.

[3] P. Guyot-Sionnest, “Colloidal quantum dots,” *Comptes Rendus Phys.*, vol. 9, no. 8, pp. 777–787, Oct. 2008.

[4] E. Jang, S. Jun, and L. Pu, “High quality CdSeS nanocrystals synthesized by facile single injection process and their electroluminescence.,” *Chem. Commun.*, no. 24, pp. 2964–2965, 2003.

[5] D. Ratchforda, K. Dziatkowskia, T. Hartsfield, X. Li, Y. Gao, and Z. Tang, “Photoluminescence dynamics of ensemble and individual CdSe/ZnS quantum dots with an alloyed core/shell interface,” *J. Appl. Phys.*, 2011.

[6] J. P. Kim, J. A. Christians, H. Choi, S. Krishnamurthy, and P. V. Kamat, “CdSeS nanowires: Compositionally controlled band gap and exciton dynamics,” *J. Phys. Chem. Lett.*, vol. 5, no. 7, pp. 1103–1109, 2014.

[7] K. Dziatkowski, D. Ratchford, T. Hartsfield, X. Li, Y. Gao, and Z. Tang, “CdSe/ZnS Colloidal Quantum Dots with Alloyed Core/Shell Interfaces: A Photoluminescence Dynamics Study,” *Energy*, vol. 120, no. 5, pp. 870–873, 2011.

[8] M. Lunz, A. L. Bradley, W.-Y. Chen, V. A. Gerard, S. J. Byrne, Y. K. Gun'ko, V. Lesnyak, and N. Gaponik, "Influence of quantum dot concentration on Förster resonant energy transfer in monodispersed nanocrystal quantum dot monolayers," *Phys. Rev. B*, vol. 81, no. 20, p. 205316, 2010.

[9] G. Kawata, Y. Ogawa, and F. Minami, "Density dependence of photoluminescence lifetime of CdSe/ZnS core-shell colloidal quantum dots," *J. Appl. Phys.*, vol. 110, no. 6, p. 64323, 2011.

Chapter 4

Epitaxial semiconductor colour-converters

As shown in the previous chapter, colloidal quantum dots and polymers such as BBEHP-PPV are potential candidates as InGaN solid-state down-converters for visible light communications (VLC), but they require advanced encapsulation schemes for long-term environmental stability [1]. In this chapter an alternative approach based on inorganic multi-quantum well (MQW) semiconductor epi-layer membranes as photo-pumped colour-converters will be introduced. This technology benefits from being based on all-inorganic semiconductors and therefore promises to be robust [2], [3]. It also leads to extremely compact sources, as the membrane can be integrated onto the source monolithically by techniques such as liquid capillary bonding. There are several options for wavelength coverage across the visible spectrum with available semiconductor alloys for MQW membranes including III-V AlGaInP (yellow to red) and InGaN (green) materials and II-VI CdMgZnSe (green to orange) materials [2], [4]. The hybrid LED demonstrators presented here are obtained by capillary-bonding a 540nm- emitting II-VI CdMgZnSe membrane and a 630nm-emitting III-V GaInP MQW membrane, respectively, onto the sapphire side of an array of 450nm InGaN micro-size LEDs (μLEDs). This offers the advantage of the high modulation bandwidths associated with these small-sized LEDs as demonstrated in Chapter 2 [5]. We chose II-VI and III-V materials for converters in this initial study because (*i*) they are readily wet etched to form epitaxial membranes, (*ii*) they can be designed to offer coverage of the visible spectrum promising white-light generation, and (*iii*) they permit an alternative approach to green and red emission at high-modulation-bandwidth, useful for *e.g.* introducing coarse wavelength division multiplexing (blue and green) into optical wireless and polymer optical fibre communications.

The present chapter is organised as follows. The hybrid devices fabrication and characterisation results for the II-VI nanomembrane are presented in section 4.1 followed by the III-VI membrane in section 4.2. Each section will present the CW and dynamic characteristics of the devices.

4.1 II-VI nanomembranes

The 450nm-wavelength µLED device used to pump the MQW membrane was fabricated using a commercial p-*i*-n GaN LED structure grown on *c*-plane sapphire, following the procedure reported in [6] and in Chapter 2. Here, the fabricated chip comprises several 100 µm x 100 µm square pixels spaced 450 µm apart, see Figure 4.1a.

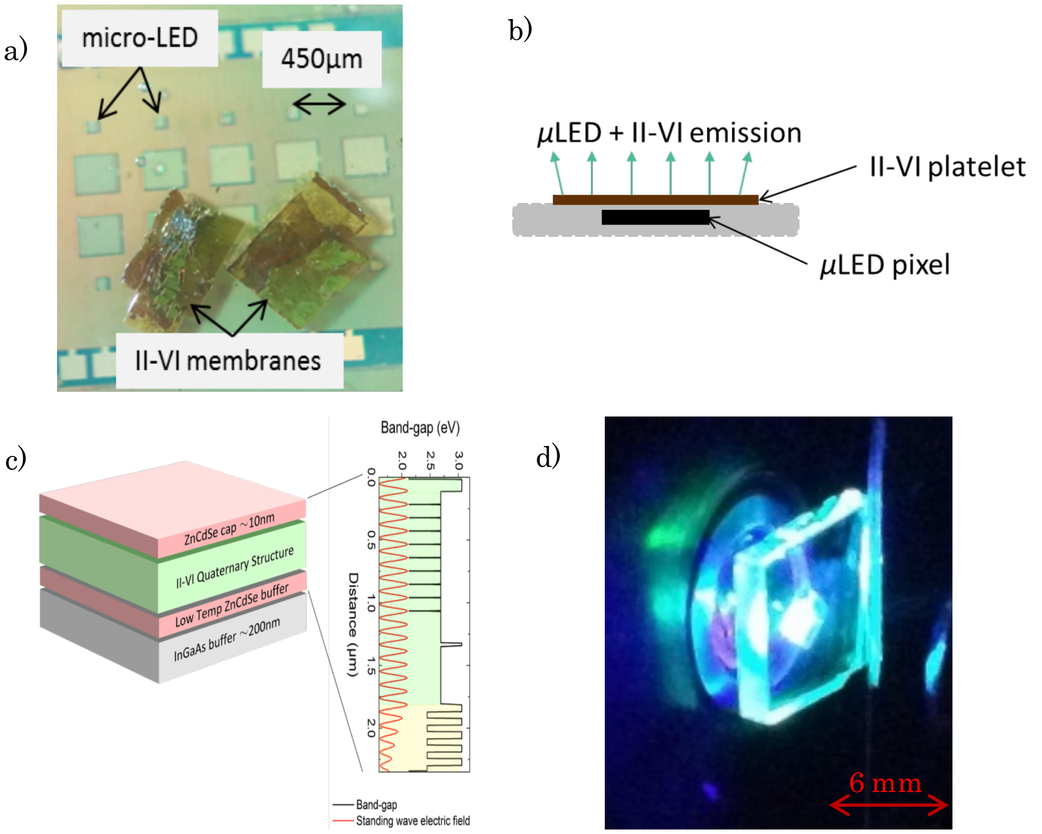

Figure 4.1 – a) Plan view optical micrograph of the hybrid device. The µLED pixels are the smaller elements as labelled, some of which are underneath the bonded II-VI membrane. Between the membrane and the underlying LEDs is the sapphire substrate, b) hybrid device schematic, c) II-VI MQW structural design and d) II-VI membrane when pumped by a blue LED.

The II-VI structure was grown by Dr. Joel De Jesus and Dr. Thor Garcia from the City College of New York. The growth was realised using molecular beam epitaxy on an InP substrate with an InGaAs buffer layer. It consists (see Table 1.1) of 9 $Zn_{0.48}Cd_{0.52}Se$ quantum wells with $(Zn_{0.5}Cd_{0.5})_{0.68}Mg_{0.32}Se$ barriers and was designed to absorb the pump light in the barriers, see also Figure 4.1c. The quantum wells emit at 540 nm in a resonant periodic gain configuration for potential alternative use as a laser gain medium [7]. The InP substrate was removed by a combination of mechanical polishing and wet etch processing using a solution of $HCl:H_3PO_4$ at a ratio of 3:1, followed by the removal of the InGaAs layer with a solution of $H_3PO_4:H_2O_2:H_2O$, at a ratio of 1:1:6 for maximum etch selectivity with the II-VI material [8]. The epi-side was fixed onto a temporary glass substrate for this step, using a wax, for mechanical support during processing. After substrate removal, the II-VI layer was transferred from the glass and liquid-capillary-bonded onto the sapphire window of the LEDs, hereinafter referred to as integrated MQW. The liquid capillary bonding technique uses the van der Waals' force to bond two smooth surfaces together. To do this, solvents or, in this particular case deionized (DI) water, can be used [9]. The resulting MQW membranes had a thickness of less than 2.5 μm and a surface area of a few mm^2 (see Figure 4.1a).

4.1.1 CW characteristics

Before dynamically characterising the integrated MQW, L-I-V curves and spectral responses from the bare and hybrid pixels were measured. For an in-depth analysis of the optoelectronic characteristics of the optical source used here, please refer to Chapter 2 section 2.2.

The normalised spectral measurements for the bare μLED, the hybrid configuration and the integrated MQW membrane (*i.e.* the contribution of the converted light at 540 nm) are presented in Figure 4.2. As depicted, the bare μLED has emission centred at 445 nm and for the pumped configuration two main peaks, one centred at 475 nm and a secondary one at 540 nm are observed. The emission at 540 nm comes from the light emitted by the II-VI MQW membrane.

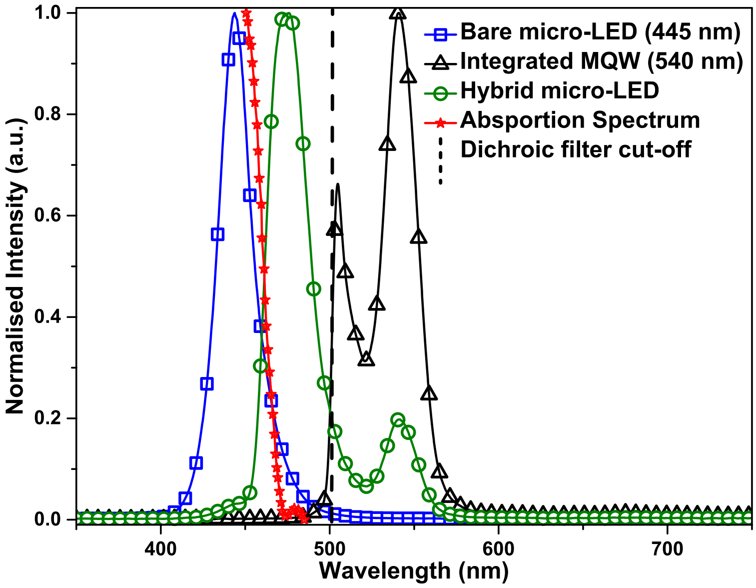

Figure 4.2 – Emission spectra from bare and hybrid pixels, together with the II-VI band-edge normalized absorption.

After the spectral response study, the absorption of the down-converter was measured. The II-VI membrane was designed to absorb 97% to 98% of 450 nm monochromatic light. Because of the linewidth of the bare μLED spectrum (23 nm FWHM) the effective μLED light absorption is 85% ± 1%. The band-edge of the membrane is at around 460 nm and therefore the long-wavelength tail of the μLED emission is not fully absorbed, explaining the 'apparent' 475nm peak in the spectrum of the integrated MQW membrane, see Figure 4.2.

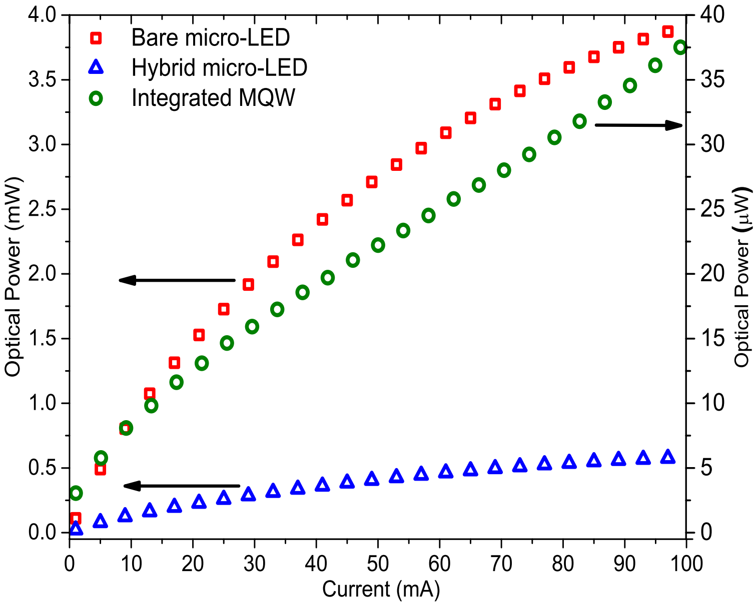

Figure 4.3 – CW optical powers of the bare, hybrid unfiltered μLED and integrated MQW membrane.

The power transfer functions (optical power versus bias current) for the bare µLED, hybrid µLEDs and integrated MQW membrane is shown in Figure 4.3. At 100mA dc, which was found to be the maximum current before thermal rollover, the measured optical powers from the bare µLED and the integrated MQW membrane (*i.e.* the colour-converted light contribution) were 4 mW and 37 µW, respectively. The MQW presented a linear conversion efficiency – defined as the ratio between 540nm over incident 450nm power – at different excitation levels of around 1% ± 0.1%. The total forward power of the hybrid µLED was 0.58 mW. The membrane structure used in this device was not primarily designed for colour-conversion, but rather as a VECSEL (Vertical External Cavity Surface Emitting Laser), and the high refractive index contrast between the membrane material and air (3.4:1) results in a significant amount of waveguided light, which is then lost through reabsorption and edge emission. Improved epi-layer design of the membrane and implementation of appropriate light extraction schemes would improve this value significantly.

4.1.2 Dynamic characteristics

The modulation properties of hybrid µLEDs are important for VLC applications and represent the main focus of this study. This section looks into the dynamic characteristics of the down-converter membranes and hybrid device configuration presenting the bandwidths and maximum achieved modulation speeds when applied in visible light communications.

4.1.2.1 Bandwidth

Following the same characterisation principles described in Chapter 2, to dynamically characterise the down-converter membranes and the hybrid device a Bias-Tee was used to combine a dc-signal (power supply) with an RF signal (network analyser). As previously explained, the network analyser was used to apply and record the RF signal and the respective response.

The -3dB optical bandwidth values were obtained through an interpolation of the bi-exponential fit determined by expression 2.11. To do so, a Matlab®

built-in function, *fminsearch*, along with the least squares method were used, see expression 2.13. The goodness of the fit, *GoF*, was determined through a function, *goodnessOfFit*, which uses the normalised mean square error method. The *GoF* is a statistical analysis that characterises how well the fit describes the measured data, *i.e.* it is a parameter often used to describe the discrepancy between a model and the obtained results. Here, *GoF=1* represents a perfect fit while *GoF<1* indicates a discrepancy between the data and the fit.

The intrinsic bandwidth values for the II-VI platelet were obtained for each bias current by fitting the data considering a possible multi-exponential decay of the luminescence. The frequency responses of the bare μLED and integrated MQW membrane when driven at 80mA bias current and their corresponding fitting curves are depicted in Figure 4.4.

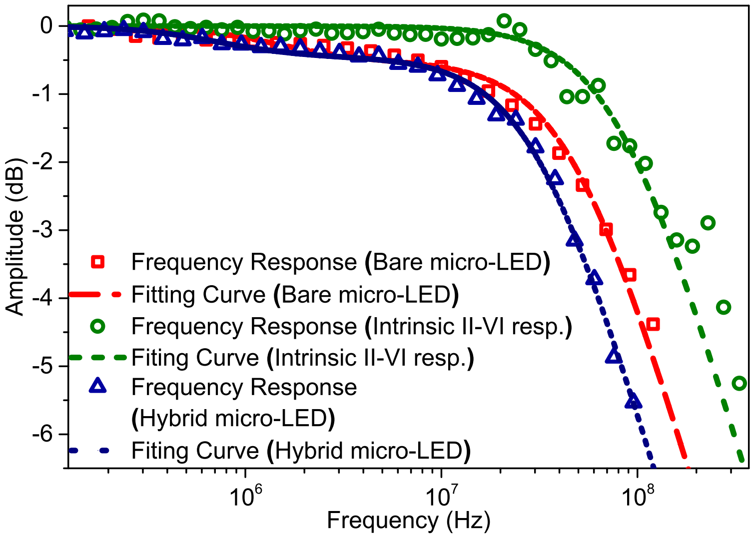

Figure 4.4 – Frequency responses for 80 mA bias current of the bare and hybrid μLED, as well as the intrinsic response of the colour-converting membrane (integrated MQW membrane), with the respective bi-exponential fits.

The data for the intrinsic response of the colour-converting membrane is obtained by removing the frequency response contribution of the bare μLED from the overall response of the hybrid device [1]. This is also plotted in Figure 4.4 along with its fit. This response is accounted for by a mono-exponential decay of the MQW membrane photoluminescence and its bandwidth is determined by the bandwidth-lifetime relation described by expression 2.7 in Chapter 2.

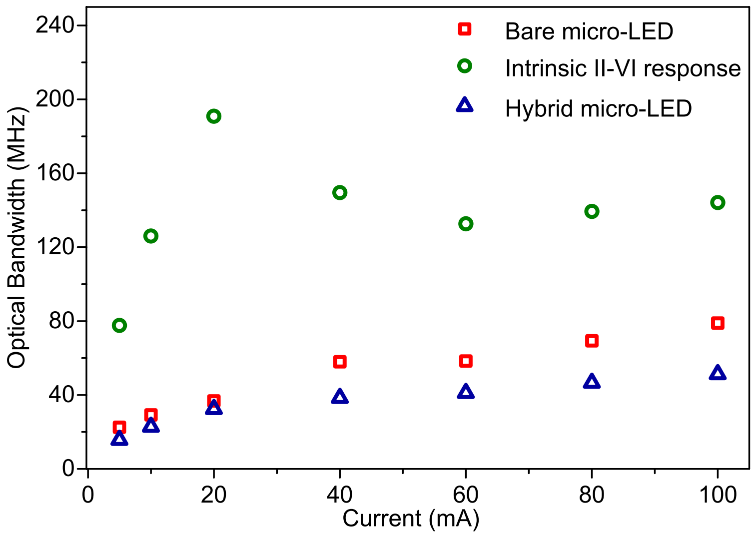

Figure 4.5 – The -3dB optical bandwidths of the bare µLED and of the hybrid µLEDs. The intrinsic bandwidth values of the membrane (integrated MQW membrane) are also plotted.

Figure 4.5 plots the optical bandwidth values versus the InGaN LED bias current for the bare and hybrid µLED as well as the intrinsic modulation bandwidth of the membrane. The data is also summarized in Table 4.1 along with the respective goodness of fit (*GoF*) values.

Table 4.1 – Table with bandwidth values, f_{co}, for the II-VI membrane (integrated MQW membrane – a long pass filter was used to remove the blue light), the bare µLED and the hybrid device, the goodness of fit, GoF and the lifetime, τ_i.

	Bare µLED		Intrinsic II-VI membrane response*			Hybrid µLED	
I (mA)	f_{co} (MHz)	*GoF*	f_{co} (MHz)	τ_i (ns)	*GoF*	f_{co} (MHz)	*GoF*
5	23±2	0.991	78±15	3.5±1.4	0.947	16±1	0.997
10	29±2	0.988	126±2	2.2±0.1	0.958	23±2	0.995
20	37±2	0.987	191±31	1.4±0.5	0.875	32±5	0.993
40	58±2	0.983	150±17	1.8±0.4	0.922	38±2	0.993
60	58±4	0.963	133±8	2.1±0.3	0.934	41±3	0.995
80	69±6	0.986	139±12	2.0±0.4	0.947	47±3	0.996
100	79±6	0.990	145±25	1.9±0.7	0.837	51±2	0.995

**Frequency response obtained through the bare and hybrid LED measurements.*

The µLED bandwidth is current dependent and reaches 79 MHz at 100 mA. This current dependency can be attributed to the reduced carrier lifetime in the InGaN µLED active region as the current, and hence the carrier density, increases [10], [11]. The typical intrinsic response of the membrane is 145 MHz, much faster than conventional phosphors. The hybrid µLED behaviour is the combination of the frequency responses of the colour-converting membrane and the underlying µLED. The result is a modulation bandwidth of 51 MHz limited by the slower of the two components, *i.e.* the µLED response in this case. Higher modulation bandwidths can be expected by using blue µLEDs of even smaller dimensions [12].

The dependence of the colour-converter bandwidth on the incident µLED pump power density was further studied. Since the µLED is in a flip-chip configuration, *i.e.* the emission occurs through the sapphire substrate, the excitation area at the membrane/sapphire interface is determined by the divergence of the µLED light and the propagation length through the sapphire. Due to the small LED size, the excitation spot incident on the membrane can in good approximation be assumed to be circular with diameter equal to the substrate thickness, *i.e.* 330 +/- 20 µm [13]. The intrinsic bandwidth data of the membrane as previously determined is then plotted again in Figure 4.6 as a function of the incident excitation power density ('integrated membrane'). For pump power density between 1 and 1.75 W/cm^2, the average intrinsic bandwidth is 145 MHz.

In order to observe in more detail the bandwidth behaviour of the MQW membrane at excitation power density below 1 W/cm^2, it was independently characterised, *i.e.* when separated from the µLED, as a stand-alone membrane. In this case the membrane was held onto a glass substrate and remotely pumped with a 450nm µLED using the set-up depicted in Figure 3.1. The results are plotted in Figure 4.6 (black squares, 'stand-alone membrane').

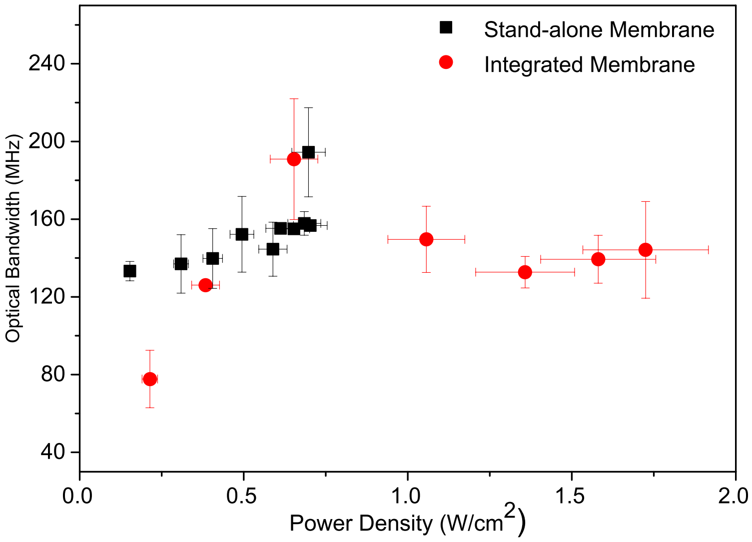

Figure 4.6 – Bandwidth dependence over different power densities.

The vertical error bars in Figure 4.6 represent the root mean square errors of the fits of the frequency responses. Overall, the presented bandwidth values are within the error bars of the surrounding points so there is no significant power density dependence of the membrane intrinsic bandwidth over a 10x range of power density. The average bandwidth over the range of 450nm light power density corresponding to the operation of the integrated MQW membrane is around 145 MHz. This corresponds to an effective carrier lifetime of 1.9 ns. This value can be corroborated by a direct time-correlated single photon counting, TCSPC, measurement of the stand-alone membrane. Such TCSPC analysis was done using an Edinburgh Instruments system using an EPL-450 Picosecond pulsed diode laser as the excitation source (450 nm). Differences in the TCSPC lifetime measurement were seen between membranes processed from the same epi-layer structure, however the average measured lifetime from a number of such membranes was found to be 1.4 ± 0.2 ns, showing reasonable consistency with the frequency response data.

The photoluminescence and the optical bandwidth of the MQW membrane, which is two-orders of magnitude higher than for phosphors, means that high-speed colour-conversion can be realized for a range of light levels that correspond to µLED operation.

4.2 III-V nanomembranes

As stated at the beginning of the chapter, as well as II-VI nanomembranes, III-V alloyed structures were also designed as down-converters for InGaN LEDs.

Here, a μLED with peak emission at 450 nm was used to optically excite the III-V MQW membrane. It was fabricated using a commercial p-*i*-n GaN structure grown on *c*-plane sapphire, following the procedure reported in [6] and in Chapter 2. The chip is made of 8 pixels of 4 different sizes, 50 x 50 μm^2, 75 x 75 μm^2, 100 x 100 μm^2 and 150 x 150 μm^2. After fabrication, the chip was mounted onto a printed circuit board and wire bonded to metal tracks connected to SMA connectors, in such a way that each pixel from the μLEDs could be individually addressed.

A second approach using an off-the-shelf OSRAM laser diode (PL450B) with peak emission at 450 nm to pump the III-V MQW bonded to a sapphire hemispherical lens was also studied. In this configuration, and in order to control heating, a metallic mount was built. Using a Peltier heatsink and a thermistor, which is a temperature sensitive resistor along with the metallic mount, the laser diode temperature was kept constant at 25^0C.

The III–V MQW membrane structure (Table 1.2) was grown by molecular beam epitaxy on a GaAs substrate. The growth was performed by Dr. Andrey Krysa from the University of Sheffield. It consists of six $Ga_{0.5}In_{0.5}P$ quantum wells with $(Al_{0.6}Ga_{0.4})_{0.51}In_{0.49}P$ barriers and was designed to absorb the pump emission in the barriers. The quantum wells emit at 648 nm in a resonant periodic gain configuration. The GaAs substrate was removed by a wet etch process using a solution of H_3PO_4:H_2O_2:H_2O in a ratio of 3:4:3, which presents an etch rate of 6 μm/min. The epitaxial film surface is fixed onto a temporary glass substrate at this stage, by liquid capillary bonding, for mechanical support during processing. After substrate removal, the III–V membrane can be transferred onto any desired substrate. In order to reduce the waveguided modes, substrates with different refractive indexes and shapes were studied, *i.e.* glass, a half-ball sapphire lens and a diamond lens.

For membranes on each substrate the forward optical power was measured under different driving conditions using the 100 x 100 μm^2 pixel and is presented in Figure 4.7. The relative maximum absorption – surface reflections were not considered here – and conversion efficiencies for each substrate are summarised in Table 4.2.

Table 4.2 – Relative absorption and relative conversion efficiency for the III-V samples on different substrates.

	III-V in between diamond lens and mirror	III-V in between sapphire lens and mirror	III-V on diamond lens	III-V on sapphire lens	III-V on flat glass
Absorption (%)	79.8	76.2	78.5	81.2	67.2
Conversion efficiency (%)	1.3	1.3	0.4	0.8	0.6

In a further development an off-the-shelf dichroic mirror designed to reflect the down-converted light was bonded onto the free membrane surface in order to increase the acquired light. This resulted in doubling of detected light power for the sapphire sample and a four-fold increase in the case of the diamond one. The placement of the mirror did not change the relative absorption of the colour-converter.

For comparison, the colour-converter relative absorption and relative efficiency were measured while it was capillary bonded to a cover glass. A lower conversion efficiency was found, however the discrepancy between the results obtained with the different bonding substrates is attributable to their different shape, size and refractive index. The sapphire half-ball lens has a diameter of 5 mm with a radius of curvature of 2.5 mm whilst the diamond lenses a diameter of 4 mm with radius of curvature of 8 mm. Besides, as indicated previously, to obtain a realistic value for the efficiency one should use an integrating sphere.

After the initial characterisation, an AlInGaP platelet was transferred from the carrier substrate on which it was processed and capillary-bonded onto the sapphire window of the μLED, completing the hybrid device [9]. The resulting MQW membranes had a thickness of less than 400 nm with a typical surface area of a few mm^2. For heat management purposes, and in order to increase the extraction efficiency based on the results presented in Figure 4.7, a sapphire half-ball lens was capillary-bonded on top of the down-converter membrane. Images of the hybrid device and membrane on a half-ball lens are shown in Figure 4.8.

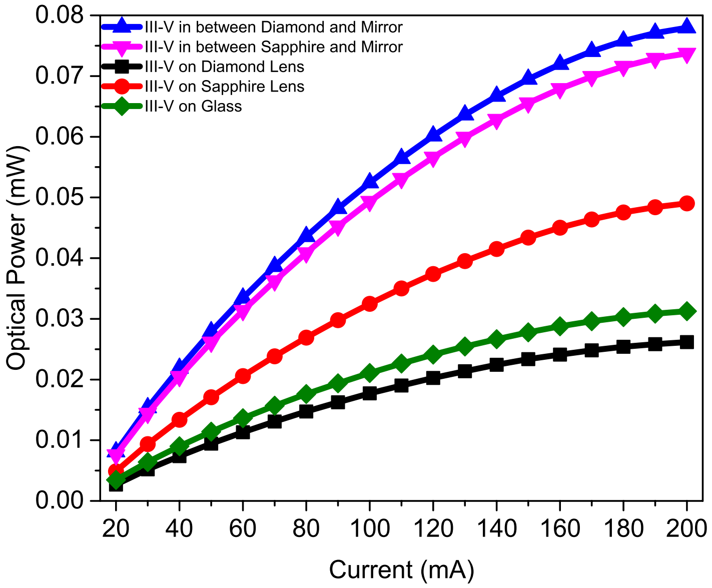

Figure 4.7 – Received output power from AlInGaP platelets on several respective substrates, measured as a function of GaN 100 x 100 μm² μLED drive current.

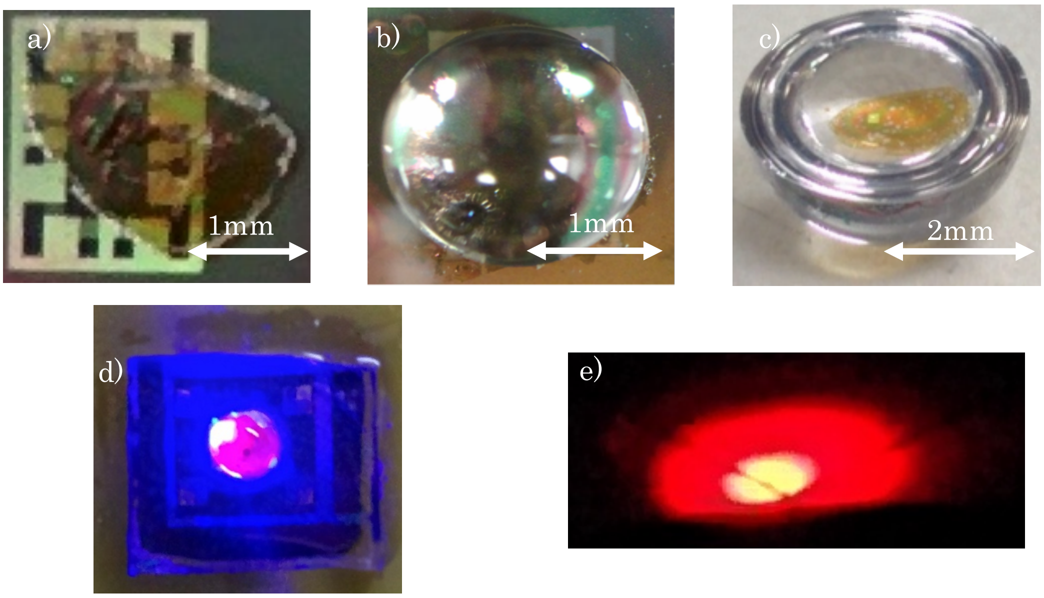

Figure 4.8 – AlInGaP platelet a) capillary bonded onto the sapphire side of a μLED chip, b) sandwiched in-between the sapphire half-ball lens and μLED windows, c) capillary bonded onto a sapphire half-ball lens, d) hybrid LED with integrated sapphire lens under operation and e) colour-converter light imaged on a screen.

4.2.1 CW characteristics

Prior to capillary bonding the platelets onto the sapphire windows of the µLEDs, each µLED pixel was optically characterised and the frequency response determined. Initially, all the pixels were driven at current of up to 200 mA. The respective optical and spectral responses of these bare µLEDs are plotted in Figure 2.11c. The AlInGaP platelet was then capillary bonded and characterised under the same conditions as the pixels. At this point, and considering the pixels' L-I-V curves, the smaller pixels, 50 µm x 50 µm and 75 µm x 75 µm, were driven up to 160 and 180 mA, which corresponds to the respective maximum bias current before thermal rollover. The acquired L-I curves are presented below, see Figure 4.9a. In addition, the spectral response at each current was acquired in order to determine the peak-emission shift due to thermal effects and band filling, see Figure 4.9b. The normalised spectral measurements for the bare µLED, the hybrid configuration and the integrated MQW membrane (*i.e.* the contribution of the converted light at 640 nm) are presented in Figure 4.9c. As depicted, the bare µLED has emission centred at 450 nm and the down-converter platelet at 640 nm. The small feature at 550 nm corresponds to the optical wavelength filter cut-off.

From Figure 4.9a one can see there is an optical power rollover from the colour-converter when individually addressed with each of the different size µLED pixels. This efficiency decrease can be attributed to a reduction of the colour-converter luminescence efficiency due to the temperature increase since there is a heat transfer from the sapphire window of the µLED to the III-V membrane. A continuous red-shift, going from 645 nm at 20 mA up to 658 nm at 200 mA was measured. The spectral emission of the AlInGaP colour-converter is expected to red-shift by approximately 0.12 nm/°C as determined from modelling based on the empirical Varshny relation [14]. Therefore, the temperature increase of the nano-membrane can be inferred to be 100°C, which is not far off the temperature rise of the sapphire surface as measured by thermal imaging (~140°C). So, in order to try to extract some of the heat, a sapphire half-ball lens was used, being 2 mm in diameter and with a refractive index of 1.77 and sphericity of 0.64. The lens was liquid capillary bonded to the III-V platelet using DI water. The resulting optical power and spectral shift were measured using the same conditions presented above. The characteristics curves for the devices after lens bonding are presented in Figure 4.10.

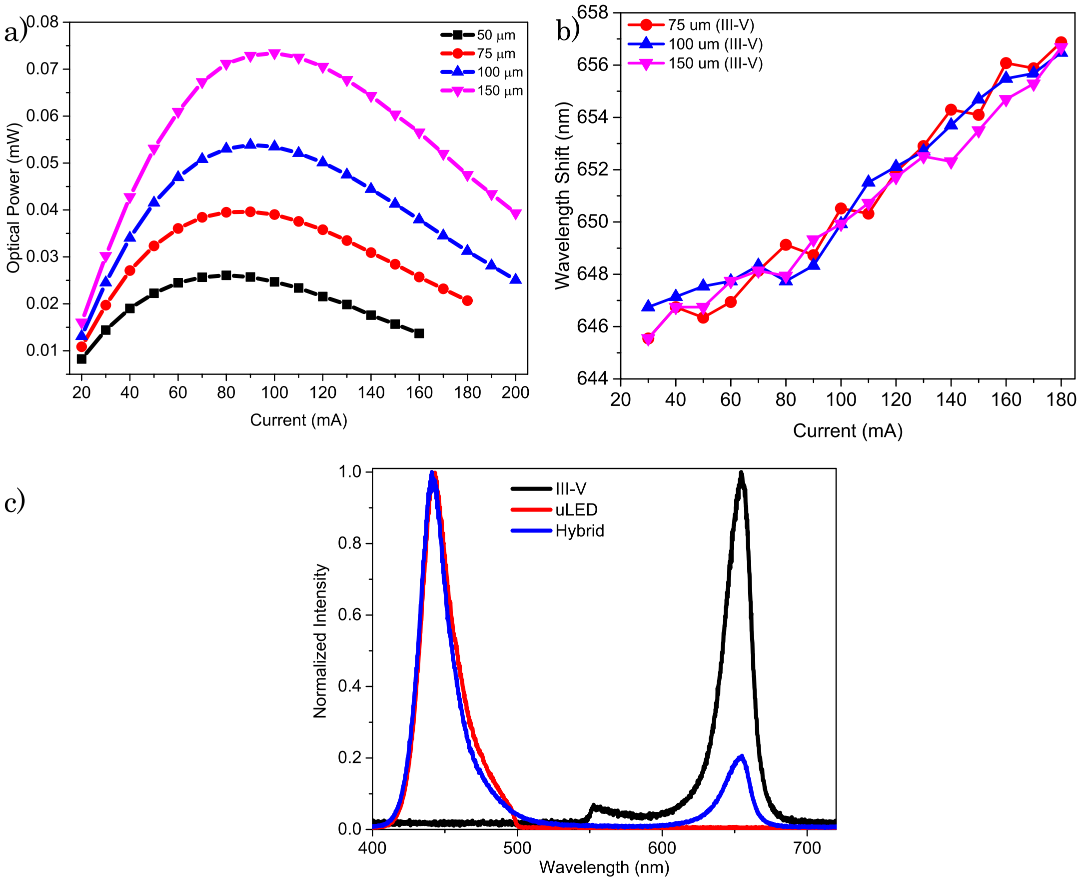

Figure 4.9 – a) L-I curves for the platelet being pumped with the different GaN μLED pixels, b) III-V spectral shift under pumping and c) normalised emission spectra from bare μLED, hybrid device and the III-V platelet. The results in a) and b) show the dependence on the size of the μLED pixel used for excitation.

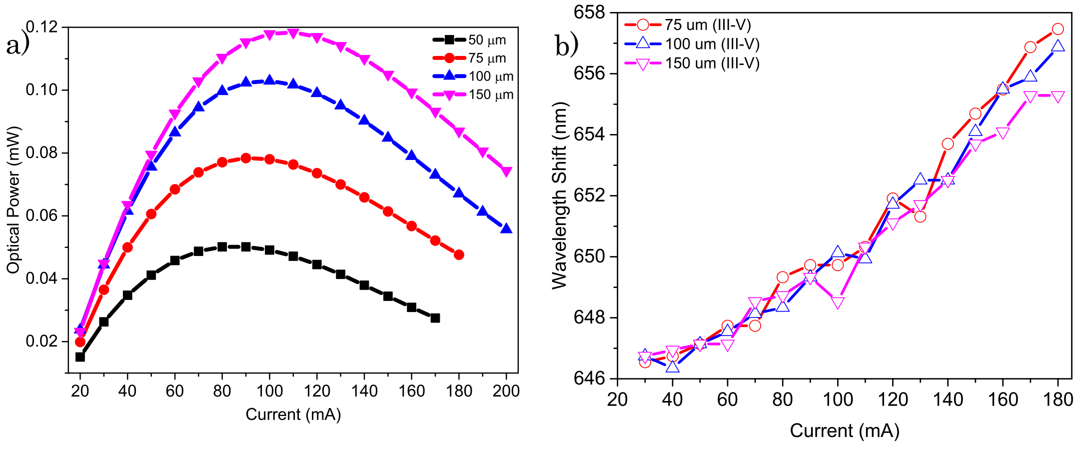

Figure 4.10 – a) L-I curves for the platelet being pumped with the different sized μLED pixels and b) the corresponding spectral shift. All results taken after the sapphire lens bonding.

From Figure 4.10, the addition of the lens is shown to increase the current density before rollover, improving the maximum output power by 63%, 92%, 98% and 95% for the squared pixels with edge size of 150, 100, 75 and 50 μm^2, respectively. A possible explanation for the lower enhancement on the biggest pixel is probably because it sits on the edge of the lens. However, analysing the spectral shift data before and after the lens bonding, the addition of the lens did not significantly improve with the heat removal. Nevertheless, its application has helped with the light extraction efficiency through the reduction of the refractive index step between the colour-converter and free-space and the lensing effect increasing the amount of the colour-converted light focused onto the photoreceiver. In order to decrease the heat behaviour a larger lens may need to be used.

The decrease in the colour-converter optical power with current is attributed to a rise in temperature. However, other possible explanations could include a dependence of non-radiative recombination with the MQW carrier density or a saturation of the nanomembrane absorption. To rule out these possibilities, the power density dependence of the converted light was further studied independently of the temperature rise caused by the μLED, by remotely pumping a nanomembrane bonded onto a 5mm diameter sapphire lens. For low pump power density, a μLED was used, otherwise a laser diode (OSRAM GaN LD) was utilised. The power density from each excitation source was calculated using a Coherent Beam Master power meter. Results plotted in Figure 4.11 demonstrate that there is no saturation of the absorption and no noticeable increase in non-radiative recombination. The optical power from the colour-converter increases linearly with the pump power density in the range from 0 up to 4 kW/cm^2. The left side of the broken x-axis shows data taken under LED pumping, whereas on the right side the data for laser diode pumping.

The converted power efficiency, *i.e.* the blue light that was effectively converted to red and was not internally reflected by the semiconductor was, for this configuration 0.88 ± 0.16%. To improve the extraction efficiency, a dichroic mirror designed to allow the excitation light from the pump to pass through but reflect the colour-converter light in the detector direction was placed in order to sandwich the membrane between it and the lens. This improved the overall best colour-conversion performance up to 1.14 ± 0.26% for an output power of 1.2 mW under LD pumping, see Figure 4.12.

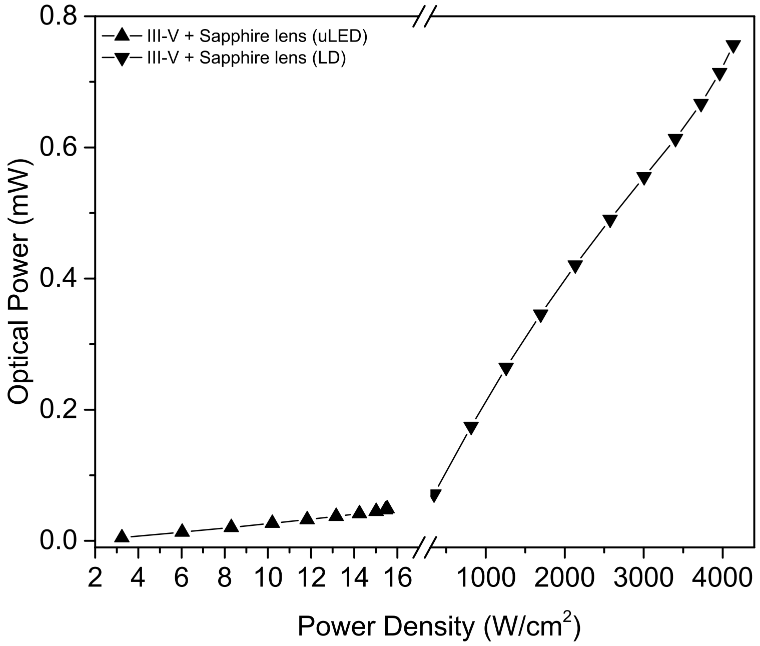

Figure 4.11 – Power density vs optical power for the III-V platelet samples bonded to sapphire lenses and pumped with a laser diode (PL450B) and a µLED.

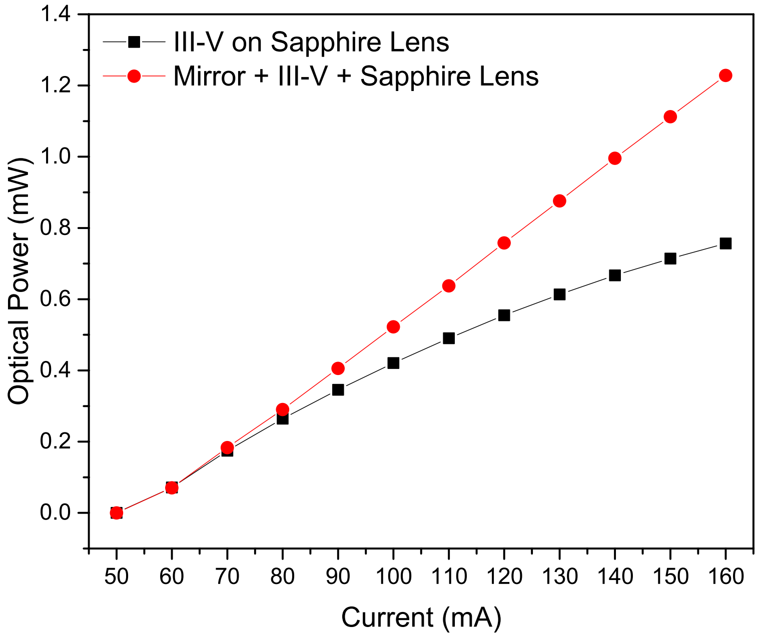

Figure 4.12 – L-I curves for the III-V platelet on sapphire and diamond lens and III-V platelet sandwiched between the previous lenses and a dichroic mirror. All results taken using GaN laser diode pumping, showing output colour converted power vs. laser diode drive current.

4.2.2 Dynamic characteristics

The dynamic characteristics of any LED device or related colour-converter such as the frequency response and data rates using high level encoding schemes are important for Visible Light Communications, as previously discussed. In this section, the frequency response of the AlInGaP platelets bonded onto the μLEDs and onto the sapphire lens are presented. Subsequently, PAM and OFDM data encoding scheme test results are presented for the hybrid configuration.

4.2.2.1 Bandwidth

The optical frequency responses of the GaN μLEDs and integrated MQW membranes were measured at different levels of bias current. The -3dB optical bandwidth values (the frequency at which the optical power is half the dc value, f_{co}) were calculated by fitting the data, assuming an exponential decay of the luminescence. This was done following the same principle and using the same methodology as described previously in the subchapter for the II-VI nanomembranes. Below are presented the bandwidths for the III-V colour-converter and the hybrid device. The frequency response of the bare GaN μLEDs pixels are presented in Chapter 2, Figure 2.14c.

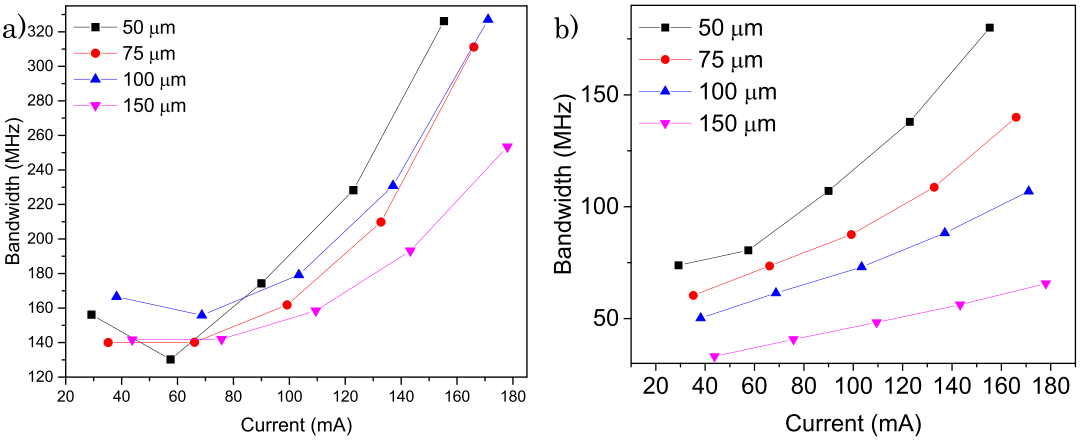

Figure 4.13 – Bandwidths for, a) the stand-alone III-V nanomembrane and c) the hybrid μLEDs (platelet integrated). The currents shown are those of the respective GaN μLED used for pumping.

The bandwidth is size and current dependent reaching a maximum of 160 MHz at around 150 mA for the hybrid red device. Similar bandwidths were found for the stand-alone µLEDs at the same driving current. Such similarity results from the fact that the hybrid response behaviour is the combination of the frequency responses of the colour-converting membrane and the underlying µLED. The result is a modulation bandwidth limited by the slower of the two components, *i.e.* the µLED response in this case. Apart from this, bandwidth current dependency of the µLEDs can be attributed to the reduced carrier lifetime in the active region as the current, and hence the carrier density, increases[12].

The intrinsic response of the nanomembrane is between 130 MHz and 320 MHz, which is at least two order of magnitude faster than conventional phosphors [10], [11]. The increase in the bandwidth with the current is linked to the increase of non-radiative recombination as the temperature of the device, and hence the nanomembrane, increases.

The frequency response of the laser diode was measured as well but, in this case, it was noticeable the system was limited by the photodiode bandwidth which is around 1.4GHz. Regardless, the nanomebrane bonded onto the sapphire lens bandwidth was measured for the laser diode excitation case and is shown in Figure 4.14.

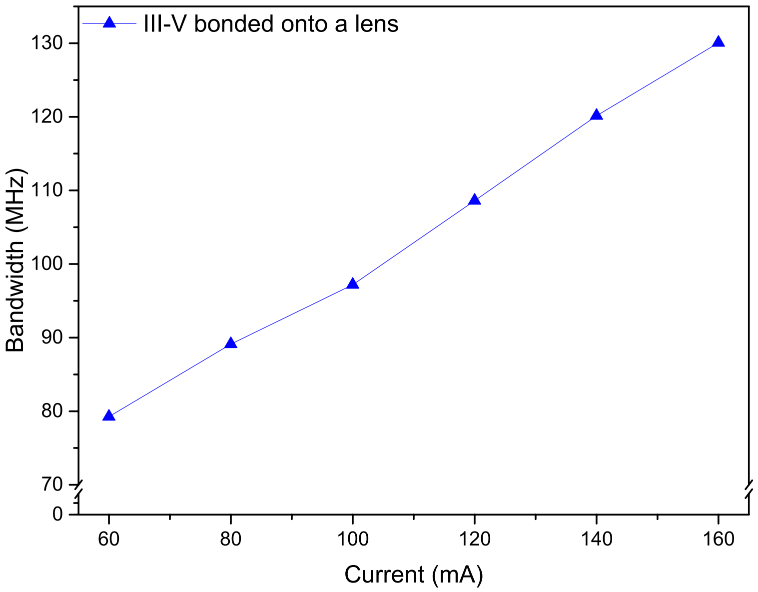

Figure 4.14 – Bandwidths under laser diode excitation of the III-V platelet bonded onto a sapphire and diamond lens and sandwiched between one of those lenses and a dichroic mirror.

As obtained previously by the µLEDs there is an increase of bandwidth with increased current injection when using a laser diode reaching a maximum bandwidth of 130 MHz at 160 mA. There is a difference between the maximum achievable bandwidths in both configurations, ~300 MHz for the hybrid device and 130 MHz for the laser diode-pumped nanomembrane. This behaviour results from higher non-radiative recombination caused by heating when the nanomembrane is integrated onto the μLED array, which is nowhere near as severe when the nanomembrane is being remotely-pumped by the laser diode.

4.2.2.2 Advanced data modulation formats

Measurements of free-space optical data transmission were carried out using the above devices. The optical set-up and the required equipment are as described in Chapter 3. In order to determine the best performing modulation scheme for this device, four different data encoding schemes were studied. Three of these were in PAM format, from two up to eight levels, and one was OFDM. The optical and electrical conditions were kept the same between the different modulation tests. All the modulation schemes were pre-loaded into the Agilent 81180A Arbitrary Waveform Generator (AWG) using a Matlab® script. For each of the pixels the driving bias and clipping conditions were optimised in order to obtain the maximum transmission data rate. When using OFDM to transmit data, the bit stream created in the Matlab® script was encoded and then converted to the frequency domain using an inverse fast Fourier transform (IFFT). This signal was then clipped to avoid nonlinear distortion caused by the transmitter and receiver components. Afterwards, it was converted into an analog-signal by an AWG. The signal was then optically transmitted and acquired by the APD. Comparing the transmitted and received signal it is then possible to determine the Bit-Error-Rate (BER) for each of the devices. The Forward-Error-Correction limit considered for these measurements is $3.8\text{x}10^{-3}$. The measured data rates for the hybrid device are presented in Figure 4.15. By comparing the data, it seems the best performing scheme for this kind of devices is 4-PAM. However, for the 150 μm x 150 μm hybrid device 4-PAM and OFDM provide very close data rates.

Table 4.3 – Data rates for the different III-V platelet/pixel combinations in MHz.

	50 x 50 μm^2	75 x 75 μm^2	100 x 100 μm^2	150 x 150 μm^2
2-PAM	775	760	735	560
4-PAM	870	860	805	615
8-PAM	720	740	680	495
OFDM	740	665	655	660

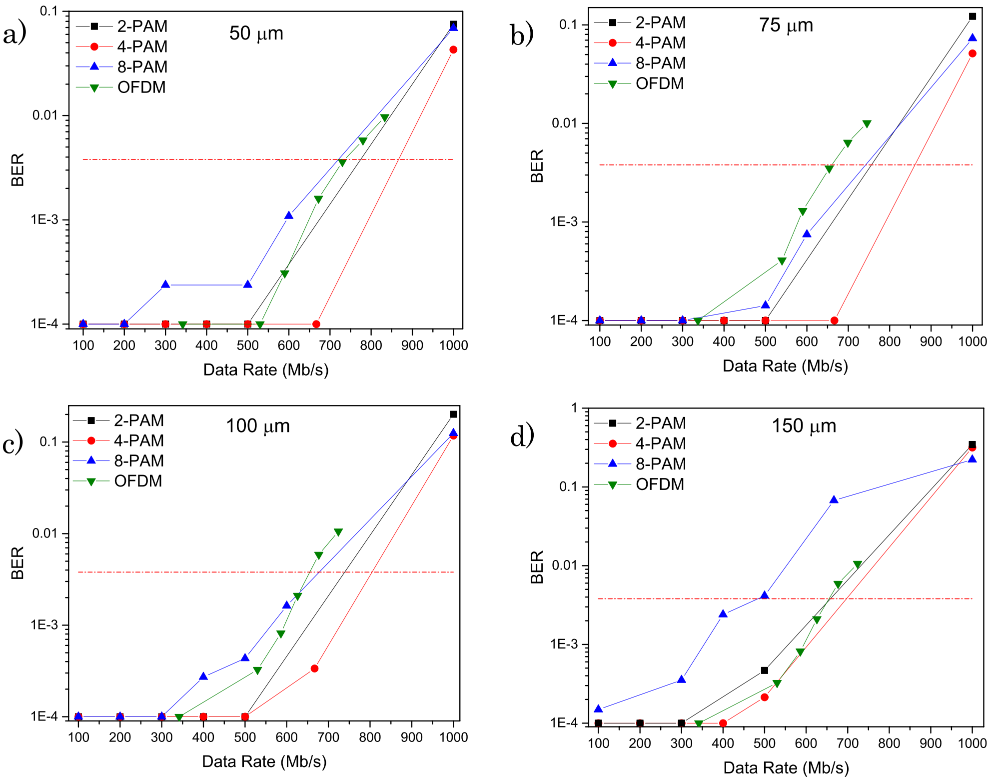

Figure 4.15 – BER vs. data rate for the hybrid device a) using 50µm x 50µm pixels, b) using 75µm x 75µm pixels, c) using 100 µm x 100µm pixels and d) using 150µm x 150 µm pixels.

From the above, the presented down-converter nanomenbrane shows much higher bandwidths and faster data rates than the standard phosphor solution which is limited to a few MHz of optical frequency response. The presented approach could furthermore be used in a WDM systems in which each wavelength can be used to transmit independent data thus expanding the system data transmission capability even further.

To infer the data transmission capability of the III-V platelet when pumped by an InGaN laser diode the same optical and electrical system were used. By adjusting the laser diode driving bias current and the swing for data modulation it was possible to achieve 1.2GB/s error-free using OFDM, see Figure 4.16.

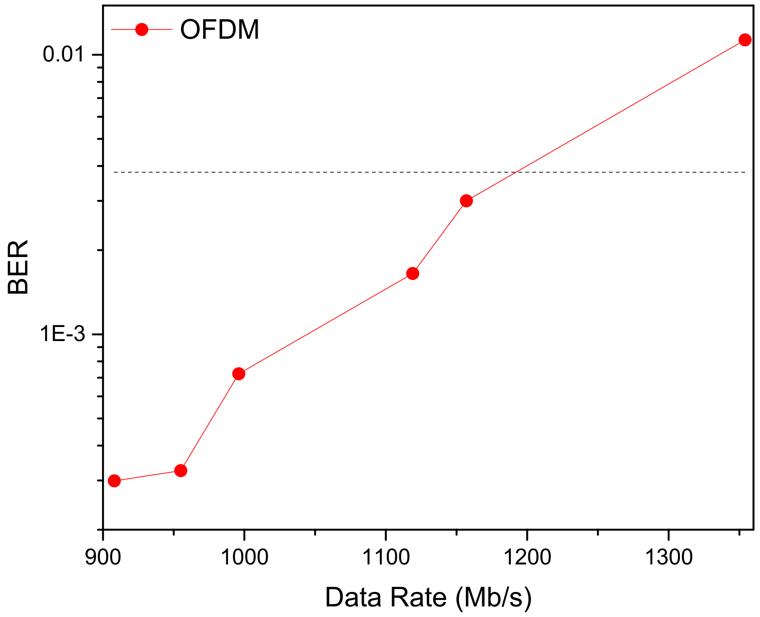

Figure 4.16 – BER vs Data Rate for the III-V platelet pumped with a laser diode.

4.3 Summary

In this chapter two approaches for integration of inorganic colour-converters based on II-VI and III-V semiconductors onto µLEDs were introduced.

The chapter started by describing the first colour-converter which was based on II-VI CdMgZnSe, the preparation steps in order to process the samples for testing and the tests performed in a continuous and a dynamic regime. It was found the II-VI semiconductor used presents an absorption and relative conversion efficiency of 85%±1% and 1%±0.1%, respectively. The total forward power of the hybrid µLED was 0.58 mW. The modulation bandwidth of the 540nm colour-converter emission was measured to be up to 51 MHz for an intrinsic bandwidth of the MQW membrane and of the underlying µLED of 145 MHz and 79 MHz, respectively.

The second part of the chapter presented an III-V AlInGaP semiconductor used as a colour-converter. Here, several approaches to improve the extraction efficiency of the colour-converter were analysed. The best performing one was based on a sapphire lens and a dichroic mirror with the semiconductor encapsulated between both. With this configuration was found an absorption and relative efficiency of 79.8%±0.1% and 1.3%±0.03%, respectively. Apart from this, after bonding the colour-converter onto the sapphire side of a flip-chip μLED a reduction of external efficiency due to the heat transfer from the μLED onto the nanomembrane was found. To reduce or suppress the heat issue a half-ball lens was capillary-bonded onto the nanomembrane, however although an improvement of colour converted light extraction efficiency was found analysis of the nanomembrane spectral shift showed heat dissipation remained an issue. Nevertheless, the maximum achieved data rate for this configuration was found to be 870 Mb/s, providing a much faster response than typical phosphors, creating the possibility of designing devices with similar properties for WDM systems. Also, it was also demonstrated that it is possible to achieve 1.2Gb/s data rate using a laser diode as optical source.

References

[1] N. Laurand, B. Guilhabert, J. McKendry, A. E. Kelly, B. Rae, D. Massoubre, Z. Gong, E. Gu, R. Henderson, and M. D. Dawson, “Colloidal quantum dot nanocomposites for visible wavelength conversion of modulated optical signals,” *Opt. Mater. Express*, vol. 2, no. 3, p. 250, Feb. 2012.

[2] M. A. Haase, J. Xie, T. A. Ballen, J. Zhang, B. Hao, Z. H. Yang, T. J. Miller, X. Sun, T. L. Smith, and C. A. Leatherdale, “II–VI semiconductor color converters for efficient green, yellow, and red light emitting diodes,” *Appl. Phys. Lett.*, vol. 96, no. 23, p. 231116, 2010.

[3] D. Schiavon, M. Binder, A. Loeffler, and M. Peter, “Optically pumped GaInN / GaN multiple quantum wells for the realization of efficient green light-emitting devices,” *Appl. Phys. Lett.*, vol. 102, no. 11, p. 113509, 2013.

[4] B. Damilano, H. Kim-Chauveau, E. Frayssinet, J. Brault, S. Hussain, K. Lekhal, P. Vennegues, P. De Mierry, and J. Massies, “Metal Organic Vapor Phase Epitaxy of Monolithic Two-Color Light-Emitting Diodes Using an InGaN-Based Light Converter,” *Appl. Phys. Express*, vol. 6, no. 9, p. 92105, 2013.

[5] J. J. D. McKendry, R. P. Green, A. E. Kelly, Z. Gong, B. Guilhabert, D. Massoubre, E. Gu, and M. D. Dawson, “High-Speed Visible Light Communications Using Individual Pixels in a Micro Light-Emitting Diode Array,” *IEEE Photonics Technol. Lett.*, vol. 22, no. 18, pp. 1346–1348, Sep. 2010.

[6] Z. Gong, S. Jin, Y. Chen, J. McKendry, D. Massoubre, I. M. Watson, E. Gu, and M. D. Dawson, “Size-dependent light output, spectral shift, and self-heating of 400 nm InGaN light-emitting diodes,” *J. Appl. Phys.*, vol. 107, no. 1, p. 13103, 2010.

[7] X. Zhou, M. Munoz, M. C. Tamargo, and Y. C. Chen, “Optically pumped laser characteristics of blue Znx′Cdy′Mg1−x′−y′Se/ZnxCdyMg1−x−ySe single quantum well lasers grown on InP,” *J. Appl. Phys.*, vol. 95, no. 1, p. 7, 2004.

[8] R. Moug, A. Alfaro-Martinez, L. Peng, T. Garcia, V. Deligiannakis, A. Shen, and M. Tamargo, “Selective etching of InGaAs/InP substrates from II-VI multilayer heterostructures,” *Phys. Status Solidi*, vol. 9, no. 8–9, pp. 1728–1731, Aug. 2012.

[9] Z. L. Liau, “Semiconductor wafer bonding via liquid capillarity,” *Appl. Phys. Lett.*, vol. 77, no. 5, p. 651, 2000.

[10] E. F. Schubert, *Light-Emitting Diodes*, 2nd ed. Cambridge University Press, 2006.

[11] R. P. Green, J. J. D. McKendry, D. Massoubre, E. Gu, M. D. Dawson, and A. E. Kelly, “Modulation bandwidth studies of recombination processes in blue and green InGaN quantum well micro-light-emitting diodes,” *Appl. Phys. Lett.*, vol. 102, no. 9, p. 91103, 2013.

[12] J. J. D. Mckendry, D. Massoubre, S. Zhang, B. R. Rae, R. P. Green, E. Gu, R. K. Henderson, A. E. Kelly, and M. D. Dawson, “Visible-Light Communications Using a CMOS-Controlled Micro-Light-Emitting-Diode Array,” *J. Light. Technol.*, vol. 30, no. 1, pp. 61–67, 2012.

[13] J. Herrnsdorf, Y. Wang, J. J. D. McKendry, Z. Gong, D. Massoubre, B. Guilhabert, G. Tsiminis, G. A. Turnbull, I. D. W. Samuel, N. Laurand, E. Gu, and M. D. Dawson, “Micro-LED pumped polymer laser: A discussion of future pump sources for organic lasers,” *Laser Photon. Rev.*, vol. 7, no. 6, pp. 1065–1078, Nov. 2013.

[14] C. Y. Liu, S. Yuan, J. R. Dong, and S. J. Chua, “Temperature dependence of photoluminescence intensity from AlGaInP/GaInP multi-quantum well laser structures,” *J. Cryst. Growth*, vol. 268, no. 1997, pp. 426–431, 2004.

Chapter 5

White light generation

This chapter will present a proof-of-concept of white light generation using the down-converters and hybrid devices introduced earlier in the thesis. As was demonstrated before, different InGaN sources can be used. Here, an OSRAM Dragon PowerStar commercial LED was used since it presents an intrinsic bandwidth similar to CQDs, around tens of MHz, as measured and demonstrated in Chapters 2 and 3. For fast response colour-converters, such as the semiconductor platelets and BBEHP-PPV polymer, a μLED or a laser diode can be used instead [1]–[3].

Solid-state white light can be generated mainly by two distinct approaches. The most typical of these uses a blue LED with a yellow down-converting material, such as a rare-earth doped phosphor, that partially converts the blue pump photons to yellow [4]–[7]. The resulting combination creates white light. The other approach ideally uses three colours such as Red, Green and Blue (RGB) LED chips [8]–[10]. However, due to 'the green gap' (see Figure 1.1) it is difficult to match the optimum wavelengths to generate white light, making this approach difficult to implement. To increase the colour temperature a yellow phosphor can be added (thus using RGBY). In both cases, one should consider the amount of light that is absorbed and transmitted through the colour-converter materials alongside the LED's efficiency droop, since an uneven and unstable power conversion efficiency will lead to different colour temperature [11]. Apart from this, heat management issues can compromise the light quality since each material device structure behaves differently resulting in an emission shift across the visible spectrum. Typical spectra for both configurations are presented in Figure 5.1.

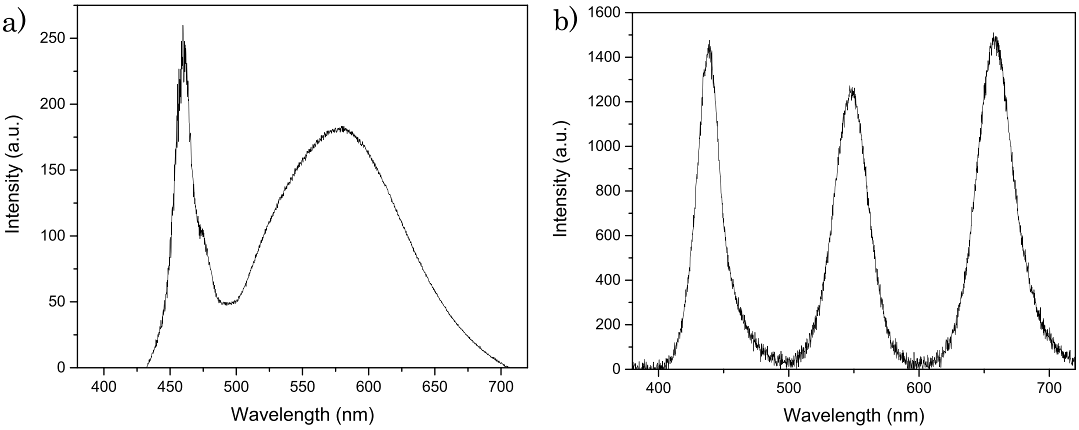

Figure 5.1 – Emission spectrum from a) a blue LED with a yellow phosphor and b) an RGB LED combination.

The spectral response of the following devices was measured using an Ocean Optics USB4000 spectrometer. For these measurements, given that the spectrometer's CCD presents a different sensitivity at different wavelengths, it was initially calibrated. To do this, a white-light calibration lamp, Ocean Optics HL-2000-CAL, was used. From the spectral response one can determine the CIE coordinates that are used as a universal reference across different systems [12]. They express how the human eye experiences light in the visible spectrum, through the tristimulus values X, Y and Z [13]. These values are determined using expressions 5.1-5.3:

$$X = \int_{380}^{780} I(\lambda)\bar{x}(\lambda)d\lambda \tag{5.1}$$

$$Y = \int_{380}^{780} I(\lambda)\bar{y}(\lambda)d\lambda \tag{5.2}$$

$$Z = \int_{380}^{780} I(\lambda)\bar{z}(\lambda)d\lambda \tag{5.3}$$

where $I(\lambda)$ is the experimentally measured spectral distribution and $\bar{x}(\lambda)$, $\bar{y}(\lambda)$ and $\bar{z}(\lambda)$, the standard CIE colour matching functions that describe the chromatic response of the observer. From this, the coordinates are then determined using expressions 5.4-5.6. Typical CIE colour plots are presented in Figure 5.5 and Figure 5.9.

$$x = \frac{X}{X + Y + Z} \tag{5.4}$$

$$y = \frac{Y}{X + Y + Z} \qquad (5.5)$$

$$z = \frac{Z}{X + Y + Z} \qquad (5.6)$$

In order to acquire the CIE coordinates and spectral response from both devices, the setup described in Chapter 2 was used.

The combination of light from a GaN LED with the emission from different colloidal quantum dots is presented first, followed by the hybrid device (μLED with capillary bonded III-V semiconductor) with a thin film of BBEHP-PPV polymer.

5.1 Commercial LED with colloidal quantum dots

White-light can be created by the combination of the studied red and green colloidal quantum dots with an off-the-shelf blue LED (OSRAM Dragon PowerStar). As seen in Figure 5.1b*,* in order to have white light one should aim to achieve a 1:1:1 ratio between the RGB colours. This means the colour-converters should present similar relative efficiency and absorption. Unfortunately, as can be seen by reference to the data presented in Chapter 3 for these samples, this was not possible to achieve due to their intrinsic properties. This issue was addressed by controlling the amount of blue excitation light going simultaneously through both samples. To do so, the less efficient green sample was partially bonded onto a 20 x 20mm^2 cover glass with the best red sample, and placed after the first set of aspheric lenses. By playing with the pump's focal point and its relative position, it was possible to tune the amount of light that was effectively going through the samples to be converted and the light going straight to the spectrometer. The converted light was then collected by another set of aspheric lenses, with NA of 0.61 and a diameter of 45 mm, followed by a 40x microscope lens, NA of 0.75, to couple the light into the spectrometer's optical fibre. For illustration, a schematic and a picture with the set-up and the samples being pumped with a μLED can be seen in Figure 5.2.

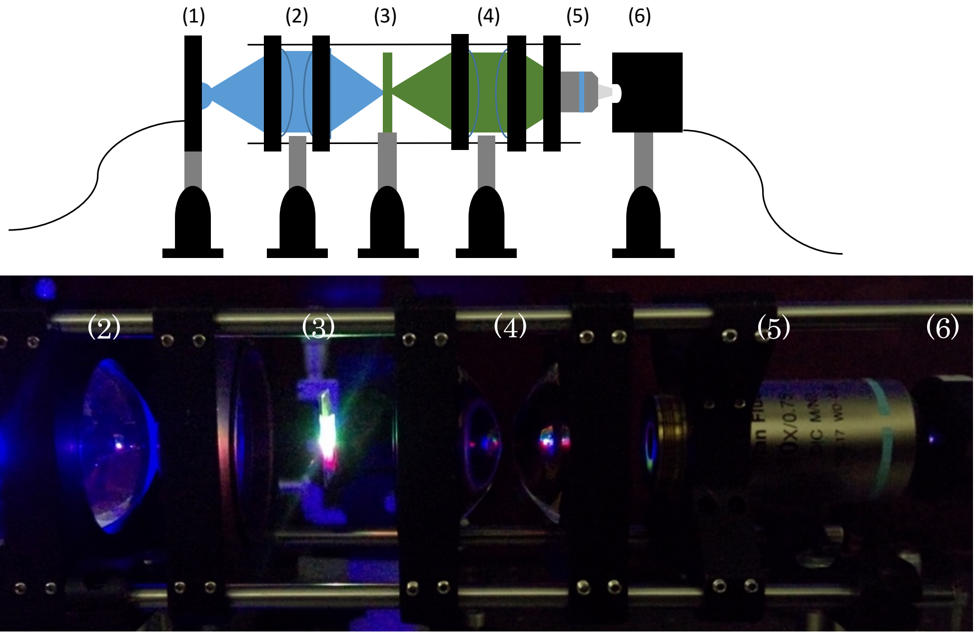

Figure 5.2 – Illustration and photograph of the set-up for white light generation with a commercial LED and the red and green colloidal quantum dot samples. (2) and (4) refer to the set of aspheric lenses, (1) to the optical source, (3) to the colour-converters, (5) to the microscope lens and (6) to the photoreceiver.

By changing the position of the glass cover coated with the bonded colour-converter quantum dots it is possible to tune the white light colour temperature, a parameter that is expressed in Kelvin, *K*. The colour temperature with a higher blue contribution is usually described as 'cool colour' – and is over 5000K – whilst colour temperature below that, ranging from yellowish to reddish wavelengths, is described as warm colour. Figure 5.3 presents spectra from three different colour temperatures from the same source. This was achieved by adjusting the ratio of each wavelength that generates white light.

From the presented spectral power distribution, and using the equations presented above, it is possible to determine the tristimulus values used to determine the CIE colour-space coordinates. In this particular case the coordinates were determined using the software Ocean Optics SpetraSuite that runs with the Ocean Optics spectrometer. The correlation between the spectra from Figure 5.3 and the colour-space is presented in Figure 5.5. As depicted, in the presented cases the colour-temperature can vary between ~5000K up to ~6000K.

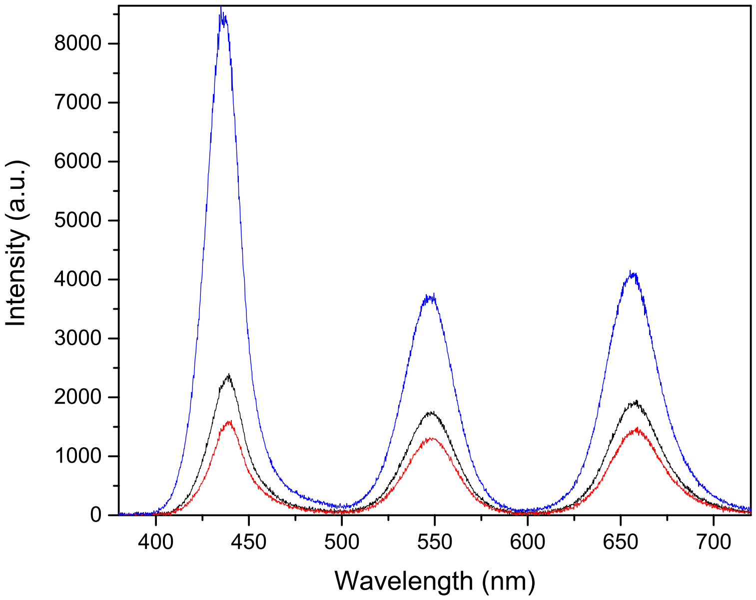

Figure 5.3 – Emission spectra of blue, green and red light from the commercial LED and the colloidal quantum dots respectively.

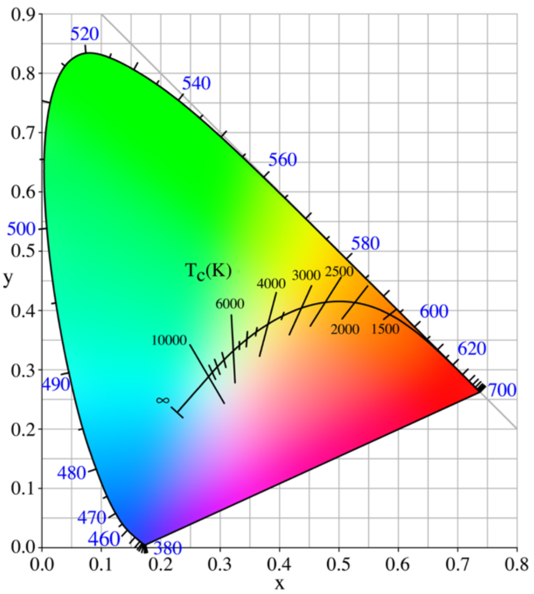

Figure 5.4 – CIE colour space displaying light sources at different colour-temperature [14].

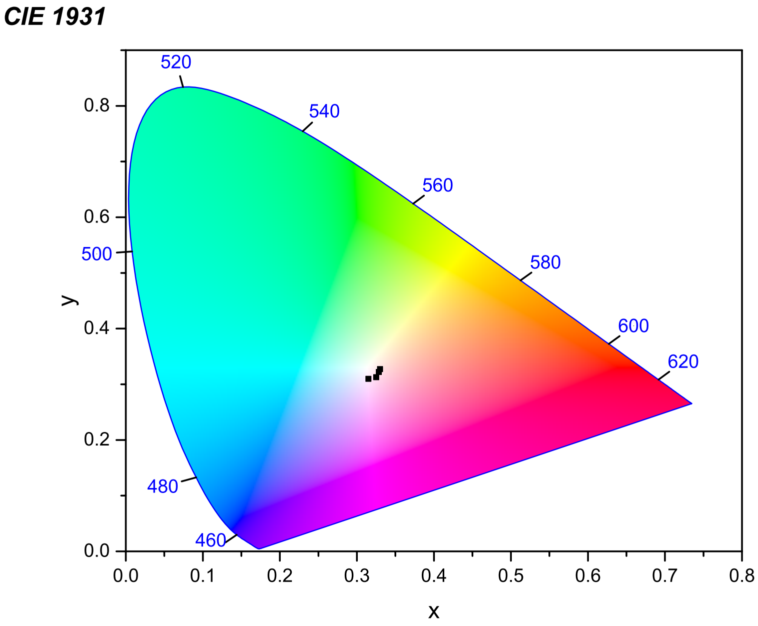

Figure 5.5 – CIE colour space for the commercial GaN LED plus red and green colloidal quantum dots configuration.

This approach proved interesting to generate white light. However, it needs further improvements since the quantum dots present different efficiencies and absorptions for the same weight ratios making it difficult to achieve a spectral ratio of 1:1:1. Another issue comes from the scattering of blue light from the source. In ideal conditions all the emitted light should go through the down-converting material.

In order to create a proof-of-concept device capable of offering a more robust approach, an alternative configuration incorporating the colour-converter materials onto the LED package was conceived. This used a multi-well mould and integration with a commercial LED as illustrated schematically in Figure 5.7a. Depending on the desired final colour and application, the mould can have different sizes and spatial distributing of the wells. For a standard white light, a mould with only two wells can be used (Figure 5.7c), each well being filled with two or more down-converter materials.

To demonstrate this approach, a PDMS polymer was used to create the wells due to its easy fabrication and manipulation. However, a better material for the mould fabrication would be a photoresist, like SU-8. This is because the quantum dot colour-converters are processed using a solvent solution, as explained in Chapter 4, which may affect the PDMS structure while not dry. Furthermore, the

SU-8 has better heat dissipation, with thermal conductivity around 0.3W/mK [15], than PDMS, which presents a thermal conductivity of ~0.15W/mK [16]. An additional consideration, in order to avoid multiple reflections and scattering at the various surfaces, is that the materials used should have similar refractive indices.

The multi-well mould designed for this device was fabricated using four small squares of glass with dimensions of 5 x 5 mm^2 and ~1.25 mm thick which were used to define the layout of the wells. In addition, a bigger glass square to simulate the thickness and size of the commercial LED packaging was used as well. After cleaning the glass squares, the largest one was placed onto an aluminium dish and the PDMS solution poured in until it was covered and left to dry. Afterwards, the other four small glasses were laid on top of the biggest glass piece and more PDMS was poured in until the sides of the small glass pieces were covered. A schematic of the process is presented in Figure 5.6. In the schematic, step 1 shows the placement the glass square that mimic the commercial LED die into a Petri dish. Step 2 shows the pouring of a polymer such as PDMS until a thin layer of polymer is achieved on top of the glass. In step 3, and after allowing some time to dry the polymer, the smaller platelets to create the wells to be filled by the colour-converters were placed on top of the PDMS. Again, the PDMS was poured into the Petri dish to form the wells. In step 4, the finished mould was then removed from the Petri dish and all the glass pieces extracted leaving behind open vacancies. At this stage, the mould can be placed on top of the LED die and filled with the desired colour-converter concentrations.

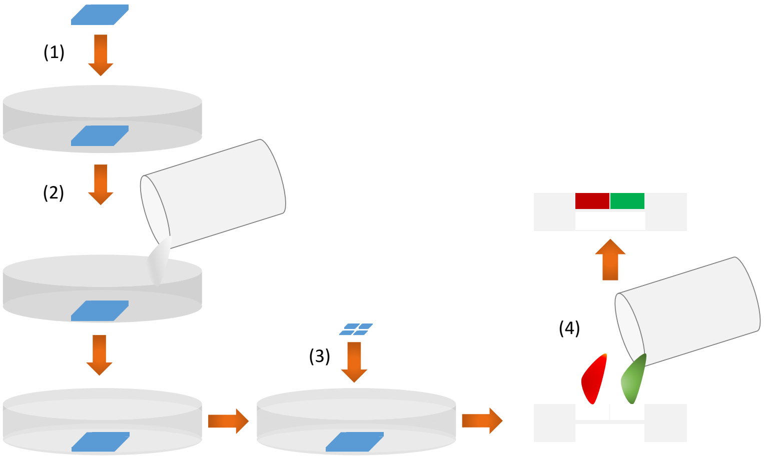

Figure 5.6 – Schematic showing the fabrication process of the PDMS moulds.

The PDMS solution was made by the combination of two silicon rubber compounds, SSR1V615A and SSRTV615B, at a ratio of 10:1.

Figure 5.7b-d, present the result of this approach for the integration of colloidal quantum dots, or other colour-converters, in PMMA using a PDMS mould onto a commercial LED.

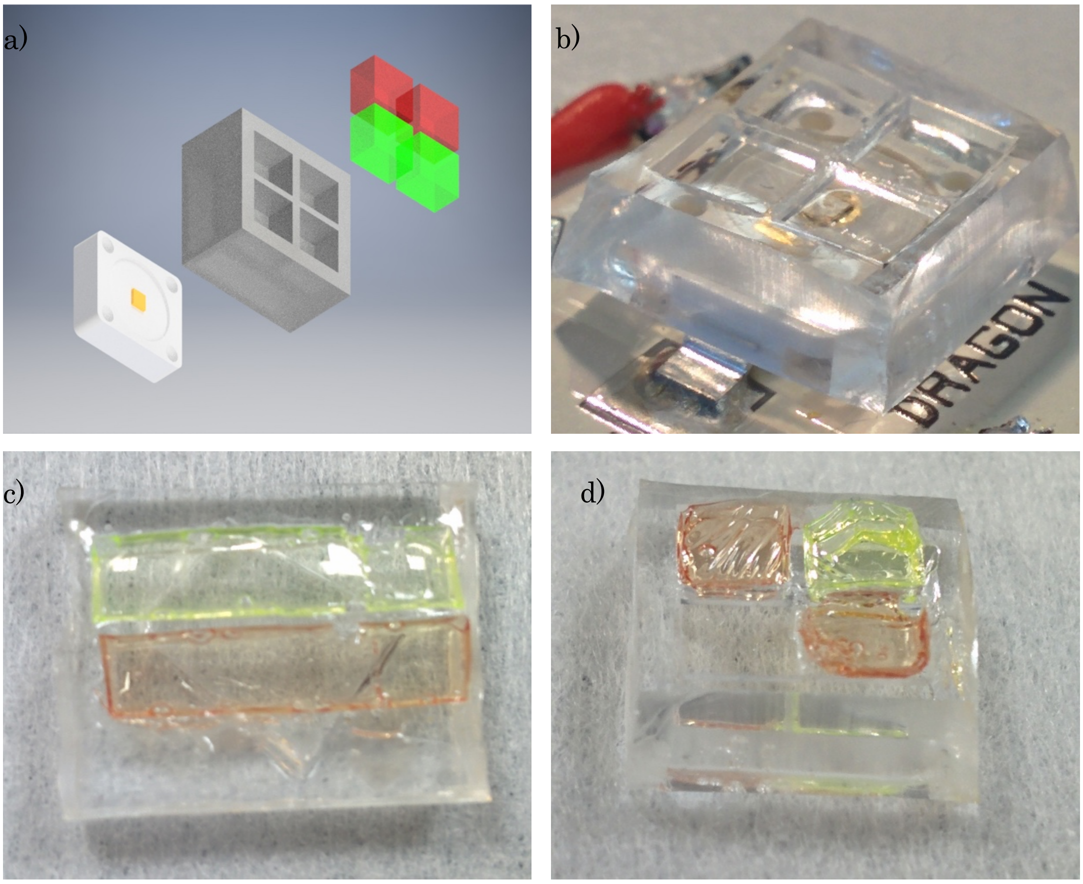

Figure 5.7 – a) PDMS mould schematic for integration onto a commercial LED, b) square PDMS mould integrated on a commercial LED, c) and d) proof-of-concept PDMS moulds filled with colloidal quantum dots.

This white-light approach could present an alternative for white-light illumination based on phosphors used in visible light communications. As demonstrated in Chapter 3, the colloidal quantum dots can be modulated up to ~27 MHz providing maximum data rates up to 500 Mbit/s. However, the main drawback in this configuration is the light source, with a limited maximum bandwidth of 11 MHz as demonstrated in Chapter 2, Figure 2.13. In order to address this limitation a laser diode or a µLED could be used.

5.2 Hybrid device for white light (GaN μLED + III-V platelet + BBEHP-PPV)

The second approach coupled a hybrid device (based on the III-V AlInGaP epitaxial platelet as presented in Chapter 4) and a thin BBEHP-PPV film (Chapter 3). The fabrication process of the film uses similar steps as was described for the CQDs. The BBEHP-PPV that is originally in a form of powder was mixed with chloroform in order to achieve a concentration of 10 mg/mL and left to stir. After achieving a uniform dispersion, PDMS was added to obtain a 4% weight ratio with the polymer. The solution was then left to stir for several days. The mixed solution can then be spin-coated or drop-coated onto a glass slide or a Petri dish. Due to the space constraint on the μLED chip, the BBEHP-PPV film was bonded initially onto a cover slide. To measure the system's overall spectral power distribution two pairs of aspheric lenses were used – ACL4532-A with NA of 0.61. They were used to collimate and then focus the light onto the green colour-converter and then from the colour-converter onto a 40x microscope lens with NA of 0.75. The microscope lens was used to couple the light into the spectrometer's optical fibre as depicted in Figure 5.8.

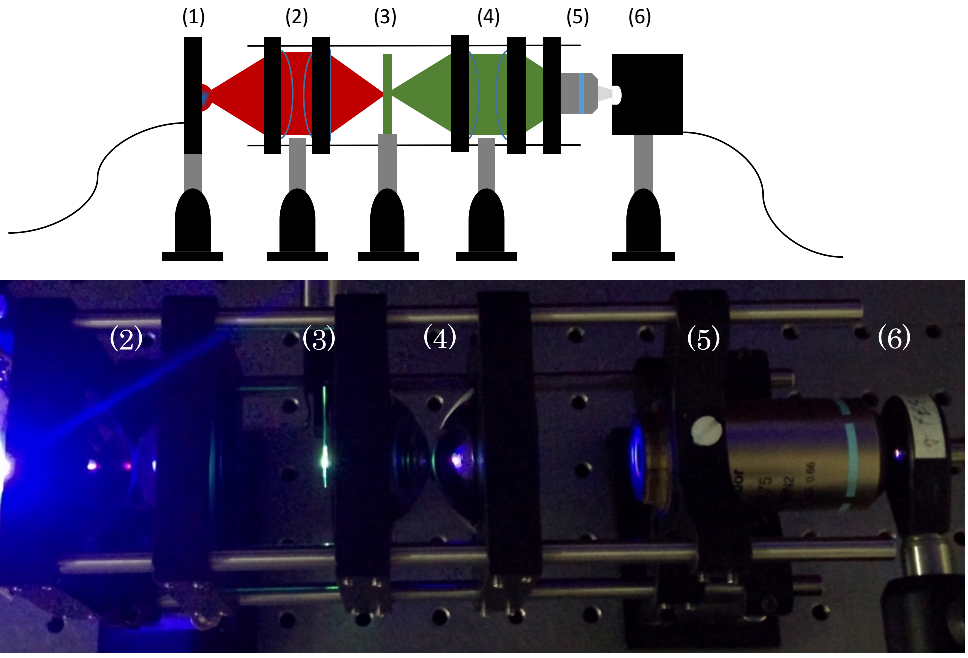

Figure 5.8 – Illustration and photograph of the set-up for white light generation combining a hybrid LED using the III-V platelet and the BBEHP-PPV film. (2) and (4) refer to the set of aspheric lenses, (1) to the optical source, (3) to the colour-converters, (5) to the microscope lens and (6) to the photoreceiver.

After aligning and calibrating the system, the spectral power response was acquired. The CIE colour space obtained for this configuration is presented in Figure 5.9.

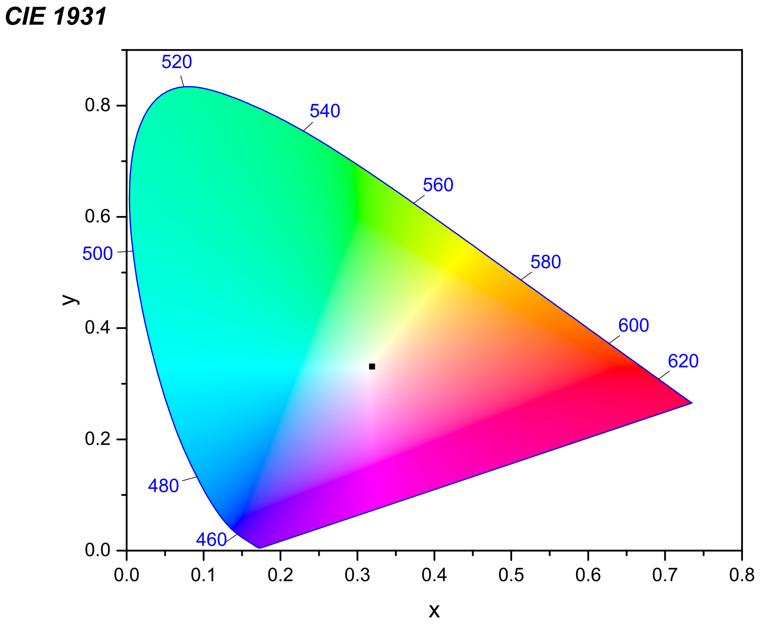

Figure 5.9 – CIE colour space for the μLED plus III-V platelet and BBEHP-PPV.

The ideal solution here would be the direct integration of both colour-converters on the μLED's sapphire window. However, and as seen already in Chapter 4, the μLEDs do not present a good cooling system, meaning most of the heat will dissipate through the down-converter materials. This will be an important limitation factor in their performance. A possible approach to address this could be the bonding of the desired colour-converters on a diamond platelet and using a lens, *e.g.* diamond or sapphire lens, to cover them. In this configuration, both materials would be encapsulated making it more reliable since the heat is dissipated through the diamond/sapphire. Besides, this 'sandwiched' configuration would act as protecting layer increasing the material's lifetime. A tentative sketch of this approach is presented below, see Figure 5.10.

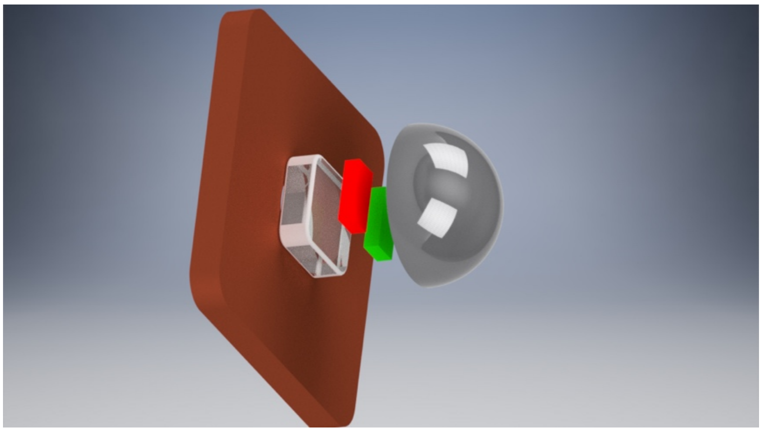

Figure 5.10 – Schematic depicting the integration of colour-converters onto a μLED followed by the bonding of a diamond or sapphire lens/platelet.

5.3 Summary

In the present chapter two approaches to achieve white light using the colour-converters used throughout this work were discussed. Both of them combine red, green and blue wavelengths. The first approach combines the blue electroluminescence of a commercial LED with the red and green photoluminescence from red and green CQDs. Here, due to the different absorption and relative efficiencies of CQDs, different weight ratios of colour-converters were used. Since the green CQDs present the best efficiency the lowest CQDs/PDMS weight ratio of 1% was used along with the best performing ratio of red CQDs/PDMS presented in Chapter 3 of 7%. By controlling the amount of blue light onto the colour-converters it is possible to generate white light as depicted in Figure 5.6. In addition, a possible integration schematic was presented.

The second approach used a hybrid LED, which results from the combination of a μLED with a red emitting platelet based on the III-V semiconductor. To generate the missing green wavelength BBEHP-PPV was used. Here, white light was also achieved. A further optimisation of this system was presented.

References

[1] D. Tsonev, H. Chun, S. Rajbhandari, J. J. D. Mckendry, S. Videv, E. Gu, M. Haji, S. Watson, A. E. Kelly, G. Faulkner, M. D. Dawson, H. Haas, and D. O. Brien, "A 3-Gb / s Single-LED OFDM-Based Wireless VLC Link Using a Gallium Nitride μLED," *IEEE Photonics Technol. Lett.*, vol. 26, no. 7, pp. 637–640, 2014.

[2] S. Watson, M. Tan, S. P. Najda, P. Perlin, M. Leszczynski, G. Targowski, S. Grzanka, and A. E. Kelly, "Visible light communications using a directly modulated 422 nm GaN laser diode.," *Opt. Lett.*, vol. 38, no. 19, pp. 3792–4, Oct. 2013.

[3] K. A. Denault, M. Cantore, S. Nakamura, S. P. Denbaars, and R. Seshadri, "Efficient and stable laser-driven white lighting," *AIP Adv.*, vol. 3, no. 7, p. 72107, 2013.

[4] M. H. Crawford, J. J. Wierer, A. J. Fischer, G. T. Wang, D. D. Koleske, G. S. Subramania, M. E. Coltrin, J. Y. Tsao, R. F. Karlicek, and J. Rensselaer, "Solid-State Lighting: Toward Smart and Ultra-Efficient Materials, Devices, Lamps and Systems," vol. 3, 2013.

[5] C. Yeh, Y. Liu, and C. Chow, "Real-time white-light phosphor-LED visible light communication (VLC) with compact size," *Opt. Express*, vol. 21, no. 22, pp. 26192–26197, 2013.

[6] J. Tuo, H. Shams, and B. Corbett, "Visible Light Communication by Using Commercial Phosphor based White LEDs," *IET Irish Signals Syst. Conf. (ISSC 2012)*, pp. 101–101, 2012.

[7] J. Vucic, C. Kottke, S. Nerreter, K. Habel, A. Büttner, K. Langer, and J. W. Walewski, "125 Mbit/s over 5 m Wireless Distance by Use of OOK-Modulated Phosphorescent White LEDs," *ECOC*, no. 1, pp. 9–10, 2009.

[8] N. Fujimoto and S. Yamamoto, “The Fastest Visible Light Transmissions of 662 Mb/s by a Blue LED, 600 Mb/s by a Red LED, and 520 Mb/s by a Green LED based on Simple OOK-NRZ Modulation of a Commercially Available RGB-type White LED using Pre-emphasis and Post- equalizing Techniques,” *ECOC*, pp. 3–5, 2014.

[9] Y. Wang, Y. Wang, N. Chi, J. Yu, and H. Shang, “Demonstration of 575-Mb/s downlink and 225-Mb/s uplink bi-directional SCM-WDM visible light communication using RGB LED and phosphor-based LED.,” *Opt. Express*, vol. 21, no. 1, pp. 1203–8, Jan. 2013.

[10] T. Komiyama, K. Kobayashi, K. Watanabe, T. Ohkubo, and Y. Kurihara, “Study of Visible Light Communication System Using RGB LED Lights,” *SICE*, 2011.

[11] A. Tsiatmas, P. M. J. Baggen, F. M. J. Willems, J.-P. M. G. Linnartz, and J. W. M. Bergmans, “An Illumination Perspective on Visible Light Communications,” *IEEE Commun. Mag.*, vol. 52, no. 7, pp. 64–71, 2014.

[12] K. Ansari, S. H. Amirshahi, and S. Moradian, “Recovery of reflectance spectra from CIE tristimulus values using a progressive database selection technique,” *Color Technol.*, no. 122, pp. 128–134, 2006.

[13] E. F. Schubert, *Light-Emitting Diodes*, 2nd ed. Cambridge University Press, 2006.

[14] Wikimedia, “CIE 1931,” 2015. [Online]. Available: https://commons.wikimedia.org/wiki/File:PlanckianLocus.png.

[15] Microchem, “SU-8 Permanent Epoxy Negative Photoresist,” *SU-8 datasheet*. [Online]. Available: http://www.microchem.com/pdf/SU-82000DataSheet2000_5thru2015Ver4.pdf.

[16] MIT, “Material Property Database,” *Material Property Database*. [Online]. Available: http://www.mit.edu/~6.777/matprops/pdms.htm.

Chapter 6

Conclusions and outlook

The work presented in this thesis focused on the characterisation and development of novel materials to be used as solid state light down-converters for GaN LED and LD visible light communications. Previous work used efficient rare-earth phosphors for VLC at expense of slow modulation speeds and a power penalty that impairs the applicability to telecommunication system. The most significant development of this study was the incorporation of fast colour-converter such as BBEHP-PPV, colloidal quantum dots, II-VI and III-V semiconductors onto solid-state light sources to achieve faster modulation speeds and tuneable colour temperature for white-light generation. The main limitation of the presented approaches is the lack of heat dissipation that impaired the efficiency and response of the down-converters and ultimately the optical sources. Using hemispherical lenses made of sapphire and diamond did not provide a conclusive outcome as heat spreaders and beneficial use in newer devices for colour-conversion. Further tests need to be carried out to assess the best configuration/approach in order to passively cool the presented devices. Nevertheless, it was shown that the integration of organic semiconductors and colloidal quantum dots onto a polymeric matrix offers a new pathway to integrate them on any desired optical source. Furthermore, this integration presented an increase of photostability and lifetime which is still an important limitation for these materials. II-VI and III-V epitaxial structures were successfully implemented onto different substrates demonstrating the high flexibility of using this kind of structures for colour-converters.

Chapter 1 provided a general insight into the physical properties and characteristics of the materials used throughout this thesis. It started by explaining the motivation behind the study of the materials selected as down-converters referring to the fact of low efficiency in the green/yellow region of the visible spectrum, known as the green gap, and the efficiency droop which impairs the light-emitting diode (LED) performance. Regardless, the huge development of solid-state lightning has allowed this device technology to mature to the point where advanced visible LEDs are now starting to pervade our daily life. This is due to their high electrical-to-optical efficiency, low power consumption and long lifetime as well as their compatibility for integration, making them greatly superior to the typical light bulbs that have been used for lighting so far [1]. An introduction to typical *p-n* diodes and heterostructures was made. The physics and principal processes behind the fluorescence phenomena of the down-converters used in this thesis were also introduced here.

Chapter 2 presented all the optical setups and the optoelectronic tests carried out to fully characterise the optical sources and the colour-converter materials. Key features to compare the down-converters' performance were discussed, *e.g.* the absorption and relative efficiency. As explained, the frequency response of the LEDs and the colour-converters are intrinsically related to the carrier recombination lifetimes. It can be determined using techniques such as time-domain and frequency-domain measurements. An insight into the working principles of both measurements was performed. In the first case, the working principle behind the TCSPC equipment and the way the lifetime is calculated was discussed. The frequency-domain experiment and the required calculations to determine the carrier lifetime was presented as well. The lifetimes obtained from both experiments are within the same range indicating both approaches are valid for lifetime determination. However, frequency-domain experiments tend to be used more often as this is required to know the colour-converters frequency response curve.

Several GaN-based optical sources were used to characterise the colour-converters. All of them showed peak emission centred around 450 nm. The commercial LED was driven up to 300 mA which corresponds to around 110 mW of excitation power and a bandwidth of 11 MHz. For free-space and nanomembrane integration, several μLEDs were used. Depending on the pixel size, they were driven up to 200 mA achieving optical powers up to 17 mW. As explained, the bandwidths are current dependent and can be attributed to the reduced carrier lifetime in the active region at higher carrier density. Thus, small pixel present higher frequency responses. Here, the maximum achieved bandwidth was 250 MHz. The use of a blue commercial laser diode as an optical source was studied as well. The maximum achieved forward optical power was 100 mW presenting bandwidths above 1.4 GHz (limited by the response of the photoreceiver).

Chapter 3 introduced the different processing steps and the results from the red and green colloidal quantum dots and the organic semiconductor, BBEHP-PPV. The integration of such colour-converters into a polymeric matrix allowed an increase of their photostability and lifetimes. Besides, the polymer's intrinsic properties such as high flexibility, high surface adhesion and repeatability, allowed the creation and new ways to incorporate such down-converters onto InGaN LEDs. Different weight ratios of quantum dots and BBEHP-PPV with the host matrix were studied. Relative efficiencies up to 9% and 1% for the green and red quantum dots respectively, were achieved. Bandwidths up to 26 MHz were measured with the best performing samples achieving free space communications at up to 500 Mbit/s. The different efficiencies and bandwidths between both types of quantum dots were related with the alloy ratios CdS_xSe_{1-x} of the core of the nanoparticles. Such colour-converters showed very promising results achieving higher bandwidths and modulation speeds than the standard phosphors.

In Chapter 4 the epitaxial structures and their incorporation onto the sapphire window of GaN μLEDs were discussed.

Initially, the integration of a II-VI epitaxial structure onto the μLED's sapphire window was presented. The structure consists of nine ZnCdSe quantum wells with CdMgZnSe barriers designed to emit at 540 nm. It was found that the quantum wells absorb around 85% ± 1% of the pump light presenting external efficiencies around 1% ± 0.1%. At maximum driving power, 37 μW of converted optical power was measured. The low converted power results from the fact the membrane structure used was not primarily designed for colour-conversion, but rather as a VECSEL (Vertical External Cavity Surface Emitting Laser). Besides, the high refractive index contrast between the membrane material and air (3.4:1) resulted in a significant amount of waveguided light, which was then lost through reabsorption and edge emission. Improved epi-layer design of the membrane and implementation of light extraction schemes would improve this value significantly. Nevertheless, the membrane presented intrinsic responses up to 145 MHz. The hybrid response achieved bandwidths up to 51 MHz. Here, the overall response was limited by the frequency response of the underlying pixels. Faster bandwidths, and consequently modulation speeds, would allow this device to present much higher responses.

III-V nanomembranes were also studied and integrated onto the sapphire window of a μLED. The chip in this device had several pixels of four different sizes, 50 x 50 μm^2, 75 x 75 μm^2, 100 x 100 μm^2 and 150 x 150 μm^2 rather than pixels of 100 x 100 μm^2 as was used for the II-VI integration. The III–V structure consists of six GaInP quantum wells with AlGaInP barriers and was designed to emit at 640 nm. The forward power conversion efficiency was found to be close to 1.2%. However, due to the effect of heat resulting from the μLED operation there was a noticeable power roll-over influencing the nanomembrane efficiency. In order to supress this issue, a hemispherical lens of sapphire was capillary-bonded onto the platelet. Spectral response tests showed the lens did not provide a good heat dissipation medium but did help to increase the extraction efficiency, reaching in some cases improvements up to 98%. The III-V intrinsic and the overall device response were measured reaching bandwidths up to 320 MHz and 170 MHz, respectively. PAM and OFDM tests were performed being the maximum achieved data link transfer of 870 Mbit/s.

Both proof-of-principle devices offer a new pathway to fast-response and robust colour-conversion system with potential application in VLC.

Chapter 6 presents some work based on the previous devices and colour-converters to generate white light. Here, a commercial LED was used to optically pump red and green quantum dots at different weight ratios. The combination of the three colours provided a white-colour temperature emission.

A white-colour was achieved as well by the combination of a BBEHP-PPV film with the III-V hybrid device presented previously.

6.1 Future work

The use of solid-state lighting and ultimately colour-converters in visible light communications should present very high external efficiencies, since the light provided from this system still needs to be used for illumination, and the devices should present high frequency responses in order to be able to transmit the maximum information possible. At the moment, the materials studied present very high bandwidths and data transmission but low external efficiencies. Several approaches could be studied to address this issue. An anti-reflective coating could be designed to reduce the reflections onto the colour-converter material. The application of higher refractive substrates in between the colour-converter and air, similar to that presented here, can also help the extraction efficiency. Besides, if properly designed and implemented this can help to improve the efficiency droop resulting from the poor heat spreading.

In the case of colour-converter embedded onto a solution-processable polymeric matrix, this can be designed in order to have a periodic grating or a photonic crystal on its surface in order to scatter light by employing a soft-lithography approach. The same principle could be used for the epitaxial membranes. The structure could be engraved onto the buffer layer or be implemented during the epitaxial semiconductor growth. However, the implementation of such features would increase the complexity of the design and the growth of such a device.

Following the same principle depicted in Figure 5.5 where a polymeric solution based on quantum dots was used to fill some wells in order to create white-light, wells etched onto the sapphire windows of the μLED could be designed to accommodate several colour-converters or a single colour-converter per pixel. This would create the possibility of having a multicolour chip where a single pixel could be down-converted to one or several colours whilst at the same time opening new possibilities for different telecommunications systems where different pixels / chips would work as different data carrier channels. Depending on the size of the wells, the colour-converters could be placed onto the desired position by using a contact printer, an Ink-Jet printer or, in the case of single colour chip by a spin- or drop-coating technique. Such approach would allow the miniaturisation of a down-converter device to the actual size of the μLED. However, heat spreading throughout the sapphire window would influence the efficiency of the colour-converter, and in this case active heat dissipation would be required.

The integration of optoelectronic devices on foreign substrates by a technique called transfer-printing where micro-fabricated LEDs or nanomembranes are detached from their growth wafer and placed onto a desirable substrate offer another interesting approach onto the integration of colour-converters with InGaN optical sources [2], [3]. Using such technique, the membranes could be placed virtually on any optical source window with the advantage of providing a careful placing.

Finally, by designing other nanomembrane structures using AlGaInP or InGaN material systems or even using different CQDs alloyed configurations with narrow emissions, it should be possible in principle to extend the wavelength coverage across the visible spectrum offering a new pathway for white light generation and Wavelength-Division Multiplexing (WDM) systems, in which each wavelength can be used for data transmission.

References

[1] C. W. Chow, C. H. Yeh, Y. Liu, and Y. F. Liu, “Digital Signal Processing for Light Emitting Diode Based Visible Light Communication,” *IEEE Photonics Soc. Newletter*, pp. 9–13, 2012.

[2] A. Carlson, A. M. Bowen, Y. Huang, R. G. Nuzzo, and J. A. Rogers, “Transfer printing techniques for materials assembly and micro/nanodevice fabrication,” *Adv. Mater.*, vol. 24, no. 39, pp. 5284–5318, 2012.

[3] T. Kim, R. Kim, and J. A. Rogers, “Microscale Inorganic Light-Emitting Diodes on Flexible and Stretchable Substrates,” *IEEE Photonics J.*, 2011.

Publications

J. M. M. Santos, B. E. Jones, P. J. Schlosser, S. Watson, J. Herrnsdorf, B. Guilhabert, J. J. D. McKendry, J. De Jesus, T. a Garcia, M. C. Tamargo, A. E. Kelly, J. E. Hastie, N. Laurand, and M. D. Dawson, “Hybrid GaN LED with capillary-bonded II–VI MQW color-converting membrane for visible light communications,” *Semicond. Sci. Technol.*, vol. 30, no. 3, p. 035012, 2015.

J. M. M. Santos, S. Rajbhandari, D. Tsonev, H. Chun, B. Guilhabert, A. B. Krysa, A. E. Kelly, H. Haas, D. C. O’Brien, N. Laurand, and M. D. Dawson, "Visible light communication using InGaN optical sources with AlInGaP nanomembrane down-converters," Opt. Express 24, 10020 (2016).

J. M. M. Santos, S.Rajbhandari, H. Jun, B. Guilhabert, M. Leitão, A. E. Kelly, D. C. O’Brien, N. Laurand, and M. D. Dawson, “Quantum Dots as colour-converters for visible light communications and solid-state white light,” ***(advanced draft)***.

Conference Presentations

J. M. M. Santos, B. E. Jones, P. J. Schlosser, S. Watson, J. Herrnsdorf, B. Guilhabert, J. J. D. McKendry, J. De Jesus, T. a Garcia, M. C. Tamargo, A. E. Kelly, J. E. Hastie, N. Laurand, and M. D. Dawson, “Hybrid GaN LED with capillary-bonded II-VI MQW colour-converting membrane for Visible Light Communications”, Oral presentation at ICOOPMA, Leeds, UK, July 2014

J. M. M. Santos, B. E. Jones, P. J. Schlosser, J. Herrnsdorf, B. Guilhabert, J. De Jesus, T. a Garcia, M. C. Tamargo, J. E. Hastie, N. Laurand, and M. D. Dawson, “Hybrid InGaN LEDs with capillary-bonded MQW colour-converting membranes”, Oral presentation at IPC 2014, San Diego, USA, October 2014

J. M. M. Santos, S. Watson, B. Guilhabert, P. J. Schlosser, A. Krysa, A. Kelly, N. Laurand, and M. D. Dawson, "Functional nanomembrane for visible light down-conversion", Oral presentation at EOSLE 2015, Munich, Germany, June 2015

J. M. M. Santos, S. Watson, B. Guilhabert, A. Krysa, A. Kelly, N. Laurand, and M. D. Dawson, "MQW nanomembrane assemblies for visible light communications", Oral presentation at IPC 2015, Washington DC, USA, October 2015

J. M. M. Santos, M. Leitao, C. Foucher, S. Rajbhandari, D. Vithanage, B. Guilhabert, G.A. Turnbull, I. D. W. Samuel, D. O'Brien, N. Laurand, and M. D. Dawson, "Fast colour conversion of InGaN sources using semiconductor nanocrystals", Oral presentation at UKNC 2016, Cambridge, UK, January 2016

J. M. M. Santos, M. Leitao, C. Foucher, S. Watson, A. E. Kelly, S. Rajbhandari, H. Chun, H. Haas, G. Faulkner, D. O'Brien, N. Laurand, and M. D. Dawson, "Colloidal quantum dots color converters for visible light communications", Oral presentation at IPC 2016, Hawaii, USA, October 2016

Publications

Semicond. Sci. Technol. **30** (2015) 035012 (7pp) doi:10.1088/0268-1242/30/3/035012

Hybrid GaN LED with capillary-bonded II–VI MQW color-converting membrane for visible light communications

Joao M M Santos[1], Brynmor E Jones[1], Peter J Schlosser[1], Scott Watson[2], Johannes Herrnsdorf[1], Benoit Guilhabert[1], Jonathan J D McKendry[1], Joel De Jesus[3], Thor A Garcia[4], Maria C Tamargo[4], Anthony E Kelly[2], Jennifer E Hastie[1], Nicolas Laurand[1] and Martin D Dawson[1]

[1] Institute of Photonics, SUPA, University of Strathclyde, 106 Rottenrow, Glasgow, G4 0NW, UK
[2] School of Engineering, University of Glasgow, Glasgow, G12 8LT, UK
[3] Department of Physics, The Graduate Center and The City College of New York, CUNY, New York, NY 10031, USA
[4] Department of Chemistry, City College of New York, 138th Street and Convent Avenue, New York, NY 10031, USA

E-mail: joao.santos@strath.ac.uk

Received 26 August 2014, revised 18 December 2014
Accepted for publication 5 January 2015
Published 27 January 2015

Abstract

The rapid emergence of gallium-nitride (GaN) light-emitting diodes (LEDs) for solid-state lighting has created a timely opportunity for optical communications using visible light. One important challenge to address this opportunity is to extend the wavelength coverage of GaN LEDs without compromising their modulation properties. Here, a hybrid source for emission at 540 nm consisting of a 450 nm GaN micro-sized LED (micro-LED) with a micron-thick ZnCdSe/ZnCdMgSe multi-quantum-well color-converting membrane is reported. The membrane is liquid-capillary-bonded directly onto the sapphire window of the micro-LED for full hybridization. At an injection current of 100 mA, the color-converted power was found to be 37 μW. At this same current, the −3 dB optical modulation bandwidth of the bare GaN and hybrid micro-LEDs were 79 and 51 MHz, respectively. The intrinsic bandwidth of the color-converting membrane was found to be power-density independent over the range of the micro-LED operation at 145 MHz, which corresponds to a mean carrier lifetime of 1.9 ns.

Keywords: photonics, GaN LED, semiconductor, color-converters, visible light communications

(Some figures may appear in colour only in the online journal)

1. Introduction

Development of light-emitting diode (LED) technology is driven mainly by the need for efficient solid-state lighting, but it is also creating opportunities for new applications such as visible light communications (VLCs) [1]. VLC requires light sources that are not only efficient but also have high modulation bandwidth and are wavelength versatile. White-emitting LEDs, and color-converted LEDs in general, are typically obtained by combining blue InGaN LEDs with down-converting phosphors. This approach is effective for illumination purposes but is not well suited to VLC because of the long (μs) excited-state lifetime of phosphors. The resulting sources have modulation bandwidths limited to ~1 MHz, whereas unconverted blue InGaN-based LEDs have bandwidths of 20 MHz up to 400 MHz depending on their formats, with single-color direct-LED-emission data links at >1 Gbit s^{-1} rate having been demonstrated [2]. There is therefore a need to explore color-converting materials with shorter excited-state lifetimes to complement rare-earth phosphors. Organic semiconductors and colloidal quantum dots are potential candidates but they necessitate advanced encapsulation schemes for long-term environmental stability [3].

Here we introduce an alternative approach based on using inorganic MQW semiconductor epi-layer membranes as photo-pumped color converters for the underlying InGaN LEDs. This technology benefits from being based on all-inorganic semiconductors and therefore promises to be robust [4, 5]. It also leads to extremely compact sources, as the membrane can be integrated (as we show) by techniques such as liquid capillary bonding. There are several options for wavelength coverage across the visible spectrum with available semiconductor alloys for MQW membranes including III–V AlGaInP (yellow to red) and InGaN (green) materials and II–VI CdMgZnSe (green to orange) materials [4, 6]. As proof-of-principle of a generic approach, the hybrid LED demonstrator discussed here is obtained by capillary-bonding a 540 nm emitting, II–VI CdMgZnSe MQW membrane onto an array of 450 nm InGaN micro-size LEDs (micro-LEDs), on the sapphire side, taking advantage of the high modulation bandwidths associated with these small-sized LEDs [7]. Micro-LEDs operate in a size regime where physical characteristics that play a major role for VLC, e.g. current density, differential carrier lifetime and junction capacitance, diverge from those of conventional format broad area LEDs. This size regime firmly applies to devices with dimensions of 100 μm (as used in this work) and below, where devices can handle kA cm^{-2} of dc current density and possess significantly higher modulation bandwidths [7]. We chose II–VI materials for converters in this initial study because (i) they are readily wet etched into epitaxial membranes, (ii) they can be designed to offer coverage of the visible spectrum promising white-light generation, and (iii) they permit an alternative approach to green emission at high-modulation-bandwidth, useful for e.g. introducing coarse wavelength division multiplexing (blue and green) into optical wireless and polymer optical fiber communications.

In the following, the hybrid device fabrication and characterization methods are described in section 2. Sections 3 and 4 report and discuss, respectively, the continuous-wave (CW) and dynamic characteristics of the hybrid source.

2. Device fabrication and characterization

2.1. Device design and fabrication

The 450 nm wavelength micro-LEDs used to pump the MQW membrane were fabricated using a commercial p-*i*-n GaN LED structure grown on *c*-plane sapphire, following the procedure reported in [8]. Here, the fabricated chip is made of several $100 \times 100\,\mu$m square micro-LEDs spaced 450 μm apart, figure 1. After fabrication, the chip was placed onto a printed circuit board and wire bonded to tracks connected to SMA connectors, such that the micro-LEDs could be addressed individually.

The II–VI MQW membrane structure was grown by molecular beam epitaxy on an InP substrate and InGaAs growth buffer. It consists of nine ZnCdSe quantum wells with CdMgZnSe barriers and was designed to absorb the pump emission in-barriers. The quantum wells emit at 540 nm in a resonant periodic gain configuration for potential alternative use as a laser gain medium [9]. The InP substrate was removed by a combination of mechanical polishing and wet etch process using a solution of HCl:H$_3$PO$_4$ in a ratio of 3:1, followed by the removal of the InGaAs layer with a solution of H$_3$PO$_4$:H$_2$O$_2$:H$_2$O, in a ratio of 1:1:6 for maximum etch selectivity with the II–VI material [10]. The epi-side is fixed onto a temporary glass substrate for this step, using a wax, for mechanical support during processing. After substrate removal, the II–VI layer was transferred from the glass and capillary-bonded using deionized water onto the sapphire window of the LEDs to complete the hybrid device [11]. The resulting MQW membranes have a thickness of less than 2.5 μm, and a typical surface area of a few mm^2. Images of the hybrid device and structural membrane layout are shown in figure 1.

2.2. Experimental setups

The device was characterized in terms of optical power, emission spectrum and modulation bandwidth prior to and after membrane integration. For the power measurements, the device under test was fixed on top of an optical power meter with a 30 mm cage plate in between to enable the optional placement of an optical long-pass filter (500 nm cut-off wavelength). Hereafter, in sections 3 and 4, we refer to the micro-LED with no membrane as the ‘bare LED’, the LED with integrated membrane as the ‘hybrid micro-LED’, and the micro-LED with membrane and filter in place at detection simply as the ‘integrated MQW membrane’. Optical spectra were recorded with an Ocean Optics USB4000 Fiber Optic Spectrometer (2.5 nm resolution).

For the frequency response and modulation bandwidth measurements, a set of aspheric lenses with focal length of 32 mm and high numerical aperture (NA = 0.612) were used to collect and focus the micro-LED emission into a Femto HSA-X-S-1G4-SI fast photoreceiver (bandwidth of 1.4 GHz). The LED device was simultaneously driven with a dc bias current and a frequency-swept modulated signal (0.250 Vpp) that were combined with a wideband (0.1–6000 MHz) Bias-Tee. An Agilent HP 8753ES network analyzer was used to provide the modulation signal and to record the device frequency response as detected by the photoreceiver. The long-pass filter was placed before the detection for measurements of the integrated MQW membrane characteristics.

The intrinsic modulation bandwidth of the stand-alone membrane was also characterized as a function of the excitation power density (section 4). For this, the membrane was supported on a glass substrate and remotely pumped with a bare micro-LED. A pair of lenses was placed directly after the bare device to focus its light onto the stand-alone membrane. Further optics were used to collect the light emitted by the membrane and focus it onto the photodetector. A Coherent® BeamMaster was used to measure the micro-LED beam size incident onto the membrane surface and hence to deduce the

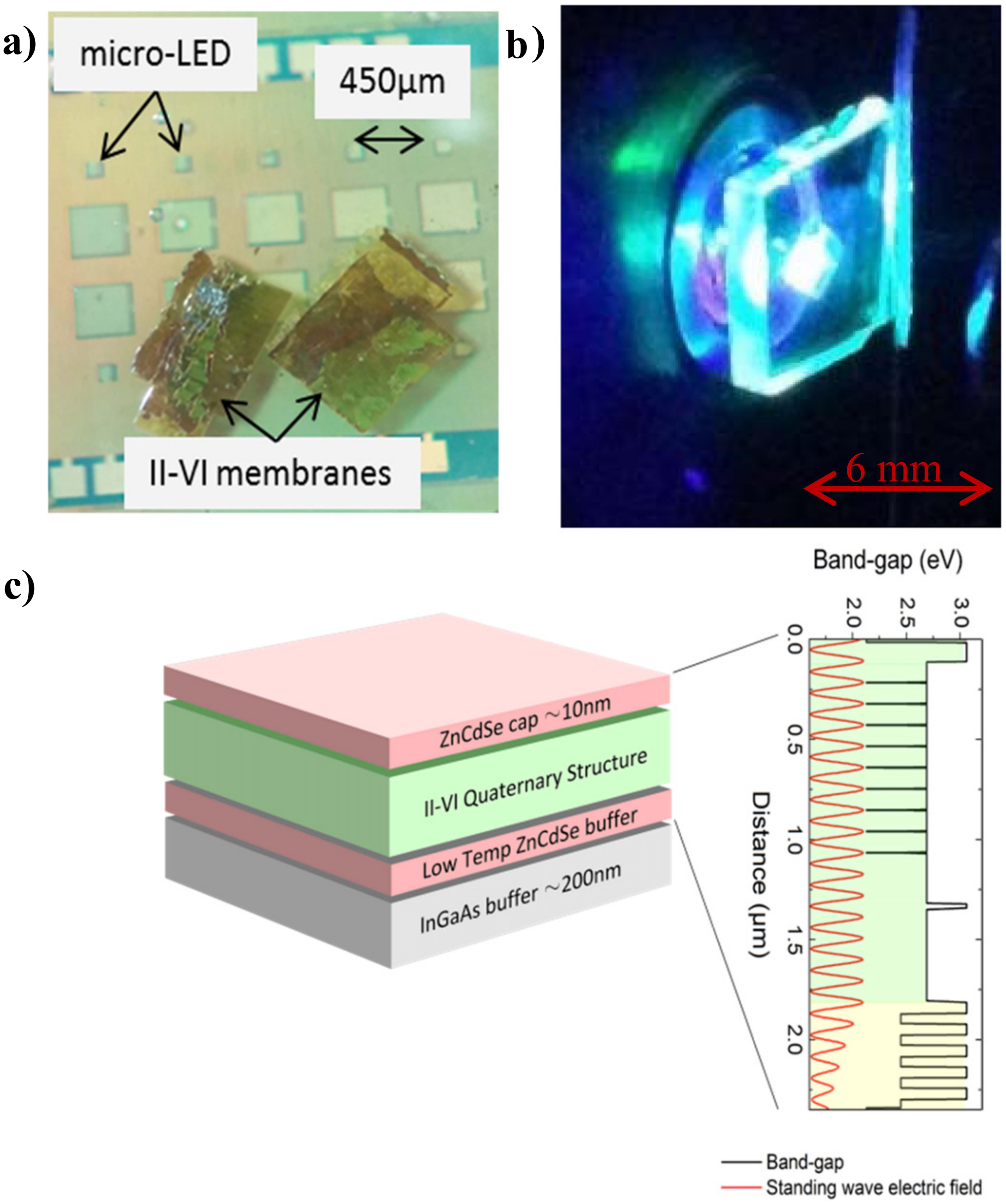

Figure 1. (a) Plan view micrograph of the hybrid device. The micro-LED pixels are the smaller elements as labeled, some of which are bonded underneath the II–VI membrane. Between the membrane and the underlying LEDs is the sapphire substrate, (b) II–VI membrane when pumped by a blue LED, (c) II–VI MQW structural design.

incident power density. The full width at half maximum (FWHM) spot-size was found to be 330 μm. The bandwidth measurement of the stand-alone membrane was otherwise as described above.

3. CW characteristics

Normalized spectral measurements for the bare micro-LED, the hybrid micro-LED and the integrate MQW membrane (i.e. the contribution of the converted light at 540 nm) are presented in figure 2. The bare micro-LED has emission centered at 445 nm. The hybrid LED spectrum shows a peak centered at 475 nm and a secondary peak at 540 nm. The emission at 540 nm comes from the light emitted by the II–VI MQW membrane. The II–VI membrane is designed to absorb 97–98% of 450 nm monochromatic light. Because of the bandwidth of the bare micro-LED spectrum (23 nm FWHM) the effective micro-LED light absorption is 85% ± 1%. The band-edge of the membrane is at around 460 nm and therefore the long-wavelength tail of the micro-LED emission is not fully absorbed, explaining the ‘apparent’ 475 nm peak in the spectrum of the integrated MQW membrane.

The power transfer functions (optical power versus bias current) for the bare, hybrid micro-LEDs and integrated MQW membrane are shown in figure 3. At 100 mA dc, which was found to be the maximum current before thermal rollover, the measured optical powers from the bare micro-LED and the integrate MQW membrane (i.e. the color-converted light contribution) are 4 mW and 37 μW, respectively. The total

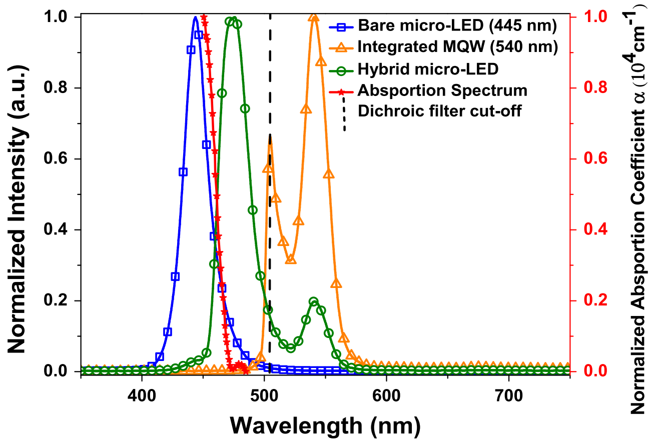

Figure 2. Emission spectra from bare and hybrid pixels and the II–VI band-edge normalized absorption.

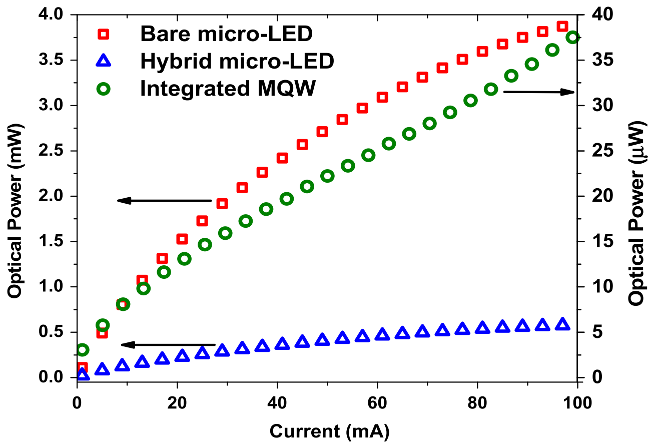

Figure 3. CW optical powers of the bare, hybrid unfiltered micro-LED and integrated MQW membrane.

power of the hybrid micro-LED is 0.58 mW. The power conversion efficiency—defined as the ratio between 540 nm over incident 450 nm power—was found to be 1% ± 0.1% as derived from the power transfer functions. The membrane structure used for this initial proof of principle was not primarily designed for color-conversion and the high index contrast between the membrane material and air (2.5:1) results in a significant amount of waveguided light, which is then lost through reabsorption and edge emission. Improved epilayer design of the membrane and implementation of light extraction schemes would improve this value significantly.

4. Dynamic characteristics

The modulation properties of the hybrid micro-LED are important for VLC applications and represent the main focus of this study. This section looks into the dynamic characteristics of the bare micro-LED and the MQW membrane and what this implies for the hybrid LED modulation properties.

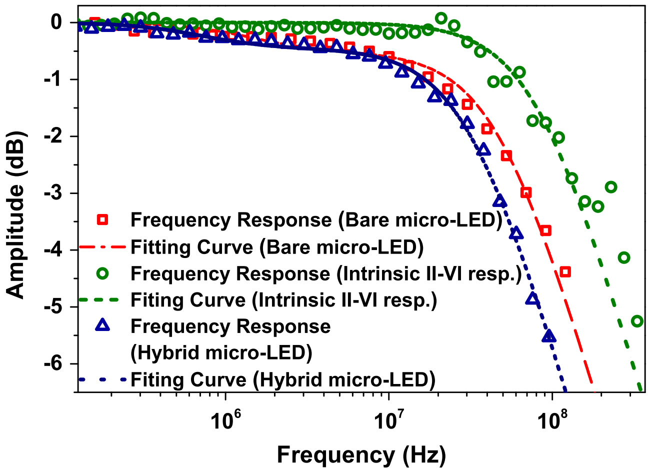

Figure 4. Frequency responses for 80 mA bias current of the bare and hybrid micro-LED, as well as the intrinsic response of the color-converting membrane (integrated MQW membrane), with the respective bi-exponential fits.

4.1. Bandwidth measurements

The electrical frequency responses of the bare micro-LED and integrated MQW membrane were measured at different levels of bias current. The −3 dB optical bandwidth values (the frequency at which the optical power is half the dc value, f_{co}) was obtained for each bias current by fitting the data, considering a possible multi-exponential decay of the luminescence. The following expressions were used for the fits [12]:

$$N(\omega) = \frac{\sum_i \frac{a_i \omega \tau_i^2}{\left(1 + \omega^2 \tau_i^2\right)}}{\sum_i a_i \tau_i}, \tag{1}$$

$$D(\omega) = \frac{\sum_i \frac{a_i \tau_i}{\left(1 + \omega^2 \tau_i^2\right)}}{\sum_i a_i \tau_i}, \tag{2}$$

$$M(\omega) = \left(N(\omega)^2 + D(\omega)^2\right)^{1/2}. \tag{3}$$

In the expressions (1)–(3), the ω and τ_i parameters represent the angular frequency of the modulation and the time constant of the ith exponential decay process, respectively. a_i is a multiplicative factor indicating the contribution strength of the ith decay process. N, D and M are the sine and cosine intensity decay transforms and the demodulation factors [12].

The frequency responses of the bare micro-LED and integrated MQW membrane when driven at 80 mA bias current and their corresponding fitting curves are depicted in figure 4. They are fitted considering a bi-exponential decay of the luminescence, one component of the decay being dominant. The resulting parameters for this particular case are, $a_1 = 0.0037$, $a_2 = 0.9963$, $\tau_1 = 0.2\,\mu\text{s}$, $\tau_2 = 3\,\text{ns}$, $f_{co} = 69\,\text{MHz}$ and $a_1 = 0.0024$, $a_2 = 0.9976$, $\tau_1 = 0.2\,\mu\text{s}$, $\tau_2 = 4.6\,\text{ns}$ and $f_{co} = 47\,\text{MHz}$ respectively.

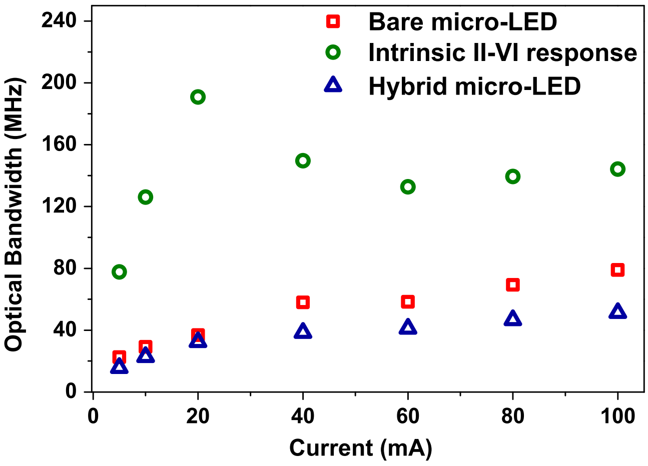

Figure 5. The −3 dB optical bandwidths of the bare μLED and of the hybrid micro-LEDs—the intrinsic bandwidth values of the membrane (integrated MQW membrane) are also plotted.

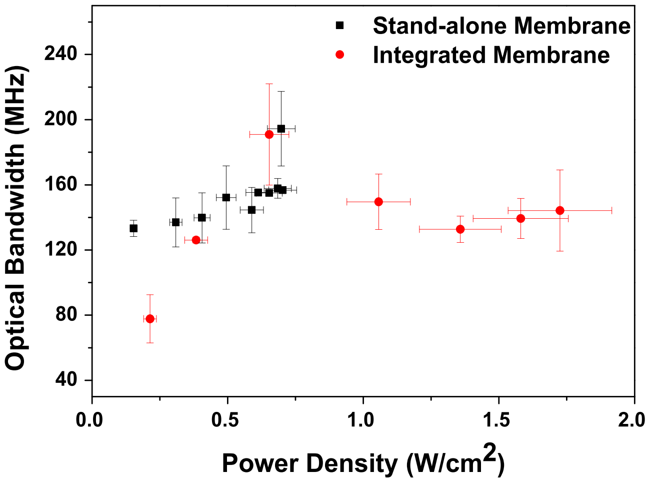

Figure 6. Bandwidth dependence over different power densities.

The data for the intrinsic response of the color-converting membrane is obtained by removing the frequency response contribution of the bare micro-LED from the overall response of the hybrid device [3]. This is also plotted in figure 4 along with its fit. This response is accounted for by a mono-exponential decay of the MQW membrane photoluminescence and its bandwidth is determined by the following bandwidth-lifetime relation,

$$f_{\mathrm{co}} = \frac{\sqrt{3}}{2\pi\tau_i}. \tag{4}$$

In equation (4), f_{co} is the optical bandwidth and τ_i the photoluminescence lifetime, also the carrier lifetime. The mono-exponential decay parameters found for this curve are, $a_1 = 1$, $\tau_1 = 2.0$ ns and $f_{\mathrm{co}} = 139$ MHz.

Figure 5 plots the optical bandwidth values versus the InGaN LED bias current for the bare and hybrid micro-LED as well as the intrinsic modulation bandwidth of the membrane. The data is also summarized in table 1 along with the respective goodness of fit (GoF) values. The GoF is a statistical analysis that characterizes how well the fit describes the measured data, i.e., is a parameter often used to describe the discrepancy between a set of raw data and a model. With GoF = 1 being a perfect fit and GoF < 1 indicating some discrepancy between data.

The micro-LED bandwidth is current dependent and reaches 79 MHz at 100 mA. This current dependency can be attributed to the reduced carrier lifetime in the InGaN micro-LED active region as the current, and hence the carrier density, increases [13, 14]. The typical intrinsic response of the membrane is 145 MHz, much faster than conventional phosphors, see also figure 6. The hybrid micro-LED behavior is the combination of the frequency responses of the color-converting membrane and the underlying micro-LED. The result is a modulation bandwidth of 51 MHz limited by the slower of the two components, i.e. the micro-LED response in this case. Higher modulation bandwidths are expected by using blue micro-LEDs of even smaller dimensions [2].

4.2. Power density dependence of the intrinsic bandwidth of the color-converting membrane

The dependence of the color-converter bandwidth on the incident micro-LED pump power density was further studied. Since the micro-LED is in flip-chip configuration, i.e. the emission occurs through the sapphire substrate, the excitation area at the membrane/sapphire interface is determined by the divergence of the micro-LED light and the propagation length through the sapphire. Due to the small LED size, the excitation spot incident on the membrane can in good approximation be assumed to be circular with diameter equal to the substrate thickness, i.e., $330 \pm 20\,\mu$m in this case [15]. The intrinsic bandwidth data of the membrane as previously determined is then plotted again in figure 6 as a function of the incident excitation power density ('integrated membrane'). For pump power density between 1 and 1.75 W cm^{-2}, the average intrinsic bandwidth is 145 MHz.

In order to observe with more confidence the bandwidth behavior of the MQW membrane at excitation power density below 1 W cm^{-2}, it was independently characterized, i.e. when separated from the micro-LED, as a stand-alone membrane. In this case the membrane was held onto a glass substrate and remotely pumped with a 450 nm micro-LED as explained in section 2. Results are plotted in figure 6 (black squares, 'stand-alone membrane').

The vertical error bars in figure 6 represent the root mean square errors of the fits of the frequency responses. Overall, the presented bandwidth values are within the error bars of the surrounding points so there is no significant power density dependence of the membrane intrinsic bandwidth. The average bandwidth over the range of 450 nm light power density corresponding to the operation of the integrated MQW membrane is around 145 MHz. This corresponds to an effective carrier lifetime of 1.9 ns. This value can be corroborated by direct time-correlated single photon counting, TCSPC, measurement of the stand-alone membrane. Such TCSPC analysis was done using an Edinburgh Instruments system using an EPL-450 Picosecond pulsed diode laser as the excitation source (450 nm). Differences in the TCSPC

Table 1. Table with bandwidth values, f_{co}, for the II–VI membrane (integrated MQW membrane—a long pass filter was used to remove the blue light), the bare micro-LED and the hybrid device, the goodness of fit, GoF and the lifetime, τ_i.

	Bare micro-LED		Intrinsic II–VI membrane response[a]			Hybrid micro-LED	
I (mA)	f_{co} (MHz)	*GoF*	f_{co} (MHz)	τ_i (ns)	GoF	f_{co} (MHz)	GoF
5	23 ± 2	0.991	78 ± 15	3.5 ± 1.4	0.947	16 ± 1	0.997
10	29 ± 2	0.988	126±2	2.2 ± 0.1	0.958	23 ± 2	0.995
20	37 ± 2	0.987	191 ± 31	1.4 ± 0.5	0.875	32 ± 5	0.993
40	58 ± 2	0.983	150 ± 17	1.8 ± 0.4	0.922	38 ± 2	0.993
60	58 ± 4	0.963	133 ± 8	2.1 ± 0.3	0.934	41 ± 3	0.995
80	69 ± 6	0.986	139 ± 12	2.0 ± 0.4	0.947	47 ± 3	0.996
100	79 ± 6	0.990	145 ± 25	1.9 ± 0.7	0.837	51 ± 2	0.995

[a] Frequency response obtained through the bare and hybrid LED measurements.

lifetime measurement were seen between membranes processed from the same epilayer structure however, the average measured lifetime from a number of such membranes was found to be 1.4 ± 0.2 ns, showing reasonable consistency with the frequency response data.

The photoluminescence and the optical bandwidth of the MQW membrane, which is two-orders of magnitude higher than for phosphors, means that high-speed color-conversion can be realized for a range of light levels that correspond to micro-LED operation.

5. Conclusions

This proof-of-concept demonstration of a hybrid micro-LED with integrated MQW membrane offers a pathway to fast-response and robust color conversion and has potential for VLC applications. The modulation bandwidth of the 540 nm hybrid micro-LED was measured to be up to 51 MHz for an intrinsic bandwidth of the MQW membrane and of the underlying micro-LED of 145 and 79 MHz, respectively. Higher modulation bandwidths of the hybrid device are expected by reducing the dimensions of the LED. The integration approach of the membrane by liquid-capillary bonding is well-suited to transfer-printing approaches [16]. It could be extended to other wavelengths using for example MQW structures based on III–V AlGaInP and/or InGaN material systems.

Acknowledgments

This research work was supported by the EPSRC Programme Grant ‘Ultra-parallel visible light communications (UP-VLC)’ (EP/K00042X/1). The authors would like to acknowledge Dr Enyuan Xie for the micro-LED fabrication.

References

[1] Jovicic A, Li J and Richardson T 2013 Visible light communication: opportunities, challenges and the path to market *IEEE Commun. Mag.* **51** 26–32

[2] Mckendry J J D, Massoubre D, Zhang S, Rae B R, Green R P, Gu E, Henderson R K, Kelly A E and Dawson M D 2012 Visible-light communications using a CMOS-controlled micro-light-emitting-diode array *J. Lightwave Technol.* **30** 61–7

[3] Laurand N, Guilhabert B, McKendry J, Kelly A E, Rae B, Massoubre D, Gong Z, Gu E, Henderson R and Dawson M D 2012 Colloidal quantum dot nanocomposites for visible wavelength conversion of modulated optical signals *Opt. Mater. Express* **2** 250

[4] Haase M A, Xie J, Ballen T A, Zhang J, Hao B, Yang Z H, Miller T J, Sun X, Smith T L and Leatherdale C A 2010 II–VI semiconductor color converters for efficient green, yellow, and red light emitting diodes *Appl. Phys. Lett.* **96** 231116

[5] Schiavon D, Binder M, Loeffler A and Peter M 2013 Optically pumped GaInN/GaN multiple quantum wells for the realization of efficient green light-emitting devices *Appl. Phys. Lett.* **102** 113509

[6] Damilano B, Kim-Chauveau H, Frayssinet E, Brault J, Hussain S, Lekhal K, Vennegues P, De Mierry P and Massies J 2013 Metal organic vapor phase epitaxy of monolithic two-color light-emitting diodes using an InGaN-based light converter *Appl. Phys. Express* **6** 092105

[7] McKendry J J D, Green R P, Kelly A E, Gong Z, Guilhabert B, Massoubre D, Gu E and Dawson M D 2010 High-speed visible light communications using individual pixels in a micro light-emitting diode array *IEEE Photonics Technol. Lett.* **22** 1346–8

[8] Gong Z, Jin S, Chen Y, McKendry J, Massoubre D, Watson I M, Gu E and Dawson M D 2010 Size-dependent light output, spectral shift, and self-heating of 400 nm InGaN light-emitting diodes *J. Appl. Phys.* **107** 013103

[9] Zhou X, Munoz M, Tamargo M C and Chen Y C 2004 Optically pumped laser characteristics of blue $Zn_{x'}Cd_{y'}Mg_{1-x'-y'}Se/Zn_xCd_yMg_{1-x-y}Se$ single quantum well lasers grown on InP *J. Appl. Phys.* **95** 7

[10] Moug R, Alfaro-Martinez A, Peng L, Garcia T, Deligiannakis V, Shen A and Tamargo M 2012 Selective etching of InGaAs/InP substrates from II–VI multilayer heterostructures *Phys. Status Solidi* **9** 1728–31

[11] Liau Z L 2000 Semiconductor wafer bonding via liquid capillarity *Appl. Phys. Lett.* **77** 651

[12] Lakowicz J R, Laczko G and Cherek H 1984 Analysis of Fluorescence decay kinetics form variable-frequency phase shift and modulation data *J. Biophys. Soc.* **46** 463–77

[13] Schubert E F 2006 *Light-Emitting Diodes* 2nd edn (Cambridge: Cambridge University Press) p 434

[14] Green R P, McKendry J J D, Massoubre D, Gu E, Dawson M D and Kelly A E 2013 Modulation bandwidth studies of recombination processes in blue and green InGaN

quantum well micro-light-emitting diodes *Appl. Phys. Lett.* **102** 091103

[15] Herrnsdorf J *et al* 2013 Micro-LED pumped polymer laser: a discussion of future pump sources for organic lasers *Laser Photonics Rev.* **7** 1065–78

[16] Trindade A J, Guilhabert B, Massoubre D, Zhu D, Laurand N, Gu E, Watson I M, Humphreys C J and Dawson M D 2013 Nanoscale-accuracy transfer printing of ultra-thin AlInGaN light-emitting diodes onto mechanically flexible substrates *Appl. Phys. Lett.* **103** 253302

Visible light communication using InGaN optical sources with AlInGaP nanomembrane down-converters

J. M. M. Santos,[1,*] S. Rajbhandari,[2] D. Tsonev,[3] H. Chun,[2] B. Guilhabert,[1] A. B. Krysa,[4] A. E. Kelly,[5] H. Haas,[3] D. C. O'Brien,[2] N. Laurand[1] and M. D. Dawson[1]

[1] *Institute of Photonics, Department of Physics, SUPA, University of Strathclyde, Glasgow, UK*
[2] *Department of Engineering Science, University of Oxford, Oxford, UK*
[3] *Li-Fi R&D Centre, Institute for Digital Communications, University of Edinburgh, Edinburgh, UK*
[4] *Electronic & Electrical Engineering, University of Sheffield, Sheffield, UK*
[5] *Electronic & Electrical Engineering, University of Glasgow, Glasgow, UK*
[*] *joao.santos@strath.ac.uk*

Abstract: We report free space visible light communication using InGaN sources, namely micro-LEDs and a laser diode, down-converted by a red-emitting AlInGaP multi-quantum-well nanomembrane. In the case of micro-LEDs, the AlInGaP nanomembrane is capillary-bonded between the sapphire window of a micro-LED array and a hemispherical sapphire lens to provide an integrated optical source. The sapphire lens improves the extraction efficiency of the color-converted light. For the case of the down-converted laser diode, one side of the nanomembrane is bonded to a sapphire lens and the other side optionally onto a dielectric mirror; this nanomembrane-lens structure is remotely excited by the laser diode. Data transmission up to 870 Mb/s using pulse amplitude modulation (PAM) with fractionally spaced decision feedback equalizer is demonstrated for the micro-LED-integrated nanomembrane. A data rate of 1.2 Gb/s is achieved using orthogonal frequency division multiplexing (ODFM) with the laser diode pumped sample.

OCIS codes: (230.0250) Optoelectronics; (230.3670) Light-emitting diodes; (250.5590) Quantum-well, -wire and -dot devices; (060.4510) Optical communications; (060.2630) Frequency modulation; (060.2605) Free-space optical communication.

References and links

1. J. J. Wierer, Jr., J. Y. Tsao, and D. S. Sizov, "Comparison between blue lasers and light-emitting diodes for future solid-state lighting," Laser Photonics Rev. **993**(6), 963–993 (2013).
2. C. W. Chow, C. H. Yeh, Y. Liu, and Y. F. Liu, "Digital signal processing for light emitting diode based visible light communication," IEEE Photonics Soc. Newletter **26**(5), 9–13 (2012).
3. L. Grobe, A. Paraskevopoulos, J. Hilt, D. Schulz, F. Lassak, F. Hartlieb, C. Kottke, V. Jungnickel, and K.-D. Langer, "High-speed visible light communication systems," IEEE Commun. Mag. **51**(12), 60–66 (2013).
4. M. R. Krames, O. B. Shchekin, R. Müller-Mach, G. O. Müller, L. Zhou, G. Harbers, and M. G. Craford, "Status and future of high-power light-emitting diodes for solid-state lighting," J. Disp. Technol. **3**(2), 160–175 (2007).
5. M. S. Shur and A. Žukauskas, "Solid-state lighting: toward superior illumination," Proc. IEEE **93**(10), 1691–1703 (2005).
6. J. Herrnsdorf, B. Guilhabert, J. J. D. McKendry, Z. Gong, D. Massoubre, S. Zhang, S. Watson, A. E. Kelly, E. Gu, N. Laurand, and M. D. Dawson, "Hybrid organic/GaN photonic crystal light-emitting diode," Appl. Phys. Lett. **101**(14), 141122 (2012).
7. M. T. Sajjad, P. P. Manousiadis, H. Chun, D. A. Vithanage, S. Rajbhandari, A. L. Kanibolotsky, G. Faulkner, D. O'Brien, P. J. Skabara, I. D. W. Samuel, and G. A. Turnbull, "Novel fast color-converter for visible light communication using a blend of conjugated polymers," ACS Photonics **2**(2), 194–199 (2015).
8. N. Laurand, B. Guilhabert, J. McKendry, A. E. Kelly, B. Rae, D. Massoubre, Z. Gong, E. Gu, R. Henderson, and M. D. Dawson, "Colloidal quantum dot nanocomposites for visible wavelength conversion of modulated optical signals," Opt. Mater. Express **2**(3), 250–260 (2012).
9. J. M. M. Santos, B. E. Jones, P. J. Schlosser, S. Watson, J. Herrnsdorf, B. Guilhabert, J. J. D. McKendry, J. De

#260251 Received 11 Mar 2016; revised 22 Apr 2016; accepted 23 Apr 2016; published 28 Apr 2016

Jesus, T. A. Garcia, M. C. Tamargo, A. E. Kelly, J. E. Hastie, N. Laurand, and M. D. Dawson, “Hybrid GaN LED with capillary-bonded II–VI MQW color-converting membrane for visible light communications,” Semicond. Sci. Technol. **30**(3), 035012 (2015).

10. D. Schiavon, M. Binder, A. Loeffler, and M. Peter, “Optically pumped GaInN / GaN multiple quantum wells for the realization of efficient green light-emitting devices optically pumped GaInN / GaN multiple quantum wells for the realization of efficient green light-emitting devices,” Appl. Phys. Lett. **102**(11), 113509 (2013).
11. M. A. Haase, J. Xie, T. A. Ballen, J. Zhang, B. Hao, Z. H. Yang, T. J. Miller, X. Sun, T. L. Smith, and C. A. Leatherdale, “II–VI semiconductor color converters for efficient green, yellow, and red light emitting diodes,” Appl. Phys. Lett. **96**(23), 231116 (2010).
12. J. J. D. McKendry, R. P. Green, A. E. Kelly, Z. Gong, B. Guilhabert, D. Massoubre, E. Gu, and M. D. Dawson, “High-speed visible light communications using individual pixels in a micro light-emitting diode array,” IEEE Photonics Technol. Lett. **22**(18), 1346–1348 (2010).
13. Z. L. Liau, “Semiconductor wafer bonding via liquid capillarity,” Appl. Phys. Lett. **77**(5), 651 (2000).
14. Z. Gong, S. Jin, Y. Chen, J. McKendry, D. Massoubre, I. M. Watson, E. Gu, and M. D. Dawson, “Size-dependent light output, spectral shift, and self-heating of 400 nm InGaN light-emitting diodes,” J. Appl. Phys. **107**(1), 013103 (2010).
15. D. O’Brien, R. Turnbull, H. Le Minh, G. Faulkner, O. Bouchet, P. Porcon, M. El Tabach, E. Gueutier, M. Wolf, L. Grobe, and J. Li, “High-speed optical wireless demonstrators: conclusions and future directions,” J. Lightwave Technol. **30**(13), 2181–2187 (2012).
16. D. Tsonev, H. Chun, S. Rajbhandari, J. J. D. Mckendry, S. Videv, E. Gu, M. Haji, S. Watson, A. E. Kelly, G. Faulkner, M. D. Dawson, H. Haas, and D. O. Brien, “A 3-Gb/s single-LED OFDM-based wireless VLC link using a gallium nitride μLED,” IEEE Photonics Soc. Newletter **26**(7), 637–640 (2014).
17. Y. C. Shen, G. O. Mueller, S. Watanabe, N. F. Gardner, A. Munkholm, and M. R. Krames, “Auger recombination in InGaN measured by photoluminescence,” Appl. Phys. Lett. **91**(14), 141101 (2007).
18. J. Hader, J. V. Moloney, B. Pasenow, S. W. Koch, M. Sabathil, N. Linder, and S. Lutgen, “On the importance of radiative and Auger losses in GaN-based quantum wells,” Appl. Phys. Lett. **92**(26), 261103 (2008).
19. E. F. Schubert, *Light-Emitting Diodes*, 2nd ed. (Cambridge University, 2006).
20. C. Y. Liu, S. Yuan, J. R. Dong, and S. J. Chua, “Temperature dependence of photoluminescence intensity from AlGaInP/GaInP multi-quantum well laser structures,” J. Cryst. Growth **268**(3-4), 426–431 (2004).
21. R. P. Green, J. J. D. McKendry, D. Massoubre, E. Gu, M. D. Dawson, and A. E. Kelly, “Modulation bandwidth studies of recombination processes in blue and green InGaN quantum well micro-light-emitting diodes,” Appl. Phys. Lett. **102**(9), 091103 (2013).
22. J. Grubor, S. Randel, K. D. Langer, and J. W. Walewski, “Broadband information broadcasting using LED-based interior lighting,” J. Lightwave Technol. **26**(24), 3883–3892 (2008).
23. S. Watson, M. Tan, S. P. Najda, P. Perlin, M. Leszczynski, G. Targowski, S. Grzanka, and A. E. Kelly, “Visible light communications using a directly modulated 422 nm GaN laser diode,” Opt. Lett. **38**(19), 3792–3794 (2013).
24. C. Lee, C. Zhang, M. Cantore, R. M. Farrell, S. H. Oh, T. Margalith, J. S. Speck, S. Nakamura, J. E. Bowers, and S. P. DenBaars, “4 Gbps direct modulation of 450 nm GaN laser for high-speed visible light communication,” Opt. Express **23**(12), 16232–16237 (2015).
25. S. Randel, F. Breyer, S. C. J. Lee, and J. W. Walewski, “Advanced modulation schemes for short-range optical communications,” IEEE J. Sel. Top. Quantum Electron. **16**(5), 1280–1289 (2010).
26. S. Loquai, R. Kruglov, B. Schmauss, C. Bunge, F. Winkler, O. Ziemann, E. Hartl, and T. Kupfer, “Comparison of modulation schemes for 10. 7 Gb/s transmission over large-core 1 mm PMMA polymer optical fiber,” J. Lightwave Technol. **31**(13), 2170–2176 (2013).

---

1. Introduction

Solid-state visible light sources based on the AlInGaN material systems have become key enablers for a number of applications including lighting and illumination, displays, and consumer electronics. For example, InGaN-based white-light emitting diodes are replacing older light bulb technologies for home and street illuminations while InGaN laser diodes are used for optical data storage and are being considered for future ultra-efficient lighting [1]. An emerging application for InGaN-based white LEDs is visible light communications (VLC), which has been gathering a lot of attention recently [2,3]. Because practical InGaN optoelectronic sources do not yet cover the entire visible spectrum (the device efficiency drops continuously for wavelengths above 500 nm [4]), a blue-emitting GaN source often needs to be combined with color-converting materials to access longer wavelengths, or generate white light. This is usually done with rare-earth phosphors, as in commercial white LEDs [5]. However, phosphors respond slowly to modulated light, which is not ideal for VLC. Other color-converting materials are therefore being researched for VLC including organic semiconductors [6,7], colloidal nanocrystals [8] and inorganic semiconductor

#260251 Received 11 Mar 2016; revised 22 Apr 2016; accepted 23 Apr 2016; published 28 Apr 2016

epilayers [9]. The latter offers an all-inorganic, photostable solution to color-conversion, which is particularly attractive for high power applications.

Recently, we have demonstrated a hybrid green-emitting LED based on a II-VI multi-quantum well (MQW) epilayer structure a couple of micron-thick for color-conversion of a blue micro-LED [9]. Other groups had previously shown similar heterogeneous hybridization of epitaxial structures as a way to push the emission of GaN LEDs to longer wavelengths [10,11]. In this work, we report the implementation of a red-emitting AlInGaP semiconductor color-converting structure and demonstrate free space VLC when it is combined with blue InGaN sources. The AlInGaP structure is a nanomembrane (NM) with a thickness below 400 nm and comprising a multi-quantum well active region. The NM format facilitates the heterogeneous integration of the color-converter with other materials and structures through capillary bonding. We focus on a device implementation where the AlInGaP NM is fully integrated with a GaN micro-LED array. The result is an array of hybrid red LEDs that benefits from the relatively high modulation bandwidth of the underlying blue micro-LEDs [12]. Additionally, we demonstrate a proof-of-principle format for remote pumping with a blue laser diode where the NM is simply bonded onto a hemispherical sapphire lens. In both implementations, VLC experiments are done by modulating the GaN-based source with the modulated blue light being transferred to red by radiative down-conversion through the NM.

The paper is organized as follows: section 2 describes the design of the AlInGaP NM and its integration with the micro-LED array and/or the hemispherical sapphire lens. A description of the micro-LED array and the characterization methods are also given. Sections 3 and 4 report and discuss, respectively, the continuous-wave (CW) characteristics of the NM-based sources, and their dynamic and VLC performance under *M*-ary pulse amplitude modulation (M-PAM) and orthogonal frequency-division multiplexing (OFDM) modulation schemes.

2. Device fabrication and characterization

2.1 Design and fabrication

The color-converter structure is based on epitaxial AlInGaP grown on GaAs substrate by metalorganic vapor phase epitaxy. The active region is made of 3 pairs of InGaP quantum wells, with AlInGaP as the barrier material, designed for a room temperature photoluminescence emission at 648 nm. The 2λ length of the MQW region (excluding the GaAs buffer) is chosen so that the finalized NM absorbs >90% of excitation light at 450 nm. To obtain the NM, the GaAs substrate is removed by wet etching using a solution of H_3PO_4:H_2O_2:H_2O at a ratio of 3:4:3. The resulting NM has a thickness of <400 nm, and a typical surface area of a few mm^2.

In the first device implementation (hybrid LED), the NM is capillary-bonded using deionized water [13] onto the sapphire window (polished epi-substrate) of the micro-LED chip [Fig. 1(a)]. This technique enables direct Van der Waal's bonding between surfaces without requiring interlayers. A 2mm diameter sapphire hemispherical lens with a refractive index of 1.7 is in turn capillary-bonded on top of the NM to finalize the hybrid device [Fig. 1(b)]. The micro-LED chip, with peak emission at 450 nm, is fabricated using a commercial p-*i*-n GaN structure grown on *c*-plane sapphire, following the procedure reported in [14]. The chip is made of 8 micro-LED pixels of 4 different sizes, 50 x 50 μm^2, 75 x 75 μm^2, 100 x 100 μm^2 and 150 x 150 μm^2. It is mounted onto a printed circuit board and wire bonded to metal tracks connected to SMA connectors, in such a way that each pixel from the micro-LED array can be individually addressed. Figure 1(c) presents a photoluminescence spectrum from the NM with a photograph as inset of the hybrid device under current injection with the color-converted light visible in the center.

In the second NM implementation, for the laser diode (LD) pumping embodiment, the NM is simply bonded to a sapphire hemispherical lens as depicted in Fig. 1(d). The other side

#260251 Received 11 Mar 2016; revised 22 Apr 2016; accepted 23 Apr 2016; published 28 Apr 2016

of the membrane is optionally placed in contact with a dielectric mirror. The 450nm LD (OSRAM PL450B) pump is mounted in a Peltier-cooled metallic mount kept at a constant temperature of 25°C.

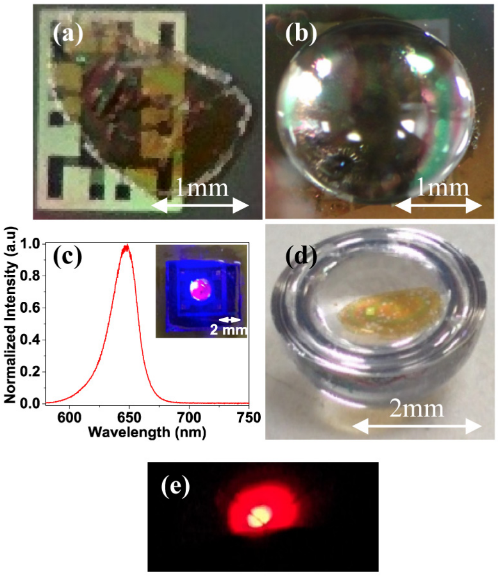

Fig. 1. MQW NM a) capillary bonded onto the sapphire window of the micro-LED chip, b) sandwiched in-between the sapphire hemispherical lens and the micro-LED window, c) spectrum with a picture in inset from the hybrid LED with integrated sapphire lens under operation, d) capillary bonded onto the sapphire hemispherical lens and e) color-converted light, imaged on a screen, from the LD-pumped NM.

2.2 Experimental methods

For reference, the stand-alone blue micro-LEDs as well as the 450nm LD were first characterized, independently of the NM, in terms of optical power, emission spectrum and modulation bandwidths. The same measurements were then done with the AlInGaP NM (integrated with the micro-LEDs or remotely excited for LD pumping).

A set of aspheric lenses with focal length of 32 mm and high numerical aperture (NA of 0.612) were used to collect and focus the emission into a Femto HSA-X-S-1G4-SI photoreceiver (bandwidth of 1.4 GHz). For bandwidth measurements, the micro-LED or LD was simultaneously driven with a dc bias current and a frequency-swept modulated signal (0.250$V_{p\text{-}p}$) that were combined through a wideband (0.1–6000 MHz) Bias-Tee. An Agilent HP 8753ES Network Analyzer was used to provide the modulation signal and to record the device frequency response as detected by the photoreceiver. A long-pass filter (550 nm cut-off wavelength) was placed before the receiver for measurements of the down-converted light. The modulation bandwidth was extracted from the detected modulation amplitude versus frequency as detailed in [8,9]. The optical spectra were recorded with an Ocean Optics USB4000 Fiber Optic Spectrometer (2.5 nm resolution).

A similar set-up was used for the VLC demonstrations of section 4, with some specifics described here. For both PAM and OFDM, the modulated signal was generated offline in MATLAB® environment and loaded to an Agilent 81150A arbitrary waveform generator (AWG) while the detection was carried out by a 1.95mm diameter avalanche photodiode (APD) connected to an Agilent MSO71043 oscilloscope [15]. The post processing of the optical signal was done offline using a MATLAB script. More information regarding the APD receiver and the OFDM test configuration can be found elsewhere [15,16].

#260251 Received 11 Mar 2016; revised 22 Apr 2016; accepted 23 Apr 2016; published 28 Apr 2016

3. CW characteristics

The curves of optical power versus drive current for the standalone micro-LEDs of different sizes are plotted in Fig. 2(a). The slope is non-linear with the current and the curves eventually roll over at the highest currents. The smaller size micro-LEDs have a roll-over point at lower driving currents because they reach higher current densities for the same drive current. This non-linear behavior with the power roll over can be ascribed to an increase of the device temperature under operation, exacerbated by the phenomenon of efficiency droop [17,18]. The temperature rise can be related to the spectral shift of the peak emission illustrated in Fig. 2(b) in the case of the 100µm LED (black squares).

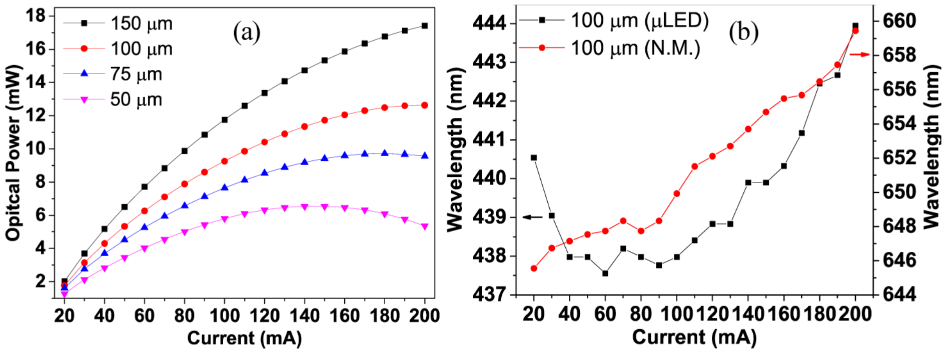

Fig. 2. a) L-I curve for each pixel in the µLED chip and b) spectral shift for the 100µm pixel and the III-V NM.

The emission from the micro-LED experiences an overall redshift of 3 nm, between 441 nm and 444 nm, between 20 mA and 200 mA. The LED peak emission wavelength starts blue-shifting at lower current before reaching a plateau (60 mA – 100 mA) and eventually red-shifting for current above 100 mA. The initial blue shift is attributed to band filling and carrier screening of piezoelectric fields in the active region. At higher current injection the reduction of the bandgap energy with temperature becomes the predominant effect, resulting in the red shift [19]. The device increase in temperature under bias current was verified through thermal imaging of the sapphire substrate of the micro-LEDs. It was found that the temperature surface of the sapphire increases by approximately 140°C between 20 and 200 mA due to self-heating. Self-heating in micro-LEDs has been previously studied [14].

Figure 3(a) plots the received optical power versus current for the hybrid micro-LEDs (650nm emission). We note that this measurement was performed with direct photodiode detection at the image plane of the set-up, without the use of an integrating sphere. The trend is similar, with the largest emitters giving the highest optical power, but the roll-over effect is more pronounced than for the stand alone micro-LEDs. For example, the 100µm stand-alone LED has a roll-over point between 180 and 200 mA whereas the equivalent hybrid LEDs roll over at 100 mA. At this current the forward power conversion efficiency (i.e. the measured power of the red hybrid LEDs divided by that of the standalone blue micro-LEDs) is close to 1.2%. The efficiency decreases continuously for higher current. This decrease is attributed to a reduction of the NM luminescence efficiency as its temperature increases, the NM being in contact with the sapphire substrate. The peak emission wavelength of this hybrid micro-LED as a function of the drive current is also plotted in Fig. 2(b) (red dots). Unlike the blue micro-LED emission, the spectrum continuously red-shifts, going from 645 nm at 20 mA up to 658 nm at 200 mA. The spectral emission of the AlInGaP NM is expected to redshift by approximately 0.12 nm/°C as determined from modeling based on the empirical Varshny relation [20]. Therefore the temperature increase of the NM can be inferred to be 100°C, which is not far off the temperature rise of the sapphire surface as measured by thermal imaging (140°C).

#260251 Received 11 Mar 2016; revised 22 Apr 2016; accepted 23 Apr 2016; published 28 Apr 2016

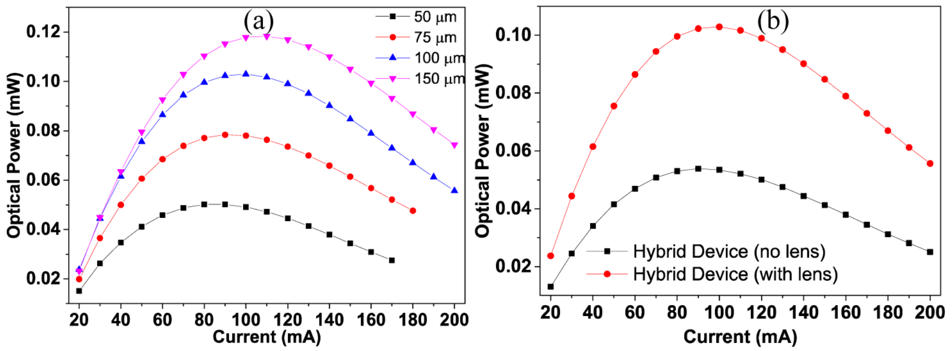

Fig. 3. a) L-I curve for the NM-hybrid devices and b) power enhancement by addition of the lens for the 100µm device.

The hemispherical lens added on top of the NM helps to increase the forward conversion efficiency as shown in Fig. 3(b) in the case of the 100µm device where the maximum output power doubles. The hemispherical lens mitigates the problem of waveguided light within the NM as well as increases the collection of photons close to the escape cone limit. It is found that the maximum output power is improved by 63%, 92%, 98% and 95% for the squared pixels with edge size of 150, 100, 75 and 50 µm, respectively. The lower enhancement for the 150µm device is probably because it sits on the edge of the lens. The addition of the lens however did not significantly improve heat removal from the NM; the red shift of the NM emission with current, with and without the lens, was found to be basically identical. For better thermal management, bigger lenses as well as active heat extraction from the lens could be used. Lenses could also be made with materials of higher thermal conductivity such as diamond.

In the description above, the decrease in the NM luminescence efficiency is attributed solely to a rise in temperature. Other possible explanations could include a dependence of non-radiative recombination on the MQW carrier density or a saturation of the NM absorption. To rule out these possibilities, the power density dependence of the converted light was further studied independently of the temperature rise caused by the micro-LED by remotely pumping a NM bonded onto a sapphire lens in the LD excitation configuration, as shown in Fig. 1(d). For low pump power density onto the NM, a micro-LED was used otherwise the LD was utilized. The spot size of the pump onto the NM surface, needed for determination of the pump power density, was measured using a beam profiler. Results plotted in Fig. 4 (black triangles) demonstrate that there is no saturation of the absorption and no noticeable increase in non-radiative recombination; the optical power from the NM increases linearly with the pump power density on a range of 0 up to 4 kW/cm^2. The left side of the broken x-axis are data under LED pumping whereas on the right side are data for LD pumping.

The converted power efficiency for this overall range is 0.88 ± 0.16%. The addition of a dielectric mirror, so that the NM is sandwiched between the lens and the mirror, increases the forward power efficiency to 1.14 ± 0.26% (red dots in Fig. 4), with an output power of 1.2 mW for a pump power density of 4 kW/cm^2.

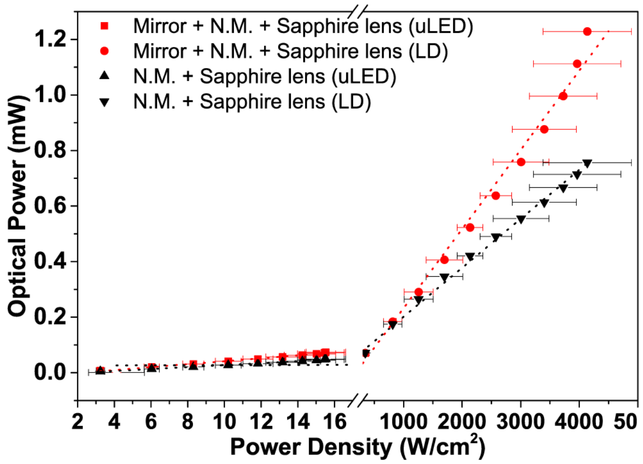

Fig. 4. Optical power vs power density for the NM bonded onto a sapphire lens and sandwiched between the sapphire lens and a dichroic mirror. Note break in the x-axis scale.

4. Dynamic characteristics

4.1 Bandwidth measurements

The optical modulation bandwidth (the frequency at which the modulated optical power is half the dc value) versus drive current for the different sizes of stand-alone and hybrid micro-LEDs are plotted in Fig. 5(a) and 5(b) respectively. The intrinsic bandwidth of NM is plotted in Fig. 5(c).

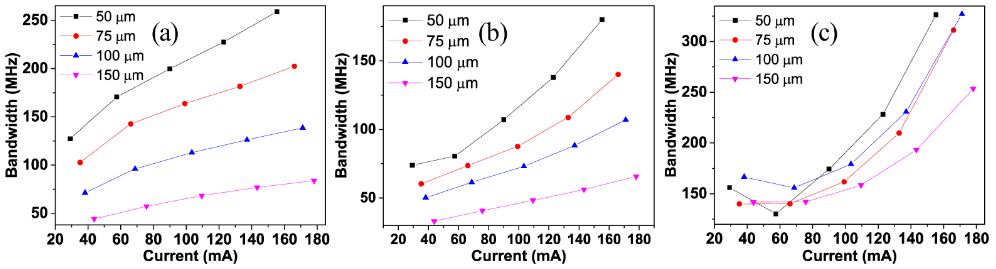

Fig. 5. Bandwidths for a) the stand-alone micro-LEDs b) the hybrid micro-LEDs and c) the NM, extracted from a) and c) as explained in [9].

The bandwidth is size- and current-dependent reaching a maximum of 260 MHz and 180 MHz at around 150 mA for the standalone micro-LED and the hybrid red device, respectively. The current dependence can be attributed to the reduced carrier lifetime in the active region of the micro-LEDs as the current, and hence the carrier density, increases [12,21]. The response of the NM, obtained by subtracting the standalone micro-LED response to the response of the hybrid device [9], further affects the bandwidth of the hybrid sources. The intrinsic response of the NM is between 130 MHz and 320 MHz, which is at least two order of magnitude faster than conventional phosphors [22]. The increase in the bandwidth with the current is linked to the increase of non-radiative recombination as the temperature of the device, hence of the NM, increases.

The frequency response of the LD could not be measured, as it was higher than the photodiode bandwidth of 1.4 GHz [23,24]. However, the laser excited bandwidth of the NM bonded onto the sapphire lens bandwidth was measured and is shown in Fig. 6.

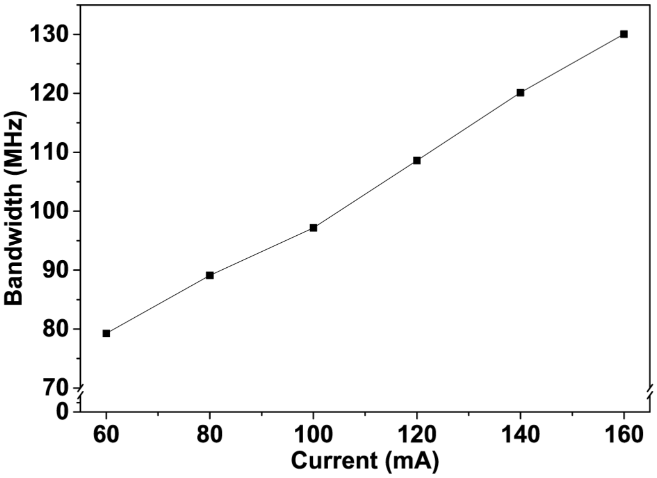

Fig. 6. Bandwidth from the LD-pumped NM-lens structure (the line is a guide to the eye).

In Fig. 6 the bandwidth is set by the intrinsic response of the NM. There is a difference between the maximum achievable bandwidth, 180 MHz for the hybrid device and 130 MHz for the LD-pumped NM. Again, this is due to the increase of non-radiative recombination caused by heating when the NM is integrated onto the micro-LED array. When remotely-pumped the heating in the NM is nowhere near as severe.

4.2 M-PAM measurements

Free-space optical data transmission, using the NM device formats described above, was carried out. The optical set-up and the required equipment were described in section 2.2. A pseudo random binary sequence (PRBS) of 10^{14}-1 was generated and encoded into appropriate PAM level, which was then loaded to the Agilent 81180A AWG. A fractionally-spaced adaptive decision feedback equalizer (DFE) was adopted at the receiver.

The BER vs. data rates for PAM scheme for the hybrid micro-LEDs are presented in Fig. 7 and the achieved data rates at BER of 3.8 x10^{-3} are summarized in Table 1. The smallest micro-LED offered the highest data rate for all modulation schemes due to its higher bandwidth. Among PAM schemes, 4-PAM with DFE offered the best performance closely followed by 2-PAM. These results follow the theoretical predictions in [25] and experimental results in [26]. It is theoretical shown in [26] that 4-PAM with DFE requires less optical power than 2-PAM with DFE when data rate is beyond 5-times the electrical bandwidth. Higher level PAM has higher power penalty due to LED and device non-linearity. Hence, non-linearity compensation is required for improved performance. The non-linearity compensation is, however, not within the scope of this paper.

Table 1. Achievable data rates at BER of 3.8×10^{-3} for the different size of hybrid micro-LEDs in Mbit/s.

	50 x 50 μm^2	75 x 75 μm^2	100 x 100 μm^2	150 x 150 μm^2
2-PAM	777	757	738	659
4-PAM	867	862	807	615
8-PAM	720	740	680	495

#260251 Received 11 Mar 2016; revised 22 Apr 2016; accepted 23 Apr 2016; published 28 Apr 2016

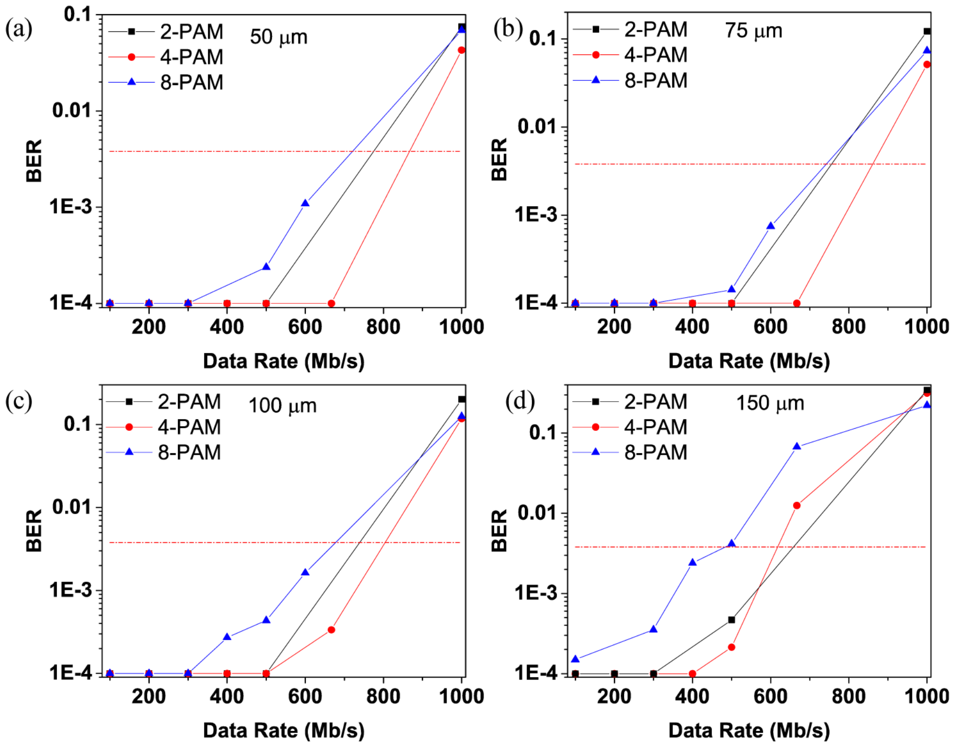

Fig. 7. BER vs Data Rate for the hybrid devices a) 50µm x 50µm pixels, b) 75µm x 75µm pixels, c) 100 µm x 100µm pixels and d) 150µm x 150 µm pixels.

DCO-OFDM data transmission using the LD-pumped NM [Fig. 1(d)] was also tested. By adjusting the LD driving bias current and the modulation depth, it was possible to achieve transmission up to 1.2 Gb/s at BER of 3.8×10^{-3} as shown in Fig. 8. The higher data rate is due to the combined higher SNR level and higher modulation bandwidth of the laser diode in comparison to the micro-LEDs.

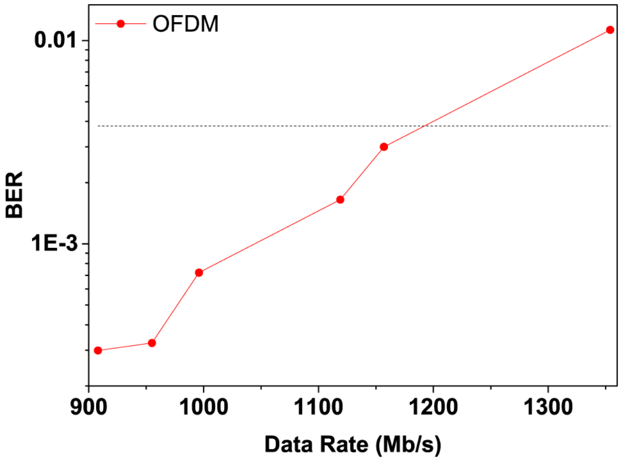

Fig. 8. BER vs Data Rate for the sample pumped with a laser diode.

5. Conclusion

In this paper, we have demonstrated VLC using InGaN sources color-converted with AlInGaP NM assemblies. The NM geometry of the converter enables integration with optics and micro-LEDs by capillary bonding. We note that this format of color-conversion is consistent with semiconductor approaches developed by some LED manufacturers in order to extent the efficiency of blue LEDs to longer wavelengths, while at the same time offering faster response than phosphors for VLC. The extraction efficiency values reported are still relatively low but could be improved by further incorporating light extraction features to the NM assembly. The maximum data rate achieved for this hybrid configuration in this paper was 870 Mb/s using 4-PAM scheme with DFE. We also reported on a NM format for remote pumping by LD. In this configuration we have shown VLC up to 1.2 Gb/s using OFDM. This second configuration would be particularly suited for high power applications with the NM bonded to optics and heat spreaders. Finally, by designing other NM structures using AlGaInP or InGaN material systems it should be possible in principle to extend the wavelength coverage across the visible spectrum.

Acknowledgments

This research work was supported by the EPSRC Programme Grant “Ultra-parallel visible light communications (UP-VLC)” (EP/K00042X/1). The authors would like to acknowledge Dr. Enyuan Xie for the micro-LED fabrication.

#260251 Received 11 Mar 2016; revised 22 Apr 2016; accepted 23 Apr 2016; published 28 Apr 2016

Conference Presentations

Hybrid GaN LED with capillary-bonded II-VI MQW color-converting membrane for Visible Light Communications

Joao M. M. Santos[1], Brynmor E. Jones[1], Peter J. Schlosser[1], Scott Watson[2], Johannes Herrnsdorf[1], Benoit Guilhabert[1], Jonathan J. D. McKendry[1], Joel De Jesus[3], Thor A. Garcia[3], Maria C. Tamargo[3], Anthony E. Kelly[2], Jennifer E. Hastie[1], Nicolas Laurand[1] and Martin D. Dawson[1]

[1]Institute of Photonics, SUPA, University of Strathclyde, 106 Rottenrow, Glasgow G4 0NW, UK
[2]School of Engineering, University of Glasgow, Glasgow, G12 8LT, UK
[3]Department of Chemistry, City College of New York, 138th Street and Convent Avenue, New York, NY 10031, USA

E-mail : joao.santos@strath.ac.uk

Abstract

The rapid emergence of gallium-nitride (GaN) light-emitting diodes for solid-state lighting has created a timely opportunity for optical communications using visible light. One important challenge to address this opportunity is to extend the wavelength coverage of GaN LEDs without compromising their modulation properties. Here, a hybrid source for emission at 540 nm consisting of a 450nm GaN micro-sized LED (micro-LED) with a micron-thick ZnCdSe/ZnCdMgSe multi-quantum-well color-converting membrane is reported. The membrane is liquid-capillary-bonded directly onto the sapphire window of the micro-LED for full hybridization. At an injection current of 100 mA, the color-converted power was found to be 37 µW. At this same current, the -3dB optical modulation bandwidth of the bare GaN and hybrid micro-LEDs were 79 MHz and 51 MHz, respectively. The intrinsic bandwidth of the color-converting membrane was found to be power-density independent over the range of the micro-LED operation at 150 MHz, which corresponds to a mean carrier lifetime of 1.85 ns.

1. Introduction

Development of light-emitting diode (LED) technology is driven mainly by the need for efficient solid-state lighting, but it is also creating opportunities for new applications such as visible light communications (VLC) [1]. VLC requires light sources that are not only efficient but also have high modulation bandwidth and are wavelength versatile. White-emitting LEDs, and color-converted LEDs in general, are typically obtained by combining blue InGaN LEDs with down-converting phosphors. This approach is effective for illumination purposes but is not well suited to VLC because of the long (µs) excited-state lifetime of phosphors. The resulting sources have modulation bandwidths limited to ~ 1 MHz, whereas unconverted blue InGaN-based LEDs have bandwidths of 20 MHz up to 400 MHz depending on their formats, with single-color direct-LED-emission data links at > 1Gbit/s rate having been demonstrated [2]. There is therefore a need to explore color-converting materials with shorter excited-state lifetimes to complement rare-earth phosphors. Organic semiconductors and colloidal quantum dots are potential candidates but there remain uncertainties over their long-term environmental stability [3].

Here we introduce an alternative approach based on using inorganic MQW semiconductor epi-layer membranes as photo-pumped color converters for the underlying InGaN LEDs. This technology benefits from being based on all-inorganic semiconductors and therefore promises to be robust [4], [5]. It also leads to extremely compact sources, as the membrane can be integrated (as we show) by techniques such as liquid capillary bonding. There are several options for wavelength coverage across the visible spectrum with available semiconductor alloys for MQW membranes including III-V AlGaInP (yellow to red) and InGaN (green) materials and II-VI CdMgZnSe (green to orange) materials [4], [6]. As proof-of-principle of a generic approach, the hybrid LED demonstrator discussed here is obtained by capillary-bonding a 540nm-emitting, II-VI CdMgZnSe MQW membrane onto an array of 450nm InGaN micro-size LEDs (micro-LEDs), taking advantage of the high modulation bandwidths associated with these small-sized LEDs [7]. We chose II-VI materials for this initial study because (i) they are readily wet etched into epitaxial membranes, (ii) they can be designed to offer coverage of the visible spectrum promising white-light generation, and (iii) they permit an alternative approach to green emission at high-modulation-bandwidth, useful for e.g. introducing coarse wavelength division multiplexing (blue and green) into optical wireless and polymer optical fiber communications.

In the following, the hybrid device fabrication and characterization methods are described in section 2. Sections 3 and 4 report and discuss, respectively, the continuous-wave (CW) and dynamic characteristics of the hybrid source.

2. Device fabrication and characterization

2.1 Device design and fabrication

The 450nm-wavelength micro-LEDs used to pump the MQW membrane were fabricated using a commercial p-*i*-n GaN LED structure grown on c-plane sapphire, following the procedure reported in [8]. Here, the fabricated chip is made of several 100 µm x 100 µm square micro-LEDs spaced 450 µm apart, Figure 1. After fabrication, the chip was placed onto a printed circuit board and wire bonded to tracks connected to SMA connectors, such that the micro-LEDs could be addressed individually.

The II-VI MQW membrane structure was grown by molecular beam epitaxy on an InP substrate and InGaAs growth buffer. It consists of 9 ZnCdSe quantum wells with CdMgZnSe barriers and is designed to emit at 540 nm in a resonant periodic gain configuration for potential alternative use as a laser gain medium [9]. The InP substrate was removed by a combination of mechanical polishing and wet etch process using a solution of HCl:H_3PO_4 in a ratio of 3:1, followed by the removal of the InGaAs layer with a solution of H_3PO_4:H_2O_2:H_2O, in a ratio of 1:1:6 for maximum etch selectivity with the II-VI material [10]. The epi-side is fixed onto a temporary glass substrate for this step, using a wax, for mechanical support during processing. After substrate removal, the II-VI layer was transferred from the glass and capillary-bonded using deionized water onto the sapphire window of the LEDs to complete the hybrid device [11]. The resulting MQW membranes have a thickness of less than 2.5 µm, and a typical surface area of a few mm^2. Images of the hybrid device are shown in Figure 1.

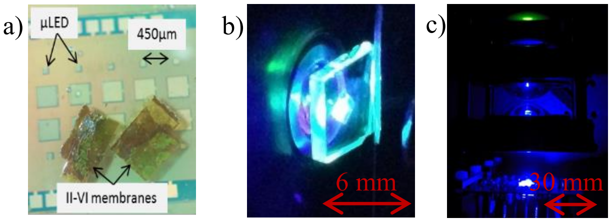

Figure 1. a) Plan view micrograph of the hybrid device. The micro-LED pixels are the smaller elements as labeled, some of which are bonded underneath the II-VI membrane. Between the membrane and the underlying LEDs is the sapphire substrate, b) II-VI membrane when pumped by a blue LED, c) hybrid device showing direct blue and color-converted green emission.

2.2 Experimental Setups

The device was characterized in terms of optical power, emission spectrum and modulation bandwidth prior to and after membrane integration. For the power measurements, the device under test was fixed on top of an optical power meter with a 30mm cage plate in between to enable the optional placement of an optical long-pass filter (500nm cut-off wavelength). Hereafter, in section 3 and 4, we refer to the micro-LED with no membrane as the ‘bare LED’, the LED with integrated membrane as the ‘unfiltered’ hybrid micro-LED, and the micro-LED with membrane and filter in place at detection simply as the ‘hybrid LED’. Optical spectra were recorded with an Ocean Optics USB4000 Fiber Optic Spectrometer (2.5nm resolution).

For the frequency response and modulation bandwidth measurements, a set of aspheric lenses with focal length of 32mm and high numerical aperture (NA = 0.612) were used to collect and focus the micro-LED emission into a Femto HSA-X-S-1G4-SI fast photoreceiver (bandwidth of 1.4 GHz). The LED device was simultaneously driven with a DC bias current and a frequency-swept modulated signal (0.250 Vpp) that were combined with a wideband (0.1 to 6000 MHz) Bias-Tee. An Agilent HP 8753ES Network Analyzer was used to provide the modulation signal and to record the device frequency response as detected by the photoreceiver. The long-pass filter was placed before the detection for measurements of the hybrid LED characteristics.

The intrinsic modulation bandwidth of the stand-alone membrane was also characterized as a function of the excitation power density (section 4). For this, the membrane was supported on a glass substrate and remotely pumped with a bare micro-LED. A pair of lenses was placed directly after the bare device to focus its light onto the stand-alone membrane. Further optics were used to collect the light emitted by the membrane and focus it onto the photodetector. A Coherent® BeamMaster was used to measure the micro-LED beam size incident onto the membrane surface and hence to deduce the incident power density. The full width at half maximum (FWHM) spot-size was found to be 330μm. The bandwidth measurement of the stand-alone membrane was otherwise as described above.

3. CW characteristics

Normalized spectral measurements for the bare micro-LED, the unfiltered hybrid micro-LED and the hybrid micro-LED (i.e. the contribution of the converted light at 540 nm) are presented in Figure 2. The bare micro-LED has emission centered at 445 nm. The hybrid LED spectrum shows a peak centered at 475 nm and a secondary peak at 540 nm. The emission at 540 nm comes from the light emitted by the II-VI MQW membrane. The II-VI membrane is designed to absorb 97 % to 98 % of 445nm monochromatic light. Because of the bandwidth of the bare micro-LED spectrum (23 nm FWHM) the effective micro-LED light absorption is 85% ± 1%. The band-edge of the membrane is at around 460 nm and therefore the long-wavelength tail of the μLED emission is not fully absorbed, explaining the 'apparent' 475nm peak in the spectrum of the hybrid device.

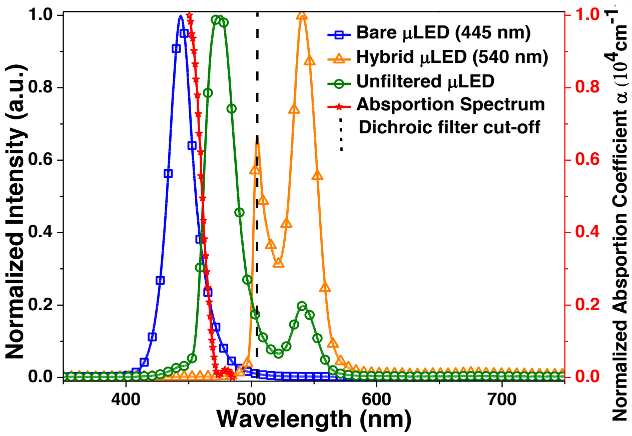

Figure 2. Emission spectra from bare and hybrid pixels and the II-VI band-edge normalized absorption.

The power transfer functions (optical power versus bias current) for the bare, unfiltered hybrid and hybrid micro-LEDs are shown in Figure 3. At 100mA DC, which was found to be the maximum current before thermal rollover, the measured optical powers from the bare micro-LED and the hybrid micro-LEDs (*i.e.* the color-converted light contribution) are 4 mW and 37 μW, respectively. The total power of the unfiltered hybrid micro-LED is 0.58 mW. The power conversion efficiency - defined as the ratio between 540nm over incident 450nm power – was found to be 1.1% ± 0.1% as derived from the power transfer functions. The membrane structure used for this initial proof of principle was not primarily designed for color-conversion and the high index contrast between the membrane material and air (2.5:1) results in a significant amount of waveguided light, which is then lost through reabsorption and edge emission. Improved epilayer design of the membrane and implementation of light extraction schemes would improve this value significantly.

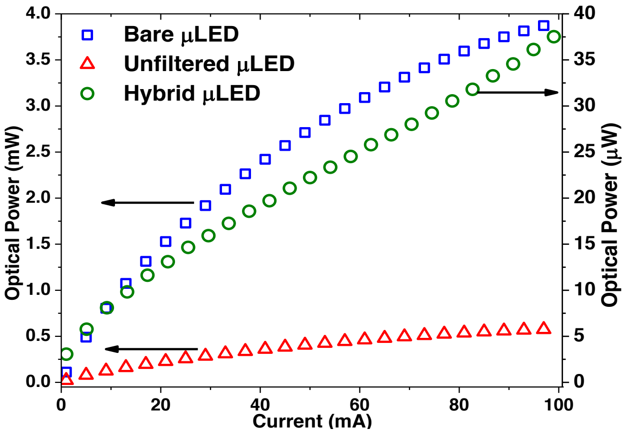

Figure 3. CW optical powers of the bare, hybrid and unfiltered μLED devices.

4. Dynamic characteristics

The modulation properties of the hybrid micro-LED are important for VLC applications and represent the main focus of this study. This section looks into the dynamic characteristics of the bare micro-LED and the MQW membrane and what this implies for the hybrid LED modulation properties.

4.1 Bandwidth measurements

The electrical frequency responses of the bare and unfiltered micro-LEDs were measured at different levels of bias current being the -3dB optical bandwidth values at each one of them obtained by fitting the data, considering a possible multi-exponential decay of the luminescence. The following expressions were used for the fits [12]:

$$N(\omega) = \frac{\sum_i \frac{a_i \omega \tau_i^2}{(1+\omega^2\tau_i^2)}}{\sum_i a_i \tau_i} \qquad (1)$$

$$D(\omega) = \frac{\sum_i \frac{a_i \tau_i}{(1+\omega^2\tau_i^2)}}{\sum_i a_i \tau_i} \qquad (2)$$

$$M(\omega) = (N(\omega)^2 + D(\omega)^2)^{1/2} \qquad (3)$$

In the expressions (1) to (3), the ω and τ_i parameters represent the angular frequency of the modulation and the time constant of the i^{th} exponential decay process, respectively. a_i is a multiplicative factor indicating the contribution strength of the i^{th} decay process. *N*, *D* and *M* are the sine and cosine intensity decay transforms and the demodulation factors [12].

The frequency responses of the bare and unfiltered hybrid micro-LEDs when driven at 80mA bias current and their corresponding fitting curves are depicted in Figure 4. They are fitted considering a bi-exponential decay of the luminescence, one component of the decay being dominant. The resulting parameters for this particular case are, $a_1 = 0.0037$, $a_2 = 0.9963$, $\tau_1 = 0.18$ μs, $\tau_2 = 3$ ns, $f_{co} = 69.3$ MHz and $a_1 = 0.0024$, $a_2 = 0.9976$, $\tau_1 = 0.24$ μs, $\tau_2 = 4.6$ ns and $f_{co} = 46.6$ MHz respectively.

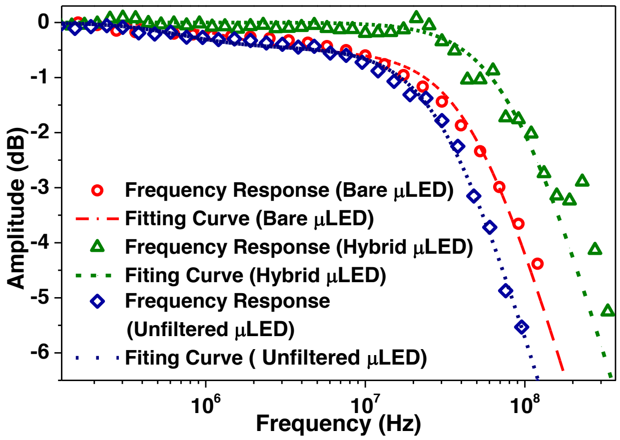

Figure 4. Frequency responses for 80 mA bias current of the bare and unfiltered micro-LED, as well as the intrinsic response of the color-converting membrane (hybrid micro-LED), with the respective bi-exponential fits.

The data for the intrinsic response of the color-converting membrane is obtained by removing the frequency response contribution of the bare micro-LED from the overall response of the unfiltered hybrid device. This is also plotted in Figure 4 along with its fit. This response is accounted for by a mono-exponential decay of the MQW membrane photoluminescence and its bandwidth is determined by the following bandwidth-lifetime relation,

$$f_{co} = \frac{\sqrt{3}}{2\pi\tau_i} \qquad (4)$$

In eq.4, f_{co} is the optical bandwidth and τ_i the photoluminescence lifetime, also the carrier lifetime. The mono-exponential decay parameters found for this curve are, $a_1 = 1$, $\tau_1 = 2.0$ ns and $f_{co} = 139.6$ MHz.

Figure 5 plots the optical bandwidth values versus the InGaN LED bias current for the bare and unfiltered hybrid micro-LED as well as the intrinsic modulation bandwidth of the membrane. The data is also summarized in Table 1 along with the respective goodness of fit (GoF) values. The GoF is a statistical analysis that characterizes how well the fit describes the measured data, *i.e*., is a parameter often used to describe the discrepancy between a set of raw data and a model. With GoF = 1 being a perfect fit and GoF < 1 indicating some discrepancy between data.

Table 1. Table with bandwidth values, f_{co}, for the II-VI membrane (hybrid micro-LED - a long pass filter was used to remove the blue light), the bare micro-LED and the unfiltered hybrid device, the goodness of fit, *GoF* and the lifetime, τ_i.

	Bare micro-LED		Intrinsic II-VI membrane response			Unfiltered Hybrid LED	
I (*mA*)	f_{co} (*MHz*)	*GoF*	f_{co} (*MHz*)	τ_i (*ns*)	*GoF*	f_{co} (*MHz*)	*GoF*
5	22.5	0.991	77.8	3.5	0.947	15.7	0.997
10	29.2	0.988	126.5	2.2	0.958	22.8	0.995
20	36.8	0.987	151.4	1.4	0.875	32.4	0.993
40	58.0	0.983	149.4	1.8	0.922	38.4	0.993
60	58.4	0.963	132.9	2.1	0.934	41.1	0.995
80	69.3	0.986	139.6	2.0	0.947	46.6	0.996
100	78.9	0.990	144.0	1.9	0.837	51.3	0.995

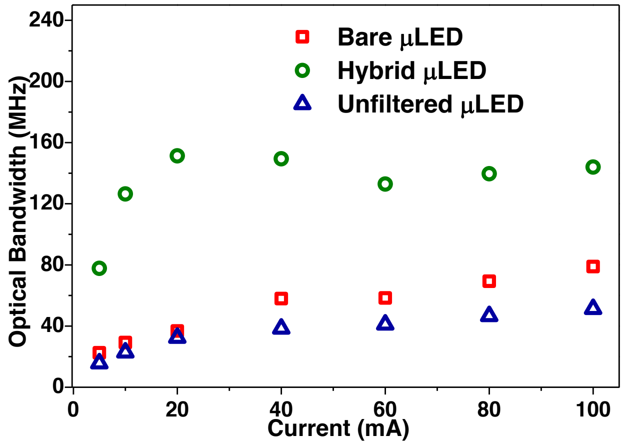

Figure 5. The -3dB optical bandwidths of the bare µLED and of the demonstrator hybrid µLED (unfiltered) – the intrinsic bandwidth values of the membrane (hybrid µLED) are also plotted.

The micro-LED bandwidth is current dependent and reaches 79 MHz at 100 mA. This current dependency can be attributed to the reduced carrier lifetime in the InGaN micro-LED active region as the current, and hence the carrier density, increases [13], [14]. The typical intrinsic response of the membrane is 145 MHz, much faster than conventional phosphors, see also Figure 6. The hybrid micro-LED behavior is the combination of the frequency responses of the color-converting membrane and the underlying micro-LED. The result is a modulation cut-off frequency of 51 MHz limited by the slower of the two components, *i.e*. the micro-LED response in this case. Higher modulation bandwidths are expected by using blue micro-LEDs of even smaller dimensions [2].

4.2 Power density dependence of the intrinsic bandwidth of the color-converting membrane

The dependence of the color-converter bandwidth on the incident micro-LED pump power density was further studied. Since the micro-LED is in flip-chip configuration, *i.e*. the emission occurs through the sapphire substrate, the excitation area at the membrane/sapphire interface is determined by the divergence of the micro-LED light and the propagation length through the sapphire. Due to the small LED size, the excitation spot incident on the membrane can in good approximation be assumed to be circular with diameter equal to the substrate thickness, *i.e*., 330 +/- 20 µm in this case [15]. The intrinsic bandwidth data of the membrane as previously determined is then plotted again in Figure 6 as a function of the incident excitation power density ('integrated membrane'). For pump power density between 1 and 1.75 W/cm^2, the intrinsic bandwidth is constant at 145 MHz.

In order to observe with more confidence the bandwidth behavior of the MQW membrane at excitation power density below 1 W/cm^2, it was independently characterized, *i.e*. when separated from the micro-LED, as a stand-alone membrane. In this case the membrane was held onto a glass substrate and remotely pumped with a 450nm micro-LED as explained in section 2. Results are plotted in Figure 6 (black squares, 'stand-alone membrane').

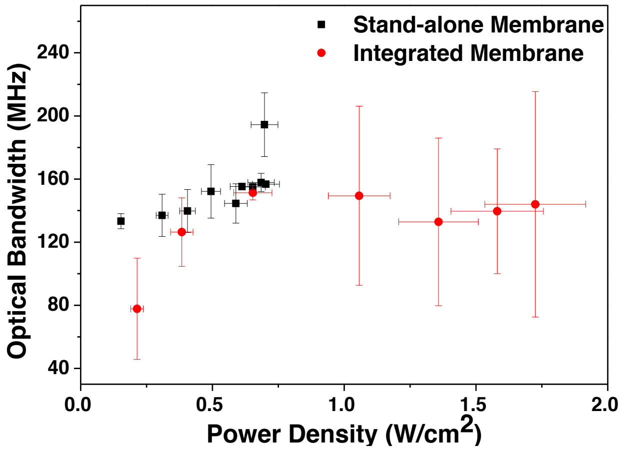

Figure 6. Bandwidth dependence over different power densities.

The vertical error bars in Figure 6**Error! Reference source not found.** represent the root mean square errors of the fits of the frequency responses. Overall, there is no significant power density dependence of the membrane intrinsic bandwidth. The average bandwidth over the range of 450nm light power density corresponding to the operation of the hybrid µLED is around 150 MHz. This corresponds to an effective carrier lifetime of 1.85 ns. This value can be corroborated by direct time-correlated single photon counting, TCSPC, measurement of the stand-alone membrane. Such TCSPC analysis was done using an Edinburgh Instruments system using an EPL-450 Picosecond pulsed diode laser as the excitation source (450 nm). Differences in the TCSPC lifetime measurement were seen between membranes processed from the same epilayer structure however, the average measured lifetime from a number of such membranes was found to be 1.36 ± 0.21 ns, showing reasonable consistency with the frequency response data.

The photoluminescence and the optical bandwidth of the MQW membrane, which is two-orders of magnitude higher than for phosphors, means that high-speed color-conversion can be realized for a range of light levels that correspond to micro-LED operation.

5. Conclusions

This proof-of-concept demonstration of a hybrid µLED with integrated MQW membrane offers a pathway to fast-response and robust color conversion and has potential for VLC applications. The modulation bandwidth of the 540nm hybrid micro-LED was measured to be up to 51 MHz for an intrinsic bandwidth of the MQW membrane and of the underlying micro-LED of 145MHz and 79 MHz, respectively. Higher modulation bandwidths of the hybrid device are expected by reducing the dimensions of the LED. The integration approach of the membrane by liquid-capillary bonding is well-suited to transfer-printing approaches [16]. It could be extended to other wavelengths using for example MQW structures based on III-V AlGaInP and/or InGaN material systems.

ACKNOWLEDGMENTS

This research work was supported by the EPSRC Programme Grant “Ultra-parallel visible light communications (UP-VLC)” (**EP/K00042X/1**). The authors would like to acknowledge Dr. Enyuan Xie for the micro-LED fabrication.

REFERENCES

[1] A. Jovicic, J. Li, and T. Richardson, “Visible Light Communication : Opportunities , Challenges and the Path to Market,” *IEEE Commun. Mag.*, no. December, pp. 26–32, 2013.

[2] J. J. D. Mckendry, D. Massoubre, S. Zhang, B. R. Rae, R. P. Green, E. Gu, R. K. Henderson, A. E. Kelly, and M. D. Dawson, “Visible-Light Communications Using a CMOS-Controlled Micro-Light-Emitting-Diode Array,” *J. Light. Technol.*, vol. 30, no. 1, pp. 61–67, 2012.

[3] N. Laurand, B. Guilhabert, J. McKendry, A. E. Kelly, B. Rae, D. Massoubre, Z. Gong, E. Gu, R. Henderson, and M. D. Dawson, “Colloidal quantum dot nanocomposites for visible wavelength conversion of modulated optical signals,” *Opt. Mater. Express*, vol. 2, no. 3, p. 250, Feb. 2012.

[4] M. A. Haase, J. Xie, T. A. Ballen, J. Zhang, B. Hao, Z. H. Yang, T. J. Miller, X. Sun, T. L. Smith, and C. A. Leatherdale, “II–VI semiconductor color converters for efficient green, yellow, and red light emitting diodes,” *Appl. Phys. Lett.*, vol. 96, no. 23, p. 231116, 2010.

[5] D. Schiavon, M. Binder, A. Loeffler, and M. Peter, “Optically pumped GaInN / GaN multiple quantum wells for the realization of efficient green light-emitting devices,” *Appl. Phys. Lett.*, vol. 113509, pp. 1–5, 2013.

[6] B. Damilano, H. Kim-Chauveau, E. Frayssinet, J. Brault, S. Hussain, K. Lekhal, P. Vennegues, P. De Mierry, and J. Massies, “Metal Organic Vapor Phase Epitaxy of Monolithic Two-Color Light-Emitting Diodes Using an InGaN-Based Light Converter,” *Appl. Phys. Express*, vol. 092105, 2013.

[7] J. J. D. McKendry, R. P. Green, A. E. Kelly, Z. Gong, B. Guilhabert, D. Massoubre, E. Gu, and M. D. Dawson, “High-Speed Visible Light Communications Using Individual Pixels in a Micro Light-Emitting Diode Array,” *IEEE Photonics Technol. Lett.*, vol. 22, no. 18, pp. 1346–1348, Sep. 2010.

[8] Z. Gong, S. Jin, Y. Chen, J. McKendry, D. Massoubre, I. M. Watson, E. Gu, and M. D. Dawson, “Size-dependent light output, spectral shift, and self-heating of 400 nm InGaN light-emitting diodes,” *J. Appl. Phys.*, vol. 107, no. 1, p. 013103, 2010.

[9] X. Zhou, M. Munoz, M. C. Tamargo, and Y. C. Chen, “Optically pumped laser characteristics of blue Znx′Cdy′Mg1−x′−y′Se/ZnxCdyMg1−x−ySe single quantum well lasers grown on InP,” *J. Appl. Phys.*, vol. 95, no. 1, p. 7, 2004.

[10] R. Moug, A. Alfaro-Martinez, L. Peng, T. Garcia, V. Deligiannakis, A. Shen, and M. Tamargo, “Selective etching of InGaAs/InP substrates from II-VI multilayer heterostructures,” *Phys. Status Solidi*, vol. 9, no. 8–9, pp. 1728–1731, Aug. 2012.

[11] Z. L. Liau, “Semiconductor wafer bonding via liquid capillarity,” *Appl. Phys. Lett.*, vol. 77, no. 5, p. 651, 2000.

[12] J. Lakowicz, *Principles of Fluorescence Spectroscopy*, 3rd ed. .

[13] E. F. Schubert, *Light-Emitting Diodes*, 2nd ed. Cambridge University Press, 2006, p. 434.

[14] R. P. Green, J. J. D. McKendry, D. Massoubre, E. Gu, M. D. Dawson, and A. E. Kelly, “Modulation bandwidth studies of recombination processes in blue and green InGaN quantum well micro-light-emitting diodes,” *Appl. Phys. Lett.*, vol. 102, no. 9, p. 091103, 2013.

[15] J. Herrnsdorf, Y. Wang, J. J. D. McKendry, Z. Gong, D. Massoubre, B. Guilhabert, G. Tsiminis, G. A. Turnbull, I. D. W. Samuel, N. Laurand, E. Gu, and M. D. Dawson, “Micro-LED pumped polymer laser: A discussion of future pump sources for organic lasers,” *Laser Photon. Rev.*, vol. 7, no. 6, pp. 1065–1078, Nov. 2013.

[16] A. J. Trindade, B. Guilhabert, D. Massoubre, D. Zhu, N. Laurand, E. Gu, I. M. Watson, C. J. Humphreys, and M. D. Dawson, “Nanoscale-accuracy transfer printing of ultra-thin AlInGaN light-emitting diodes onto mechanically flexible substrates,” *Appl. Phys. Lett.*, vol. 103, no. 25, p. 253302, 2013.

Hybrid InGaN LEDs with capillary-bonded MQW color-converting membranes

J. M. M. Santos[1], B. E. Jones[1], P. J. Schlosser[1], J. Herrnsdorf[1], B. Guilhabert[1], J. De Jesus[2], T. A. Garcia[2],
M. C. Tamargo[2], J. E. Hastie[1], N. Laurand[1] and M. D. Dawson[1]

[1] *Institute of Photonics, University of Strathclyde, Glasgow G4 0NW, UK*
[2] *Department of Chemistry, City College of New York, New York NY 10031, USA*
E-mail: *joao.santos@strath.ac.uk*

Abstract: Hybrid sources consisting of 450nm InGaN LEDs with capillary-bonded micron-thick multi-quantum-well color-converting membranes are reported. Such sources are attractive for visible light communications and a 540nm-emitting hybrid LED having a 57MHz modulation bandwidth is demonstrated.

Introduction: The development and widespread adoption of LED technologies are creating opportunities for visible light communications (VLC), where visible light sources are used to transmit data [1]. VLC requires sources that are not only efficient but also wavelength-versatile, *e.g.* white LEDs that could combine the functions of illumination and data transfer as well as discrete-color LEDs ideally covering the entire visible spectrum. Typical white LEDs, and visible color-converted LEDs in general, are obtained by combining blue InGaN-based LEDs with rare-earth color-converting phosphors. This approach is efficient but not suited for VLC. The modulation bandwidth of resulting color-converted LEDs is limited to ~ 1 MHz whereas unconverted blue InGaN-based LEDs have bandwidths of 20 MHz up to 400 MHz depending on their formats, with single-color data links at > 1Gbit/s rate demonstrated [2].

Here, we look at an alternative color-conversion approach for VLC that is based on a blue-emitting LED optically pumping a micron-thick inorganic semiconductor epilayer membrane. The latter is made of a multi-quantum-well (MQW) active region and can be directly bonded by capillarity onto the sapphire window of a LED for full integration. The amount of LED light absorbed and the converted wavelength are set by the design of the membrane active region. We report a 540nm hybrid LED demonstrator obtained in this way by capillary-bonding a II-VI CdMgZnSe MQW membrane onto an array of 450nm InGaN micron-size LEDs. The intrinsic optical bandwidth of the II-VI membrane in this demonstrator is measured to be 180 MHz while the bandwidth of the full hybrid green LED is 57 MHz when driven at 100 mA (the bandwidth of the blue LED alone is 85 MHz).

Fabrication: An array in a flip-chip format of individually addressable 450nm micro-LEDs, each 100 µm x 100 µm in size, is used. The full LED device fabrication follows the same processes as described in ref [3]. The sapphire substrate of the array acts as an interface for capillary-bonding a MQW color-converting membrane. The MQW membranes have typically a surface area of a few mm^2 and are only a few microns thick as the growth substrate is removed by appropriate wet etching. For the latter, the structure is first fixed onto a temporary glass substrate using an epoxy and then exposed to selective chemical etching. HCl and H_3PO_4:H_2O_2:H_2O are used to etch away, respectively, the InP substrate and the InGaAs buffer layer to form II-VI membranes. The hybrid device is finalized by removing the membrane from the temporary glass substrate and by bonding it onto the sapphire window of the micro-LED array (Fig 1a).

Experimental results: A typical bare single micro-LED emits an optical power of 4 mW at 450 nm for a 100mA DC driving current (*i.e.* a 40W/cm^2 power density for a 1kA/cm^2 current density). The 2.5µm-thick II-VI membrane of the demonstrator device absorbs 85% of the micro-LED 450nm emission and emits an optical power of 40 µW centered at 540 nm (Fig. 1b). The blue-to-green color conversion efficiency (1-2%) is currently limited by waveguided light and by the overall membrane conversion efficiency. Improved epilayer design and implementation of light extraction schemes should improve this value significantly. The modulation bandwidths of the bare LED and hybrid LED were measured using a modulation signal of varying frequency on top of a DC bias (typ. 500mV amplitude peak-to-peak) and a fast photodiode for the detection. The modulation bandwidth is defined as the frequency where the detected optical (electrical) power drops by 3 dB (6 dB). The electrical frequency responses of the bare blue LED and of the hybrid green LED are plotted in Fig. 2a in the case where the InGaN LED bias current is 80 mA. The intrinsic response of the membrane can be obtained from these data. Figure 2b summarizes the -3dB optical bandwidth values versus the InGaN LED bias current again for the bare and hybrid LED. The intrinsic response characteristics of the membrane are also plotted. The latter is close to 180 MHz while the bare micro-LED bandwidth is current-dependent and reaches up to 85 MHz. This current dependency can be attributed to the reduced carrier lifetime in the InGaN LED active region as the current, hence the carrier density, increases. The hybrid device behavior is the combination of the frequency responses of the color-converting membrane and the underlying LED. The result is a modulation cut-off frequency of 57 MHz limited by the slower of the two components, *i.e.* the micro-LED response in this case. Higher modulation bandwidths are expected by using blue LEDs of even smaller dimensions [2].

Conclusion: This demonstration of a hybrid LED with integrated MQW membrane offers a pathway to fast-response color conversion and proves that the concept is attractive for VLC. There are several options for wavelength coverage across the visible spectrum with available semiconductor alloys for MQW membranes including III-V AlGaInP (yellow to red), InGaN (green) and II-VI CdMgZnSe (green to orange) [4,5]. The technology has the benefits of being based on all-inorganic semiconductors and is therefore inherently robust. It also leads to extremely compact sources. Finally, the device geometry is well suited for high-resolution transfer-printing [6] and related integration concepts will be discussed.

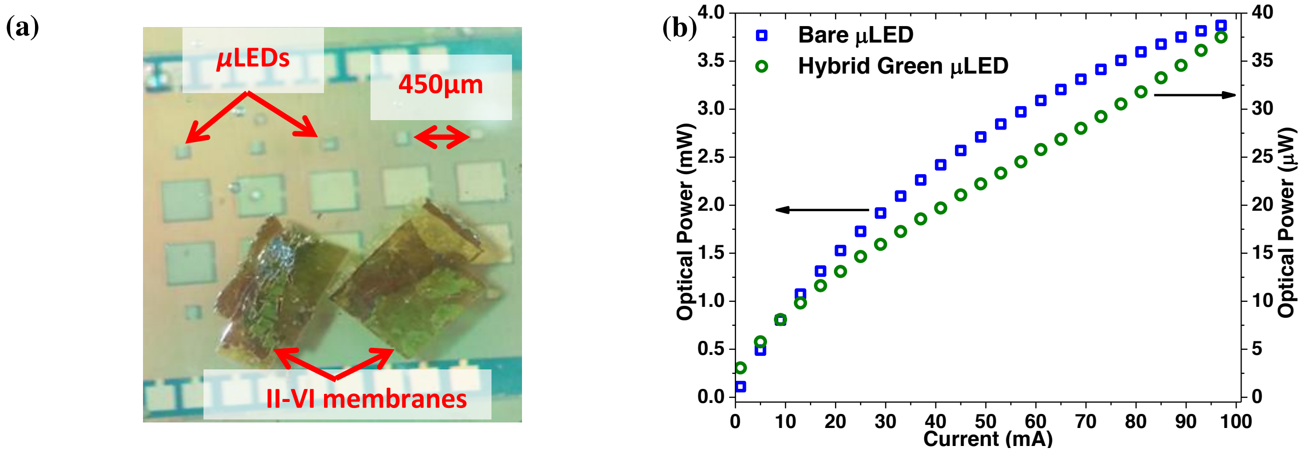

Figure 1: a) Photograph of the hybrid device; b) Optical powers of the devices measured in DC (bare and hybrid).

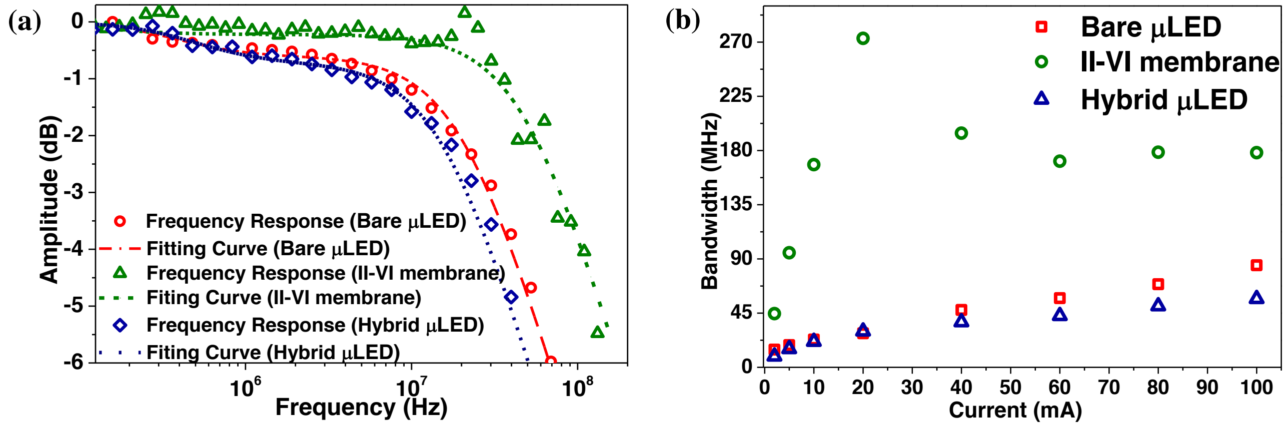

Figure 2: a) Frequency response of the μLED and the color-converter with the respective bi-exponential fits at same injected current; b) The -3dB optical bandwidths of the bare LED and of the demonstrator hybrid LED – the intrinsic bandwidth values of the membrane are also plotted.

References

[1] Elgala H. *et al.*, IEEE Xplore, 1127–1134 (2009)
[2] Mckendry J. *et al.*, Photon. Technol. Lett. **22**, 1346 (2010)
[3] Gong. Z, *et al.*, Appl. Phys. Lett. **107**, 013103 (2010)
[4] Schiavon D. *et al.*, Appl. Phys. Lett. **102**, 113509 (2013)
[5] Haase M. A. *et al.*, Appl. Phys. Lett. **96**, 231116 (2010)
[6] Trindade A.J. *et al.*, Appl. Phys. Lett. **103**, 253302 (2013)

Functional nanomembrane for visible light down-conversion

J. M. M. Santos,[1] S. Watson,[2] B. Guilhabert,[1] Peter J. Schlosser,[1] A. Krysa, [3] A. E. Kelly,[2] N. Laurand,[1] M. D. Dawson[1]

[1]University of Strathclyde, Institute of Photonics, Physics, Glasgow, UK
[2]University of Glasgow, Electronic & Electrical Engineering, Glasgow, UK
[3]University of Sheffield, Electronic & Electrical Engineering, Sheffield, UK
email: joao.santos@strath.ac.uk

Summary

We report a color down-converting scheme for blue InGaN lasers and LEDs based on a multi-quantum-well nanomembrane, itself hybridized onto a hemispherical lens for light-extraction enhancement. The fast modulation response (> 80 MHz) of this color-converter makes it suitable for visible light communications.

Introduction

Color-conversion of blue-emitting InGaN LEDs and lasers is a key element in applications like solid-state lighting, illumination and visible light communications (VLC) [1-3]. For these, maximizing conversion efficiency, thermal and power stability, controlling spatial distribution, as well as simplifying device integration of the converter, are all crucial. In the case of VLC, the down-converter is also required to respond quickly to modulation, thereby eliminating standard phosphor materials as a viable option [3].

Here, we demonstrate a down-converting scheme that utilizes an inorganic multi-quantum-well (MQW) nanomembrane (NM). Because the NM is optically pumped, there is no need for doping. The approach therefore enables, in principle, blue-to-green, blue-to-yellow/orange and blue-to-red conversion through proper design of the MQW region using GaN and AlInGaP alloys. Furthermore, the mechanical properties of NMs facilitate hybridization with a range of materials and optical elements for added functionalities (light extraction, directionality, thermal management etc.). The demonstrator that we report is an AlInGaP NM optimized for absorption at 450 nm and emission at 650 nm. It is hybridized with a hemispherical lens. Details about the fabrication and characterization of this converter are given in the following.

Fabrication and characterization

The MQW region was grown by molecular beam epitaxy on a GaAs substrate. It has a total of 6 InGaP/AlInGaP quantum wells distributed by pairs over the 5λ/2 sub-cavity that forms the NM. The active region is enclosed by two 10nm InGaP capping layers. The structure is designed for >90% absorption of 450nm light. The NM is obtained by chemical removal of the GaAs substrate. For this step, the sample is held

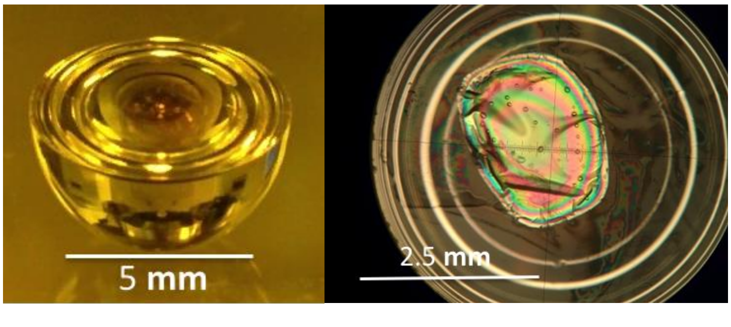

Fig. 1 (Left) photograph of the NM deposited onto the hemispherical lens; (right) close-up on the NM side

onto a sapphire hemispherical lens using a polyethylene glycol wax. This wax can be subsequently removed by floating the sample followed by capillary bonding of the sample to the lens. The final NM color-converter is shown in Fig. 1. The conversion characteristics were measured by exciting the NM with a 450nm microsize LED (100µmx100µm area), collecting the down-converted light on the convex side of the lens. The NM photoluminescence is displayed in Fig. 2. The enhancement effect of the lens on the downconverted light is demonstrated by comparing emission from the sample with that of an equivalent, reference NM deposited onto a flat glass (n=1.5) substrate (Fig. 3). This 4x enhancement in light extraction is due to the higher refractive index of sapphire (n=1.77) and the convex lens shape. Both combine to reduce the amount of light waveguided in the NM. We note that a bigger enhancement is expected if using a lens material with a refractive index closer to that of the NM (n=3.4). The frequency response of the color-converter was measured by modulating the LED. The intrinsic -3dB optical bandwidth of the converter is between 80 MHz and 90 MHz for the range of LED current of 20 mA to 180 mA. This bandwidth is more than two orders of magnitude higher than for the phosphors that are commonly used in color-converted InGaN LEDs.

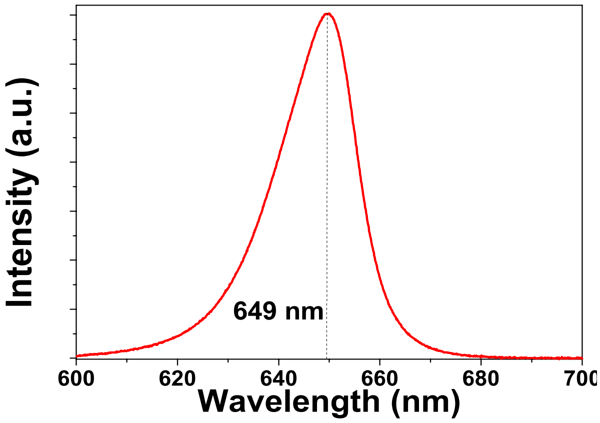

Fig. 2. Photoluminescence spectrum

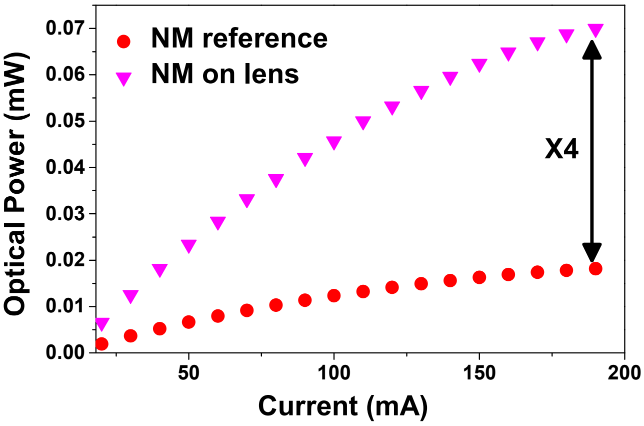

Fig. 3 Down-converted power versus LED current for the NM/lens sample and the reference structure

Conclusion

We have reported a red-emitting AlInGaP MQW nanomembrane hybridized onto a hemispherical lens to color-convert a blue InGaN LED. The lens structure very simply adds a light extraction functionality to the color-converting properties of the NM. We expect that this approach can be extended to other wavelengths across the visible. It is attractive for VLC applications as well as for high-power laser conversion.

References

[1] J. McKittrick and L. E. Hea-Rohwer, *J. Am. Ceram. Soc.*, **97**, 1327, 2014
[2] J. J. Wiere, Jr et al., *Laser Photonics Rev.*, **7**, 963, 2013
[3] J. Grubor et al., *J. Lightwave Technol.*, **26**, 3883, 2008

MQW nanomembrane assemblies for visible light communications

J. M. M. Santos[1], S. Watson[2], B. Guilhabert[1], A. Krysa[3], A. E. Kelly[2], N. Laurand[1] and M. D. Dawson[1]

[1]Institute of Photonics, University of Strathclyde, Glasgow, UK
[2]University of Glasgow, Electronic & Electrical Engineering, Glasgow, UK
[3]University of Sheffield, Electronic & Electrical Engineering, Sheffield, UK
E-mail: joao.santos@strath.ac.uk

Abstract: We report color-conversion of InGaN LEDs and lasers using an AlInGaP multi-quantum-well nanomembrane. In particular, we demonstrate free-space OOK data transmission at 180 Mb/s from a laser diode blue-to-red converted by a heterogeneous nanomembrane/sapphire lens assembly.

Introduction: InGaN optoelectronics can be combined with efficient down-converting materials for applications in LED- and laser-based lighting and illumination [1-3]. The concept can be extended to visible light communications (VLC), which uses solid-state visible sources to transmit data, with the added requirement of a short excited-state lifetime for the color-converting material so that sources can be modulated at high speed [4 – 6]. In this work, we report color-conversion of 450nm micro-LEDs and of a 450nm laser diode (LD) with structures based on an AlInGaP inorganic MQW nanomembrane (NM). One advantage of the inorganic NM over alternative color-converters is its photo- and thermal stability. The thermal performance of the NM can be increased by judicious heterogeneous integration with other materials, *e.g.* sapphire or diamond, which can further be shaped to improve extraction efficiency. This capability makes inorganic NMs ideal candidates for color conversion of high power light sources. In the following, we describe the fabrication of the NM color-converting structure and devices. We then discuss the experimental characterization of a corresponding hybrid LED and of a remote color-converter for the LD. We also report on the initial demonstration of free-space OOK data transmission of the latter.

Fabrication: The color-converter MQW region was grown by molecular beam epitaxy on a GaAs substrate. It has a total of 6 InGaP/AlInGaP quantum wells distributed in pairs over a $5\lambda/2$ sub-cavity enclosed by two 10nm InGaP capping layers. This structure is designed to absorb more than 90% at 450 nm and for re-emission in the red at 650 nm but other wavelengths are possible by modifying the design. After processing, the membranes have typically a surface area of a few mm^2 and are several hundred nanometers thick, which helps ensure efficient Van der Waals bonding and assembly of multi-element structures as described below. For processing, the MQW structure is first fixed onto a temporary glass holder using DI-water for adherence and then exposed to selective chemical etching to remove the GaAs substrate. After the membrane is separated from the temporary glass substrate by floating in water, it is, for the hybrid LED, bonded by capillarity onto the sapphire window (polished epi-substrate) of the micro-LED array (Fig 1a). A sapphire or diamond lens, with a hemispherical diameter of 2 mm and 4 mm and focal length of 0.5 mm and 4 mm respectively, is subsequently bonded on top to improve light extraction (Fig 1.b). The micro-LED array used for the fully hybridized LED (Fig 1b) was designed in a flip-chip format with individually addressable 450nm-emitting square pixels ranging from 150 µm x 150 µm down to 50 µm x 50 µm in size. The full LED device fabrication follows the same processes as described in [7]. For the remote LD pumping samples, the membrane is simply bonded to the sapphire or diamond lens after the floating step. An optional dielectric mirror can be added.

Experimental results: All samples were studied in terms of L-I-V and modulation bandwidth responses. Different pixel sizes were measured in the case of the hybrid LED. The converted optical power from the NM depends on the size of the pixel (Fig 1c). A typical hybrid micro-LED of 150 µm x 150 µm has a maximum optical power of 0.12 mW with peak emission at 650 nm. This is currently limited by thermal rollover as there is no heat-sinking implemented, but the sapphire lens already helps to spread the heat. It was found that the color-converter's extracted power efficiency when using a diamond or sapphire lens was 0.96 ± 0.23%. The electrical-to-optical bandwidth of the hybrid LED was up to 65 MHz, the intrinsic

NM bandwidth being 130 MHz. The extracted power can be further increased by adding a high-reflectivity mirror on one side of the NM, as was done for one of the LD-pumped samples. In this case the color-converter's efficiency was 1.14 ± 0.26% compared to 0.42 ± 0.02% with no mirror. Data transmission was carried out under remote LD pumping on a converter with no mirror. The DC signal was combined with the RF one, in a 2^7-1 PRBS OOK scheme, using a Bias-Tee. Error-free data at 180 Mb/s for a BER of 10^{-9} was obtained (Fig 2b). With improvements in the LD driving conditions and the use of high level encoding schemes such OFDM we expect to be able to push the data rate to Gb/s levels.

Conclusion: We report nanomembrane-based fast-response color conversion and prove that the concept is attractive for VLC with, in principle, wavelength coverage across the visible spectrum possible with III-V AlGaInP (yellow to red), InGaN (green) and II-VI CdMgZnSe (green to orange) [8, 9] epitaxial alloys. We have shown a fully integrated hybrid LED and demonstrated OOK error-free transmission at 180 Mb/s (BER of 10^{-9}) for a LD-pumped NM. Finally, we note that the NM geometry is attractive for controlled nano-assembly using transfer-printing [10] and recent advances on the printing of AlInGaP NMs for color conversion applications will also be presented

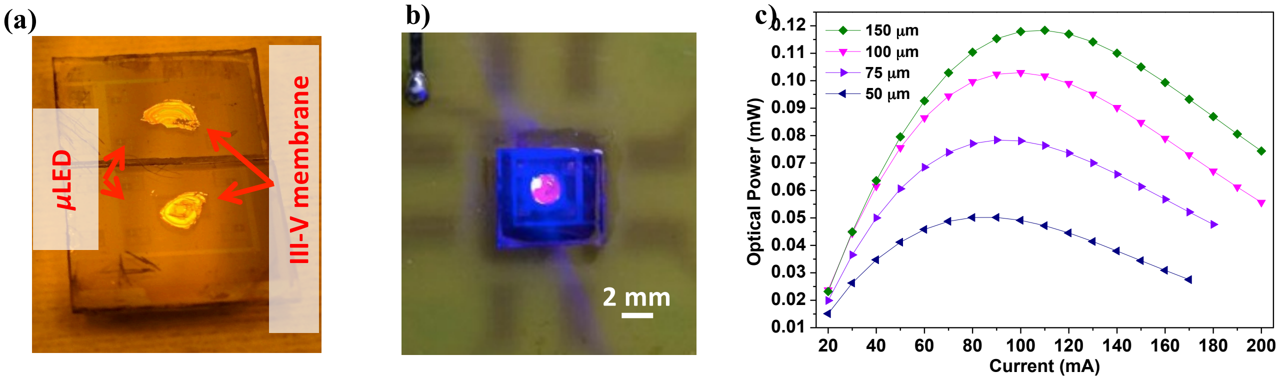

Figure 1: a) Two micro-LED chips with capillary-bonded AlInGaP membranes, b) Hybrid LED with integrated sapphire lens under operation and c) Hybrid LED L-I curve for different micro-LED pixel sizes.

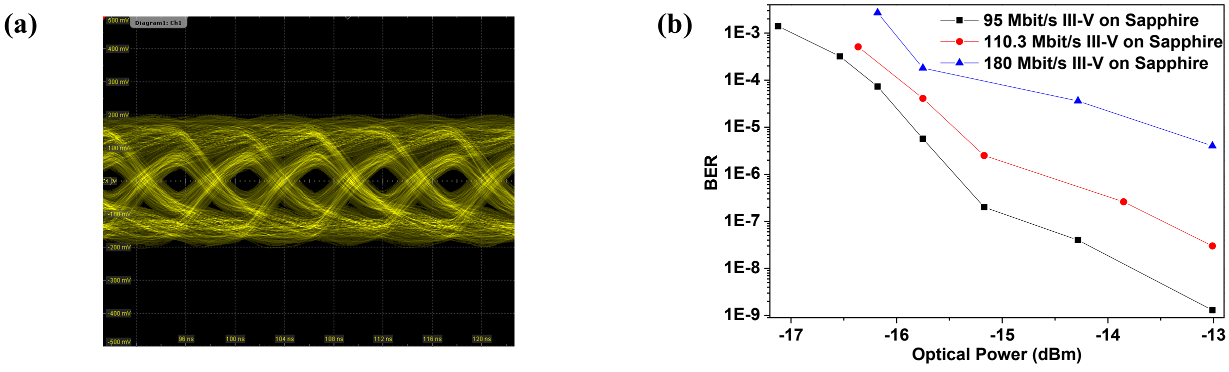

Figure 2: a) Eye-diagram at 180Mbits/s, b) OOK modulation BER for the NM/sapphire lens structure.

References

[1] J. J. Wierer *et al.*, Laser Photonics Rev., 963–993 (2013)
[2] I. L. Azevedo *et al.*, Proc. IEEE, 481–510 (2009)
[3] K. a. Denault *et al.*, AIP Adv., 0–6, (2013)
[4] J.M.M. Santos *et al.*, Semicond. Sci. Technol., 035012 (2015)
[5] J. J. D. McKendry *et al.*, IEEE Photonics Technol. Lett., 1346–1348 (2010)
[6] S. Watson *et al*, Opt. Lett., 3792–4 (2013)
[7] Z. Gong *et al.*, J. Appl. Phys., 013103 (2010)
[8] D. Schiavon *et al*, Appl. Phys. Lett., 113509 (2013)
[9] M. A. Haase *et al.*, Appl. Phys. Lett., 231116, (2010)
[10] A. J. Trindade *et al.*, Appl. Phys. Lett., 253302, (2013)

Fast colour conversion of InGaN sources using semiconductor nanocrystals

J. M. Santos[1], M. Leitao[1], C. Foucher[1], S. Rajbhandari[2], D. Vithanage[3], B. Guilhabert[1],
G. A. Turnbull[3], I. D. W. Samuel[3], D. O'Brien[2], N. Laurand[1] and M. D. Dawson[1]

1) Institute of Photonics, Department of Physics, University of Strathclyde, Glasgow, G1 1RD, UK
2) Department of Engineering Science, University of Oxford, Oxford OX1 3PJ, UK
3) School of Physics and Astronomy, University of St Andrews, St Andrews KY16 9SS, UK

Visible light communication using InGaN light sources colour-converted with colloidal quantum dot structures is reported. Free-space data transmission up to 500 Mb/s is demonstrated.

Semiconductor nanocrystals, or colloidal quantum dots (CQDs), can act as efficient downconverters for InGaN sources, e.g. LEDs [1]. Advantages of CQDs over other types of converting phosphors for this utilisation include their soft-material processing capabilities, their narrow linewidth photoluminescence (PL) and the fine colour tunability. In turn, CQDs can be combined with blue InGaN LEDs for high performance white light sources having high colour quality [1], and for enabling a wide gamut display technology that is found in CQD-enhanced LCD screens. Applications of InGaN-based light sources other than lighting and displays are also emerging. One of these is visible light communications (VLC), which exploits the relatively high bandwidth of InGaN lasers and/or LEDs in order to transmit data over free space or, in some instances, through fibre and waveguide systems. Here again, CQDs can enable both white and single-colour sources with attractive characteristics. Narrow emission for example will facilitate implementation of wavelength division multiplexing. In addition, CQDs have shorter PL lifetime than the rare-earth phosphors commonly used in commercial LEDs, and are therefore more suited to VLC [2].

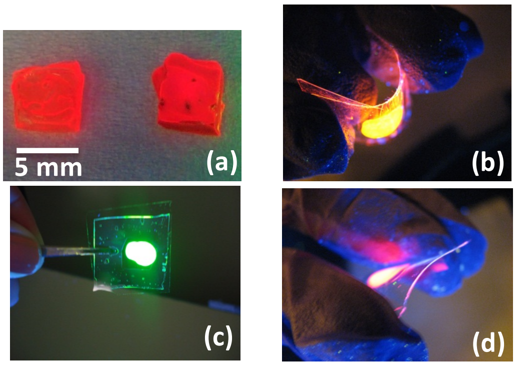

Fig. 1. (a) Red CQD composite converters, and (b), (c) and (d), Flexi-glass CQD converters

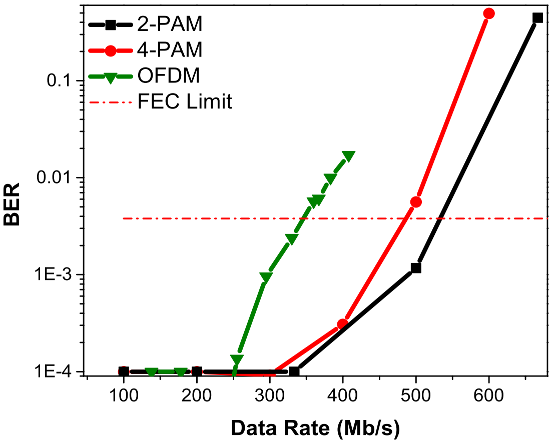

Fig. 2. Free-space transmission; BER vs data rate for different modulation schemes

In this work, we explore two formats of CQD colour-converters for blue-emitting InGaN sources. The CQDs are alloyed-core CdSeS/ZnS structure with a 6nm nominal diameter and emission in the green (540nm), yellow (575nm) and red (630nm). In the solid state, the photoluminescence quantum efficiency is 62%, 54% and 18% for the green, yellow and red CQDs respectively. The first format of converter consists of a polymeric composite film that incorporates the CQDs at weight concentrations of 1% and 10 %. Nanocomposite films with thickness of 1.2 mm were fabricated (see Fig. 1(a)) and the effect of the CQD concentration on the static and dynamic PL characteristics will be discussed. The second format of converter utilises CQDs in neat form that are encapsulated with flexible glass. For this, a 30μm-thick glass sheet was diced into 2 x 2 cm^2 membranes. A CQD/chloroform solution was drop coated onto one glass membrane and a second membrane was then added to seal the CQD structure. The final flexi-glass CQD colour-converting structures are thin enough to retain flexibility (see Fig. 1(b) and (d)).

Both the composite and flexi-glass colour-converters can be placed in contact with an InGaN source or, alternatively, remotely pumped. A 450nm microLEDs was used as the blue InGaN source in our experiments. The CQD structures are designed for >99% absorption of light at this wavelength. The forward power conversion efficiency was measured to be up to 14% depending on the wavelength, the type and the concentration of the converters. We note that there is room for improvement as no light extraction features were utilised. One way to incorporate such feature would be to directly patterned the CQDs by soft-lithography, e.g. with grating structures [3-4].

The -3dB modulation bandwidth of the CQD converters is comprised between 10 MHz and 30 MHz, again depending on the exact converter parameters. In turn, we demonstrate free-space data transmission ranging from 200 Mb/s up to 500 Mb/s per wavelength using pulse amplitude modulation (PAM) or orthogonal frequency division modulation (OFDM) and considering a forward error correction (FEC) limit of $3.8\text{x}10^{-3}$. For the experiment, the 450nm microLED was DC-biased and coupled to the CQD colour-converters. Otherwise, details of the experimental set-up are similar to what is described in [5]. Figure 2 represents the data for the red CQD composite. For all the above CQD samples, under the same conditions, PAM leads to superior data rates than OFDM.

In conclusion, we report two formats of CQD downconverters for use with InGaN optical sources and demonstrate free space VLC with data rates up to 500 Mb/s per wavelength.

[1] T. Erdem and H. V. Demir, 'Color science of nanocrystal quantum dots forlighting and displays' Nanophotonics 2(1), pp. 57–81 (2013)

[2] N. Laurand, B. Guilhabert, J. McKendry, A. E. Kelly, B. Rae, D. Massoubre, Z. Gong, E. Gu, R. Henderson, and M. D. Dawson 'Colloidal quantum dot nanocomposites for visible wavelength conversion of modulated signals', Optical Materials Express, 2(3), pp. 250-260 (2012)

[3] J. Herrnsdorf, B. Guilhabert, J. McKendry, Z. Gong, D. Massoubre, S. Zhang, S. Watson, A. E. Kelly, E. Gu, N. Laurand, and M. D. Dawson 'Hybrid organic/GaN photonic crystal light-emitting diode', Applied Physics Letters 101(14), 141122 (2012)

[4] R. Clatyton Shallcross, G. S. Chawla, F. Saneeha Marikkar, S. Tolbert, J. Pyun, and N. R. Armstrong 'Efficient CdSe nanocrystal diffraction gratings prepared by microcontact molding', ACS Nano, 3(11), pp. 3629-3637 (2009)

[5] D. Tsonev, H. Chun, S. Rajbhandari, J. J. D. Mckendry, S. Videv, E. Gu, M. Haji, S. Watson, A. E. Kelly, G. Faulkner, M. D. Dawson, H. Haas, and D. O. Brien, "A 3-Gb / s single-LED OFDM-based weireless VLC link using a gallium nitride μLED," IEEE Photonics Technology Letters, 26 (7)., pp. 637-640 (2014)

Colloidal quantum dot color converters for visible light communications

J. M. Santos,[1] M. Leitao,[1,*] C. Foucher,[1] B. Guilhabert,[1] S. Watson,[2] A. E. Kelly,[2] S. Rajbhandari,[3,§] H. Chun,[3]
H. Haas,[4] G. Faulkner,[3] D. C. O'Brien,[3] N. Laurand[1,*] and M. D. Dawson[1]

[1] *Institute of Photonics, Department of Physics, SUPA, University of Strathclyde, Glasgow*
[2] *School of Engineering, University of Glasgow, Glasgow, UK*
[3] *Department of Engineering Science, University of Oxford, Oxford, UK*
[4] *Li-Fi R&D Centre, Institute for Digital Communications, University of Edinburgh, Edinburgh, UK*

***Abstract*— The properties and performance of CdSSe/ZnS colloidal quantum dot composite materials for use as InGaN LED color converters in visible light communications applications is reported. 500Mb/s optical wireless transmission is demonstrated.**

I. INTRODUCTION

The electronic and optical properties of colloidal quantum dots (CQDs) make them appealing for color conversion of InGaN-based LEDs [1]. In particular, CQDs possess key advantages over phosphors, typically used in the down-conversion of blue-emitting InGaN LEDs, for applications in visible light communications (VLC), where LEDs are used to transmit data. The shorter excited state lifetimes of CQDs mean they should perform better at higher modulation speeds [2,3] while their wavelength versatility and narrow emission spectrum pave the way for color multiplexing as a way to further increase data rates.

Recently, a single blue-emitting microsize LED (microLED) was used to demonstrate VLC at several Gb/s [4]. However, high-speed VLC (>100 Mb/s) at longer wavelengths using CQDs has not yet been achieved [2]. In this context, we study a CQD/Polymethyl methacrylate (PMMA) composite material for color converting a blue microLED. Color-conversion at different wavelengths is demonstrated and the effect of the CQD concentration on the converted light properties is discussed. It is shown that VLC at several hundreds Mb/s data rates is achievable with CQDs.

II. MATERIALS AND METHODOLOGY

The CQDs used in this work are green emitting (intrinsic emission at 540 nm) and red emitting (630 nm) alloyed-core/shell CdSSe/ZnS nanocrystals with a 6nm mean diameter. Engineering of the energy levels in such CQDs is obtained by changing the alloy composition of the core. To form the composite, the CQDs are incorporated into a PMMA matrix at different CQD-to-PMMA weight ratio (1% and 10%). The nominal thickness of the CQD/PMMA converters under study is 1mm. Two such converters can be seen in the inset of Fig. 1.

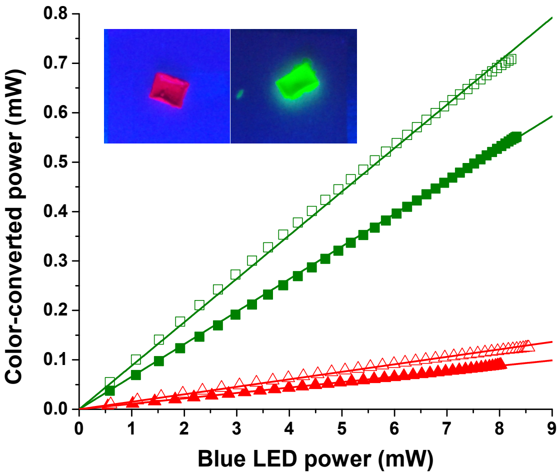

Fig. 1: Color-converted power vs. LED power for 1% (filled squared) and 10% (open square) green CQDs and for 1% (filled triangles) and 10% (open triangles) red CQDs. Inset: Red and green CQD composite samples under UV illumination.

The color converters are remotely excited with a square 100×100µm^2, 450nm-emitting microLED [5] for the characterization of the forward conversion spectrum, power efficiency and optical modulation bandwidth. Forward converted emission includes the losses of the collecting optics and is detected under continuous-wave microLED excitation with a power meter or a spectrometer. For the modulation bandwidth measurements, the microLED is dc-biased and modulated with a 0.25Vpp frequency-swept signal while the detection is done with a high-speed photodiode (1.4GHz bandwidth). Photoluminescence (PL) lifetimes are also measured using time-correlated single photon counting (Edinburgh Instruments).

VLC in free space over a meter is demonstrated using two-level pulse amplitude modulation (PAM). In this case a pulse function arbitrary generator provides the data stream to the microLED and the detection of the color-converted light is done with an avalanche photodiode. The received signal is post-processed using a Matlab script. More details about the VLC experiment can be found in [6].

[§] *S. R. is now at the University of Coventry*

[*] *Corresponding authors: miguel.leitao@strath.ac.uk and nicolas.laurand@strath.ac.uk*

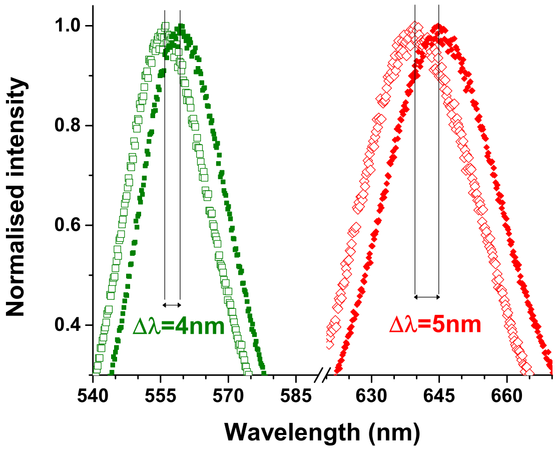

Fig. 2: (Left) Color-converted spectra for the 1% (open square) and 10% (filled squares) green CQD composite. (Right) 1% (open diamonds) and 10% (filled diamonds) red CQD composite. Note the break in the x axis.

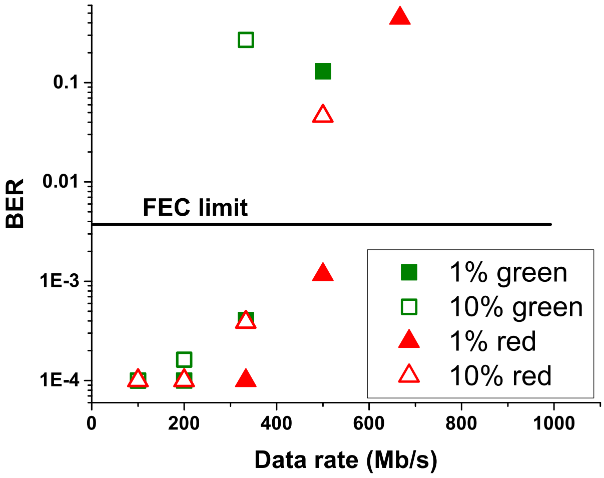

Fig. 3: BER vs. data rates for VLC experiments using 2-PAM.

III. RESULTS AND DISCUSSIONS

The plots of Fig. 1 represent the forward emitted light converted by the CQD samples vs. the incident microLED power. In terms of raw power conversion, the samples with the highest CQD concentration (10%) perform better, simply because they absorb more of the incident LED light. The efficiency of the samples, defined as the ratio of the forward color converted light (collected by the system) by the absorbed microLED power, is 8 +/- 2% for the green CQDs and 1.5 +/ 0.5% for the red CQDs. The higher efficiency of the green CQDs is attributed to the different alloy composition of the core that leads to a lower lattice mismatch with the ZnS shell than in the case of the red CQDs.

The spectra of the converted light are shown in Fig. 2. For both green and red CQDs, the spectrum shifts to longer wavelengths at higher CQD concentration because of self-absorption. The shift between the sample with 1% and 10% CQD concentration is around 5 nm. The 1% samples are already red shifted significantly when compared with more diluted samples (data not shown) with the intrinsic peak emission of the green and red CQDs at, respectively, 540 nm and 630 nm. Interestingly, the optical modulation bandwidths of the CQD samples are lower at higher CQD concentration: 15 MHz and 12 MHz for, respectively, the 1% and 10% green samples, and 27 MHz vs 17 MHz, respectively, for the 1% and 10% red samples. Measured PL lifetimes are consistent with these bandwidth values: respectively 16 ns vs. 22 ns for the green CQDs and 10 ns vs. 15 ns for the red CQD samples. This ‘slowing down’ of the color-conversion dynamics is attributed to the self-absorption effect, which is also at the origin of the spectral shift and is significant at higher CQD concentration.

The bit-error rate (BER) as a function of the data rate for VLC demonstrations using 2-PAM modulation is plotted in Fig. 3. The BER limit is 3.8x10^{-3}, considering forward error correction (FEC) could be applied. It is seen that the sample that performs the best under these conditions is the 1% red CQD samples, i.e. the color converter that has the highest modulation bandwidth, with a data rate above 500 Mb/s. The green CQD samples are more efficient but their slower modulation bandwidths means that under the same conditions the achievable data rate is a bit lower, close to 400 Mb/s. These results are consistent with both bandwidth and PL lifetime measurements. While the PL lifetimes of CQDs is their limiting factor for such application, their efficiency and narrow emission linewidths means that >1 Gb/s transmission should be possible given these results.

IV. CONCLUSION

In summary, we have demonstrated that CQDs could be utilized for color-conversion of InGaN microLEDs in VLC applications. We have reported on the properties of a format of CQD composite, operation at two different wavelengths, and discussed the effect of CQD concentration on the spectral and dynamics properties of the color-converters. 500Mb/s VLC at a single wavelength was reported.

ACKNOWLEDGMENT

This work was supported by the EPSRC programme Grant ‘Ultra-parallel visible light communications’, EP/K00042X/1. The authors acknowledge Dr. E. Xie for the microLED fabrication. Supporting data is available:
DOI: 10.15129/6440a143-7255-40cf-a214-44a79fcf11c6

REFERENCES

[1] T. Erdem and H. V. Demir, Nanophotonics 2, 1, pp. 57-81 (2013).
[2] N. Laurand et al., Optical Material Express 2, 3, pp. 250-260 (2012).
[3] J. Grubor et al., J. Lightwave Technol. 26, 24, pp. 3883-3892 (2008).
[4] D. Tsonev et al., IEEE Photonics Technol. Lett. 26, 7, pp. 637-640 (2014).
[5] Z. Gong et al., J. Appl. Phys. 107, 013103 (2010).
[6] D. C. O’Brien et al., J. Light. Technol. 30, pp. 2181-2187 (2012).